Underwater Acoustic Modelling for Synthetic Aperture Sonar

Alan J. Hunter
B.E. (Hons I)

A thesis presented for the degree of
Doctor of Philosophy
in
Electrical and Computer Engineering
at the
University of Canterbury,
Christchurch, New Zealand.

June 2006

ABSTRACT

Underwater acoustic modelling is an important aspect of Synthetic Aperture Sonar (SAS) system design and algorithm development. Sea-trials are an expensive and time-consuming exercise and simulations provide an efficient and economic alternative. However, there are few simulators (in the open literature) that can efficiently provide realistic SAS data for large, complicated scenes.

Conventional side-scan sonar simulators are not suitable for SAS data simulation. These simulators utilise narrow-beam and narrow-band approximations; typical SAS systems are wide-beam and wide-band and these approximations are invalid. Moreover, conventional side-scan sonar is a non-coherent imaging technique and SAS processing relies on the phase. Existing SAS simulators are capable of modelling very simple scenes only. They utilise a decomposition of the scene into point or smooth facet primitives, which is very inefficient. Many primitives are required and this imposes a severe restriction on scene complexity and size.

This thesis presents a rigorous mathematical framework for the modelling of SAS imagery. A novel acoustic scattering model is developed and its implementation in a wide-beam and wide-band, multiple-receiver Interferometric SAS (InSAS) simulator is detailed. The scattering model utilises a decomposition of the scene into rough (rather than smooth) facet primitives. The use of rough facet primitives provides a significant increase in computational efficiency since scenes are decomposed into fewer primitives. This facilitates the simulation of larger and more complicated scenes.

Each rough facet is characterised by its far-field beampattern. The statistics of the beampattern are related to the facet shape and roughness statistics using the Kirchhoff approximation. The beampattern is realised from its first and second-order statistics. The SAS imagery is obtained using a coherent sum of the facet responses and occlusions and multiple-scattering are resolved by ray-tracing. The simulator is implemented for use on a parallel computing cluster.

The simulator is shown to provide realistic SAS data that is qualitatively and quantitatively similar to real data. The simulated results are considered, in many ways, superior to the simulated results in the literature.

ACKNOWLEDGEMENTS

First and foremost, I would like to thank my supervisors Dr. Michael Hayes and Prof. Peter Gough. Michael has been a friend and a role-model. His methodical approach to problem solving has had great influence on my work; it is the most valuable skill that I have learnt during my time as a post-graduate student. Peter's intuitive approach and wealth of knowledge has been invaluable. In particular, his practical 'sanity checks' helped to keep me on the right path. Michael and Peter, I am indebted to you both for sharing your skills and providing me with so many opportunities.

Thanks to everyone in the Electrical and Computer Engineering Department at the University of Canterbury. Many thanks to the sonar boys and the 'R9' crew: Hayden Callow, Steve Fortune, Phil Barclay, Ed Pilbrow, Stewart Hardie, Lóic Sibeud, Mark Noonchester, and Dave Mulligan. It has been a pleasure working with you all. Hayden deserves a special mention for his guidance and useful suggestions during the early stages of my research.

I would like to acknowledge the people involved in the examination of this thesis. I am grateful to Dr. Gary Sammelmann from the Naval Surface Warfare Centre in Panama City, Florida and Prof. Mal Heron from James Cook University in Queensland, Australia; thank you for your thorough reviews and useful comments and suggestions for improvements. Thanks also to Dr. Andrew Bainbridge-Smith for chairing the defence.

I appreciate the financial support that I have received throughout my research. I would like to thank the University of Canterbury for granting me a doctoral scholarship. I would also like to acknowledge the IEEE Oceanic Engineering Society (OES) and the Marine Technology Society (MTS) for their student sponsorships, which allowed me to attend conferences in France and Singapore. Partial support from the U.S. Office of Naval Research (ONR), contract number N61331-06.T.1814 is gratefully acknowledged.

Many thanks to my software testers, Phil and Mark, and to the people that helped me proof-read this thesis and various other documents: Mike, Peter, Hayden, Ed, and my sister Louise. Thanks also to Prof. Manell Zakharia from Ecole Navale in Britanny, France for many useful discussions on ocean acoustics, Dr. Peter Smith for useful discussions on statistics, and Dave van Leeuwen for assistance with the cluster. I appreciate your useful contributions to this work.

I am grateful to the team at the Naval Surface Warfare Centre for inviting me to spend some time with them in Panama City. In particular, I would like to thank Dan Brown and Dan Cook for showing me around the region and introducing me to some fine southern cuisine.

Before beginning my Ph.D., I worked at Broadcast Communications Ltd (BCL). I would like to thank Bill Bryant and the Christchurch Engineering Consultants team for providing me with some excellent practical experience during this period.

I have had a number of flatmates over the years and I would like to thank them for their friendship. In particular, thanks to Dan Donnell and James Alexander (the Mandeville St Posse) for so many great memories. Dan deserves special mention for distracting me from my thesis work with lengthy discussions on philosophy, politics, and sci-fi. Thanks also to my good friends Fai Chan and Rosemary Sivertsen.

I would like to express my gratitude to my family. Thanks to my grandad Maurice Hunter and my uncle Wayne Hunter for inspiring me to follow a career in science and computing from a young age. Thanks Mum and Dad for your support and encouragement and thanks to my sister, Louise. Finally, I would like to thank my girlfriend, Sarah, for always being there for me. Sarah, I am looking forward to our future overseas adventures.

PREFACE

This work began as a study into the effects of sea-surface multipath in synthetic aperture sonar (SAS) imagery as an extension of the work done by Bryn Davis [Davis 2001]. Davis characterised the multipath point-spread function for the shallow water environment. The task for this research project was to develop a 3-D acoustic scattering model and SAS simulator so that the effects of sea-surface multipath could be studied further [Hayes 2004, Hayes *et al.* 2005, Hunter and Hayes 2005a]. It was immediately apparent that SAS image simulation was a difficult problem due to the huge computational requirements of acoustic wave modelling. Therefore, the focus changed from studying multipath scattering to developing an accurate and efficient SAS simulator.

The SAS simulator that was developed has been an invaluable tool for the Acoustics Research Group at the University of Canterbury. The sonar was not operational throughout most of the period of time that this research was conducted. Thus, the simulator has been used extensively to produce data for the development and testing of algorithms during this period.

In addition to the simulation of SAS imagery, research was also conducted on fast hierarchical back-projection reconstruction [Hunter *et al.* 2003a] and algorithms for an inertial navigation system [Pilbrow *et al.* 2002]. However, the research in these areas is not considered in this thesis.

PUBLICATIONS

A number of local and international conferences were attended throughout the course of research. The authored and co-authored papers are listed here in order of presentation: [Hunter *et al.* 2003b, Hunter *et al.* 2003a, Hunter and Hayes 2004, Hunter and Hayes 2005a, Hunter and Hayes 2005b, Hayes *et al.* 2005, Hunter *et al.* 2006a, Hunter *et al.* 2006b, Gough *et al.* 2006].

ASSUMED KNOWLEDGE

It is assumed that the reader of this thesis has a good background in partial differential calculus, Fourier methods, and signal processing. The reader is also assumed to be

familiar with the synthetic aperture imaging technique. Suggested background reading includes: [Strauss 1992] for partial differential calculus, [Bracewell 1986] for Fourier methods, and [Bahar 1990] for signal processing. However, there are a myriad of good textbooks available on these topics. Fourier imaging techniques are covered thoroughly in [Soumekh 1994] and a good background in synthetic aperture radar (SAR) can be found in [Carrera *et al.* 1995, Jakowatz *et al.* 1996, Soumekh 1999]. The differences between SAR and SAS are detailed in [Hayes and Gough 1992, Hawkins 1996, Callow 2003].

AUTHOR'S CONTRIBUTIONS

This thesis presents a number of original contributions to the fields of acoustic wave scattering and synthetic aperture sonar.

Scattering model – A major contribution is the extension of the standard Kirchhoff model for acoustic wave scattering. The model is extended to encompass scattering from facets with small-scale surface roughness. A scene can be decomposed into far fewer rough (rather than smooth) facets, thus, significantly reducing the computational cost of simulation. The extended Kirchhoff model is developed in Section 3.3 and the first and second-order statistics of the rough facet beampattern are derived in Sections 3.4 and 3.5. Section 3.6 details the realisation of a beampattern from the beampattern statistics and Section 3.7 derives the results for Gaussian roughness statistics. Corrections to the derivation of the standard Kirchhoff model are also given in Section 3.2.1.

SAS simulator – The extended Kirchhoff model is the basis of a multiple-receiver InSAS simulator. The simulator is capable of modelling arbitrary scenes and imaging geometries. It is able to produce simulated imagery of larger and more complicated scenes than other simulators in the literature. The simulator is described in Chapter 4. Section 4.3 details a novel Fourier domain technique that further increases the efficiency of the scattering model for triangular facets. The technique utilises the Fourier warping theorem (derived in Appendix A) and allows the calculation of the Fourier transform of an arbitrary triangular aperture from a single pre-calculated lookup table for a reference triangular aperture. The technique is then applied to the efficient modelling of time-variant facets in Section 4.3.3, partially occluded facets in Section 4.3.4, and temporal Doppler effects in Section 4.3.5. The parallel implementation of the simulator is outlined in Section 4.5.

Simulated results – The simulated results are shown in Chapter 5. These are considered, in many ways, to be superior to simulated results in the literature. The

simulated imagery demonstrates many of the important features of real SAS imagery, including coherent speckle noise, shadows cast by proud objects, aspect-dependent scattering and shadowing, and sea-surface multipath.

CONTENTS

Chapter 1

INTRODUCTION

Acoustic waves (or sound waves) provide the best means of exploration in the underwater environment. Acoustic waves propagate well underwater much like electromagnetic waves do in the Earth's atmosphere or in the vacuum of space. Electromagnetic waves (in the form of visible light) are our primary means of exploring the environment in our everyday lives. On a larger scale, the broad electromagnetic spectrum is utilised to explore our greater surroundings from the surface of the Earth to distant stars and galaxies. However, the use of electromagnetic waves is not practical in the underwater environment since the high conductivity of water impedes propagation. Furthermore, the conductivity of sea water is increased due to dissolved ion content and the penetration of electromagnetic waves into sea water is typically on the order of centimetres to tens of metres. Acoustic waves are almost unimpeded in water (particularly at low frequencies) due to its high density and are well suited for interrogating the underwater environment.

The ability to *see* underwater using acoustic waves is advantageous to many diverse fields in ocean science and engineering. Over 70% of the Earth's surface is covered by ocean and, with the floor beneath this expanse of sea water predominantly uncharted, mapping the Earth's seafloor is an important scientific goal. In addition, many commercial gains can be achieved – from planning underwater communication links or oil and gas pipelines to discovering underwater mining resources. Besides mapping the seafloor, the ability to see underwater allows us to explore underwater man-made objects. For example, monitoring the aforementioned communications links and pipelines, and locating underwater archaeological sites. In a military defense capacity, acoustic waves are useful for locating submarines and mines and for guiding underwater weaponry.

Underwater robotics is a topic of great research interest at present. Autonomous underwater robots or AUV/UUVs (autonomous/unmanned underwater vehicles) are usually equipped with acoustic imaging devices. In the future, AUVs will allow us to monitor and explore the seafloor with the same ease that we can monitor the Earth's surface using current air and space-borne radar technology.

1.1 UNDERWATER ACOUSTIC IMAGING

The science of acoustic imaging has existed, in a crude sense, for a long time. With the advent of sea-faring craft, echo detection became a way of avoiding running vessels aground. Some evidence exists of Phoenician fishermen (circa 500 B.C.) using the echoes of ringing bells to detect nearby headlands concealed by fog. Echo detection and its extension, echo location, became popular techniques after the sinking of the Titanic in 1911, with the first patent filed within two weeks of the disaster [Urick 1975]. The echo location patent was granted for location of icebergs using sound in air. The inventor, J. F. Richardson, was soon awarded another patent for the application of the same technique underwater. Underwater echo location became more important with the threat of submarine warfare in World War I and a range of techniques using steerable arrays came into use. These simple techniques have since evolved into the modern field of acoustic imaging, or sonar. An extensive history of acoustics and acoustic imaging can be found in [Hunt 1978] and [Urick 1975].

1.1.1 Echo detection and location

Echo detection and echo location are methods of detecting the presence and whereabouts of objects based on the time delay between a transmitted signal and the received echoes. The range to a target can be inferred from the propagation speed and the time delay using the relation

$$r = c\,\frac{\tau}{2}, \tag{1.1}$$

where r is the range, c is the (constant) propagation speed, and τ is the time delay.

An array is required to perform echo location in range and direction. The time delay between echoes received at elements in the array is used to infer the direction to the target as shown in Figure 1.1. The angle to the target is given by

$$\theta = \sin^{-1}\left(\frac{c\Delta\tau}{\Delta y}\right) \tag{1.2}$$

for plane waves incident on the array, where $\Delta\tau$ is the time delay between elements and Δy is the element spacing. For a narrow-band system, the phase difference between elements is used.

1.1.2 Range resolution and pulse compression

The range resolution of a pulsed echo detection/location system is proportional to the duration of the pulse. It is desirable to use a pulse of short duration to achieve good range resolution. However, large instantaneous power is required to generate a short pulse with sufficient energy and there are physical limitations on the maximum

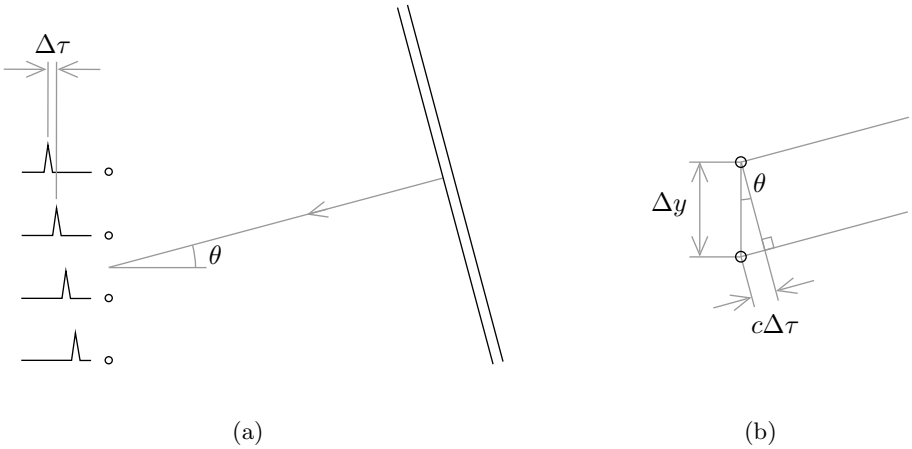

Figure 1.1 The direction to a target can be determined using the time-delay (or phase difference) between echo arrivals at array elements.

amplitude in water that prevent this (owing to non-linear effects such as cavitation [Urick 1975]); a long pulse is desirable in this respect.

Pulse-compression is a technique for obtaining high range resolution using a wide-bandwidth pulse of long duration [Hovanessian 1980, Hayes and Gough 1992]. Upon reception, the echo is correlated with the transmitted signal, or matched-filtered, i.e.,

$$e(t) = \int_{-\infty}^{\infty} e'(\tau)\, s(\tau + t)\ d\tau, \tag{1.3}$$

where $s(t)$ is the transmitted signal and $e'(t)$ is the echo. The result is an auto-correlation of the pulse that has a duration proportional to the bandwidth. The range resolution of a pulse-compressed echo is

$$\delta_r = \frac{c}{2B}, \tag{1.4}$$

where B is the signal bandwidth. The echo signals considered in this thesis are assumed to be pulse-compressed.

1.1.3 LFM chirp signal

The linear frequency-modulated (LFM) chirp[1] signal is commonly used in sonar and radar applications. The instantaneous frequency of the pulse increases (an *up-chirp*) or

[1] At audio frequencies and for a duration of approximately 1 s, the signal resembles a *chirp* sound.

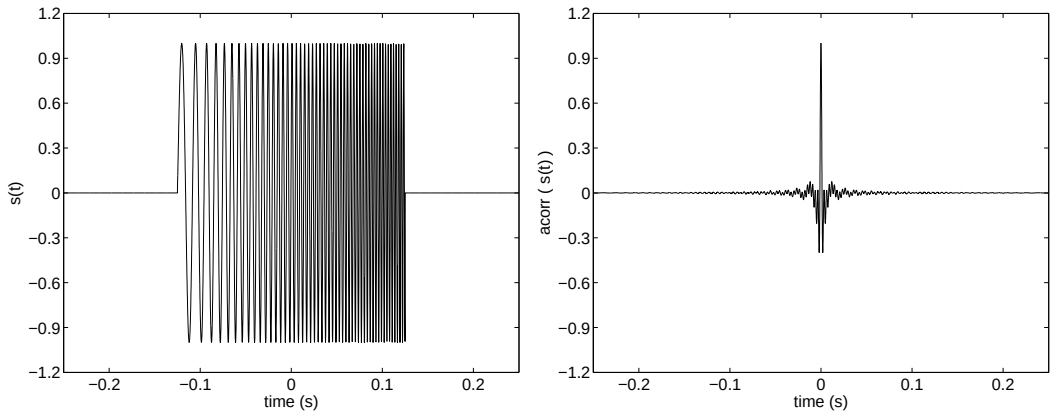

(a) up-chirp (b) auto-correlation

Figure 1.2 The LFM chirp signal is commonly used in sonar and radar applications. The instantaneous frequency of the chirp increases or decreases linearly with time.

decreases (a *down-chirp*) linearly with time. A complex chirp is given by the expression:

$$s\left(t\right) = \text{rect}\left(\frac{t}{T}\right) \exp\left(j2\pi f_c t + j\pi K t^2\right), \tag{1.5}$$

where f_c is the centre frequency, $K = B/T$ is the chirp rate, B is the chirp bandwidth, and T is the chirp length. The chirp spectrum can be approximated by

$$S\left(f\right) \approx \text{rect}\left(\frac{f - f_c}{B}\right) \sqrt{\frac{j}{K}} \ \exp\left(-j\pi \frac{\left(f - f_c\right)^2}{K}\right) \tag{1.6}$$

using the principle of stationary phase [Hawkins 1996], which is valid for a large time-bandwidth product, $B \times T$. The exact spectrum involves Fresnel integrals [Cook and Bernfeld 1967]. A chirp signal and its autocorrelation are shown in Figure 1.2. Other phase coded waveforms such as hyperbolic chirps, pseudo-random noise sequences, etc. [Cook and Bernfeld 1967, Rihaczek 1969, Brookner 1978, Skolnik 1990], are not considered here.

1.2 SIDE-SCAN SONAR

The term *sonar* is derived from the expression – sonic (or sound) navigation and ranging. It is analogous to the term *radar*, which is derived from the expression – radio detection and ranging. Sonar encompasses all systems that use sound for detection, location, or imaging.

A side-scan sonar is a particular type of imaging sonar that operates in a side-scan geometry (as opposed to depth-sounders or forward-looking sonars). The sonar is

either towed or mounted on a ship or AUV; it traverses the scene transmitting signals, or *pings*, to the side, perpendicular to a nominally linear trajectory[2] as illustrated in Figure 1.3. The signals are transmitted at regular intervals of time or space and the echoes from subsequent pings are combined in a series of raster lines to form a sonar image.

1.2.1 Image resolution

The resolution of side-scan sonar imagery in the range direction is given by the expression for echo detection (1.4) and the resolution in the along-track direction (the direction of travel) is proportional to the projection of the beam on the seafloor – this projection is termed the *footprint*. The 3 dB width of the beam is given by[3]

$$\theta_{3\,\mathrm{dB}} \approx \frac{\lambda}{D}, \tag{1.7}$$

where D is the along-track aperture length, $\lambda = c/f$ is the wavelength, and f is the frequency (see Section 2.3.5). Thus, the along-track resolution is

$$\begin{aligned} \delta_y &= r \sin\left(\theta_{3\,\mathrm{dB}}\right) && (1.8) \\ &\approx \frac{r\lambda}{D}, && (1.9) \end{aligned}$$

where r is the range. The along-track resolution is dependent on the range, frequency, and the dimensions of the physical aperture. The resolution is improved by narrowing the beam; this can be achieved by using higher frequencies and/or a longer aperture. However, high frequencies are attenuated more severely in sea water and long apertures are inconvenient.

1.2.2 Range ambiguity

The extent of the imagery in the range direction is limited at the maximum unambiguous range. The repeating pulse transmission causes echoes from beyond this range to appear as echoes in subsequent pings. The maximum unambiguous range is determined by the ping rate f_p, i.e.,

$$r_s = \frac{c}{2f_p}. \tag{1.10}$$

The unambiguous range can be increased by reducing the ping rate. However, this can lead to under-sampling for SAS unless the speed is reduced also (see Section 1.3.2).

[2] The circular side-scan geometry for circular spotlight SAS [Curlander and McDonough 1992] is not considered here.

[3] This is actually the 3.9 dB beamwidth for a rectangular aperture. However, this approximation is used in most derivations of the SAS along-track resolution. The approximation results in a theoretical resolution that is slightly worse than stated.

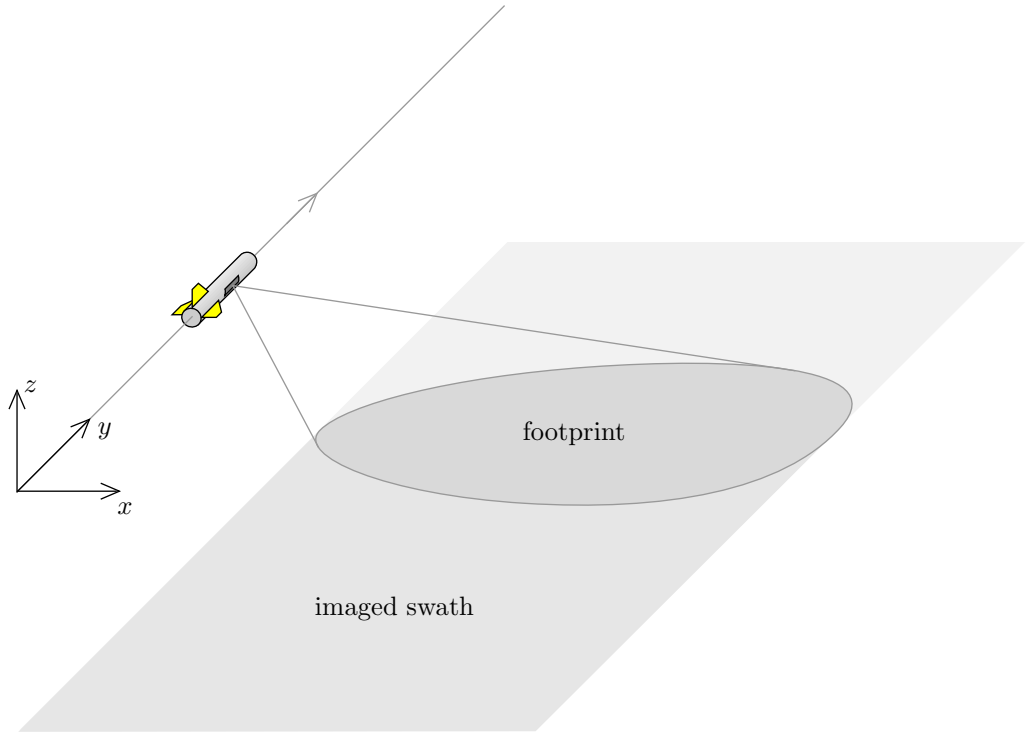

Figure 1.3 In the side-scan geometry, the sonar transmits signals to the side, perpendicular to the nominally linear trajectory.

A better technique is to employ alternating orthogonal signals [Curlander and McDonough 1992]; this is the approach used in space-borne SAR where multiple signals are in flight simultaneously. However, the use of orthogonal chirp signals results in degradation of the signal-to-noise ratio (SNR) [Axelsson 2001].

1.3 SYNTHETIC APERTURE SONAR (SAS)

Synthetic aperture processing is a technique used to improve the resolution of sonar and radar imagery. It is typically a post-processing technique. However, real-time processing is becoming more common-place [Hansen *et al.* 2005, Jean 2006]. A synthetic aperture sonar (SAS) operates in the same manner as a conventional side-scan sonar. However, it retains the phase information of the echoes; it is a coherent imaging system unlike conventional sonar, which is non-coherent. The additional information in the phase is used to synthesise an aperture that is longer than the physical aperture of the system, hence, improving the along-track resolution. The aperture synthesis is achieved by coherent integration of the echoes from subsequent pings [Curlander and McDonough 1992, Soumekh 1994, Carrera *et al.* 1995, Jakowatz *et al.* 1996].

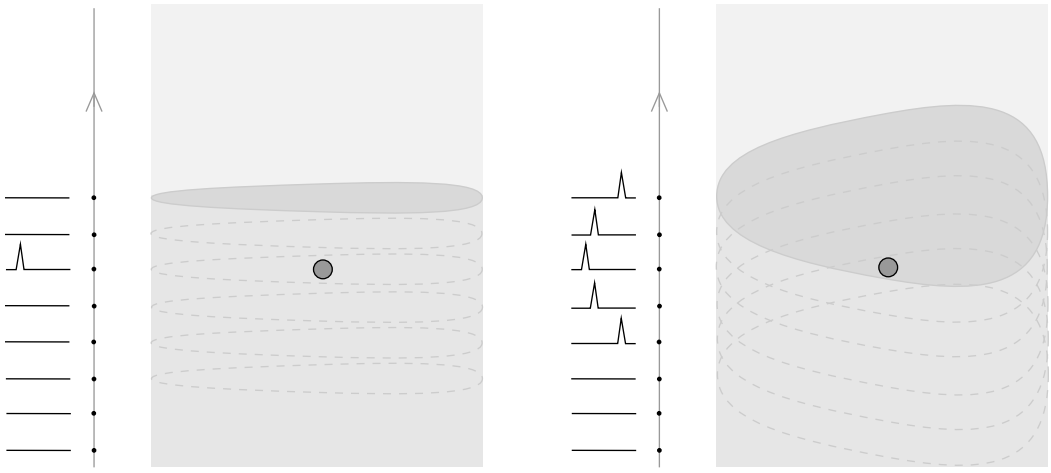

(a) narrow-beam sonar (b) wide-beam sonar

Figure 1.4 A conventional side-scan sonar utilises a narrow beam to obtain high along-track resolution. Conversely, a SAS achieves high resolution using a wide beam.

1.3.1 Along-track resolution

High along-track resolution is obtained in conventional side-scan sonar by utilising a narrow beam as shown in Figure 1.4(a). Contrary to conventional sonar, higher resolution can be obtained in SAS by using a wider beam. The wider beam illuminates points in the scene over a larger number of pings as shown in Figure 1.4(b), which allows for coherent integration over a longer synthetic aperture. The maximum synthetic aperture length is determined by the length of the trajectory for which a point in the scene is visible, i.e., within the footprint; this is dependent on the range.

The along-track resolution for a SAS is given by

$$\delta_y = \frac{r\lambda}{2L}, \tag{1.11}$$

where L is the synthetic aperture length. It is important to note the inherent factor of two improvement over conventional side-scan sonar [Soumekh 1994, Hawkins 1996]. The synthetic aperture length is given by

$$L = \frac{r}{\lambda D} \tag{1.12}$$

for a physical aperture of length D at a range r. Substituting the expression for the synthetic aperture length into (1.11) yields a theoretical resolution of

$$\delta_y = \frac{D}{2}. \tag{1.13}$$

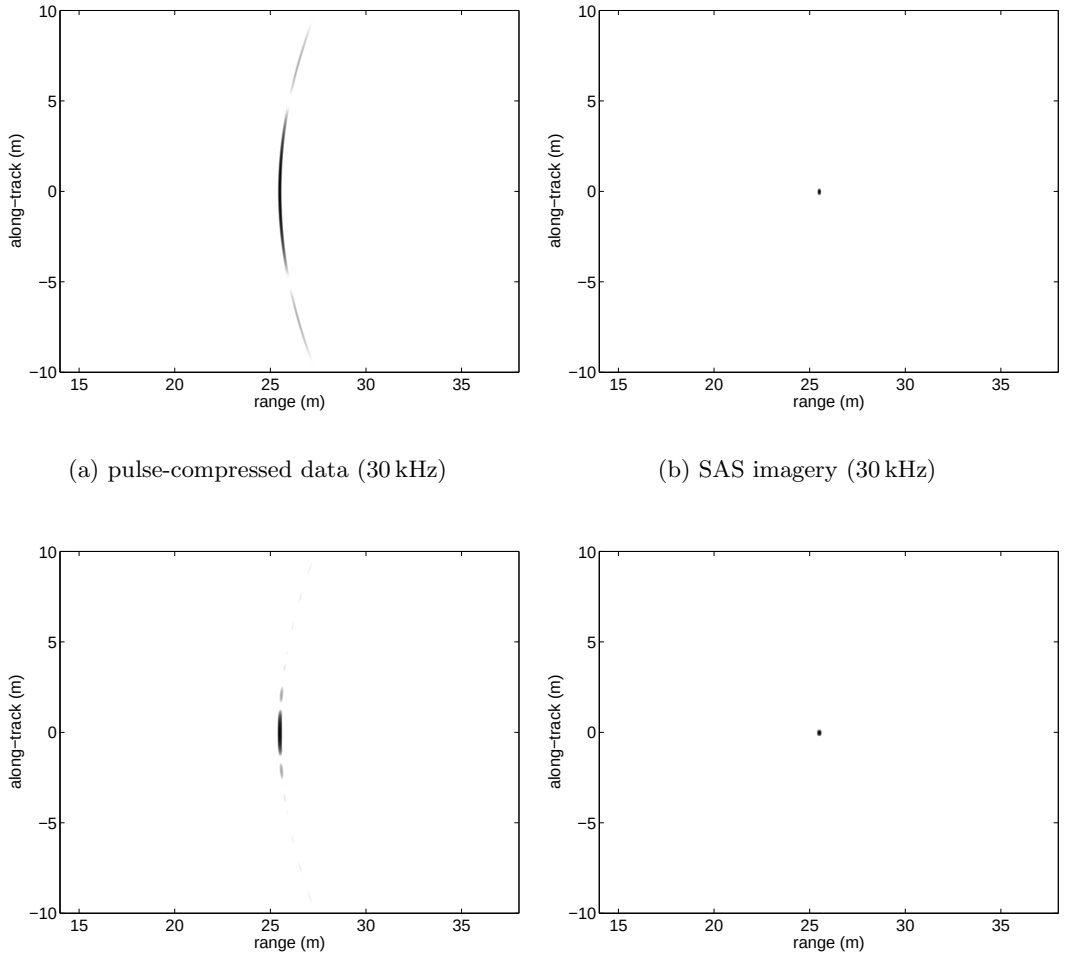

(a) pulse-compressed data (30 kHz)

(b) SAS imagery (30 kHz)

(c) pulse-compressed data (100 kHz)

(d) SAS imagery (100 kHz)

Figure 1.5 The simulated point-scatterer is imaged using the specifications of the KiwiSAS (see Section 5.1). The point is located at $\mathbf{x}_k = (25, 0, -5)$ m relative to a nominally linear sonar trajectory. Figures (a) and (b) show the raw data and reconstructed imagery at 30 kHz and Figures (c) and (d) show the raw data and reconstructed imagery at 100 kHz.

Thus, the SAS image resolution is independent of range and frequency. Example SAS imagery is shown in Figure 1.5 for a point target using the specifications of the KiwiSAS (see Section 5.1); this imagery demonstrates the resolution improvement.

The range and frequency independence of SAS imagery makes it a very desirable technology. Unlike conventional sonar, low frequencies can be employed whilst retaining high resolution. This facilitates high-resolution long-range and sub-surface imaging.

1.3.2 Sampling constraints

The synthetic aperture is a spatially sampled array. Therefore, it must adhere to the Nyquist sampling constraint. The along-track sample spacing is given by

$$\Delta y = \frac{v}{f_p}, \tag{1.14}$$

where v is the (constant) speed of the sonar and f_p is the temporal ping rate. In order to satisfy the Nyquist theorem [Bahar 1990], the along-track sample rate, $1/\Delta y$, must be greater than twice the maximum spatial frequency of the physical aperture. Under-sampling causes aliasing and results in grating lobe artefacts in the SAS imagery [Hawkins 1996].

A rectangular aperture has infinite spatial frequency extent and aliasing cannot be avoided. However, an accepted constraint limits the aliasing at the 3 dB width of the main lobe giving an along-track sampling constraint of

$$\Delta y \leq \frac{D}{2} \tag{1.15}$$

[Douglas and Lee 1992]. However, this results in aliasing of the main lobe. A better constraint uses the null-null width of the main lobe giving a sampling constraint of

$$\Delta y \leq \frac{D}{4} \tag{1.16}$$

[Hawkins 1996].

The along-track sampling constraint limits the sonar speed and/or the ping rate. A multiple-receiver along-track array can be used to overcome these limitations [Douglas and Lee 1993]. Using multiple receivers, the sampling constraint is relaxed to

$$\Delta y \leq N\frac{D}{4}, \tag{1.17}$$

where N is the number of receivers [de Heering 1982, Gilmour 1978]. However, this complicates the synthetic aperture processing [Callow 2003].

1.3.3 Synthetic aperture reconstruction algorithms

Synthetic aperture processing requires a coherent integration of subsequent pings in the echo data. While synthetic aperture processing is not detailed here (there are many good texts that cover the subject thoroughly [Curlander and McDonough 1992, Soumekh 1994, Carrera *et al.* 1995, Jakowatz *et al.* 1996]), the various synthetic aperture reconstruction algorithms are outlined.

Correlation algorithm (matched filtering) – The coherent integration of the echo data can be performed in a number of ways but the most intuitive approach is the correlation algorithm. This algorithm was used in the earliest synthetic aperture systems [Neilson 1991]. The algorithm performs a matched-filtering for the system. It operates by correlating the echo data with the expected point-spread function. For a linear trajectory, the point-spread function (PSF) is range-dependent and a correlation is performed for every range. For a non-linear trajectory, the PSF has range and along-track dependence and a correlation is required for each image pixel. The computational efficiency of the correlation algorithm is of the order M^2N^2, where M is the number of along-track pixels and N is the number of range pixels; it is very computation intensive. However, the algorithm benefits from being easily adapted to account for platform motion and Doppler effects.

Fast correlation – Fast correlation is a Fourier domain equivalent of the correlation algorithm [Gough and Hawkins 1997]. The range-variant PSF is approximated by the PSF at the centre range and the correlation is performed in the Fourier domain. The approximation is valid local to the centre range [Hayes 1989, Hayes and Gough 1992]. Thus, the algorithm operates on partitioned range blocks (where the approximation is acceptable) that are later combined in a mosaic. The fast correlation algorithm has a computational efficiency of between $(M \log_2 N)^2$ for a single block and M^2N^2 for the equivalent of the correlation algorithm. Although the fast correlation algorithm is more efficient than the correlation algorithm, it does not benefit from the same flexibility.

Filtered back-projection – Back-projection is a reconstruction algorithm used extensively in medical imaging for the similar synthetic aperture processing in computed tomography (CT) [Cho *et al.* 1993, Liang and Lauterbur 2000]. It is also used for SAR and SAS image reconstruction [Desai and Jenkins 1992, Lockwood *et al.* 2001]. The back-projection algorithm operates by *back-projecting* the echoes for each ping over spherical arcs of all possible contributing points. This is followed by a range filtering step to obtain the reconstructed image. The back-projection algorithm has a computational efficiency of M^2N; it is more efficient than the correlation method and it has the same flexibility.

Fast hierarchical back-projection (FHBP) – More recently, hierarchical back-projection algorithms have received considerable attention [Basu and Bresler 2000, Basu and Bresler 2002]. Fast factorised back-projection (FFBP) [M$^{\text{c}}$Corkle and Rofheart 1996, Banks 2002, Ulander *et al.* 2003] and fast polar back-projection (FPBP) [Frölind 2004, Shippey *et al.* 2005] operate by applying an approximation for the back-projection algorithm to a hierarchy of low to high resolution data-sets. The hierarchical

process has an inherent factor of two improvement for each level of the hierarchy (referred to as a stage), which results in a theoretical computational efficiency of order $M \log_2 (MN)$. This is equivalent to the efficiency of the wavenumber and chirp-scaling algorithms. However, the number of stages is restricted by the image dimensions and the efficiency is typically worse than the stated theoretical value [Hunter *et al.* 2003a]. The benefit of the hierarchical approach is that the algorithm can be stopped at any stage to give a reduced resolution image. This makes it ideal for real-time operation. FFBP and FPBP benefit from the same flexibility as the correlation and back-projection algorithms.

Wavenumber (ω–k) algorithm – The wavenumber algorithm was taken from the seismic imaging field [Stolt 1978]. It was first modified for SAR [Cafforio *et al.* 1991b, Cafforio *et al.* 1991a, Milman 1993] and then SAS [Hawkins and Gough 1995b]. The algorithm operates in the Fourier domain and it is often referred to as the ω-k algorithm for this reason (referring to the temporal and spatial frequency ordinates). The Fourier-domain data is remapped using the appropriate transformation of coordinates – the Stolt mapping – and then inverse Fourier transformed to obtain the reconstructed data [Soumekh 1994]. The wavenumber algorithm is very simple to implement and it is fast; it has a computational efficiency of order $M \log_2 (MN)$. The major problem with the wavenumber algorithm is its requirement for regularly sampled data, which makes motion compensation more difficult. The wavenumber algorithm has been chosen to reconstruct the imagery throughout this thesis due to its simplicity and computational efficiency.

Other popular SAS reconstruction algorithms include the range-Doppler [Bamler 1992, Carrera *et al.* 1995, Curlander and McDonough 1992] and chirp-scaling algorithms [Cumming *et al.* 1992, Runge and Bamler 1992, Raney *et al.* 1994]. The reader is referred to [Hawkins 1996] for a thorough description and comparison of synthetic aperture algorithms and their application to SAS imaging.

A number of stages are typically involved in the SAS processing chain in addition to the aperture synthesis. Before reconstruction the deviations from a linear trajectory must be estimated and corrected. Autofocus techniques can then be employed to correct for residual uncompensated motion. For an interferometric SAS (InSAS), the reconstructed imagery is used to obtain an estimate of the scene topography. Finally, the imagery and bathymetry is interpreted for the detection and classification of targets and features. The stages of the SAS processing chain are outlined in Figure 1.6.

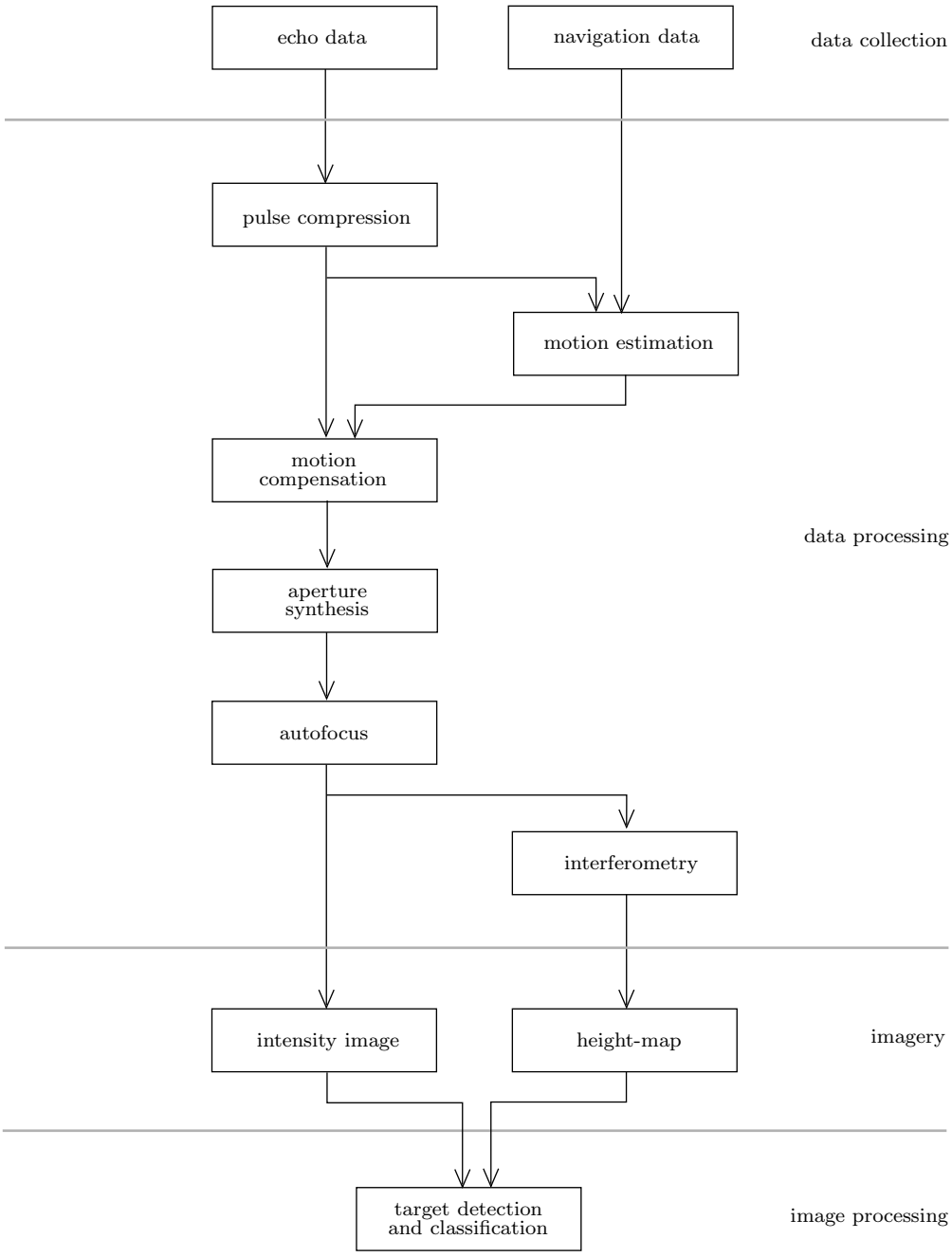

Figure 1.6 A typical SAS processing chain.

1.3.4 Motion compensation and autofocus

The synthetic aperture reconstruction algorithms are sensitive to uncompensated deviations from an assumed linear trajectory. Uncompensated deviations result in corruption of the reconstructed imagery. Therefore, estimation of the motion and compensation of the echo data is required.

Unwanted motion is inevitable in any towed or AUV-based sonar due to the variability of the ocean environment, e.g., due to currents, wave motion, etc. Navigation systems can be used to provide an estimate of the platform motion or, alternatively, autofocus techniques can be used to estimate the motion from the echo data. Often a combination of the two is employed.

A navigation system can be internal and/or external to the sonar platform. An internal navigation system consists of a collection of sensors, e.g., gyroscopes, accelerometers, magnetometers, Doppler velocity logs, etc., that are used to estimate the position and orientation of the sonar. An external navigation system achieves this by triangulation of the sonar position using passive or active sonar. However, determination of the sonar orientation using an external navigation system is more difficult. The reader is referred to [Pilbrow 2007] for an in-depth analysis of SAS navigation systems.

The autofocus technique uses the echo data itself to estimate and correct the sonar motion. This technique is desirable since it does not require additional navigation hardware. Another advantage is that autofocus algorithms can account for variations in the medium, which cause image corruption and are difficult to measure. A number of autofocus algorithms are available, including shear average, prominent point, displaced phase-centre (DPC or DPCA), phase curvature (PCA), and phase gradient autofocus (PGA) algorithms. The reader is referred to [Callow 2003] and [Fortune 2005] for a comprehensive description and comparison of SAS autofocus algorithms.

1.3.5 Interferometric SAS (InSAS)

An interferometric sonar (or radar) employs a vertical receiver array to estimate the topography of the imaged scene. The time-delay (or phase difference) between echoes received at elements in the array is used to infer the angle of the echo arrivals as described for the echo location system in Section 1.1.1. This is then used to determine the height as shown in Figure 1.7. The result is a 3-D bathymetric reconstruction.

A problem with the approach is determining which echoes correspond to the same regions of the scene; this is referred to as the registration problem. It is a paradox since the registration of the data requires knowledge of the (unknown) seafloor topography. For an investigation of InSAS the reader is referred to [W. W. Bonifant 1999], [Banks 2002], and [Barclay 2006].

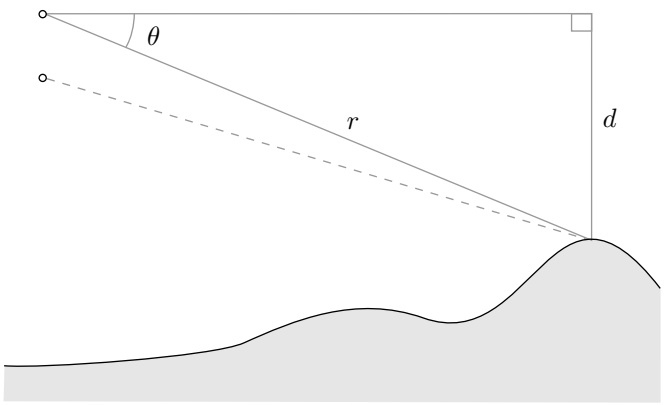

Figure 1.7 An interferometric sonar estimates the topography using the time-delay (or phase difference) between echoes received at the elements in a vertical array. The phase difference can be used to determine the angle of arrival θ and, by the Pythagoras theorem, the depth d can be inferred.

1.4 SAS IMAGE SIMULATION

A major problem in the research of underwater acoustic imaging is the difficulty in obtaining accurate ground-truth. For radar, the imagery can be compared with aerial photography or surveys. However, optical visibility is no more than a few metres underwater and sufficiently accurate surveys are typically infeasible. Without accurate ground-truth, the validation of acoustic imagery is difficult.

Simulated data provides a means of assessing the performance of acoustic imaging algorithms. A known scene model is used to generate the echo data. Thus, the reconstructed imagery can be compared with the model. Furthermore, the ability to generate simulated data reduces the need for time-consuming and expensive sea-trials.

1.4.1 Conventional side-scan simulators

There are a number of sonar simulators in the open literature and several of these are specific to conventional side-scan sonar. However, conventional side-scan simulators are not suitable for SAS data simulation. Side-scan sonars typically use narrow-beam and narrow-band approximations. In general, SAS systems are wide-band and wide-beam and these approximations are invalid. Moreover, conventional side-scan sonar is a non-coherent imaging technique and SAS processing relies on the phase coherence from ping to ping. Regardless, the conventional side-scan simulators are summarised here for completeness.

Heriot-Watt simulator – One of the first comprehensive side-scan simulators was developed by the Ocean Systems Laboratory at Heriot-Watt University in Edinburgh, Scotland. The simulator was initially developed by Dr. Bell for her Ph.D. thesis

[Bell 1995]. It uses ray-tracing [Foley *et al.* 1997] to model the acoustic wave propagation and assumes Lambertian scattering [Foley *et al.* 1997] for the diffuse back-scattered field. The simulator has since been extended in a collaborative research project with the Defense Evaluation and Research Agency (DERA), which is now QINETIQ, and the Engineering and Physical Sciences Research Council (EPSRC). Bell's simulator has been used recently for model-based detection and classification of mines [Bell *et al.* 2004].

Limerick simulator – A more recent side-scan simulator has been developed by the Mobile and Marine Robotics Group at the University of Limerick, Ireland [Riordan *et al.* 2005]. The simulator uses ray-tracing and the Jackson back-scattering model [Mourad and Jackson 1989] to generate the imagery. It is similar to Bell's simulator. However, real-time operation is achieved through the use of a view-dependent mesh refinement scheme [Hoppe 1997, Kim and Lee 2001]. Use of the mesh refinement scheme has achieved an order of magnitude increase in computational efficiency.

The SAS simulators described in the next section are capable of generating data for a conventional side-scan sonar. However, the converse does not apply.

1.4.2 SAS/SAR simulators

The simulation of coherent sonar or radar imagery is a more difficult problem than the simulation of non-coherent imagery. The conventional side-scan simulators employ a non-coherent assumption for simplification. However, the formation of conventional side-scan sonar imagery is, in general, a coherent process. For instance, the imagery generated by the non-coherent simulators described in the previous section does not exhibit coherent speckle noise [Dainty *et al.* 1975], which is present in most side-scan sonar imagery. Although the phase is not important for conventional side-scan image generation it does affect the imagery and should not be ignored.

SWAT – There are a number of SAS simulators that have been described in the open literature. However, the Shallow Water Acoustics Toolkit (SWAT) [Sammelmann 2001, Sammelmann 2003] was the first simulator capable of producing realistic SAS imagery. SWAT was developed and is currently maintained by Dr. Sammelmann at the Naval Surface Warfare Centre (previously the Coastal Systems Station or CSS) in Panama City, Florida. Sammelmann has been developing and maintaining SWAT, for which he holds a patent [Sammelmann 1998], for the last 10 years.

The SWAT simulator employs two scattering models. Targets of interest are modelled using analytic expressions; these are available for simple targets such as spheres, cylinders, etc. and more complicated targets can be constructed from these primitives. The sea-floor reverberation is modelled as a collection of points or small facets

using the Kirchhoff approximation (see Section 3.2.1). Wave propagation is modelled by ray-tracing and the ray-tracing code employs a novel ray interpolation scheme for increased efficiency [Sammelmann 2005]. Sub-surface penetration is modelled using a Bragg scattering approximation. In addition, SWAT models a number of second-order effects including sea-surface multipath and volume scattering from bubble clouds, etc.

The SWAT simulator is very comprehensive. However, it does pose some limitations. The use of analytic expressions for the targets, although accurate and efficient, restricts the class of simulated scenes and the reverberation model assumes a flat seafloor geometry.

SARAS – The development of SWAT was pre-dated by the Synthetic Aperture Radar Advanced Simulator (SARAS) [Franceschetti *et al.* 1992, Migliaccio 1992], [Franceschetti *et al.* 1998a, Franceschetti *et al.* 2001, Franceschetti *et al.*] for SAR image simulation. SARAS was developed by Prof. Franceschetti at the University of Naples, Italy. It has since been extended for modelling InSAR imagery [Franceschetti *et al.* 1998b] and the spotlight imaging geometry [Carrera *et al.* 1995, Franceschetti *et al.* 2002]. Franceschetti has also been involved in developing numerical scattering models for SAR applications [Franceschetti *et al.* 2000].

SARAS employs the Kirchhoff approximation to model the scattering from a facet-based scene representation. The simulator employs a narrow-beam approximation. This is justified by assuming the beamwidth of the synthetic aperture (rather than the physical aperture). However, this assumption is questionable. The raw echo data is then obtained by convolution of the SAR imagery with the point-spread function for the SAR. Although the narrow-beam assumption greatly increases the simulation efficiency, it neglects the wide-beam effects.

Other SAS simulators – Recently there has been more interest in the simulation of SAS imagery and a number of groups have developed their own SAS simulators [Davis 2001, Banks 2002, Robert *et al.* 2005, Quesson *et al.* 2005, Groen 2006]. These simulators all use the standard Kirchhoff model with ray-tracing.

1.5 THESIS OUTLINE

This thesis considers the problem of data simulation for synthetic aperture sonar. Chapter 2 gives an introduction to the fundamentals of fluid dynamics and acoustic wave theory; this is required for the development of the scattering model in Chapter 3. The simple point scattering model is described first, followed by the standard Kirchhoff scattering model for smooth facets. A novel extension of the Kirchhoff model is then introduced. The proposed model is capable of simulating rough facets; the use of rough (as opposed to smooth) facets yields a significant increase in computational

efficiency. Chapter 4 details the implementation of the proposed scattering model in the simulator and a number of implementation enhancements are given; the parallel implementation of the code is also described. Finally, the results from the simulator are demonstrated in Chapter 5 and conclusions and suggestions for future research are given in Chapter 6.

Chapter 2

ACOUSTIC WAVE PROPAGATION AND SCATTERING

Sound is defined as a transient disturbance in a fluid medium[1]. Such disturbances behave as acoustic waves governed by the differential equations of fluid mechanics theory. In this chapter, the fundamental principles of acoustics are explored. The acoustic wave equation is introduced and used to explain the wave phenomena of propagation and scattering. Propagation and scattering are two (coupled) mechanisms that describe the behaviour of acoustic wave fields. Propagation concerns the spatio-temporal evolution of the field and scattering concerns the behaviour of the field at discontinuities in the medium.

Acoustic propagation in homogeneous and (continuous) inhomogeneous media are detailed in Sections 2.3 and 2.4 and further developed using ray theory in Section 2.4.3. Acoustic scattering is outlined in Section 2.5 and an acoustic scattering model is detailed in Chapter 3. A brief summary of fluid mechanics theory is presented next, followed by acoustic field theory in Section 2.2.

2.1 FLUID MECHANICS THEORY

Fluid mechanics is a vast field of study with many applications, including aerodynamics, geology, and, of course, acoustics. An in-depth discussion of fluid mechanics is best left to one of the many texts available on the subject, e.g., [Munson *et al.* 1998]. However, the fundamental quantities and concepts are summarised here as foundation for later theory development.

[1] A fluid medium is considered a material continuum that is unable to support shear stress, i.e., the gas and liquid states of matter. The more general elastic medium (encompassing the solid state of matter) is not considered here.

2.1.1 Fluid characteristics

The state of a fluid medium is defined by its density, pressure, and temperature, and by the motion of its constituent elements. These parameters are inter-related and dependent on the spatial coordinates $\mathbf{x} = (x, y, z)$ and time t. The relationship between the parameters depends on the characteristics of the fluid.

The fluid density ρ is a scalar field describing the quantity of mass within a unit volume;

$$\rho(\mathbf{x}, t) = \lim_{\Delta V \to 0} \frac{\Delta m(\mathbf{x}, t)}{\Delta V}, \tag{2.1}$$

where Δm is the mass contained within the volume ΔV, and ρ has units of kg/m^3. Fluid pressure p is a scalar field describing the force exerted per unit area;

$$p(\mathbf{x}, t) = \lim_{\Delta A \to 0} \frac{\Delta F(\mathbf{x}, t)}{\Delta A}, \tag{2.2}$$

where ΔF is the (normal) force exerted on the area ΔA, and p has units of N/m^2 (Pa). The equation of state,

$$p = p(\rho, T), \tag{2.3}$$

relates the pressure to the density and temperature T for a given fluid and can be represented by the bulk modulus of elasticity B.

The bulk modulus characterises a fluid's resistance to compression and relates the differential change in pressure ∂p to the differential change in density $\partial \rho$. The bulk modulus is defined by

$$B(\rho, T) = \rho \frac{\partial}{\partial \rho} p(\rho, T) \tag{2.4}$$

and has units of pressure (Pa). For liquids the bulk modulus is large, meaning a large pressure change is required to effect a small change in density. Conversely, the bulk modulus is small for gases. For many applications the bulk modulus may be considered constant, e.g., for small variations about an equilibrium state

$$B \approx \rho_0 \frac{\partial}{\partial \rho} p(\rho_0, T_0), \tag{2.5}$$

where ρ_0 and T_0 are the equilibrium density and temperature. An incompressible fluid ($B = \infty$) has constant density irrespective of pressure and temperature.

Fluid motion is defined by the velocity $\mathbf{v}$. Fluid velocity is a vector field describing the average motion of the constituent elements of fluid and has units of m/s. For many applications the velocity field may be considered irrotational[2], i.e., the curl of the field is zero;

$$\nabla \times \mathbf{v}(\mathbf{x}, t) = \mathbf{0}, \tag{2.6}$$

[2]Rotational flow is significant in highly viscous fluids and near fluid boundaries or in turbulence.

where $\nabla = (\partial/\partial x, \partial/\partial y, \partial/\partial z)$ is the Laplacian operator and $\times$ denotes the cross product. An irrotational velocity field may be considered the spatial gradient of a scalar field;

$$\mathbf{v}(\mathbf{x}, t) = \nabla\psi(\mathbf{x}, t) \tag{2.7}$$

[Ziomek 1995], where the scalar field ψ is called the velocity potential and has units of m^2/s. In general, the relationship between the velocity potential and the fluid pressure or density is complicated. However, the velocity potential is related to the fluid pressure by the approximation

$$p(\mathbf{x}, t) \approx -\rho_0 \frac{\partial}{\partial t}\psi(\mathbf{x}, t) \tag{2.8}$$

for small variations about an equilibrium state in an inviscous fluid [Ziomek 1995].

The viscosity of a fluid is a measure of its resistance to flow; it may be thought of as internal friction. For an incompressible fluid, the viscosity is defined by the expression

$$\tau_{ij}(\mathbf{x}, t) = \mu D_{ij}(\mathbf{x}, t) - p(\mathbf{x}, t)\,\delta_{ij} \tag{2.9}$$

[Spencer 1980]. The coefficient of shear viscosity μ relates the stress tensor field $\boldsymbol{\tau}$ to the deformation (or rate of strain) tensor field $\mathbf{D}$ given by

$$D_{ij}(\mathbf{x}, t) = \frac{\partial}{\partial x_j} v_i(\mathbf{x}, t) + \frac{\partial}{\partial x_i} v_j(\mathbf{x}, t), \tag{2.10}$$

where $v_i = \mathbf{v}\cdot\hat{\mathbf{x}}_i$, $x_i = \mathbf{x}\cdot\hat{\mathbf{x}}_i$, $\hat{\mathbf{x}}_i$ is the unit vector in the i^{th} dimension, and $\cdot$ denotes the dot product. $\boldsymbol{\delta}$ is the Kronecker delta and $\boldsymbol{\tau}$ and $\boldsymbol{D}$ are second-order tensors [Bourne and Kendall 1977]. The stress tensor is a generalisation of the pressure field p and has units of Pa. It encompasses the shear stresses in addition to the normal (pressure) stress. The shear viscosity has units of $\mathrm{Pa}\cdot\mathrm{s}$ and is the principal means by which energy is dissipated as heat in a fluid. A viscous fluid is often referred to as a *lossy* fluid for this reason. Viscosity is highly temperature dependent. However, it is usually constant[3] for a fixed temperature.

Fluids exhibit a number of other characteristics [Munson *et al.* 1998]: A second coefficient of viscosity η (or coefficient of bulk viscosity) is required to describe compressible viscous fluids; a coefficient of thermal conductivity κ is required to describe heat flow; and different fluids have different chemical compositions, resulting in further characteristics. In particular, the bulk viscosity and chemical composition affect energy losses in acoustic wave propagation as detailed in Section 2.3.7.

The characteristics described here are usually sufficient to distinguish one fluid from another. Often, fluid characteristics are simplified by assuming the fluid is incompressible, inviscous, and that the velocity field is irrotational. Such assumptions are

[3]Fluids for which the relationship between stress and deformation is non-linear are referred to as non-Newtonian and are not considered here.

made at various stages in the derivation of the acoustic wave equation and the velocity potential is used to define the fluid state throughout this thesis.

2.1.2 Navier-Stokes equations

Fluid behaviour is governed by the constitutive equations of fluid mechanics theory: the conservation of mass, momentum, and energy laws. Collectively, these equations are known as the Navier-Stokes equations. The conservation of mass law states that mass cannot be created nor destroyed, i.e., that the temporal rate of change of mass is zero. This is specified by the equation of continuity,

$$\frac{\partial \rho}{\partial t} + \mathbf{v} \cdot (\nabla \rho) = 0. \tag{2.11}$$

The conservation of momentum law is a generalisation of Newton's second law of motion, which states that the temporal rate of change of momentum is equal to the net applied force. This is specified by Cauchy's equation of motion,

$$\frac{\partial}{\partial t}(\rho \mathbf{v}) + \mathbf{v} \cdot \nabla (\rho \mathbf{v}) = -\nabla p + \left(\frac{4}{3}\mu + \eta\right) \nabla (\nabla \cdot \mathbf{v}), \tag{2.12}$$

for an irrotational velocity field. The conservation of energy law is equivalent to the first law of thermodynamics, which requires that the total energy of the fluid remains constant. This law is not presented here since it is not necessary in the derivation of the wave equation due to the assumption that the process is either isothermal (constant temperature) or adiabatic (constant entropy) [Kinsler *et al.* 2000].

The six variables, ρ, p, $\mathbf{v} = (v_x, v_y, v_z)$, and T, are related via the Navier-Stokes equations, which constitute five independent differential equations. With the inclusion of the equation of state (2.3), this set of equations facilitates the solution of all fluid mechanics problems. However, these equations are highly non-linear and, in general, an exact analytic solution cannot be obtained. For most applications approximations to the Navier-Stokes equations are required in order to obtain a solution.

2.2 ACOUSTIC FIELD THEORY

A transient disturbance in the state of a fluid medium is referred to as an acoustic disturbance. Acoustic disturbances travel away from the source (or propagate) in a wave-like manner and at a speed determined by the medium characteristics. Two types of wave can exist in an elastic medium: transverse waves and longitudinal waves. The velocity field is non-zero in the direction of propagation for a longitudinal wave and non-zero perpendicular to the direction of propagation for a transverse wave. The longitudinal wave-type is dominant in a fluid medium and is referred to as an acoustic wave.

The Navier-Stokes equations describe the many modes of fluid behaviour including acoustic wave behaviour. For small-scale acoustic disturbances, linear approximations to the Navier-Stokes equations may be used to obtain a simplified governing equation: the linear acoustic wave equation[4].

2.2.1 Acoustic wave equation

Acoustic disturbances can be regarded as deviations of the fluid state about an equilibrium state, i.e.,

$$p\left(\mathbf{x},t\right)=p_0+p'\left(\mathbf{x},t\right), \tag{2.13}$$

for the pressure field, where p_0 is the equilibrium (or ambient) pressure and p' is the deviation, which is termed the acoustic pressure. Similar formulations can be made for the other state variables. The acoustic quantities are considered for the remainder of the thesis, and the prime denoting the acoustic quantity is omitted. Thus, p represents the acoustic pressure, ρ the acoustic density, etc.

The linear approximation to the equation of state can be obtained from (2.5) and is given by

$$p=c^2\rho, \tag{2.14}$$

where

$$c=\sqrt{\frac{B}{\rho_0}} \tag{2.15}$$

is the propagation speed. The linear approximations to the Navier-Stokes equations are given by

$$\frac{\partial\rho}{\partial t}+\rho_0\nabla\cdot\mathbf{v}=0 \tag{2.16}$$

and

$$\rho_0\frac{\partial}{\partial t}\mathbf{v}=-\nabla p+\left(\frac{4}{3}\mu+\eta\right)\nabla\left(\nabla\cdot\mathbf{v}\right). \tag{2.17}$$

These approximations are valid for small-scale acoustic disturbances.

The linear approximations (2.14), (2.16), and (2.17) can be combined to yield the linear acoustic wave equation for the velocity potential,

$$\left(1+\frac{\left(\frac{4}{3}\mu+\eta\right)}{\rho_0c^2}\frac{\partial}{\partial t}\right)\nabla^2\psi\left(\mathbf{x},t\right)-\frac{1}{c^2}\frac{\partial^2}{\partial t^2}\psi\left(\mathbf{x},t\right)=0 \tag{2.18}$$

[Ziomek 1995], which, for inviscous fluid media, reduces to

$$\nabla^2\psi\left(\mathbf{x},t\right)-\frac{1}{c^2}\frac{\partial^2}{\partial t^2}\psi\left(\mathbf{x},t\right)=0. \tag{2.19}$$

[4]The terms *acoustic wave equation* or *wave equation* will be used henceforth to mean the *linear acoustic wave equation*. Non-linear acoustic wave behaviour is not considered here.

The acoustic pressure, density, etc., can be shown to obey similar wave equations. In general, the propagation speed is space and time-variant, i.e., $c = c(\mathbf{x}, t)$. Media for which the propagation speed is constant are referred to as homogeneous and the more general media is referred to as inhomogeneous.

The wave equation is a hyperbolic partial differential equation (PDE) [Strauss 1992] that governs the behaviour of small-scale acoustic disturbances. An infinite number of solutions to this equation exist. However, a unique solution can be obtained by imposing appropriate boundary conditions. Boundary conditions are specific to each environment and are discussed in Section 2.2.3.

2.2.2 Helmholtz equation

An alternative representation of the acoustic wave equation can be developed in the temporal frequency domain. Taking the Fourier transform [Bracewell 1986] of the wave equation (2.18) yields an elliptic PDE; the Helmholtz equation,

$$\nabla^2 \psi(\mathbf{x}, f) + K^2 \psi(\mathbf{x}, f) = 0, \tag{2.20}$$

where

$$\psi(\mathbf{x}, f) = \int_{-\infty}^{\infty} \psi(\mathbf{x}, t) \exp(-j\ 2\pi f t)\ dt \tag{2.21}$$

is the Fourier transform of the acoustic velocity potential $\psi(\mathbf{x}, t)$ and f is the temporal frequency,

$$K = \frac{1}{\sqrt{1 + j\ 2\pi f \tau}}\ k \tag{2.22}$$

is the complex wavenumber,

$$k = \frac{2\pi f}{c} \tag{2.23}$$

is the (real) temporal wavenumber, and

$$\tau = \frac{\frac{4}{3}\mu + \eta}{\rho_0 c^2} \tag{2.24}$$

is the viscous relaxation time. For inviscous fluid media, (2.20) reduces to

$$\nabla^2 \psi(\mathbf{x}, f) + k^2 \psi(\mathbf{x}, f) = 0. \tag{2.25}$$

The complex wavenumber is assumed for the remainder of the thesis (unless otherwise stated) and is, henceforth, represented by the symbol k (instead of K) for notational convenience.

The Helmholtz equation describes the behaviour of *time-harmonic* waves of the form $\exp(j2\pi f t)$. This *mixed* notation (used extensively throughout the literature)

confuses the time and frequency domains and is not used here. Instead, a more consistent approach is employed where $\psi(\mathbf{x}, f)$ is given by (2.21), i.e., $\psi(\mathbf{x}, f)$ is the frequency-domain representation of the acoustic velocity potential $\psi(\mathbf{x}, t)$.

2.2.3 Boundary conditions

To solve the wave equation, or any differential equation, the appropriate boundary conditions must be established. A boundary condition is a restriction on the solution to meet the physical constraints imposed by the environment. Imposing sufficient boundary conditions reduces the solution space to a unique result corresponding to the physically realised field. A differential equation for which the boundary condition is sufficiently specified is referred to as *well posed*.

The three common boundary conditions are the Dirichlet, Neumann, and Robin (or mixed) boundary conditions. These boundary conditions are specified by

$$g(\mathbf{x}', f) = h(\mathbf{x}', f), \tag{2.26}$$

$$\frac{\partial}{\partial \hat{\mathbf{n}}} g(\mathbf{x}', f) = h(\mathbf{x}', f), \tag{2.27}$$

and

$$\frac{\partial}{\partial \hat{\mathbf{n}}} g(\mathbf{x}', f) + A\, g(\mathbf{x}', f) = h(\mathbf{x}', f) \tag{2.28}$$

respectively, where g is the solution to the differential equation and h is the condition to be satisfied on a surface S, $\hat{\mathbf{n}}$ is the unit normal on S, and $\mathbf{x}'$ is a point on S. The operator $\partial/\partial\hat{\mathbf{n}} = \hat{\mathbf{n}} \cdot \nabla$ denotes the directional derivative and A is a constant.

In acoustics, a soft boundary (or pressure-release boundary) corresponds to the Dirichlet boundary condition for the pressure field, i.e., $p = 0$. The sea-surface can be approximated by a soft boundary. A hard boundary corresponds to the Neumann boundary condition for the velocity field, i.e., $\partial \mathbf{v}/\partial \hat{\mathbf{n}} = 0$. Hard boundaries are specified for the surfaces of rigid objects. The Robin boundary condition is specified for boundaries that are neither soft nor hard. The sea-floor is an example of this type of boundary. However, it can be approximated by a soft or hard boundary in some cases [Kinsler *et al.* 2000].

2.2.4 Green's functions

A Green's function is a special solution to a differential equation. It is the solution for an impulse source, which satisfies a given set of boundary conditions. There are an infinite number of Green's functions for the wave equation. However, the imposed boundary conditions isolate the unique Green's function for a particular problem. Once a Green's function has been found, it can be used to find the solution for arbitrary source distributions [Duffy 2001].

The free-space Green's function is of particular interest. It is the Green's function for a homogeneous environment and is defined by the equation

$$\nabla^2 G\left(\mathbf{x}, \mathbf{x}', f\right) + k^2 G\left(\mathbf{x}, \mathbf{x}', f\right) = -\delta\left(\mathbf{x} - \mathbf{x}'\right), \tag{2.29}$$

where G is the free-space Green's function, δ is the Dirac delta function, and $\mathbf{x}'$ is the position of the source. Solving (2.29) yields the expression for the free-space Green's function:

$$G\left(\mathbf{x}, \mathbf{x}', f\right) = G\left(\mathbf{r}, f\right) = \frac{\exp\left(-jkr\right)}{4\pi r}, \tag{2.30}$$

where

$$\mathbf{r} = \mathbf{x} - \mathbf{x}' \tag{2.31}$$

and

$$r = |\mathbf{r}|. \tag{2.32}$$

This solution is valid in the source-free region $\mathbf{x} \neq \mathbf{x}'$. The form of the free-space Green's function is intuitively satisfying. The amplitude component $1/4\pi r$ describes the attenuation due to spherical spreading and the phase component $\exp\left(-jkr\right)$ describes a linear evolution of the phase.

The form of the Green's function is, in general, dependent upon the source position and the boundary conditions. Consequently, Green's functions can be difficult to find. Often the Green's function is obtained via approximations to the differential equation or the boundary conditions. Alternatively, numerical methods can be used. Green's functions are used throughout the thesis. In particular, the free-space Green's function is utilised to approximate the Green's function for inhomogeneous media.

2.3 PROPAGATION IN HOMOGENEOUS MEDIA

Acoustic waves propagate away from the source of an acoustic disturbance; this phenomenon is referred to as acoustic radiation. In homogeneous media, acoustic radiation and propagation can be described using the Kirchhoff-Helmholtz integral. In general, however, fluid media are inhomogeneous. Nevertheless, often the region around an acoustic source can be considered homogeneous. The Kirchhoff-Helmholtz integral can be used to determine the radiation from a source and other methods can be used to model the propagation in inhomogeneous regions.

2.3.1 Kirchhoff-Helmholtz integral

The Kirchhoff-Helmholtz integral (KHI) is an expression relating the value of the field ψ at a position $\mathbf{x}$ to the values of the field and its normal-derivative $\partial\psi/\partial\hat{\mathbf{n}}$ (the boundary conditions) over a closed surface S. The KHI was derived first by Helmholtz

in acoustics followed by Kirchhoff in electromagnetics [Kirchhoff 1882]. Here a scalar acoustic field is considered; extension to a vector field is covered in [Goodman 1968].

Given a surface S, that encloses the homogeneous, source-free volume V, the value of the field at a point $\mathbf{x}$ inside V is given by

$$\psi(\mathbf{x}) = \iint_S \left(G(\mathbf{x}' - \mathbf{x}) \frac{\partial}{\partial \hat{\mathbf{n}}} \psi(\mathbf{x}') - \psi(\mathbf{x}') \frac{\partial}{\partial \hat{\mathbf{n}}} G(\mathbf{x}' - \mathbf{x}) \right) d\mathbf{x}', \tag{2.33}$$

where $\hat{\mathbf{n}}$ is the unit normal on S and G is the free-space Green's function [Duffy 2001]. It is important to note that the Green's function is defined about the observation point $\mathbf{x}$, i.e., it is a function of $\mathbf{x}' - \mathbf{x}$. The frequency-dependence of the functions ψ and G have been suppressed here for notational convenience. Substitution of the free-space Green's function (2.30) and its normal derivative,

$$\frac{\partial}{\partial \hat{\mathbf{n}}} G(\mathbf{x}' - \mathbf{x}) = \left(jk + \frac{1}{r} \right) \cos(\mathbf{r}, \hat{\mathbf{n}}) G(\mathbf{r}), \tag{2.34}$$

into (2.33) yields the KHI;

$$\psi(\mathbf{x}) = \iint_S \frac{\exp(-jkr)}{4\pi r} \left(\frac{\partial}{\partial \hat{\mathbf{n}}} - \left(jk + \frac{1}{r} \right) \cos(\mathbf{r}, \hat{\mathbf{n}}) \right) \psi(\mathbf{x}') \, d\mathbf{x}', \tag{2.35}$$

where $\mathbf{r} = \mathbf{x} - \mathbf{x}'$ and

$$\cos(\mathbf{a}, \mathbf{b}) = \frac{1}{|\mathbf{a}| \, |\mathbf{b}|} \, \mathbf{a} \cdot \mathbf{b} \tag{2.36}$$

is the direction cosine. The geometry for the interior and exterior formulations of the KHI are shown in Figure 2.1. It should be noted that the Sommerfield radiation condition (discussed in Section 2.3.3) is assumed when using the exterior formulation.

The KHI reduces the problem of finding a solution to the (3-dimensional) wave equation to the evaluation of a (2-dimensional) surface integral. This simplifies the problem. However, solving the surface integral or even determining the boundary conditions can be difficult. Often approximations to the surface and the boundary conditions are used in order to solve the KHI.

2.3.2 Radiation from an acoustic projector

An acoustic source is something that perturbs the state of a fluid medium, i.e., something that radiates acoustic waves. A projector is an acoustic source that is driven by a desired, deterministic signal. The (electrical) signal is converted to mechanical energy and coupled to the fluid medium. Here, a vibrating plate is considered. This is the most common form for an acoustic projector. The plate vibrates in the direction of the surface normal, altering the pressure at its surface. The KHI can be used to determine the radiated field.

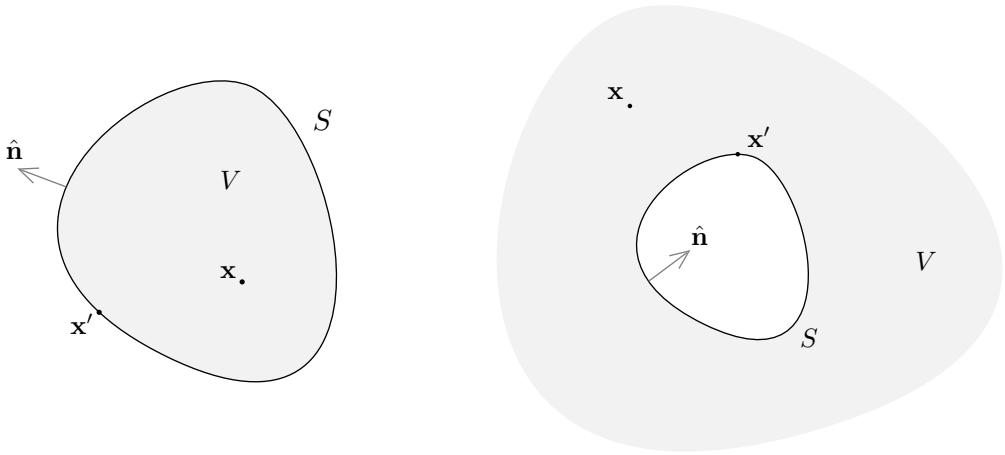

(a) interior formulation (b) exterior formulation

Figure 2.1 The Kirchhoff-Helmholtz integral (KHI) is defined on the surface S enclosing the source-free, homogeneous volume V. The geometries for the two formulations of the KHI are shown here. In the exterior formulation, the bounding surface is completed by a surface at infinity. The integral contribution from this surface can be neglected if the Sommerfield radiation condition is assumed.

Using the exterior formulation of the KHI, a surface is constructed around the projector that is infinitesimally removed from its surface as shown in Figure 2.2. The value of the field and its derivative on the projector surface are known and the KHI can be used to determine the radiated field. The field on the surface can be approximated by a plane wave, i.e.,

$$\psi_+\left(\mathbf{x}'\right) = S\left(f\right)\ \exp\left(-jk\ \hat{\mathbf{n}}_-\cdot\mathbf{x}'\right), \tag{2.37}$$

$$\psi_-\left(\mathbf{x}'\right) = -S\left(f\right)\ \exp\left(+jk\ \hat{\mathbf{n}}_-\cdot\mathbf{x}'\right), \tag{2.38}$$

for the front and back surfaces S_+ and S_-, respectively, where $\hat{\mathbf{n}}_-$ is the front-facing surface normal (see Figure 2.2) and $S\left(f\right)$ is the temporal spectrum of the transmitted signal[5]. This ignores the higher-order modes of oscillation, such as bending. Taking the normal derivatives of (2.37) and (2.38) gives

$$\frac{\partial}{\partial\hat{\mathbf{n}}_+}\psi_+\left(\mathbf{x}'\right) = jk\ \psi_+\left(\mathbf{x}'\right), \tag{2.39}$$

$$\frac{\partial}{\partial\hat{\mathbf{n}}_-}\psi_-\left(\mathbf{x}'\right) = jk\ \psi_-\left(\mathbf{x}'\right). \tag{2.40}$$

Substituting the expressions (2.37) to (2.40) into the KHI (2.35), yields an expression

[5]In general, the transmitted signal spectrum varies across the projector surface.

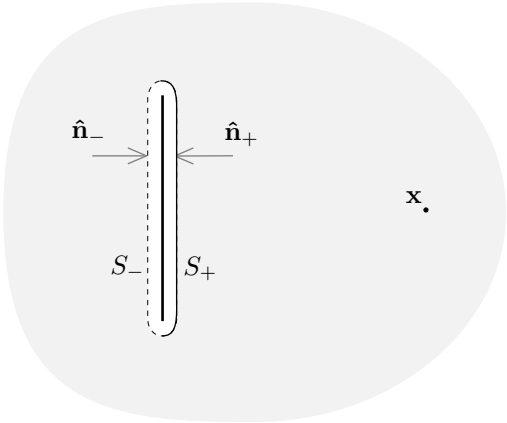

Figure 2.2 The exterior formulation of the KHI is used to determine the radiation from a vibrating plate projector. A surface is constructed around the projector that is infinitesimally removed from its surface. The *end-caps* are infinitesimally small and the integral contribution can be neglected here.

for the radiated field:

$$\psi(\mathbf{x}) = S(f) \iint_{S_+} \frac{\exp(-jkr)}{4\pi r} \; 2\left(jk + \frac{1}{r}\right) \cos(\mathbf{r}, \hat{\mathbf{n}}_-) \; d\mathbf{x}'. \tag{2.41}$$

The KHI can be used to determine the field radiated from other projector geometries such as spheres and cylinders [Morse 1968]. However, these are not considered here.

Usually a projector is attached to a supporting structure. To model this, the boundary conditions on the back surface can be specified by

$$\psi_-(\mathbf{x}') = 0, \; \frac{\partial}{\partial \hat{\mathbf{n}}_-} \psi_-(\mathbf{x}') = 0, \tag{2.42}$$

in a naive attempt at modeling the attenuation of the field behind the projector. These boundary conditions are equivalent to the Kirchhoff boundary conditions discussed in the following section. Substituting equations (2.37), (2.39), and (2.42) into the KHI (2.35) yields a similar expression for the radiated field:

$$\psi(\mathbf{x}) = S(f) \iint_{S_+} \frac{\exp(-jkr)}{4\pi r} \; \left[jk + \left(jk + \frac{1}{r}\right) \cos(\mathbf{r}, \hat{\mathbf{n}}_-)\right] \; d\mathbf{x}'. \tag{2.43}$$

This is a simple approximation and a more rigorous approach such as the finite element method [Hawkins and Gough 1995a] should be employed if accurate modeling of the projector and its supporting structure is required.

The signal spectrum $S(f)$ describes the motion of the projector. This can differ from the input (electrical) signal spectrum $V(f)$ and it is influenced by the projector design and the properties of the fluid medium. The relationship between the input signal and the motion of the projector is complicated [Pilbrow 2007]. However, it can

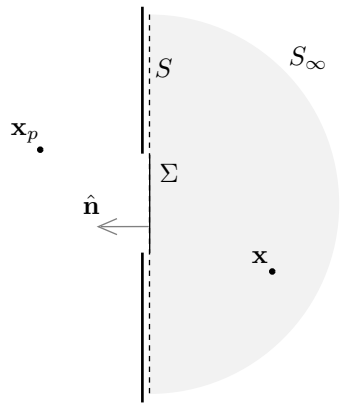

Figure 2.3 The interior formulation of the KHI is used to determine the diffraction of waves by an aperture. A hemispherical surface is constructed that is infinitesimally removed from the aperture surface. Assuming the Sommerfield radiation condition, the hemisphere can be expanded to infinity to enclose the half-space and the integral contribution from the surface at infinity S_∞ can be ignored.

be approximated empirically for a given projector to give a transfer function $H(f)$;

$$S(f) = H(f)\, V(f)\,. \tag{2.44}$$

For simplicity, the transfer function $H(f) = 1$ is assumed here. However, it is a simple matter to include the transfer function for a particular projector using the expression (2.44).

2.3.3 Diffraction by an aperture

In electromagnetics, the re-radiation (or diffraction) of waves passing through an aperture is often considered, e.g., for the field radiated from the end of a waveguide. This situation does not occur often in underwater acoustics. However, the result is included here for completeness and to illustrate the interior formulation of the KHI.

Using the interior formulation of the KHI, a hemispherical surface is constructed that is infinitesimally removed from the screen and aperture as shown in Figure 2.3. Waves impinging on the aperture are re-radiated into the hemispherical volume. The hemisphere is expanded to infinity, enclosing the half-space, and the integral contribution from the surface at infinity S_∞ can be ignored assuming the Sommerfield radiation condition is satisfied. This leaves the contribution from the integral over the remaining surface S only.

The Sommerfield radiation condition states that the field decays to zero at least as quickly as a diverging spherical wave. This boundary condition is specified by

$$\lim_{R\to\infty} R\left(\frac{\partial}{\partial\hat{\mathbf{n}}}\psi\left(\mathbf{x}'\right) + jk\psi\left(\mathbf{x}'\right)\right) = 0, \tag{2.45}$$

where R is the radius of the hemisphere.

Consider a point source located at a position $\mathbf{x}_p$ behind the screen, i.e., outside the bounding volume. In absence of the screen, the field due to the point source is given by

$$\psi_i\left(\mathbf{x}'\right) = S\left(f\right)\frac{\exp\left(-jkr_i\right)}{4\pi r_i}, \tag{2.46}$$

and the normal derivative is

$$\frac{\partial}{\partial\hat{\mathbf{n}}}\psi_i\left(\mathbf{x}'\right) = -\left(jk+\frac{1}{r_i}\right)\cos\left(\mathbf{r}_i,\hat{\mathbf{n}}\right)\psi_i\left(\mathbf{x}'\right), \tag{2.47}$$

where

$$\mathbf{r}_i = \mathbf{x}' - \mathbf{x}_p. \tag{2.48}$$

When the screen is present, the field directly in front of it can be approximated by the Kirchhoff boundary conditions.

The Kirchhoff boundary conditions specify that, on S, the field and its derivative are zero everywhere except in the region Σ within the aperture, where it is equal to the unperturbed incident field ψ_i, i.e.,

$$\psi\left(\mathbf{x}'\right) = \begin{cases} \psi_i\left(\mathbf{x}'\right), & \mathbf{x}'\in\Sigma \\ 0, & \text{elsewhere} \end{cases} \tag{2.49}$$

$$\frac{\partial}{\partial\hat{\mathbf{n}}}\psi\left(\mathbf{x}'\right) = \begin{cases} \frac{\partial}{\partial\hat{\mathbf{n}}}\psi_i\left(\mathbf{x}'\right), & \mathbf{x}'\in\Sigma \\ 0, & \text{elsewhere} \end{cases}. \tag{2.50}$$

This is intuitively satisfying, since the integral contribution over Σ is expected to dominate. However, forcing the field and its derivative to zero leads to a mathematical inconsistency; it implies that the field is zero for *all* space [Goodman 1968]. Regardless, the field determined using the Kirchhoff boundary conditions agrees well with experimental results [Goodman 1968]. An alternative derivation of the KHI (the Rayleigh-Sommerfield formulation) alleviates the mathematical inconsistency due to the Kirchhoff boundary conditions by employing an alternative Green's function (the Rayleigh-Sommerfield Green's function) [Goodman 1968]. However, this Green's function imposes additional boundary conditions and the result is not necessarily more correct than the Kirchhoff formulation [Wolf and Marchand 1964].

Substituting the expressions (2.46) to (2.50) into the KHI (2.35) yields the Fresnel-Kirchhoff diffraction formula:

$$\begin{aligned}\psi\left(\mathbf{x},\mathbf{x}_i\right) = S\left(f\right)\iint_{\Sigma}&\frac{\exp\left(-jk\left(r_i+r\right)\right)}{\left(4\pi\right)^2 r_i r} \\ &\times\left[\left(jk+\frac{1}{r_i}\right)\cos\left(\mathbf{r}_i,-\hat{\mathbf{n}}\right)+\left(jk+\frac{1}{r}\right)\cos\left(\mathbf{r},-\hat{\mathbf{n}}\right)\right]\,d\mathbf{x}'.\end{aligned} \tag{2.51}$$

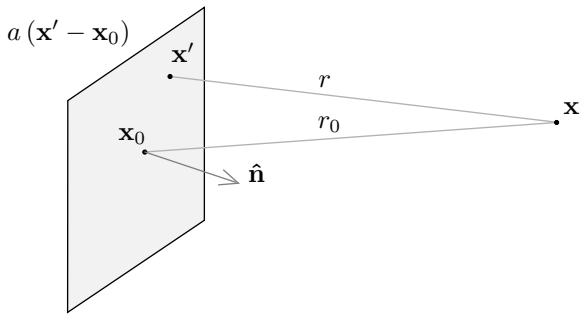

Figure 2.4 The KHI can be evaluated using an integral over the entire plane when the projector is defined by the aperture function a. The point $\mathbf{x}'$ lies in the plane and the aperture function is defined about the centre $\mathbf{x}_0$.

2.3.4 Fresnel approximation

The expressions for the radiated and diffracted fields, (2.41), (2.43), and (2.51), are valid at any distance from the source. However, often the field is evaluated at a distance where simplifying approximations can be made. The two common approximations are the Fresnel and Fraunhoffer approximations. The expression for the field radiated from an acoustic source (2.43) is used to illustrate these.

When the distance from the source is large, the expression for the radiated field can be approximated by

$$\psi(\mathbf{x}) = jk \ (1 + \cos(\mathbf{r}_0, \hat{\mathbf{n}})) \ S(f) \iint_{-\infty}^{\infty} a(\mathbf{x}'') \frac{\exp(-jkr)}{4\pi r} \, d\mathbf{x}'', \tag{2.52}$$

where $1 + \cos(\mathbf{r}_0, \hat{\mathbf{n}})$ is termed the obliquity factor, $\hat{\mathbf{n}}$ is the front-facing surface normal (see Figure 2.4), and

$$\mathbf{r}_0 = \mathbf{x} - \mathbf{x}_0, \tag{2.53}$$

where $\mathbf{x}_0$ is the position of the aperture centre. Here the aperture function a is introduced; this describes the shape of the aperture[6]. The integral is performed over the plane containing the aperture. The origin for the integral is at the aperture centre $\mathbf{x}_0$ and

$$\mathbf{r} = \mathbf{x} - \mathbf{x}_0 - \mathbf{x}''. \tag{2.54}$$

This geometry is illustrated in Figure 2.4.

At sufficiently large distances, the magnitude term $1/4\pi r$, can be approximated using

$$r \approx r_0. \tag{2.55}$$

[6]The term aperture is often used to refer to an acoustic projector; the terms projector and aperture can be used interchangeably.

For the phase term $-jkr$, a binomial expansion can be employed. The approximation

$$r \approx |\mathbf{x} - \mathbf{x}_0| - \frac{(\mathbf{x} - \mathbf{x}_0)}{|\mathbf{x} - \mathbf{x}_0|} \cdot \mathbf{x}'' + \frac{1}{2} \frac{|\mathbf{x}''|^2}{|\mathbf{x} - \mathbf{x}_0|} \tag{2.56}$$

is obtained by retaining the first and second-order terms. This is termed the Fresnel approximation.

The Fresnel approximation simplifies the expression for the radiated field (2.52) by reducing the integral to a Fresnel transform [Soumekh 1994] of the aperture function. The region of validity for this approximation encompasses all space beyond the near-field region (a few wavelengths λ from the aperture). The region of space between the near field and Fraunhoffer regions (see Section 2.3.5) is termed the Fresnel region; this is illustrated in Figure 2.5(d). Figure 2.5 shows the field obtained by the Fresnel approximation compared with the exact field for a rectangular aperture.

2.3.5 Fraunhoffer approximation and beampatterns

The Fraunhoffer approximation provides a further simplification of the phase term $-jkr$. The second-order term is omitted from the Fresnel approximation (2.56), yielding the Fraunhoffer approximation:

$$r \approx |\mathbf{x} - \mathbf{x}_0| - \frac{(\mathbf{x} - \mathbf{x}_0)}{|\mathbf{x} - \mathbf{x}_0|} \cdot \mathbf{x}''. \tag{2.57}$$

The Fraunhoffer approximation for the radiated field is obtained by substituting (2.57) into the expression for the radiated field (2.52), giving

$$\psi(\mathbf{x}) = jk \ (1 + \cos(\mathbf{r}_0, \hat{\mathbf{n}})) A\left(\frac{f}{c} \ \frac{1}{r_0}\mathbf{r}_0\right) \ S(f) \ \frac{\exp(-jkr_0)}{4\pi r_0}, \tag{2.58}$$

where

$$A(\mathbf{u}) = \iint_{-\infty}^{\infty} a(\mathbf{x}'') \exp\left(-j2\pi \ \mathbf{x}'' \cdot \mathbf{u}\right) \ d\mathbf{x}'' \tag{2.59}$$

is the Fourier transform of the aperture function.

The Fraunhoffer approximation provides an expression for the radiated field that can be evaluated analytically in some cases or, in general, using the Fast Fourier Transform (FFT) algorithm [Bracewell 1986]. The region of validity for the Fraunhoffer approximation is termed the Fraunhoffer region or the far-field and is considered to encompass all space beyond the distance

$$R = \frac{2L^2}{\lambda}, \tag{2.60}$$

where L is the largest dimension of the aperture; this measure is termed the Rayleigh

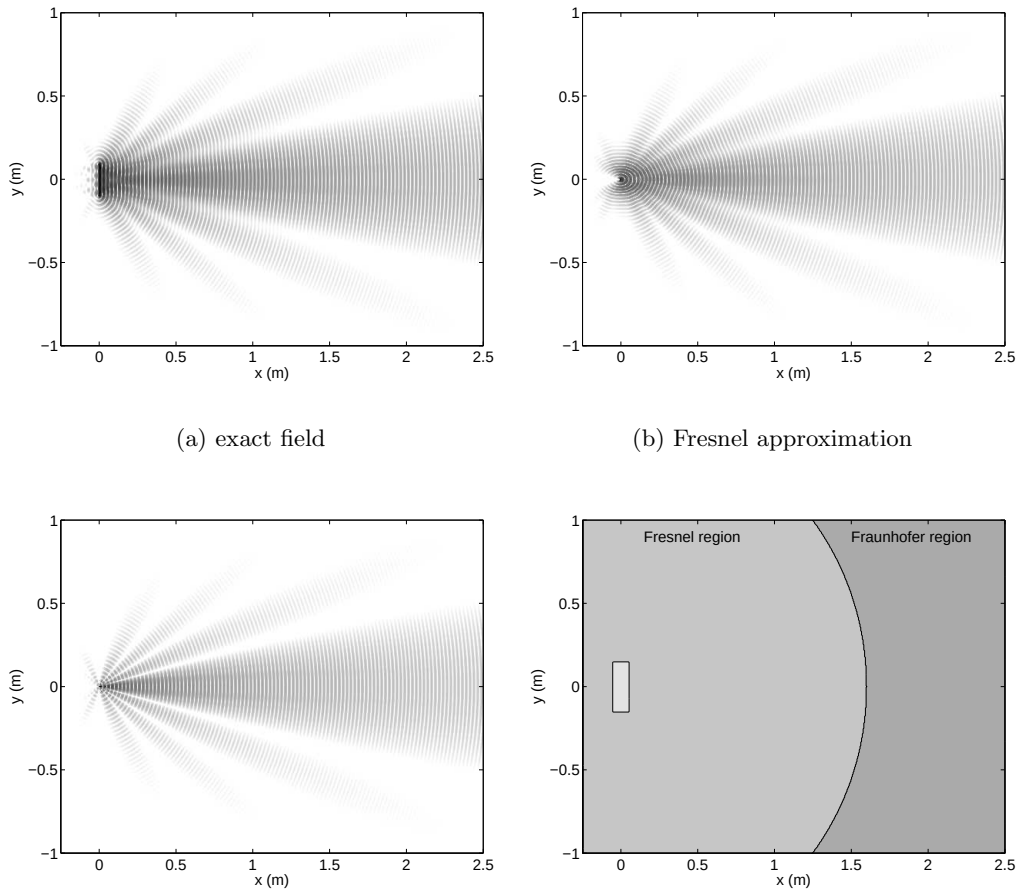

(a) exact field

(b) Fresnel approximation

(c) Fraunhoffer approximation

(d) regions of validity

Figure 2.5 Approximations to the expression for the radiated field can be made when the field is evaluated at a sufficiently large distance. These approximations are illustrated for a rectangular projector with a dimension of 0.2 m that is excited by a unity-amplitude, 30 kHz sinusoid. The Fraunhoffer approximation is valid beyond the Rayleigh distance (1.6 m) and the Fresnel approximation is valid beyond a distance of a few wavelengths (5–15 cm). The remaining region is termed the near-field.

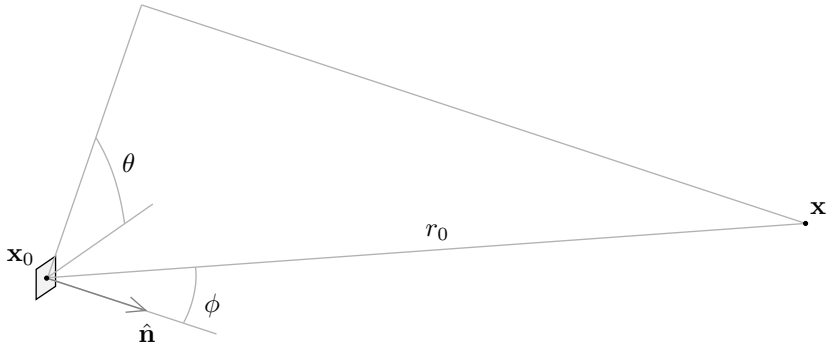

Figure 2.6 The aperture beampattern is the component of the Fraunhoffer approximation for the radiated field that is independent of range. It is a function of the angles θ and ϕ from the aperture centre $\mathbf{x}_0$ to the point $\mathbf{x}$.

distance [Goodman 1968]. Beyond this distance the field can assumed to be spherically spreading from a point source. The region of validity is illustrated in Figure 2.5(d). Figure 2.5 shows the field obtained using the Fraunhoffer approximation compared with the Fresnel approximation and the exact field.

The range-independent component,

$$B(\theta, \phi) = jk \ (1 + \cos\phi) \, A\left(\frac{f}{c} \ \cos\theta \ \sin\phi, \frac{f}{c} \ \sin\theta \ \sin\phi\right), \tag{2.61}$$

of the Fraunhoffer approximation (2.58) is termed the aperture beampattern. The beampattern describes the effect of the aperture on the radiated field in the Fraunhoffer region. It is dependent on the angles θ and ϕ from the aperture centre $\mathbf{x}_0$ to the point $\mathbf{x}$ as shown in Figure 2.6. Re-writing the far-field expression (2.58) gives

$$\psi(\mathbf{x}) = S(f) \ B(\theta, \phi) \ \frac{\exp(-jkr_0)}{4\pi r_0}. \tag{2.62}$$

For a rectangular aperture, which is a common aperture shape, the aperture function and its Fourier transform are given by

$$a(x) = \text{rect}\left(\frac{x}{L}\right) \tag{2.63}$$

and

$$A(u) = L \ \text{sinc}(Lu) \tag{2.64}$$

in one dimension, where L is the aperture length. Extension to the more general 2-dimensional case is detailed in Section 3.2.3. An example beampattern is shown in Figure 2.7.

The beampattern can be characterised by the width of the mainlobe (the beamwidth) and the sidelobe ratio. Two common definitions for the beamwidth are the null-null beamwidth and the 3 dB beamwidth. For a rectangular aperture, the null-null and 3 dB

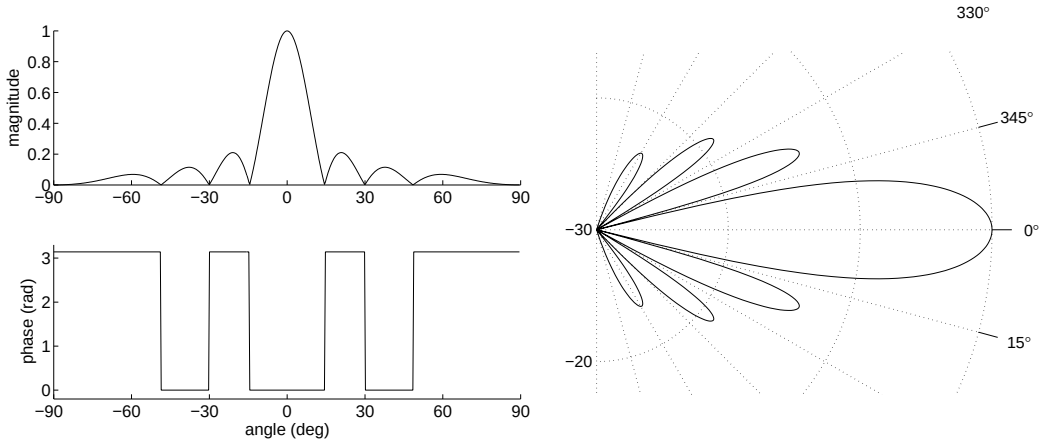

(a) magnitude and phase

(b) magnitude (polar plot)

Figure 2.7 Under the Fraunhoffer approximation, the radiated field can be represented by the far-field beampattern. The Far-field beampattern is shown here for a rectangular projector with a dimension of 0.2 m that is excited by a 30 kHz sinusoid.

beamwidths are given by

$$\theta_{\text{null}} = 2\sin^{-1}\left(\frac{\lambda}{L}\right) \tag{2.65}$$

and

$$\theta_{3\,\text{dB}} \approx 0.88\frac{\lambda}{L}, \tag{2.66}$$

where $\lambda = c/f$ is the wavelength. The sidelobe ratio is dependent on the aperture function only; it is independent of scale and frequency. For a rectangular aperture, the sidelobe ratio is 13 dB. That is, the maximum sidelobe peak is 13 dB below the peak of the mainlobe.

Often a weighting is applied to the aperture, i.e.,

$$a\left(\mathbf{x}\right) = \text{win}\left(\mathbf{x}\right)\text{rect}\left(\mathbf{x}\right), \tag{2.67}$$

where win is a particular window function, e.g., the Blackman-Harris window. In practice, the weighting could be due the physical construction of the aperture or due to the responses of individual elements in an array. By weighting the aperture, the sidelobe ratio can be altered. Increasing the sidelobe ratio increases the beamwidth. However, usually a large sidelobe ratio is desired and a trade-off is established.

2.3.6 Projector/hydrophone reciprocity

Acoustic waves are detected using a hydrophone. That is, a device that converts mechanical (acoustic) energy to an electrical signal. This is the opposite function of a projector and a reciprocal relationship can be established; a projector can function as

a hydrophone and vice versa [Kinsler *et al.* 2000]. Consequently, the analysis presented in the previous sections, Section 2.3.2 to Section 2.3.5, is valid for both projectors and hydrophones. In practice, however, projectors and hydrophones are designed to operate at significantly different levels; the hydrophone is sensitive to low energy signals and the projector transmits high energy signals.

2.3.7 Attenuation

Transmitted acoustic energy undergoes a number of losses as it propagates away from the acoustic source. In addition to the spreading loss associated with the Green's function (2.30), acoustic energy is lost by absorption, that is, it is lost as heat due to internal friction and thermal conduction and, in sea water, due to chemical relaxation processes [Fisher and Simmons 1977]. Leakage and scattering losses are also considered for transmission through an acoustic waveguide [Morse 1968]. However, waveguides are not considered here.

The transmission loss or attenuation is defined by

$$\alpha = -20 \log \left(\frac{|\psi|}{|\psi_0|} \right) \tag{2.68}$$

for a plane wave, where ψ_0 is the field at a distance of 1 m from the source and α has units of dB. The spreading loss is given by

$$\alpha_s = 20 \log (4\pi r) \tag{2.69}$$

for a spherically spreading wave, where r is the distance from the source. The absorption losses are complicated and are typically modelled using empirical formulae. The absorption loss in sea water is approximated by

$$\alpha_{\text{seawater}} = \left(\frac{A}{f_1^2 + f^2} + \frac{B}{f_2^2 + f^2} + C \right) f^2 \tag{2.70}$$

in dB/ km, where

$$A = 0.0024 S \exp (0.032T - 0.011z + 1.8 (\text{pH} - 8)) \tag{2.71}$$

$$B = 0.63 S \exp (0.071T - 0.17z) \tag{2.72}$$

$$C = 4.9 \times 10^{-10} \exp (-0.038T - 0.040z) , \tag{2.73}$$

T is the temperature in degrees Celsius, S is the salinity in parts per thousand (ppt), z is the depth in metres, pH is the pH level, and

$$f_1 = 780 \exp (0.034T) \tag{2.74}$$

$$f_2 = 42000 \exp (0.056T) \tag{2.75}$$

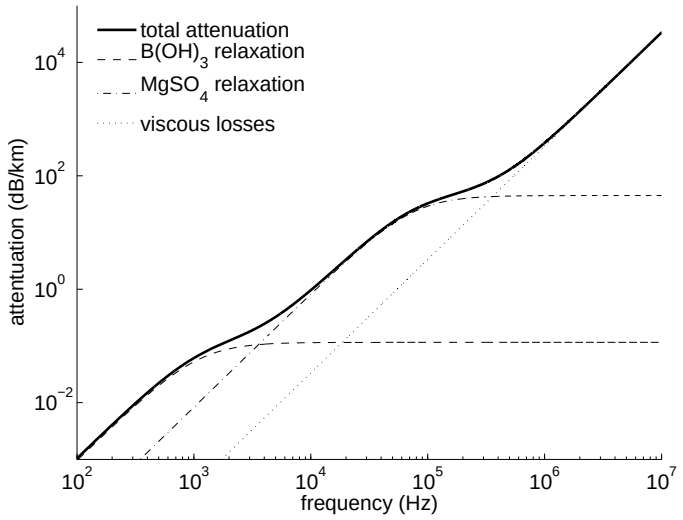

Figure 2.8 The absorption losses in sea water are due to internal friction and the chemical relaxation processes for boric acid and magnesium sulphate. The absorption loss is shown here for a temperature of 10 deg, a salinity of 35 ppt, and a depth of 0 m.

[Fisher and Simmons 1977]. The first term is due to the chemical relaxation of boric acid, $B(OH)_3$, the second term is due to the chemical relaxation of magnesium sulphate, $MgSO_4$, and the last term is due to the shear and bulk viscosity. The losses due to thermal conduction are negligible. A more comprehensive formula is given by [Francois and Garrison 1982]. Figure 2.8 shows the absorption losses in sea water.

The absorption loss in the seafloor sediment is dependent on its composition, i.e., the grain size, density, etc. These parameters vary greatly for different regions and at different depths. A general empirical formula is not easily defined and, typically, the absorption loss (and other properties, such as scattering characteristics) are obtained from tabulated empirical measurements, e.g., [Hamilton 1980, Hamilton and Bachman 1982].

2.4 PROPAGATION IN INHOMOGENEOUS MEDIA

An inhomogeneous fluid medium has space, time, and frequency-variant properties; these manifest as variations in the acoustic propagation speed. Acoustic wave propagation is affected by inhomogeneities, resulting in deviations of the wave field from that predicted by the theory developed for a homogeneous medium.

2.4.1 Sound speed profile

The sound speed profile is a persistent inhomogeneity of the ocean environment. The sound speed is governed by the density and elasticity of the medium (2.15). These properties are highly space and time-variant and comprehensive measurements of the sound

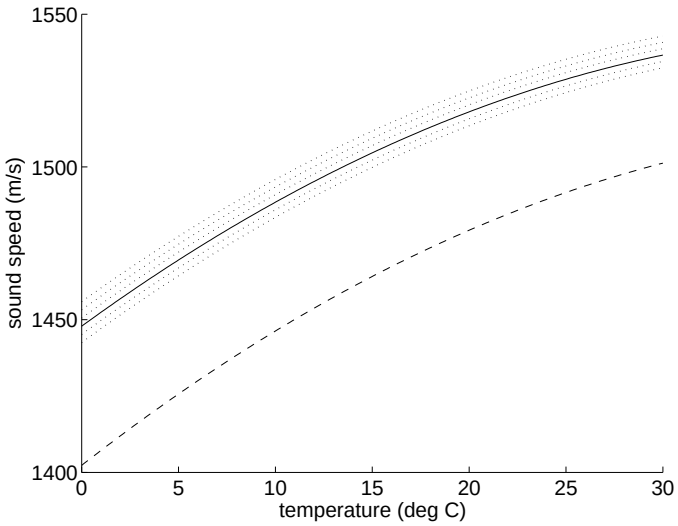

Figure 2.9 Medwin's empirical formula relates the sound speed to the temperature, salinity, and depth. It is valid for the temperature range 0–30 deg, for salinity levels up to 45 ppt, and up to 1 km depth. The solid line represents sea water with a salinity of 34 ppt and the dashed line represents fresh water.

speed are difficult to obtain. Instead, empirical relationships can be used to determine the sound speed based on the depth and measurements of salinity and temperature.

Sound speed is a complicated function of salinity, temperature, and depth and several empirical relationships have been developed [Del Grosso 1974, Wilson 1960]. The formulas of Wilson are regarded as the most comprehensive. However, the expressions are complicated and have been simplified, for example, by [Leroy 1968], and [Medwin 1975]. Medwin's simplified formula for sound speed c, is given by

$$c = 1449.2 + 4.6T - 0.055T^2 + (1.34 - 0.010T)\,(S - 35) + 0.016z. \tag{2.76}$$

Medwin's formula is valid within the temperature range 0–30 deg, for salinity levels up to 45 ppt, and up to 1 km depth. While Wilson's formulas are recommended when accurate knowledge of the medium parameters is available, Medwin's formula is used here since errors due to inaccurate knowledge of the medium parameters typically dominate over errors in the formula. The variation of sound speed with temperature and salinity is shown in Figure 2.9 at atmospheric pressure. The sound speed is shown to increase with salinity and temperature and, from (2.76), it can be seen that the sound speed increases linearly with increasing depth.

The salinity and temperature of the world's oceans are space and time-variant; this is particularly true for the temperature. However for acoustic propagation, the salinity can be considered constant over very large regions and the temperature can often be assumed to change only with depth over a local region [Etter 1991]. These parameters are also time-dependent. However, they may be considered constant within a small

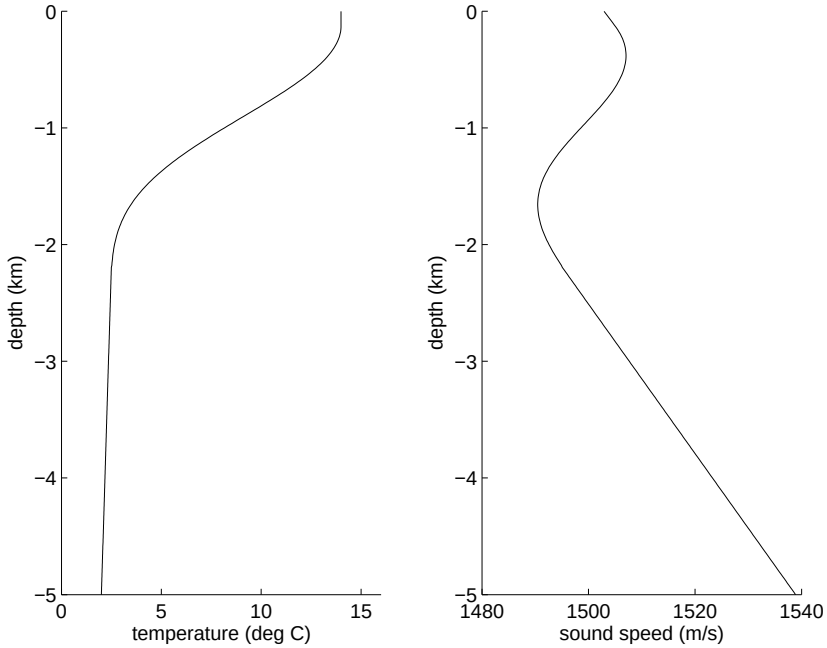

Figure 2.10 The sound speed profile is a function of temperature, salinity, and depth. For a local region, the salinity is assumed constant and the temperature is assumed to vary only with depth. The first 200 m is referred to as the mixing zone where the temperature is roughly constant with depth due to wind and wave activity (an exception is for calm conditions, which results in a seasonal thermocline). From 200 m to 1.5 km is the main thermocline where the temperature decreases linearly with depth. Beyond this is the deep isothermal layer, which is a constant temperature of around 4 deg. A typical sound speed profile is shown here for a salinity of 34 ppt.

window of time. Figure 2.10 shows a typical temperature profile and its associated sound speed profile.

2.4.2 Propagation models

The free-space Green's function (2.30) is not applicable in the presence of inhomogeneities. Therefore, it cannot be used to model the propagation of acoustic waves in inhomogeneous media; a more complicated Green's function is required. For continuous inhomogeneities, deviation from the propagation predicted by the free-space Green's function is referred to as refraction. For discontinuities in the medium, the deviation is referred to as diffraction or scattering. These mechanisms are both forms of wave propagation. However, typically, they are treated differently.

An analytic form of the Green's function is difficult to obtain for an inhomogeneous medium except for the most trivial cases, e.g., a simple waveguide. Thus, numerical methods and/or simplifying assumptions must be made to obtain a solution.

The finite difference (FD) [Smith 1985, Chung 2002] and finite element (FE) methods [Burnett 1988, Solin 2006] are general purpose techniques for the numerical solution of partial differential equations. In the FD method, space is discretised to a regular

grid, reducing the PDE to a simple linear equation for each of the discrete volumes. The method can be employed in the frequency domain using the Helmholtz equation (2.20), where Fourier synthesis is employed to obtain a broadband solution. Alternatively, the acoustic wave equation (2.18) can be discretised in space and time in the so-called finite difference time-domain method (FDTD) [Taflove and Hagness 2000]. The FE method is a generalisation of the FD method.

The FD and FE methods provide a complete numerical solution to the PDE including both propagation and scattering mechanisms. However, the FD and FE methods are computationally intensive. The discretisation requires a grid that is much smaller than the acoustic wavelength and the smallest feature. Therefore, it is restricted to solutions over very small 3-D domains or 2-D domains. Often the 2-D solution is extended to the so-called 2.5-D approximation of the 3-D solution [Zhou and Greenhalgh 1998]. The FD and FE methods are not a good choice for a 3-D SAS simulator due to the computational requirements.

The elliptic Helmholtz equation is approximated by a parabolic equation in the parabolic equation (PE) method [Jensen *et al.* 1993]. A range-marching algorithm [Hardin and Tappert 1973] can then be used to efficiently solve the equation using the FFT. The range-marching algorithm can be employed for a dominant one-way propagation, i.e., in a waveguide. Therefore, it is not suitable for a SAS simulator, where backscattering is important. Other approximate solutions use the wavenumber integration and normal mode methods [Jensen *et al.* 1993]. However, these are suited to waveguide propagation also.

2.4.3 Ray theory

Ray theory provides a high-frequency approximation to the Helmholtz equation. It is an intuitive approach, which significantly predates its formal mathematical formulation; the original concept of rays is attributed to Euclid in the 3$^{\text{rd}}$ century BC. Rays have been used extensively for modelling electromagnetic and acoustic wave propagation [Rohan 1991, Jensen *et al.* 1993]. In particular, ray-tracing is a popular technique for modelling the propagation of visible light in modern computer graphics applications [Foley *et al.* 1997]. The ray theory is derived here and the practical implementation of an acoustic ray-tracer is given in Section 4.4.

The ray solution of the Helmholtz equation is obtained by assuming the solution is of the form

$$\psi(\mathbf{x}) = a(\mathbf{x}) \exp(j\phi(\mathbf{x})), \tag{2.77}$$

where a is a (real) amplitude function and ϕ is a (real) phase function. Substitution of

the solution (2.77) into the Helmholtz equation (2.20) gives

$$\nabla^2 a(\mathbf{x}) - a(\mathbf{x})\left[|\nabla\phi(\mathbf{x})|^2 + k^2(\mathbf{x})\right] + j\left[a(\mathbf{x})\nabla^2\phi(\mathbf{x}) + 2(\nabla a(\mathbf{x}))\cdot(\nabla\phi(\mathbf{x}))\right] = 0, \tag{2.78}$$

where

$$k(\mathbf{x}) = \frac{2\pi f}{c(\mathbf{x})} \tag{2.79}$$

is the wavenumber and $c(\mathbf{x})$ is the space-variant sound speed. Equating the real and imaginary components gives the equations

$$\nabla^2 a(\mathbf{x}) - \left[|\nabla\phi(\mathbf{x})|^2 + k^2(\mathbf{x})\right] a(\mathbf{x}) = 0 \tag{2.80}$$

$$a(\mathbf{x})\nabla^2\phi(\mathbf{x}) + 2(\nabla a(\mathbf{x}))\cdot(\nabla\phi(\mathbf{x})) = 0. \tag{2.81}$$

The second equation (2.81) is termed the transport equation.

The key approximation in ray theory is a high-frequency approximation. Re-arranging (2.80) gives

$$\frac{1}{k^2(\mathbf{x})}\left[\frac{\nabla^2 a(\mathbf{x})}{a(\mathbf{x})} - |\nabla\phi(\mathbf{x})|^2\right] - 1 = 0. \tag{2.82}$$

Then assuming the phase function, ϕ, is more rapidly varying than the amplitude function, a, i.e., that

$$\left|\frac{\nabla^2 a(\mathbf{x})}{a(\mathbf{x})}\right| \ll |\nabla\phi(\mathbf{x})|^2, \tag{2.83}$$

which is best satisfied at high frequencies, (2.82) can be approximated by

$$|\nabla\phi(\mathbf{x})|^2 \approx k^2(\mathbf{x}), \tag{2.84}$$

where $\nabla\phi(\mathbf{x})$ describes a set of curves (or rays) normal to the surfaces of constant phase (or wavefronts), $\phi(\mathbf{x}) =$ constant, as shown in Figure 2.11. This is termed the Eikonal equation and it is a first-order, non-linear, PDE.

While the Eikonal equation is non-linear, it is easily solved for each individual ray in the local coordinates of the ray. The set of rays can be expressed as a magnitude and a direction vector, i.e.,

$$\nabla\phi(\mathbf{x}) = |\nabla\phi(\mathbf{x})|\,\hat{\mathbf{n}}(\mathbf{x}), \tag{2.85}$$

where

$$\hat{\mathbf{n}}(\mathbf{x}) = \begin{pmatrix} n_x(\mathbf{x}) \\ n_y(\mathbf{x}) \\ n_z(\mathbf{x}) \end{pmatrix}, \tag{2.86}$$

and n_x, n_y, n_z are the direction cosines. Expressing the direction cosines as parametric

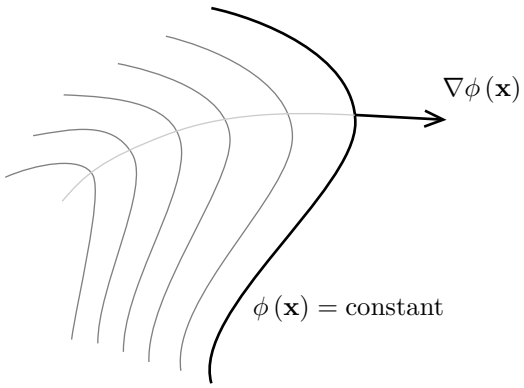

Figure 2.11 Rays and wavefronts.

functions of the variable s gives

$$n_x\,(\mathbf{x}) = \frac{dx}{ds} \tag{2.87}$$

$$n_y\,(\mathbf{x}) = \frac{dy}{ds} \tag{2.88}$$

$$n_z\,(\mathbf{x}) = \frac{dz}{ds}, \tag{2.89}$$

where ds is an infinitesimal arc length along a particular ray. Here, a single ray has been isolated implicitly in the parametric formulation of the direction cosines. The ray is denoted by the subscript n. Taking the derivative of the phase function, ϕ_n, with respect to s gives

$$\frac{d}{ds}\phi_n\,(\mathbf{x}) = \frac{\partial}{\partial x}\phi_n\,(\mathbf{x})\,\frac{dx}{ds} + \frac{\partial}{\partial y}\phi_n\,(\mathbf{x})\,\frac{dy}{ds} + \frac{\partial}{\partial z}\phi_n\,(\mathbf{x})\,\frac{dz}{ds}, \tag{2.90}$$

or, using (2.86), (2.87) to (2.89), and (2.84),

$$\frac{d}{ds}\phi_n\,(\mathbf{x}) = \nabla\phi_n\,(\mathbf{x}) \cdot \hat{\mathbf{n}}\,(\mathbf{x}) \tag{2.91}$$

$$= k\,(\mathbf{x})\,. \tag{2.92}$$

The solution of the Eikonal equation can then be obtained by integrating (2.92), giving

$$\phi_n\,(\mathbf{x}) = \phi_n\,(\mathbf{x}\,(0)) + \int_0^s k\left(\mathbf{x}\left(s'\right)\right)\,ds' \tag{2.93}$$

for the phase function.

Similarly, the solution of the transport equation (2.81) yields an expression for the amplitude function [Ziomek 1995]. The ray solution to the Helmholtz equation (2.77) is obtained by summing the solutions for the set of rays (the eigenrays) that pass through

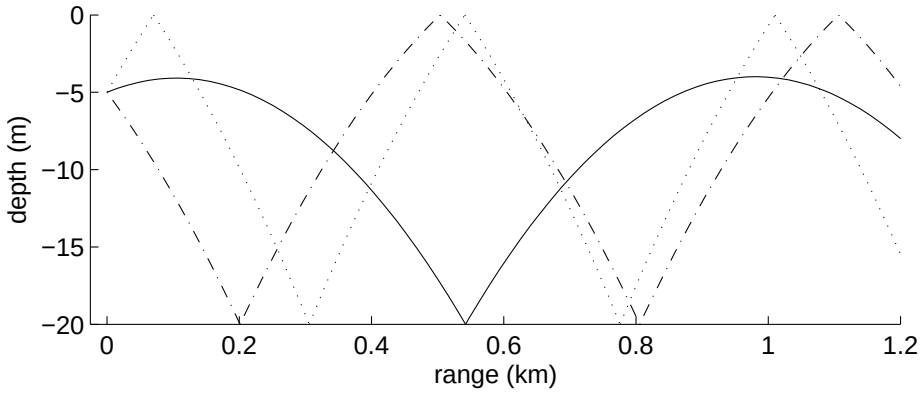

(a)

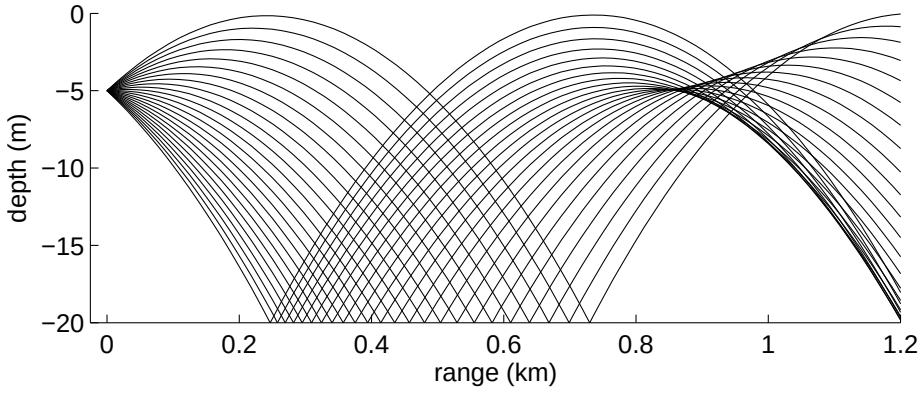

(b)

Figure 2.12 In shallow water, it is often assumed that the temperature is constant with depth in the so-called mixing layer. Therefore, the sound speed increases linearly with depth and the medium is downward refracting. The three ray modes are bottom-bottom, bottom-surface, and surface-bottom, illustrated by the solid, dashed, and dotted rays respectively in Figure (a).

the point $\mathbf{x}$, i.e.,

$$\psi(\mathbf{x}) = \sum_{n=0}^{N-1} a_n(\mathbf{x}) \exp(j\phi_n(\mathbf{x})) \tag{2.94}$$

where N is the number of eigenrays[7].

Figure 2.12 shows some example ray-traces for a typical shallow water sound speed profile.

[7]In practice, the infinitesimally thin rays are approximated by *ray tubes* or *beams* [Jensen *et al.* 1993], which can be summed globally, removing the need to calculate eigenrays.

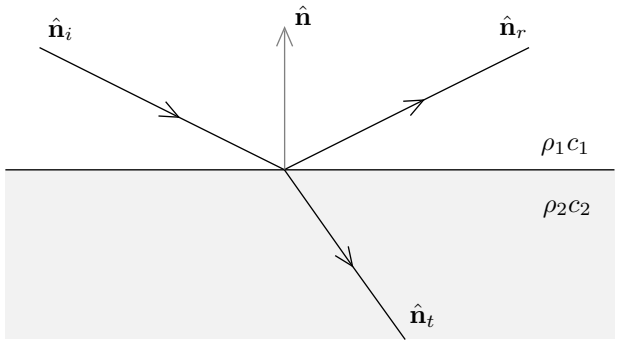

Figure 2.13 Scattering from a planar interface is described by Snell's law.

2.5 ACOUSTIC WAVE SCATTERING

Acoustic wave scattering occurs due to discontinuities in the medium. There are many discontinuities present in the ocean environment. The water column contains many suspended scatterers, such as: unconsolidated sediment, gas bubbles, and marine life, e.g., fish and plankton. The air-sea interface and the sea-sediment interface cause significant scattering as well as rocks, gas bubbles, shellfish, etc, on and beneath the seafloor. In addition to the natural scatterers, many man-made objects can be found in the water column and on/beneath the seafloor, e.g., submarines, mines, sunken ships/aircraft, and pipelines to name a few.

2.5.1 Reflection from a planar interface

Many scattering surfaces can be approximated locally by a planar interface. The seafloor and sea surface are often considered planar, e.g., for a calm sea surface.

Consider an infinite planar interface between two half-spaces containing different media as shown in Figure 2.13. The two media are defined by the densities and sound speeds[8], ρ_1, c_1, and ρ_2, c_2. For an incident plane wave,

$$\psi_i(\mathbf{x}) = A_i \ \exp\left(-jk_1 \ \hat{\mathbf{n}}_i \cdot \mathbf{x}\right), \tag{2.95}$$

reflected and transmitted plane waves are generated in order to satisfy the boundary conditions at the interface, i.e.,

$$\psi_r(\mathbf{x}) = A_r \ \exp\left(-jk_1 \ \hat{\mathbf{n}}_r \cdot \mathbf{x}\right) \tag{2.96}$$

$$\psi_t(\mathbf{x}) = A_t \ \exp\left(-jk_2 \ \hat{\mathbf{n}}_t \cdot \mathbf{x}\right) \tag{2.97}$$

[8]The sound speed is for the compressional wave. For elastic scattering the shear wave speed should be considered also.

medium type	**density** ($\mathrm{kg/m^3}$)	**sound speed** ($\mathrm{m/s}$)
air	1	330
fresh water	1000	1450
sea water	1000	1500
rock	3000	6000
steel	8000	4500

Table 2.1 Typical medium properties.

where A_r and A_t are the amplitudes of the reflected and transmitted waves and $\hat{\mathbf{n}}_r$ and $\hat{\mathbf{n}}_t$ are the directions of propagation. The magnitudes and directions of the transmitted and reflected waves can be determined using Snell's law.

The amplitude of the reflected field is obtained from the reflection coefficient,

$$R = \frac{A_r}{A_i} \tag{2.98}$$

$$= \frac{Z_2 \hat{\mathbf{n}}_i \cdot \hat{\mathbf{n}} - Z_1 \hat{\mathbf{n}}_t \cdot \hat{\mathbf{n}}}{Z_2 \hat{\mathbf{n}}_i \cdot \hat{\mathbf{n}} + Z_1 \hat{\mathbf{n}}_t \cdot \hat{\mathbf{n}}} \tag{2.99}$$

where

$$Z_1 = \rho_1 c_1, \tag{2.100}$$

$$Z_2 = \rho_2 c_2 \tag{2.101}$$

are the acoustic impedances of the two media for an incident plane wave. The amplitude of the transmitted field is obtained from the transmission coefficient,

$$T = \frac{\rho_1}{\rho_2} (1 + R) \tag{2.102}$$

[Ziomek 1995]. The direction of the reflected field is given by

$$\hat{\mathbf{n}}_r = \hat{\mathbf{n}}_i - 2 (\hat{\mathbf{n}}_i \cdot \hat{\mathbf{n}}) \hat{\mathbf{n}} \tag{2.103}$$

and the direction of the transmitted field is given by

$$\hat{\mathbf{n}}_t = \frac{c_2}{c_1} (\hat{\mathbf{n}}_i - (\hat{\mathbf{n}}_i \cdot \hat{\mathbf{n}}) \hat{\mathbf{n}}) + \left(\sqrt{1 - \left(\frac{c_2}{c_1} \right)^2 \left(1 - (\hat{\mathbf{n}}_i \cdot \hat{\mathbf{n}})^2 \right)} \right) \hat{\mathbf{n}}, \tag{2.104}$$

where $\hat{\mathbf{n}}$ is the surface normal.

Typical values of density and sound speed are given in Table 2.1 and Table 2.2.

sediment type	**grain size** (mm)	**density** (kg/ m^3)	**sound speed** (m/ s)
very fine silt	0.15	1960	1850
fine silt	0.18	1990	1870
medium silt	0.21	2030	1900
course silt	0.30	2100	1940
very fine sand	0.50	2210	2010
fine sand	0.84	2340	2080
medium sand	1.4	2470	2150
coarse sand	2.4	2610	2220
very course sand	4.0	2750	2290

Table 2.2 Typical sediment properties at 10 m depth in salt water ($c = 1500\,\mathrm{m/s}$).

2.5.2 Rough surface scattering

Most scattering surfaces are not planar. Many man-made objects are smooth and can be approximated locally as planar surfaces. However, natural objects are typically rough and the modelling of rough surface scattering is a very difficult problem.

Numerical models – The rough surface scattering problem can be solved numerically using general purpose techniques such as FD and FE. However, this is computationally intensive. Instead, the regions on either side of the scattering surface can be considered homogeneous and the KHI (2.35) can be employed. This is termed the integral equation method. The KHI can be solved numerically using the FE method, where it is referred to as the boundary element method (BEM) [Kirkup 1998] or the method of moments (MoM) [Moore and Pizer 1984]. While the problem is simpler due to the reduced dimensionality, this approach is still computationally intensive and it is only suitable for small domains. Another approach uses stochastic sampling in order to evaluate the KHI, this is referred to as a Monte-Carlo method [Newman and Barkema 1999].

Analytic models – Simplifying assumptions can be made to reduce the complexity of the KHI. These are referred to as analytic techniques, since they can often be used to obtain an analytic solution. The most common analytic techniques are the small perturbation method [Rice 1951] and the Kirchhoff approximation [Beckmann and Spizzichino 1987]. These employ small amplitude and small gradient approximations respectively. The small perturbation method and the Kirchhoff approximation have been unified in the small-slope approximation [Voronovich 1985, Thorsos 1995] and this has since been generalised to include multiple scattering in the non-local small-slope approximation [Voronovich 1996].

Chapter 3

ACOUSTIC SCATTERING MODEL

A common approach to solving scattering problems is to decompose the scattering objects into a number of primitive elements. These are chosen for easy decomposition of the objects and such that the scattering from each primitive is simple to model. This simplifies the modelling of scattering from complicated objects and scenes.

Common primitive types are point and facet-scatterers. For example, the scattering model in the previous simulator, which is described in the following section, uses points to approximate the scene, while the SWAT and SARAS scattering models [Sammelmann 2003, Franceschetti *et al.* 1992] utilise facets. Realistic scenes must be decomposed into a large number of points or facets; this is a problem since the computational complexity scales with the number of scatterers.

The model that is described in this chapter is a generalisation of the facet-based models. It uses rough (rather than smooth) facets as primitive elements. By using rough facets, the scene can be decomposed into a smaller number of scatterers as illustrated in Figures 3.1 and 3.2. Consequently, the model is more efficient.

The simple point-based model is described in Section 3.1, followed by the model for smooth facets in Section 3.2. The scattering from rough facets is considered in Section 3.3, and Sections 3.4 to 3.6 detail the statistical realisation of the scattered field. The implementation of the scattering model in the simulator is given in the following chapter.

3.1 POINT-SCATTERER MODEL

The point-scatterer model utilised in the previous simulator (developed by Dr. Hayes) has not been published in the literature. However, its form is implicit in the SAS reconstruction algorithms [Hawkins 1996, Callow 2003]; the reconstruction algorithms are essentially the inverse of the point-scatterer model. This is a significant weakness in the reconstruction algorithms since aspect-dependence is neglected. The point-scatterer model is described here for completeness and to illustrate the short-comings of the model and those of the reconstruction algorithms.

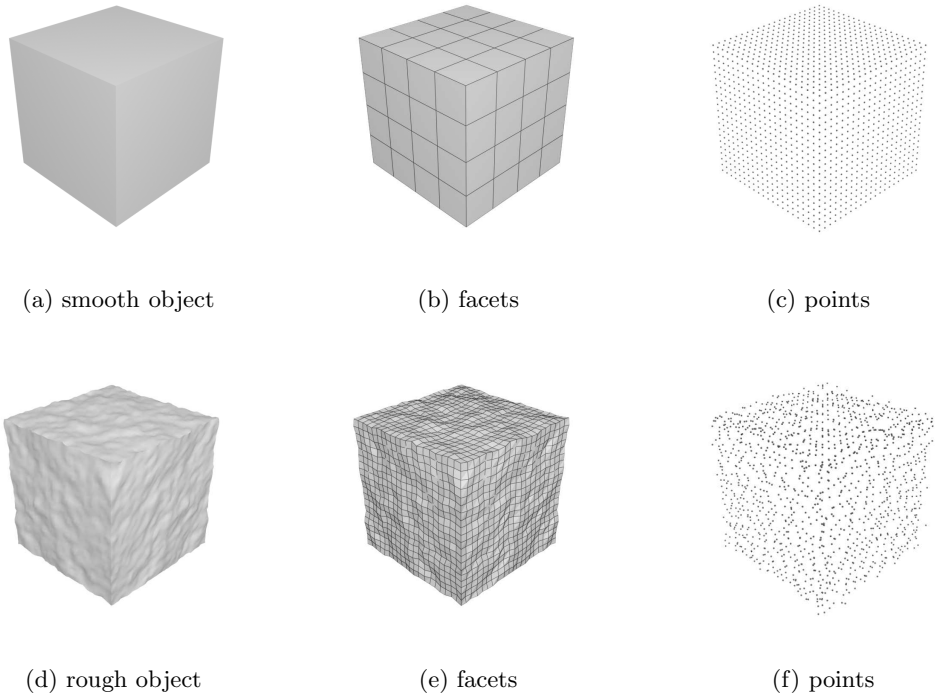

(a) smooth object (b) facets (c) points

(d) rough object (e) facets (f) points

Figure 3.1 The simple facet-based model utilises smooth facets to approximate the scattering object. For smooth objects, the facet-based model is more efficient than the point-based model. The point model approximates the surfaces using infinitesimal points and many scattering primitives are required. However, the efficiency of the facet model is comparable to the point model for rough objects.

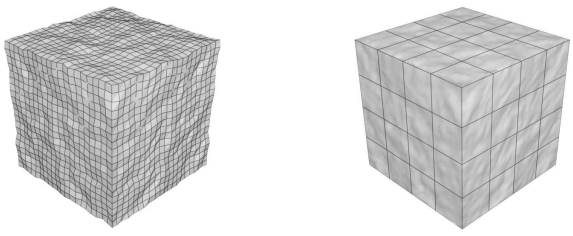

(a) smooth facets (b) rough facets

Figure 3.2 Rough facets can be employed instead of smooth facets to approximate the scattering object. For a rough object, this results in fewer scattering primitives and increased efficiency.

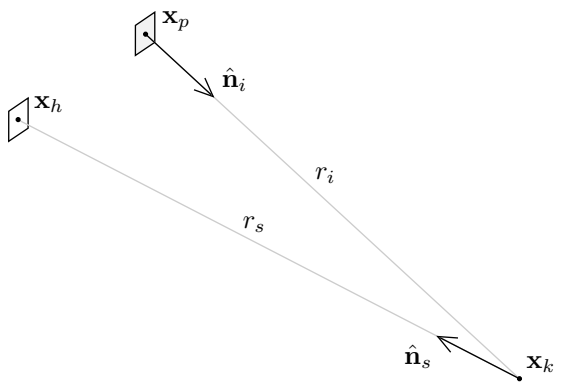

Figure 3.3 A point-scatterer is an infinitesimally small scattering object that re-radiates energy in an omni-directional pattern. Here, a point-scatterer located at $\mathbf{x}_k$ is excited by a projector located at $\mathbf{x}_p$ and the scattered field is detected by a hydrophone located at $\mathbf{x}_h$.

The point-scatterer model has the advantage of being easy to understand and simple to implement. The scattering from a point is simple to model and any surface can be decomposed into a collection of points. Moreover, a scattering volume can be decomposed into a collection of points; this is perhaps the biggest advantage over the facet-based models, which are not well-suited for volume scattering problems. Nevertheless, the point-scatterer model has many disadvantages.

The point-scatterer model has less physical basis than the facet-based models since the relationship between the scattering properties of the points and the properties of the scattering media is somewhat arbitrary (see Section 3.1.2). However, the major disadvantage of the model is its poor efficiency. On order of ten scatterers are required per wavelength to adequately represent a continuous surface[1], i.e., on order of one hundred scatterers per square wavelength of area or one thousand scatterers per cubic wavelength of volume are required.

3.1.1 Scattering from a point

A point-scatterer is an infinitesimally small scattering object and so it should not scatter any energy due to its infinitesimally small extent. However, in the point-scatterer model each point represents a portion of a larger scattering object and a non-zero scattering strength is assigned; determination of the scattering strength is detailed in Section 3.1.2. Alternatively, an ideal (non-realisable) point-scatterer can be considered and an arbitrary scattering strength can be assigned.

Consider a point-scatterer with scattering strength A located at $\mathbf{x}_k$, a projector located at $\mathbf{x}_p$, and a hydrophone located at $\mathbf{x}_h$; this is illustrated in Figure 3.3. A point-scatterer re-radiates energy in an omni-directional pattern. Thus, for a point in

[1]This can be shown empirically.

the far-field of the transducers, the scattered field at the location of the hydrophone is given by

$$\psi_s\left(\mathbf{x}_h, \mathbf{x}_p, f\right) = S\left(f\right) B_p\left(\hat{\mathbf{n}}_i, f\right) A \; \frac{\exp\left(-j2\pi f/c\left(r_i + r_s\right)\right)}{\left(4\pi\right)^2 r_i r_s}, \tag{3.1}$$

where

$$\begin{aligned} \mathbf{r}_i &= \mathbf{x}_k - \mathbf{x}_p, & (3.2)\\ r_i &= \left|\mathbf{r}_i\right|, & (3.3)\\ \hat{\mathbf{n}}_i &= \mathbf{r}_i / r_i, & (3.4) \end{aligned}$$

for the incident field and

$$\begin{aligned} \mathbf{r}_s &= \mathbf{x}_h - \mathbf{x}_k, & (3.5)\\ r_s &= \left|\mathbf{r}_s\right|, & (3.6)\\ \hat{\mathbf{n}}_s &= \mathbf{r}_s / r_s, & (3.7) \end{aligned}$$

for the scattered field, B_p is the projector beampattern, which is given in Section 2.3.5, and S is the temporal spectrum of the transmitted signal.

3.1.2 Scattering strength

The scattering properties of an object can be defined using the scattering cross-section. That is, the ratio of the incident and scattered acoustic intensities. The scattering cross-section is given by

$$\sigma_s = 4\pi \frac{\left|\psi_s\right|^2}{\left|\psi_i\right|^2}, \tag{3.8}$$

where ψ_i and ψ_s are the incident and scattered fields of the acoustic velocity potential; the ratio is normalised by the factor 4π. An incident plane wave is considered and the scattered field is evaluated at a distance 1 m from the object.

The (constant) beampattern of a point-scatterer is termed the scattering strength and it is related to the scattering cross-section by

$$|A| = \sqrt{\sigma_s}. \tag{3.9}$$

The scattering strength of a point-scatterer is usually specified in terms of back-scattering from an equivalent sphere. Scattering from an arbitrary sphere is complicated and it is covered by the Lorenz-Mie theory [Mie 1908, Morse 1968]. However, the scattering expressions are simplified for spheres that are much larger and much smaller than the wavelength.

For a sphere that is much larger than the wavelength, the dominant scattering mechanism is due to specular reflection and, for a co-located projector and hydrophone, the scattering cross-section can be approximated by

$$\sigma_s = \pi a^2, \tag{3.10}$$

where a is the radius of the sphere. In this case, the scattering cross-section is equivalent to the cross-sectional area of the sphere, which is independent of frequency, and the back-scattering can be modelled by an apparent point-scatterer. The location of the point is dependent on the location of the transducers; the point is located a distance $a/2$ from the centre of the sphere towards the co-located transducers [Urick 1975].

The scattering from a small sphere was first considered by Rayleigh [Rayleigh 1945]. The so-called Rayleigh scattering theory is applicable to spheres much smaller than the wavelength and the scattering cross-section is given by

$$\sigma_s = \frac{\pi^2 V^2}{r^2 \lambda^4} \left(1 + \frac{3}{2}\cos\theta\right)^2, \tag{3.11}$$

where $V = 4/3\pi a^3$ is the volume of the sphere, $\theta = \pi - \cos^{-1}(\hat{\mathbf{n}}_i \cdot \hat{\mathbf{n}}_s)$ is the angle between the directions of incidence and observation, and r is the distance from the centre of the sphere to the observation point. For co-located transducers, the scattering cross-section (3.11) reduces to

$$\sigma_s = 1082 \frac{a^6}{\lambda^4}, \tag{3.12}$$

at a distance $r = 1\,\mathrm{m}$, and the sphere can be modelled by a fixed point-scatterer with a frequency-dependent scattering strength. The more general expressions for scattering from a sphere are not considered here.

A problem with the point-scatterer model is relating the scattering strengths of each point to the properties of the object. This is simple for a sparse collection of point-like objects (e.g., schools of fish, bubble clouds, etc.) but, in general, it is not easily achieved. While an object can be decomposed into a collection of spheres, determination of the sphere sizes and properties is not easily defined. For surface scattering, the most common approach is to decompose the object into small facets; these are then approximated as point-scatterers. The scattering cross-section of a facet is given by

$$\sigma_s \approx \left(\frac{A}{\lambda}\right)^2 \cos^2\theta \tag{3.13}$$

for co-located transducers, where A is the area of the facet and θ is the angle between the incident direction and the facet normal. This expression is obtained by evaluating the expression for the facet beampattern (3.38) for a small, rigid facet.

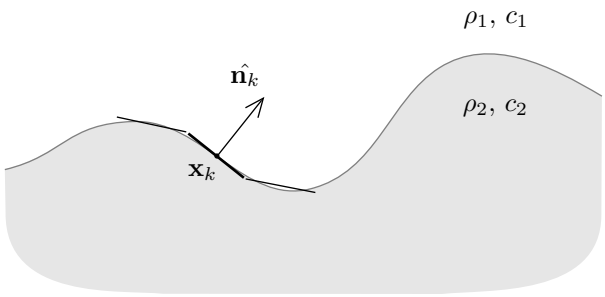

Figure 3.4 A scattering surface can be approximated using facets. The facets are characterised by their shape, location $\mathbf{x}_k$, normal $\hat{\mathbf{n}}_k$, and the acoustic impedances of the two media, $Z_1 = \rho_1 c_1$ and $Z_2 = \rho_2 c_2$.

3.1.3 Occlusions and multiple scattering

Occlusions and multiple scattering can be incorporated into the point-scatterer model by use of the ray-tracing technique. Ray theory is detailed in Section 2.4.3 and ray-tracing is covered for the facet model in Section 4.4; the results of Section 4.4 are applicable to the point-scatterer model. Rays are traced from each point-scatterer to the projector and hydrophones for each position along the trajectory of the sonar. The scattering from the points is scaled appropriately wherever the rays are intercepted by an opaque or semi-opaque object and the rays are traced recursively for multiple scattering between the points.

The computational efficiency of the ray-tracing technique is inversely proportional to the number of rays. Thus, ray-tracing is inefficient for the point-scatterer model where, typically, many points are required. This problem is compounded severely by the introduction of multiple scattering.

3.2 SCATTERING FROM A FACET

The facet-scatterer model has been used extensively in many types of scattering problems. The SWAT and SARAS simulators employ this model [Sammelmann 2001, Franceschetti *et al.* 1992]. Facet primitives are more efficient than point primitives when modelling smooth surfaces since fewer facets are required. However, the required number of facets can be comparable to the point model when considering rough surfaces, as illustrated in Figure 3.1, and this is the major disadvantage of the model.

A facet is defined as a planar scattering surface of finite extent, where a scattering surface is the interface between two media with different acoustic properties (density and sound speed). Facets can be used to approximate arbitrary scattering surfaces. Triangular facets are typically employed since any surface can be tessellated (decomposed) into a continuous collection of triangles [Foley *et al.* 1997]. Each facet is

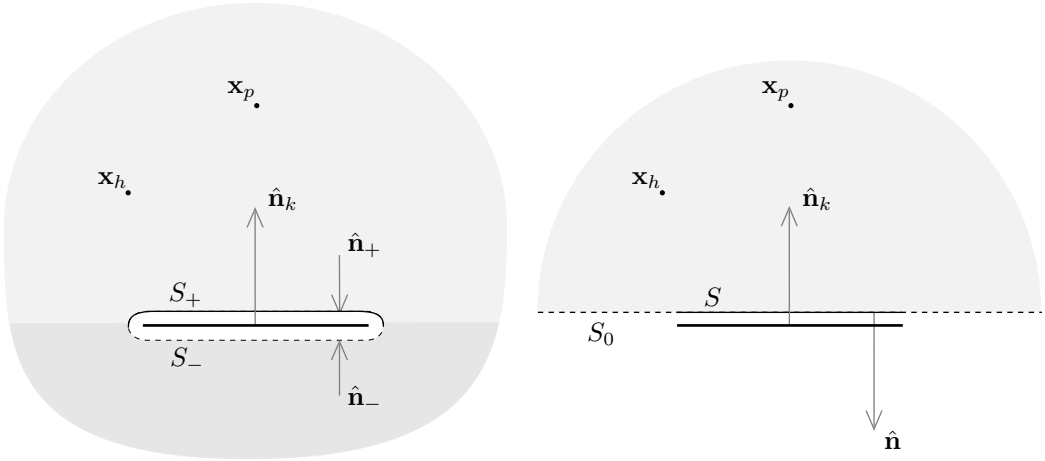

(a) exterior formulation (b) interior formulation

Figure 3.5 The interior or exterior formulation of the KHI can be used to determine the field scattered from a facet. For the exterior geometry, the facet is bounded by a front surface, S_+, and a back surface, S_-, with surface normals $\hat{\mathbf{n}}_+$ and $\hat{\mathbf{n}}_-$ respectively. For the interior formulation, the facet is bounded by a front surface, S, and a surface at infinity. The field and its derivative is assumed zero for the portion of the surface, S_0, that is not directly in front of the facet.

characterised by its shape, position, and orientation, and the scattering properties of the facet are related to the acoustic impedances of the two media. This is an advantage over the point-scatterer model, which is not well-posed for surface scattering problems. Figure 3.4 illustrates the tessellation of a scattering surface into a collection of facets.

3.2.1 Kirchhoff formulation of the scattered field

The interior or exterior formulation of the KHI can be used to determine the field scattered from a facet. The results are equivalent for smooth surfaces but there is debate over which formulation is more accurate for rough surfaces [Ogilvy 1991]. The geometries for the exterior and interior formulations are shown in Figure 3.5. The solution is defined for all space in the exterior formulation, while the interior formulation yields a result for the half-space only. The interior formulation can be constructed to consider either half-space.

Using the exterior formulation of the KHI, a surface is constructed around the facet that is infinitesimally removed from its surface as shown in Figure 3.5(a). The value of the field and its derivative on the surface can be approximated by considering plane wave reflection and transmission at an infinite planar interface as described in Section 2.5.1. This is the Kirchhoff approximation and it is justified when the extent of the facet is much larger than the wavelength of the incident field and when the facet is in the far-field of the transducers [Beckmann and Spizzichino 1987]. In practice,

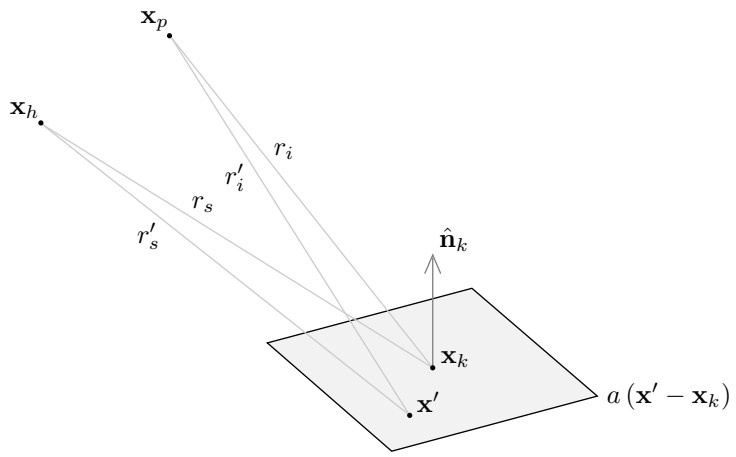

Figure 3.6 The facet-scatterer has a surface normal $\hat{\mathbf{n}}_k$ and its shape is described by the aperture function a. The facet is located at $\mathbf{x}_k$ and it is imaged by a projector and hydrophone at $\mathbf{x}_p$ and $\mathbf{x}_h$.

the facet is a part of some larger surface and, although the extent of the facet might be small, the approximation is valid if the curvature of the entire scattering surface is sufficiently large.

Consider a facet-scatterer located at $\mathbf{x}_k$, a projector located at $\mathbf{x}_p$, and a hydrophone located at $\mathbf{x}_h$. The facet has a surface normal, $\hat{\mathbf{n}}_k$, and its shape is described by the aperture function, $a\,(\mathbf{x})$. This is illustrated in Figure 3.6.

The field incident upon the facet can be approximated by

$$\psi_i\left(\mathbf{x}'\right) \approx S\,(f)\,B_p\,(\hat{\mathbf{n}}_i, f)\,\frac{\exp\left(-j2\pi f/c_1\ r_i\right)}{4\pi r_i}\exp\left(-j2\pi f/c_1\ \hat{\mathbf{n}}_i \cdot \left(\mathbf{x}' - \mathbf{x}_k\right)\right) \tag{3.14}$$

in the far-field of the projector, where r_i is the distance from the projector to the centre of the facet (3.3) and $\hat{\mathbf{n}}_i$ is the direction of the incident planar wavefronts (3.4). The reflected and transmitted fields at the infinite planar interface are given by

$$\psi_r\left(\mathbf{x}'\right) = R\ S\,(f)\,B_p\,(\hat{\mathbf{n}}_i, f)\,\frac{\exp\left(-j2\pi f/c_1\ r_i\right)}{4\pi r_i}\exp\left(-j2\pi f/c_1\ \hat{\mathbf{n}}_r \cdot \left(\mathbf{x}' - \mathbf{x}_k\right)\right) \tag{3.15}$$

and

$$\psi_t\left(\mathbf{x}'\right) = T\ S\,(f)\,B_p\,(\hat{\mathbf{n}}_i, f)\,\frac{\exp\left(-j2\pi f/c_2\ r_i\right)}{4\pi r_i}\exp\left(-j2\pi f/c_2\ \hat{\mathbf{n}}_t \cdot \left(\mathbf{x}' - \mathbf{x}_k\right)\right), \tag{3.16}$$

where c_1 and c_2 are the sound speeds in each medium. Expressions for the reflection coefficient R, the transmission coefficient T, and the directions of reflection and transmission, $\hat{\mathbf{n}}_r$ and $\hat{\mathbf{n}}_t$, are given in Section 2.5.1.

The scattered field on the front and back surfaces of the facet[2] can be approximated using the reflected and transmitted fields for the infinite planar interface, i.e.,

$$\psi_+ \left(\mathbf{x}'\right) \approx \psi_r \left(\mathbf{x}'\right), \tag{3.17}$$

$$\psi_- \left(\mathbf{x}'\right) \approx \psi_t \left(\mathbf{x}'\right). \tag{3.18}$$

The normal derivatives are given by

$$\frac{\partial}{\partial \hat{\mathbf{n}}_+} \psi_+ \left(\mathbf{x}'\right) = j \frac{2\pi}{\lambda_1} \, \hat{\mathbf{n}}_r \cdot \hat{\mathbf{n}}_k \, \psi_r \left(\mathbf{x}'\right) \tag{3.19}$$

and

$$\frac{\partial}{\partial \hat{\mathbf{n}}_-} \psi_- \left(\mathbf{x}'\right) = -j \frac{2\pi}{\lambda_2} \, \hat{\mathbf{n}}_t \cdot \hat{\mathbf{n}}_k \, \psi_t \left(\mathbf{x}'\right), \tag{3.20}$$

where $\lambda_1 = c_1/f$ and $\lambda_2 = c_2/f$ are the wavelengths in each medium. These boundary conditions correct those used regularly in the literature [Beckmann and Spizzichino 1987, Ogilvy 1991].

Beckmann and Ogilvy use the total field for the front surface ($\psi_+ = \psi_i + \psi_r$) and impose the Kirchhoff boundary condition on the back surface ($\psi_- = 0$). The back surface is assumed to be *in shadow*. The field on the back surface is only in shadow when there is no transmitted field, i.e., when the magnitude of the reflection coefficient is unity. Thus, the results derived from these boundary conditions are in error and the expressions derived using the interior and exterior formulations of the KHI do not agree; the exterior formulation is incorrect. The newly proposed boundary conditions, (3.17) and (3.18), correct this error.

The form of the Green's function is dependent on the locations of the points $\mathbf{x}$ and $\mathbf{x}'$. The Green's function is given by

$$G_+ \left(\mathbf{x}, \mathbf{x}', f\right) = \frac{\exp\left(-j2\pi f/c_1 \; r\right)}{4\pi r} \tag{3.21}$$

when both points are in the first medium, and

$$G_- \left(\mathbf{x}, \mathbf{x}', f\right) = \frac{\exp\left(-j2\pi f/c_2 \; r\right)}{4\pi r} \tag{3.22}$$

when they are in the second medium. The general expression for the Green's function is more complicated. However, since the point $\mathbf{x}'$ is on the interface (in the limit), the form of the Green's function is dependent only on the location of the point $\mathbf{x}$. Thus, the Green's function expressions (3.21) and (3.22) are sufficient for the problem.

[2]The two sides of a facet are referred to as the front and the back; the media containing the front and back surfaces are designated the first and second media respectively. The facet normal is defined on the front surface in the direction of the first medium.

The scattered field is determined by substituting expressions (3.17) to (3.22) into the KHI (2.35), giving

$$\psi_{s+}\left(\mathbf{x}_h,\mathbf{x}_p,f\right)=j\frac{2\pi}{\lambda_1}\,S\left(f\right)B_p\left(\hat{\mathbf{n}}_i,f\right)\frac{\exp\left(-j2\pi f/c_1\;r_i\right)}{4\pi r_i}$$
$$\times\left[R\iint\limits_{S_+}\left(\hat{\mathbf{n}}'_s+\hat{\mathbf{n}}_r\right)\cdot\hat{\mathbf{n}}_k\;\frac{\exp\left(-j2\pi f/c_1\;r'_s\right)}{4\pi r'_s}\exp\left(-j2\pi f/c_1\;\hat{\mathbf{n}}_r\cdot\left(\mathbf{x}'-\mathbf{x}_k\right)\right)\;d\mathbf{x}'\right.$$
$$\left.-\,T\iint\limits_{S_-}\left(\hat{\mathbf{n}}'_s+\frac{\lambda_1}{\lambda_2}\hat{\mathbf{n}}_t\right)\cdot\hat{\mathbf{n}}_k\;\frac{\exp\left(-j2\pi f/c_1\;r'_s\right)}{4\pi r'_s}\exp\left(-j2\pi f/c_2\;\hat{\mathbf{n}}_t\cdot\left(\mathbf{x}'-\mathbf{x}_k\right)\right)\;d\mathbf{x}'\right] \tag{3.23}$$

for a projector and hydrophone in the first medium and

$$\psi_{s-}\left(\mathbf{x}_h,\mathbf{x}_p,f\right)=j\frac{2\pi}{\lambda_2}\,S\left(f\right)B_p\left(\hat{\mathbf{n}}_i,f\right)\frac{\exp\left(-j2\pi f/c_1\;r_i\right)}{4\pi r_i}$$
$$\times\left[R\iint\limits_{S_+}\left(\hat{\mathbf{n}}'_s+\frac{\lambda_2}{\lambda_1}\hat{\mathbf{n}}_r\right)\cdot\hat{\mathbf{n}}_k\;\frac{\exp\left(-j2\pi f/c_2\;r'_s\right)}{4\pi r'_s}\exp\left(-j2\pi f/c_1\;\hat{\mathbf{n}}_r\cdot\left(\mathbf{x}'-\mathbf{x}_k\right)\right)\;d\mathbf{x}'\right.$$
$$\left.-\,T\iint\limits_{S_-}\left(\hat{\mathbf{n}}'_s+\hat{\mathbf{n}}_t\right)\cdot\hat{\mathbf{n}}_k\;\frac{\exp\left(-j2\pi f/c_2\;r'_s\right)}{4\pi r'_s}\exp\left(-j2\pi f/c_2\;\hat{\mathbf{n}}_t\cdot\left(\mathbf{x}'-\mathbf{x}_k\right)\right)\;d\mathbf{x}'\right] \tag{3.24}$$

for a projector in the first medium and a hydrophone in the second medium, where

$$\mathbf{r}'_s = \mathbf{x}_h-\mathbf{x}', \tag{3.25}$$
$$r'_s = \left|\mathbf{r}'_s\right|, \tag{3.26}$$
$$\hat{\mathbf{n}}'_s = \frac{\mathbf{r}'_s}{r'_s}. \tag{3.27}$$

The expressions for the scattered field can be simplified to

$$\psi_{s+}\left(\mathbf{x}_h,\mathbf{x}_p,f\right)\approx j\frac{2\pi}{\lambda_1}\,S\left(f\right)B_p\left(\hat{\mathbf{n}}_i,f\right)\frac{\exp\left(j2\pi f/c_1\;r_i\right)}{4\pi r_i}\;R$$
$$\times\iint\limits_{S_+}\left(\hat{\mathbf{n}}'_s+\hat{\mathbf{n}}_r\right)\cdot\hat{\mathbf{n}}_k\;\frac{\exp\left(-j2\pi f/c_1\;r'_s\right)}{4\pi r'_s}\exp\left(-j2\pi f/c_1\;\hat{\mathbf{n}}_r\cdot\left(\mathbf{x}'-\mathbf{x}_k\right)\right)\;d\mathbf{x}', \tag{3.28}$$

$$\psi_{s-}\left(\mathbf{x}_h,\mathbf{x}_p,f\right)\approx -j\frac{2\pi}{\lambda_2}\,S\left(f\right)B_p\left(\hat{\mathbf{n}}_i,f\right)\frac{\exp\left(-j2\pi f/c_1\;r_i\right)}{4\pi r_i}\;T$$
$$\times\iint\limits_{S_-}\left(\hat{\mathbf{n}}'_s+\hat{\mathbf{n}}_t\right)\cdot\hat{\mathbf{n}}_k\;\frac{\exp\left(-j2\pi f/c_2\;r'_s\right)}{4\pi r'_s}\exp\left(-j2\pi f/c_2\;\hat{\mathbf{n}}_t\cdot\left(\mathbf{x}'-\mathbf{x}_k\right)\right)\;d\mathbf{x}', \tag{3.29}$$

when the extent of the facet is sufficiently large, since the contributions from the second integrals in (3.23) and (3.24) are small. The interior formulation of the KHI yields the same expressions for the scattered field, (3.28) and (3.29)[3].

The scattered field in the first medium is assumed for the remainder of this chapter (unless otherwise stated). However, it is a simple matter to derive the results that follow using the scattered field in the second medium instead. The subscripts denoting the two media are, henceforth, suppressed for notational convenience.

3.2.2 Facet beampattern

The scattering from a facet is characterised, in the far-field, by its beampattern, which has a Fourier relationship with the facet shape. The Fourier transform can be computed analytically for simple shapes, such as rectangles and triangles, and it can be computed numerically for arbitrary shapes using the FFT [Bracewell 1986].

Using the Fraunhoffer approximation described in Section 2.3.5,

$$r'_s \approx r_s \tag{3.30}$$

for the magnitude term and

$$r'_s \approx r_s - \hat{\mathbf{n}}_s \cdot \left(\mathbf{x}' - \mathbf{x}_k\right), \tag{3.31}$$

for the phase term. The expression for the scattered field (3.28) is then reduced to

$$\psi_s\left(\mathbf{x}_h, \mathbf{x}_p, f\right) = S\left(f\right) \frac{\exp\left(-j2\pi f/c \ \left(r_i + r_s\right)\right)}{\left(4\pi\right)^2 r_i r_s} B_p\left(\hat{\mathbf{n}}_i, f\right) B\left(\hat{\mathbf{n}}_i, \hat{\mathbf{n}}_s, f\right), \tag{3.32}$$

where

$$B\left(\hat{\mathbf{n}}_i, \hat{\mathbf{n}}_s, f\right) = \ j\frac{2\pi}{\lambda} \ R \cdot \left(\hat{\mathbf{n}}_s + \hat{\mathbf{n}}_r\right) \cdot \hat{\mathbf{n}}_k \ A\left(\frac{f}{c}\left(\hat{\mathbf{n}}_r - \hat{\mathbf{n}}_s\right)\right) \tag{3.33}$$

is the (range-independent) beampattern of the facet,

$$A\left(\mathbf{u}\right) = \iint_{-\infty}^{\infty} a\left(\mathbf{x}'\right) \exp\left(-j2\pi \ \mathbf{x}' \cdot \mathbf{u}\right) \ d\mathbf{x}' \tag{3.34}$$

is the Fourier transform of the aperture function evaluated over the plane containing the facet, and $\left(\hat{\mathbf{n}}_s + \hat{\mathbf{n}}_r\right) \cdot \hat{\mathbf{n}}_k$ is the obliquity factor. The facet beampattern is a function of the angles from the centre of the facet to the projector, θ_i, ϕ_i, and the angles to the hydrophone, θ_s, ϕ_s, as illustrated in Figure 3.7. The beampattern can be expressed

[3]The discrepancy between the result obtained using the interior formulation and the (unsimplified) result obtained using the exterior formulation can be attributed to the mathematical inconsistency associated with the interior formulation of the KHI (see Section 2.3.3).

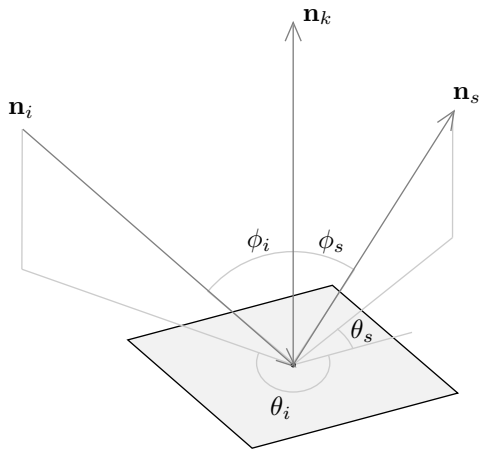

Figure 3.7 The facet beampattern is a function of the angles from the centre of the facet to the projector, θ_i, ϕ_i, and the angles to the hydrophone, θ_s, ϕ_s.

using these angles, giving

$$B\left(\theta_i, \phi_i, \theta_s, \phi_s, f\right) = j\frac{2\pi}{\lambda} R \cdot \left(\cos\phi_i + \cos\phi_s\right) \times A\left(-\frac{f}{c}\left(\cos\theta_i \sin\phi_i + \cos\theta_s \sin\phi_s\right), \frac{f}{c}\left(\sin\theta_i \sin\phi_i - \sin\theta_s \sin\phi_s\right)\right). \tag{3.35}$$

The expression for the scattered field is reduced to the product of a range-dependent component and an angle-dependent component. De-coupling the expression in this way provides a fast method of evaluating the field that is comparable in efficiency to the point-scatterer model. The plane wave approximation for the incident field and use of the transducer and facet beampatterns is valid when the Rayleigh criterion (2.60) is satisfied. The approximations are justified for most SAS imaging geometries. However, the criterion becomes restrictive for multiple scattering between facets within a complex object. The beampattern can be evaluated analytically for simple facet shapes; this is detailed in the following sections for rectangular and triangular facets. For more complicated shapes, the beampattern can be calculated using the FFT; this is detailed in Sections 3.3 to 3.6.

3.2.3 Rectangular facet

The rectangle is a common facet shape. It is particularly useful for describing flat objects such as a flat sea floor or sea surface. The aperture function is defined by

$$a_R\left(x, y\right) = \text{rect}\left(\frac{x}{L_x}\right) \text{rect}\left(\frac{y}{L_y}\right), \tag{3.36}$$

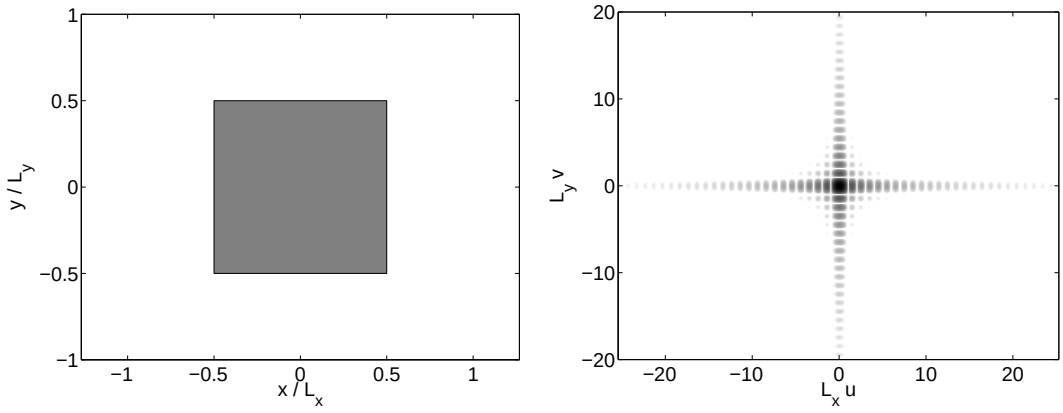

(a) aperture function

(b) Fourier transform

Figure 3.8 The rectangle lies in the x-y plane and is centred at the origin. It has sides of length L_x and L_y that are aligned with the axes.

for a rectangular facet in the x-y plane and aligned with the axes, where L_x and L_y are the dimensions of the rectangle. The Fourier transform of this aperture function is given by

$$A_R(u,v) = L_x L_y \operatorname{sinc}(L_x u) \operatorname{sinc}(L_y v), \tag{3.37}$$

where $L_x L_y$ is the area of the facet. The rectangular aperture function and its Fourier transform are shown in Figure 3.8.

Substituting the Fourier transform (3.37) into the beampattern expression (3.33) yields the beampattern for the rectangular facet;

$$\begin{aligned} B_R(\hat{\mathbf{n}}_i, \hat{\mathbf{n}}_s, f) = j\frac{2\pi}{\lambda}\ R \cdot (n_{sz} + n_{rz})\ \ L_x L_y \\ \times\ \operatorname{sinc}\left(L_x \frac{f}{c}(n_{rx} - n_{sx})\right) \operatorname{sinc}\left(L_y \frac{f}{c}(n_{ry} - n_{sy})\right), \end{aligned} \tag{3.38}$$

where $\hat{\mathbf{n}}_k = (0,0,1)$ since the facet lies in the x–y plane, $\hat{\mathbf{n}}_r = (n_{rx}, n_{ry}, n_{rz})$, and $\hat{\mathbf{n}}_s = (n_{sx}, n_{sy}, n_{sz})$. The beampattern of an arbitrarily oriented facet is discussed in Section 4.2.2.

3.2.4 Right-angle triangular facet

The triangle is an important facet shape since any surface can be tessellated into a continuous collection of triangles [Foley *et al.* 1997]. The beampattern for a triangular facet can be derived analytically; the Fourier transform of a triangle is given in Appendix A. However, a unit right-angle triangle is considered here. The beampattern for a triangular facet with arbitrary shape and orientation can be determined from the

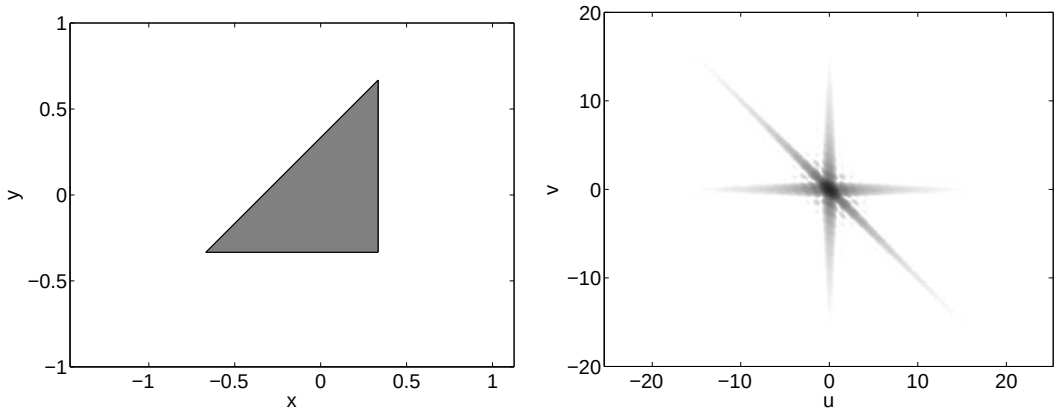

(a) aperture function

(b) Fourier transform

Figure 3.9 The unit right-angle triangle lies in the x-y plane with its centroid at the origin. It has sides of length 1 m that are aligned with the axes.

expression for a unit right-angle triangle as described in Section 4.2.2.

The aperture function is defined by

$$a_T(x,y) = \text{rect}\left(\frac{x-y}{2} - \frac{1}{3}\right) \text{rect}\left(x + \frac{1}{6}\right) \text{rect}\left(y - \frac{1}{6}\right) \tag{3.39}$$

for a unit right-angle triangle in the x-y plane and aligned with the axes. The Fourier transform of this aperture function is given by

$$A_T(u,v) = \frac{j}{2\pi u} \exp\left(j\pi \frac{1}{3}(u-v)\right) \left[\exp(-j\pi u)\,\text{sinc}(v) - \text{sinc}(u+v)\right]. \tag{3.40}$$

The triangular aperture function and its Fourier transform are shown in Figure 3.9.

Substituting the Fourier transform (3.40) into the beampattern expression (3.33) yields the beampattern for the unit right-angle triangular facet;

$$B_T(\hat{\mathbf{n}}_i, \hat{\mathbf{n}}_s, f) = R\, \frac{n_{sz} + n_{rz}}{n_{sx} - n_{rx}} \exp\left(j\pi \frac{1}{3}\frac{f}{c}(n_{rx} - n_{sx} - n_{ry} + n_{sy})\right)$$
$$\times \left[\exp\left(j\pi \frac{f}{c}(n_{sx} - n_{rx})\right) \text{sinc}\left(\frac{f}{c}(n_{ry} - n_{sy})\right) - \text{sinc}\left(\frac{f}{c}(n_{rx} - n_{sx} + n_{ry} - n_{sy})\right)\right]. \tag{3.41}$$

3.2.5 Example beampatterns

Some example beampatterns are shown in Figures 3.10 and 3.11. The scattered energy is concentrated around the specular directions of transmission and reflection, $\hat{\mathbf{n}}_t$ and

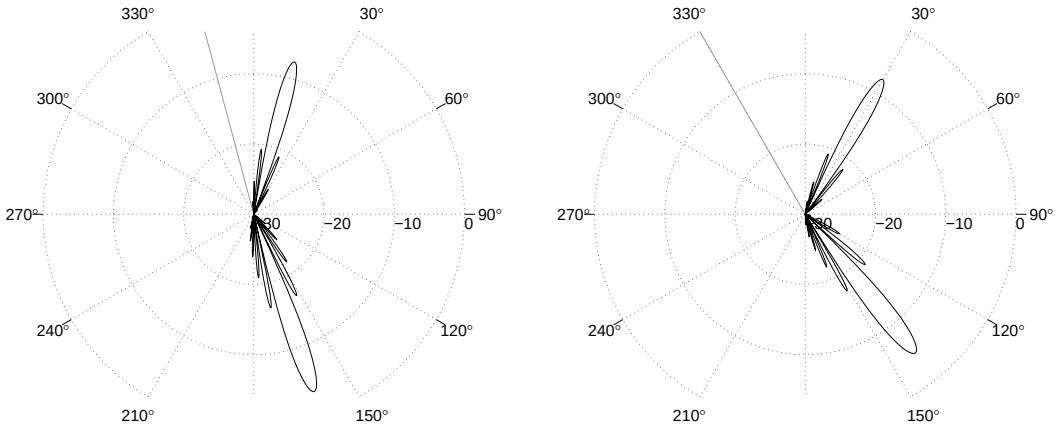

(a) $\phi_i = 15\,\text{deg}$ (b) $\phi_i = 30\,\text{deg}$

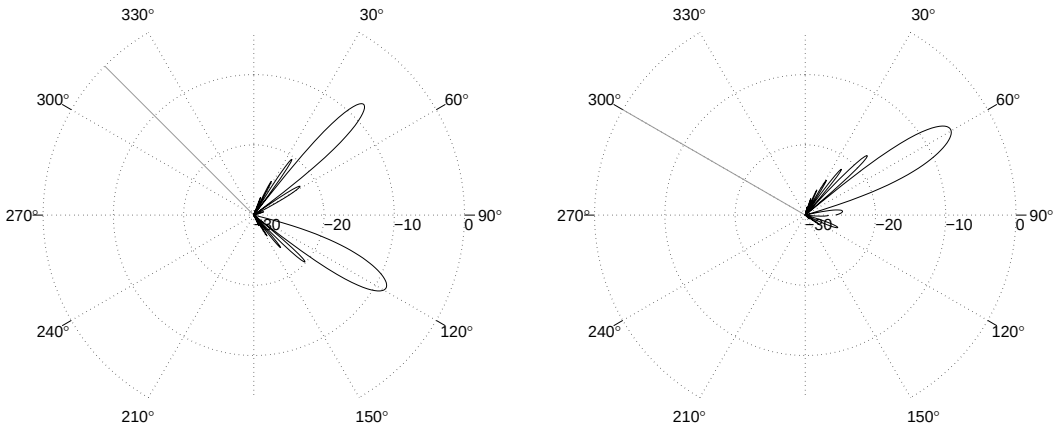

(c) $\phi_i = 45\,\text{deg}$ (d) $\phi_i = 60\,\text{deg}$

Figure 3.10 The beampattern of a facet is dependent on the direction of the incident field. The beampatterns of a facet are shown here for varying angles of incidence. The facet is 0.5 m in length and the beampatterns are calculated using a frequency of 30 kHz. The upper medium is sea water and the lower medium is fine silt. Penetration into the lower medium is reduced at shallow angles and there is no penetration beyond the critical angle, $\phi_i \approx 60\,\text{deg}$. The 0 dB reference is the magnitude of the incident plane wave.

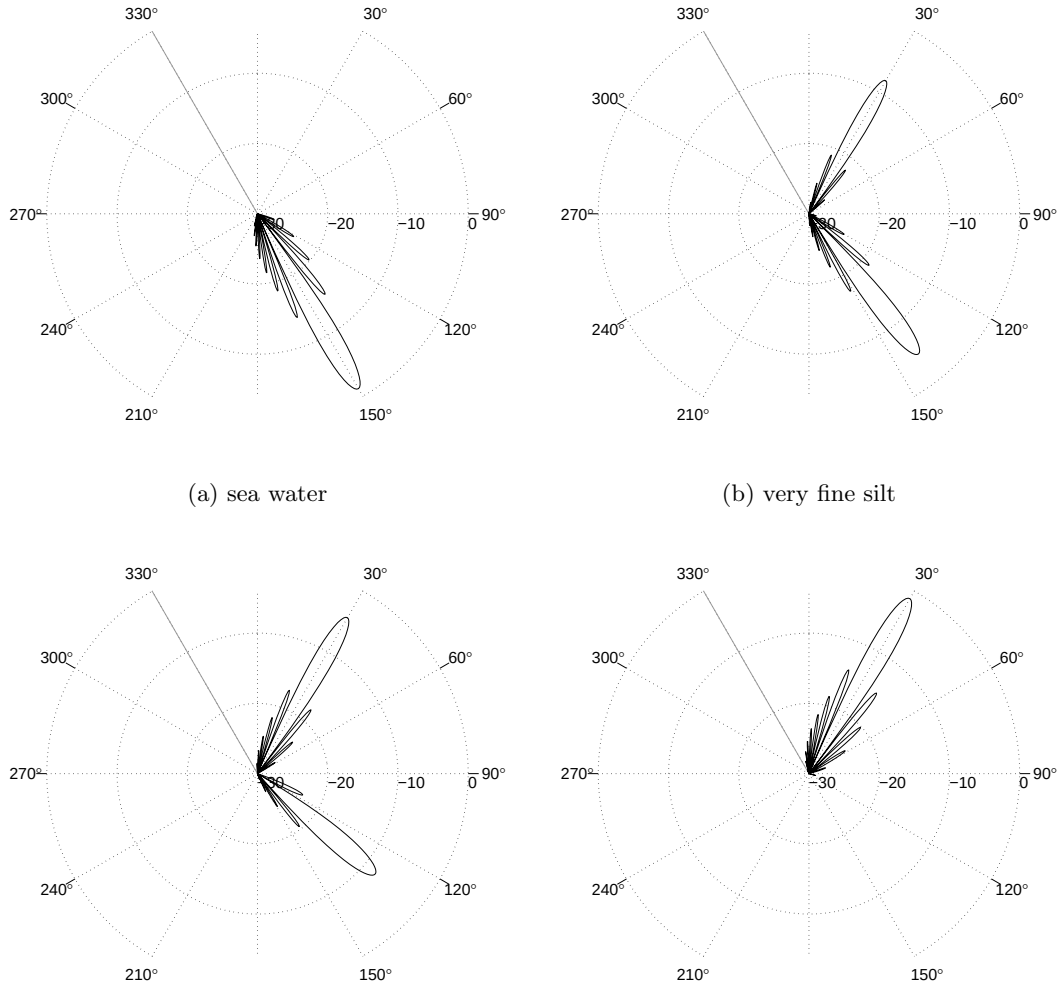

(a) sea water

(b) very fine silt

(c) very coarse sand

(d) rock

Figure 3.11 The beampattern of a facet is dependent on the properties of the media on each side of the facet. The beampatterns are shown here for water-water, water-silt, water-sand, and water-rock interfaces. Penetration into the lower medium decreases with increasing acoustic mis-match between the media. The 0 dB reference is the magnitude of the incident plane wave.

$\hat{\mathbf{n}}_r$. In Figure 3.10 the angle of the incident field is varied. Penetration into the second medium is reduced at shallow angles and there is no penetration into the second medium beyond the critical angle. In Figure 3.11 the properties of the second medium are varied. Penetration into the second medium decreases as the mis-match of acoustic impedances between the media increases. These results agree with those expected for an infinite interface.

3.3 SCATTERING FROM A ROUGH FACET

A rough surface can be modelled using a collection of smooth triangular facets. However, this is inefficient; it is comparable in efficiency to using points. Instead, rough facets can be employed. Fewer rough facets are required to model a rough surface and the use of these primitives is more efficient. The simulator detailed in Chapter 4 employs the rough facet scattering model described in this chapter.

A rough facet is defined as a nominally planar scattering surface of finite extent. The facet shape is described by the aperture function, a, and the deviations of the surface from the mean plane are described by the height function, $h = h(\mathbf{x}')$. The scattering from the facet is related to the facet shape and orientation, the acoustic properties of the two media, and the roughness statistics of the height function. The statistics of the beampattern are determined from these and used to generate a beampattern realisation.

3.3.1 Rough facet beampattern

The scattering geometry for a rough facet is illustrated in Figure 3.12. Using the Fraunhoffer approximation,

$$r_s' \approx r_s - \hat{\mathbf{n}}_s \cdot \left(\mathbf{x}' - \mathbf{x}_k + h\left(\mathbf{x}'\right)\hat{\mathbf{n}}_k\right) \tag{3.42}$$

and similarly for the incident field,

$$r_i' \approx r_i + \hat{\mathbf{n}}_i \cdot \left(\mathbf{x}' - \mathbf{x}_k + h\left(\mathbf{x}'\right)\hat{\mathbf{n}}_k\right), \tag{3.43}$$

where $\hat{\mathbf{n}}_k$ is the normal for the mean plane.

Substitution of (3.42) and (3.43) into the expression for the scattered field (3.28), yields the expression

$$\begin{aligned} B\left(\hat{\mathbf{n}}_i, \hat{\mathbf{n}}_s, f\right) = j\frac{2\pi}{\lambda} \iint_{-\infty}^{\infty} R \cdot \left(\hat{\mathbf{n}}_s + \hat{\mathbf{n}}_r\right) \cdot \hat{\mathbf{n}} \ \left[a\left(\mathbf{x}'\right) \exp\left(-j2\pi f/c \ q_z h\left(\mathbf{x}'\right)\right)\right] \\ \times \exp\left(-j2\pi \ \frac{f}{c}\mathbf{q}_x \cdot \mathbf{x}'\right) \ d\mathbf{x}' \end{aligned} \tag{3.44}$$

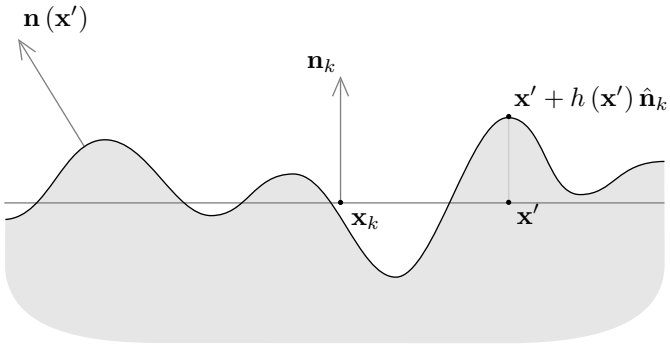

Figure 3.12 The height function, h, describes the deviation of the rough surface from the mean plane. The mean plane is defined by the normal, $\hat{\mathbf{n}}_k$.

for the beampattern of a rough facet, where

$$q_z = (\hat{\mathbf{n}}_r - \hat{\mathbf{n}}_s) \cdot \hat{\mathbf{n}}_k \tag{3.45}$$

and

$$\mathbf{q}_x = (\hat{\mathbf{n}}_r - \hat{\mathbf{n}}_s) - q_z \hat{\mathbf{n}}_k \tag{3.46}$$

are the normal and tangential components of the vector $\hat{\mathbf{n}}_r - \hat{\mathbf{n}}_s$. The reflection coefficient, $R = R(\hat{\mathbf{n}})$, and the obliquity factor, $(\hat{\mathbf{n}}_s + \hat{\mathbf{n}}_r) \cdot \hat{\mathbf{n}}$, are retained within the integral since the surface normal, $\hat{\mathbf{n}} = \hat{\mathbf{n}}(\mathbf{x}')$, is dependent on the position $\mathbf{x}'$ for a rough surface.

The beampattern can be approximated by

$$\begin{aligned} B(\hat{\mathbf{n}}_i, \hat{\mathbf{n}}_s, f) \approx & j\frac{2\pi}{\lambda}\, R \cdot (\hat{\mathbf{n}}_s + \hat{\mathbf{n}}_r) \cdot \hat{\mathbf{n}}_k \\ & \times \iint_{-\infty}^{\infty} \left[a(\mathbf{x}') \exp\left(-j2\pi f/c\; q_z h(\mathbf{x}')\right) \right] \exp\left(-j2\pi\, \frac{f}{c} \mathbf{q}_x \cdot \mathbf{x}'\right)\, d\mathbf{x}' \end{aligned} \tag{3.47}$$

when the reflection coefficient and the obliquity factor are assumed constant. This approximation is valid when the radius of curvature of the surface is large relative to the wavelength [Ogilvy 1991]. The integral in the expression (3.47) is recognisable as the Fourier transform of the function $a(\mathbf{x}') \exp(-j2\pi f/c\; q_z h(\mathbf{x}'))$ evaluated at the spatial frequencies $\mathbf{u} = f/c\; \mathbf{q}_x$.

To obtain a better approximation for the beampattern expression, the reflection coefficient is assumed constant and partial integration (or integration by parts) is performed. The result is equivalent to the approximation (3.47) with the addition of terms that Beckmann denotes *edge effects*. These terms can be ignored when the extent of the facet is sufficiently large [Beckmann and Spizzichino 1987]. The reflection coefficient is a complicated function of the surface normal and it is difficult to reduce the beam-

pattern to a manageable expression when retaining the reflection coefficient within the integral [Beckmann and Spizzichino 1987].

3.3.2 Statistics of the facet beampattern

The height function for a rough facet is a random process and, therefore, the beampattern of a rough facet is a random process also. A particular realisation of the height function yields a realisation of the beampattern, which is unique for each facet. The roughness described by the height function is assumed to be small and unresolvable by the imaging system. Therefore, statistical representation of the height function is sufficient. Any features that are resolvable by the imaging system should be modelled completely.

It is desirable to realise each beampattern directly and without realisation of the corresponding height function. However, direct realisation of the beampattern requires knowledge of its statistics. In the sections that follow, the first and second-order beampattern statistics are determined. In Section 3.6, the realisation of the beampattern from these statistics is detailed.

The beampattern can be considered the sum of a specular component[4] and a diffuse component, i.e.,

$$B\left(\hat{\mathbf{n}}_i, \hat{\mathbf{n}}_s, f\right) = B_c\left(\hat{\mathbf{n}}_i, \hat{\mathbf{n}}_s, f\right) + B_d\left(\hat{\mathbf{n}}_i, \hat{\mathbf{n}}_s, f\right), \tag{3.48}$$

where the specular component,

$$B_c\left(\hat{\mathbf{n}}_i, \hat{\mathbf{n}}_s, f\right) = E\left\{B\left(\hat{\mathbf{n}}_i, \hat{\mathbf{n}}_s, f\right)\right\}, \tag{3.49}$$

is the deterministic mean of the beampattern, the diffuse component,

$$B_d\left(\hat{\mathbf{n}}_i, \hat{\mathbf{n}}_s, f\right) = B\left(\hat{\mathbf{n}}_i, \hat{\mathbf{n}}_s, f\right) - B_c\left(\hat{\mathbf{n}}_i, \hat{\mathbf{n}}_s, f\right), \tag{3.50}$$

is the random variation about this mean, and the operator $E\left\{\cdot\right\}$ denotes the expected value. The specular component dominates for a smooth facet and the diffuse component dominates for a very rough facet.

3.4 FIRST-ORDER STATISTICS

A random process is described by its statistics. The first-order statistics give the probability distribution of a single sample from the process. Here, the first-order statistics of the facet beampattern are considered, that is, the specular component and the

[4]The specular component is sometimes referred to as the coherent component in the literature. This terminology is not used here to avoid confusion with phase coherence. However, the subscript c, for coherent, is used to denote the specular field.

mean intensity of the diffuse component. The second-order statistics are covered in Section 3.5.

3.4.1 Specular component

The specular component is the deterministic mean of the beampattern. It is determined by taking the expected value of the beampattern expression (3.47), giving

$$B_c\left(\hat{\mathbf{n}}_i, \hat{\mathbf{n}}_s, f\right) = j\frac{2\pi}{\lambda}\, R \cdot \left(\hat{\mathbf{n}}_s + \hat{\mathbf{n}}_r\right) \cdot \hat{\mathbf{n}}_k \times \iint_{-\infty}^{\infty} a\left(\mathbf{x}'\right) \exp\left(-j2\pi f/c\ \mathbf{q}_x \cdot \mathbf{x}'\right) E\left\{\exp\left(-j2\pi f/c\ q_z\ h\left(\mathbf{x}'\right)\right)\right\}\, d\mathbf{x}'. \tag{3.51}$$

The expectation factor in this expression is given by

$$E\left\{\exp\left(-j2\pi f/c\ q_z\ h\right)\right\} = \int_{-\infty}^{\infty} p\left(h\right) \exp\left(-j2\pi f/c\ q_z\ h\right)\ dh, \tag{3.52}$$

where p is the probability density function of the height distribution. The expectation can be recognised as the characteristic function of the height distribution evaluated at $\nu = f/c\ q_z$. The remaining integral in the expression (3.51) is the Fourier transform of the aperture function. Thus, the specular component of the beampattern is given by

$$B_c\left(\hat{\mathbf{n}}_i, \hat{\mathbf{n}}_s, f\right) = j\frac{2\pi}{\lambda}\, R \cdot \left(\hat{\mathbf{n}}_s + \hat{\mathbf{n}}_r\right) \cdot \hat{\mathbf{n}}_k\ A\left(\frac{f}{c}\mathbf{q}_x\right) \Phi\left(\frac{f}{c}q_z\right), \tag{3.53}$$

where

$$\Phi\left(\nu\right) = \int_{-\infty}^{\infty} p\left(h\right) \exp\left(-j2\pi\ \nu\ h\right)\ dh \tag{3.54}$$

is the characteristic function, i.e., the Fourier transform of the probability density function. The expression for the specular component of the beampattern is deterministic and its form is similar to the expression for the beampattern of a smooth facet (3.33)[5].

3.4.2 Mean intensity of the diffuse component

The diffuse component is the random variation of the beampattern about its mean value. The diffuse component has zero mean. Therefore it is specified to the first order

[5]The expression for a smooth facet can be obtained by letting $p\left(h\right) = \delta\left(h\right)$.

by its mean intensity, which is given by

$$\begin{aligned} I_d\left(\hat{\mathbf{n}}_i, \hat{\mathbf{n}}_s, f\right) &= E\left\{\left|B_d\left(\hat{\mathbf{n}}_i, \hat{\mathbf{n}}_s, f\right)\right|^2\right\} \\ &= E\left\{\left|B\left(\hat{\mathbf{n}}_i, \hat{\mathbf{n}}_s, f\right)\right|^2\right\} - I_c\left(\hat{\mathbf{n}}_i, \hat{\mathbf{n}}_s, f\right), \end{aligned} \tag{3.55}$$

where

$$I_c\left(\hat{\mathbf{n}}_i, \hat{\mathbf{n}}_s, f\right) = \left|B_c\left(\hat{\mathbf{n}}_i, \hat{\mathbf{n}}_s, f\right)\right|^2 \tag{3.56}$$

$$= \frac{(2\pi)^2}{\lambda^2}\left|R \cdot \left(\hat{\mathbf{n}}_s + \hat{\mathbf{n}}_r\right) \cdot \hat{\mathbf{n}}_k\right|^2 \left|W\left(\frac{f}{c}\mathbf{q}_x\right)\right|^2 \left|\Phi\left(\frac{f}{c}q_z\right)\right|^2. \tag{3.57}$$

is the intensity of the specular component (3.53).

Substitution of the beampattern expression (3.47) into the expression for the intensity (3.55) gives

$$\begin{aligned} I_d\left(\hat{\mathbf{n}}_i, \hat{\mathbf{n}}_s, f\right) =& \frac{(2\pi)^2}{\lambda^2}\left|R \cdot \left(\hat{\mathbf{n}}_s + \hat{\mathbf{n}}_r\right) \cdot \hat{\mathbf{n}}_k\right|^2 \\ &\times \iiiint_{-\infty}^{\infty} a\left(\mathbf{x}'\right) a^*\left(\mathbf{x}''\right) \exp\left(-j2\pi f/c\ \mathbf{q}_x \cdot \left(\mathbf{x}'' - \mathbf{x}'\right)\right) \\ &\times E\left\{\exp\left(-j2\pi f/c\ q_z\left(h\left(\mathbf{x}''\right) - h\left(\mathbf{x}'\right)\right)\right)\right\}\ d\mathbf{x}'\ d\mathbf{x}'' \\ &- I_c\left(\hat{\mathbf{n}}_i, \hat{\mathbf{n}}_s, f\right). \end{aligned} \tag{3.58}$$

where $.^*$ denotes complex conjugation. The expectation factor in this expression can be recognised as the second-order characteristic function of the height distribution,

$$\Phi\left(\nu_1, \nu_2, \mathbf{x}', \mathbf{x}''\right) = \iint_{-\infty}^{\infty} p\left(h_1, h_2, \mathbf{x}', \mathbf{x}''\right) \exp\left(-j2\pi\left(\nu_1 h_1 + \nu_2 h_2\right)\right)\ dh_1\ dh_2, \tag{3.59}$$

evaluated at $\nu_1 = -f/c\ q_z$ and $\nu_2 = f/c\ q_z$, where $p\left(h_1, h_2\right)$ is the second-order probability density function of the height distribution. Thus,

$$\begin{aligned} I_d\left(\hat{\mathbf{n}}_i, \hat{\mathbf{n}}_s, f\right) =& \frac{(2\pi)^2}{\lambda^2}\left|R \cdot \left(\hat{\mathbf{n}}_s + \hat{\mathbf{n}}_r\right) \cdot \hat{\mathbf{n}}_k\right|^2 \\ &\times \iiiint_{-\infty}^{\infty} a\left(\mathbf{x}'\right) a^*\left(\mathbf{x}''\right) \Phi\left(-\frac{f}{c}\ q_z, \frac{f}{c}\ q_z, \mathbf{x}', \mathbf{x}''\right) \\ &\times \exp\left(-j2\pi f/c\ \mathbf{q}_x \cdot \left(\mathbf{x}'' - \mathbf{x}'\right)\right)\ d\mathbf{x}'\ d\mathbf{x}'' \\ &- I_c\left(\hat{\mathbf{n}}_i, \hat{\mathbf{n}}_s, f\right). \end{aligned} \tag{3.60}$$

The height distribution is assumed stationary in order to reduce the beampattern expression to a manageable form. Under this assumption, the height distribution and

its characteristic function are dependent only on the difference between the points $\mathbf{x}'$ and $\mathbf{x}''$, i.e.,

$$\Phi\left(\nu_1, \nu_2, \mathbf{x}', \mathbf{x}''\right) = \Phi\left(\nu_1, \nu_2, \mathbf{x}'' - \mathbf{x}'\right). \tag{3.61}$$

This is reasonable for many rough surfaces.

Expressing the characteristic function using the Fourier transform, i.e.,

$$\Phi\left(\nu_1, \nu_2, \Delta\mathbf{x}\right) = \iint_{-\infty}^{\infty} \chi\left(\nu_1, \nu_2, \mathbf{u}\right) \exp\left(j2\pi\ \Delta\mathbf{x} \cdot \mathbf{u}\right)\ d\mathbf{u}, \tag{3.62}$$

and substituting into the expression for the intensity (3.60) gives

$$\begin{aligned} E\left\{\left|B_d\left(\hat{\mathbf{n}}_i, \hat{\mathbf{n}}_s, f\right)\right|^2\right\} = & \frac{(2\pi)^2}{\lambda^2}\left|R \cdot \left(\hat{\mathbf{n}}_s + \hat{\mathbf{n}}_r\right) \cdot \hat{\mathbf{n}}_k\right|^2 \\ & \times \iiiint_{-\infty}^{\infty} a\left(\mathbf{x}'\right) a^*\left(\mathbf{x}''\right) \chi\left(-\frac{f}{c}\ q_z, \frac{f}{c}\ q_z, \mathbf{u}\right) \\ & \times \exp\left(-j2\pi\left(f/c\ \mathbf{q}_x - \mathbf{u}\right) \cdot \left(\mathbf{x}'' - \mathbf{x}'\right)\right)\ d\mathbf{x}'\ d\mathbf{x}''\ d\mathbf{u} \\ & - I_c\left(\hat{\mathbf{n}}_i, \hat{\mathbf{n}}_s, f\right), \end{aligned} \tag{3.63}$$

which can be reduced to

$$\begin{aligned} E\left\{\left|B_d\left(\hat{\mathbf{n}}_i, \hat{\mathbf{n}}_s, f\right)\right|^2\right\} = & \frac{(2\pi)^2}{\lambda^2}\left|R \cdot \left(\hat{\mathbf{n}}_s + \hat{\mathbf{n}}_r\right) \cdot \hat{\mathbf{n}}_k\right|^2 \\ & \times \iint_{-\infty}^{\infty} \left|A\left(\mathbf{u} - \frac{f}{c}\mathbf{q}_x\right)\right|^2 \chi\left(-\frac{f}{c}q_z, \frac{f}{c}q_z, \mathbf{u}\right)\ d\mathbf{u} \\ & - I_c\left(\hat{\mathbf{n}}_i, \hat{\mathbf{n}}_s, f\right). \end{aligned} \tag{3.64}$$

The intensity of the diffuse component is the result of a correlation between the Fourier transform of the squared magnitude of the aperture function and the Fourier transform of the characteristic function.

3.5 SECOND-ORDER STATISTICS

The higher-order statistics of a random process describe the correlations between samples of the process; the second-order statistics describe the correlation between two samples. The second-order statistics of the diffuse beampattern component are considered here. These are dependent on the transducer locations and the temporal frequencies. The statistics are time-dependent for a time-variant facet. However, any temporal variations are assumed to be slow, i.e., facet shape and roughness are assumed constant within the time taken for the scattering events. For simplicity, the scattered field is assumed to have Gaussian-distributed real and imaginary components [Goodman 1985]

and, since a Gaussian is described completely by its first and second-order statistics, the higher-order statistics are not required.

3.5.1 Mutual coherence function

The second-order statistics of the diffuse beampattern component are specified by the auto-covariance function [Goodman 1985]. The auto-covariance can be calculated in space and time, where it is referred to as the mutual coherence function, or in space and temporal frequency, where it is referred to as the two-frequency mutual coherence function. The two-frequency mutual coherence function is used in the following analysis and it is referred to, henceforth, as the coherence function.

The coherence function for the diffuse beampattern component is a function of four spatial positions and two frequencies; it is range-independent and it is given by

$$\begin{aligned}\Gamma\left(\hat{\mathbf{n}}_{i1},\hat{\mathbf{n}}_{i2},\hat{\mathbf{n}}_{s1},\hat{\mathbf{n}}_{s2},f_1,f_2\right) &= E\left\{B_d\left(\hat{\mathbf{n}}_{i1},\hat{\mathbf{n}}_{s1},f_1\right)B_d^*\left(\hat{\mathbf{n}}_{i2},\hat{\mathbf{n}}_{s2},f_2\right)\right\}\\ &= E\left\{B\left(\hat{\mathbf{n}}_{i1},\hat{\mathbf{n}}_{s1},f_1\right)B^*\left(\hat{\mathbf{n}}_{i2},\hat{\mathbf{n}}_{s2},f_2\right)\right\}\\ &\quad - B_c\left(\hat{\mathbf{n}}_{i1},\hat{\mathbf{n}}_{s1},f_1\right)B_c^*\left(\hat{\mathbf{n}}_{i2},\hat{\mathbf{n}}_{s2},f_2\right),\end{aligned} \tag{3.65}$$

$$\hat{\mathbf{n}}_{i1} = \frac{\mathbf{x}_k-\mathbf{x}_{p1}}{|\mathbf{x}_k-\mathbf{x}_{p1}|}, \tag{3.66}$$

$$\hat{\mathbf{n}}_{i2} = \frac{\mathbf{x}_k-\mathbf{x}_{p2}}{|\mathbf{x}_k-\mathbf{x}_{p2}|}, \tag{3.67}$$

and

$$\hat{\mathbf{n}}_{s1} = \frac{\mathbf{x}_k-\mathbf{x}_{h1}}{|\mathbf{x}_k-\mathbf{x}_{h1}|}, \tag{3.68}$$

$$\hat{\mathbf{n}}_{s2} = \frac{\mathbf{x}_k-\mathbf{x}_{h2}}{|\mathbf{x}_k-\mathbf{x}_{h2}|}, \tag{3.69}$$

$\mathbf{x}_{p1}$, $\mathbf{x}_{h1}$ and $\mathbf{x}_{p2}$, $\mathbf{x}_{h2}$ are two sets of transducer positions, and f_1 and f_2 are two temporal frequencies; this is illustrated in Figure 3.13. Substitution of the beampattern expression into the expression for the coherence function yields,

$$\begin{aligned}&\Gamma\left(\frac{f_1}{c}\mathbf{q}_{x1},\frac{f_1}{c}q_{z1},\frac{f_2}{c}\mathbf{q}_{x2},\frac{f_2}{c}q_{z2}\right) = \iiiint_{-\infty}^{\infty} a\left(\mathbf{x}'\right)a^*\left(\mathbf{x}''\right)\\ &\times\exp\left(-j2\pi\left(\frac{f_2}{c}\mathbf{q}_{x2}\cdot\mathbf{x}''-\frac{f_1}{c}\mathbf{q}_{x1}\cdot\mathbf{x}'\right)\right)E\left\{-j2\pi\left(\frac{f_2}{c}q_{z2}\;h\left(\mathbf{x}''\right)-\frac{f_1}{c}q_{z1}\;h\left(\mathbf{x}'\right)\right)\right\}\\ &\quad d\mathbf{x}'\,d\mathbf{x}'' - B_c\left(\frac{f_1}{c}\mathbf{q}_{x1}\right)B_c^*\left(\frac{f_2}{c}\mathbf{q}_{x2}\right),\end{aligned} \tag{3.70}$$

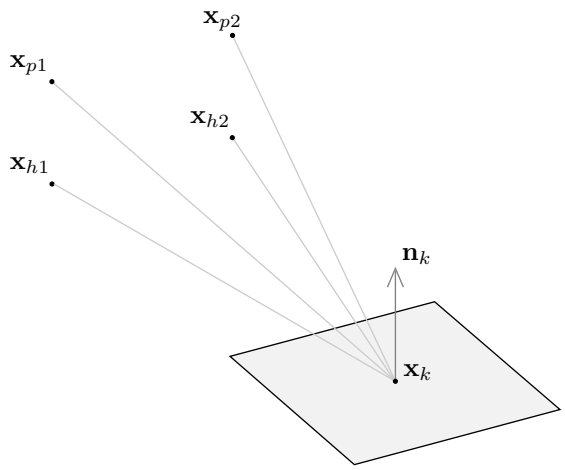

Figure 3.13 The two-frequency mutual coherence function describes the correlation of the diffuse beampattern component for the transducer locations $\mathbf{x}_{p1}$, $\mathbf{x}_{h1}$ and $\mathbf{x}_{p2}$, $\mathbf{x}_{h2}$, and for the temporal frequencies f_1 and f_2.

where the deterministic quantities, e.g., the reflection coefficient and the obliquity term, have been suppressed for notational convenience. The coherence function is reduced from a function of fourteen variables (two projector positions, two hydrophone positions, and two frequencies) to a function of only six variables. The expectation in the expression (3.70) can be recognised as the second-order characteristic function of the height distribution (3.59). Thus,

$$\begin{aligned}\Gamma\left(\frac{f_1}{c}\mathbf{q}_{x1}, \frac{f_1}{c}q_{z1}, \frac{f_2}{c}\mathbf{q}_{x2}, \frac{f_2}{c}q_{z2}\right) &= \iiiint_{-\infty}^{\infty} a\left(\mathbf{x}'\right) a^*\left(\mathbf{x}''\right) \Phi\left(-\frac{f_1}{c}q_{z1}, \frac{f_2}{c}q_{z2}, \mathbf{x}'' - \mathbf{x}'\right) \\ &\times \exp\left(-j2\pi\left(\frac{f_2}{c}\mathbf{q}_{x2}\cdot\mathbf{x}'' - \frac{f_1}{c}\mathbf{q}_{x1}\cdot\mathbf{x}'\right)\right) d\mathbf{x}'\, d\mathbf{x}'' \\ &- B_c\left(\frac{f_1}{c}\mathbf{q}_{x1}\right) B_c^*\left(\frac{f_2}{c}\mathbf{q}_{x2}\right).\end{aligned} \tag{3.71}$$

Then expressing the characteristic function by its Fourier transform (3.62) gives,

$$\begin{aligned}\Gamma\left(\frac{f_1}{c}\mathbf{q}_{x1}, \frac{f_1}{c}q_{z1}, \frac{f_2}{c}\mathbf{q}_{x2}, \frac{f_2}{c}q_{z2}\right) &= \iiiiiint_{-\infty}^{\infty} a\left(\mathbf{x}'\right) a^*\left(\mathbf{x}''\right) \chi\left(-\frac{f_1}{c}q_{z1}, \frac{f_2}{c}q_{z2}, \mathbf{u}\right) \\ &\times \exp\left(-j2\pi\left(\frac{f_2}{c}\mathbf{q}_{x2}\cdot\mathbf{x}'' - \frac{f_1}{c}\mathbf{q}_{x1}\cdot\mathbf{x}'\right)\right) \exp\left(-j2\pi\mathbf{u}\left(\mathbf{x}'' - \mathbf{x}'\right)\right) d\mathbf{x}'\, d\mathbf{x}''\, d\mathbf{u} \\ &- B_c\left(\frac{f_1}{c}\mathbf{q}_{x1}\right) B_c^*\left(\frac{f_2}{c}\mathbf{q}_{x2}\right),\end{aligned} \tag{3.72}$$

which can be reduced to

$$\Gamma\left(\frac{f_1}{c}\mathbf{q}_{x1}, \frac{f_1}{c}q_{z1}, \frac{f_2}{c}\mathbf{q}_{x2}, \frac{f_2}{c}q_{z2}\right) = \iint_{-\infty}^{\infty} A\left(\mathbf{u} - \frac{f_1}{c}\mathbf{q}_{x1}\right) A^*\left(\mathbf{u} - \frac{f_2}{c}\mathbf{q}_{x2}\right) \times \chi\left(-\frac{f_1}{c}q_{z1}, \frac{f_2}{c}q_{z2}, \mathbf{u}\right) d\mathbf{u} - B_c\left(\frac{f_1}{c}\mathbf{q}_{x1}\right) B_c^*\left(\frac{f_2}{c}\mathbf{q}_{x2}\right). \tag{3.73}$$

This collapses to the expression for the intensity (3.64) when $\mathbf{q}_{x1} = \mathbf{q}_{x2}$, $q_{z1} = q_{z2}$, and $f_1 = f_2$.

3.6 REALISATION OF THE FACET BEAMPATTERN

Each unique facet has a unique beampattern realisation. The beampattern can be generated by evaluating the Fourier transform of the aperture function appropriately phased by the realisation of the height function (3.47). However, the weighting of the apparent height function is dependent on the temporal frequency and the direction vectors. Thus, a 2-D Fourier transform must be performed for each frequency and for each unique geometry; this is inefficient. Instead, the beampattern can be generated directly from the statistics derived in the previous sections. The specular component of the beampattern is deterministic and it is simple to generate using (3.53). However, direct realisation of the diffuse component is more complicated. In general, the diffuse component can be realised using the Karhunen-Loéve decomposition [Van Trees 1968] but this is not considered here. Instead, a quasi-stationary approximation is employed and the diffuse component is realised by windowing a stationary process in Section 3.6.2.

3.6.1 Stationarity

The statistics of the diffuse component are given by the coherence function (3.73);

$$\Gamma\left(\boldsymbol{\zeta}_1, \xi_1, \boldsymbol{\zeta}_2, \xi_2\right) = \iint_{-\infty}^{\infty} A\left(\mathbf{u} - \boldsymbol{\zeta}_1\right) A^*\left(\mathbf{u} - \boldsymbol{\zeta}_2\right) \chi\left(-\xi_1, \xi_2, \mathbf{u}\right) d\mathbf{u} - B_c\left(\boldsymbol{\zeta}_1\right) B_c^*\left(\boldsymbol{\zeta}_2\right), \tag{3.74}$$

where $\boldsymbol{\zeta}_1 = f_1/c\ \mathbf{q}_{x1}$, $\boldsymbol{\zeta}_2 = f_2/c\ \mathbf{q}_{x2}$, $\xi_1 = f_1/c\ q_{z1}$, and $\xi_2 = f_2/c\ q_{z2}$. Realisation of the diffuse component is simple when the statistics are stationary [Van Trees 1968], i.e., when the coherence function is of the form

$$\Gamma\left(\boldsymbol{\zeta}_1, \xi_1, \boldsymbol{\zeta}_2, \xi_2\right) = \Gamma\left(\Delta\boldsymbol{\zeta}, \Delta\xi\right), \tag{3.75}$$

where $\Delta\boldsymbol{\zeta} = \boldsymbol{\zeta}_2 - \boldsymbol{\zeta}_1$ and $\Delta\xi = \xi_2 - \xi_1$.

A random process with the prescribed stationary statistics can be generated by passing white noise through the appropriate linear filter. The auto-covariance of the filter output,

$$n\left(\boldsymbol{\zeta},\xi\right)=\iiint_{-\infty}^{\infty}w\left(\boldsymbol{\zeta}',\xi'\right)h\left(\boldsymbol{\zeta}-\boldsymbol{\zeta}',\xi-\xi'\right)\;d\boldsymbol{\zeta}'\,d\xi', \tag{3.76}$$

is given by

$$\begin{aligned}\Gamma\left(\boldsymbol{\zeta}_1,\xi_1,\boldsymbol{\zeta}_2,\xi_2\right)=&E\left\{n\left(\boldsymbol{\zeta}_1,\xi_1\right)n^*\left(\boldsymbol{\zeta}_2,\xi_2\right)\right\}\\ =&\iiiint\limits_{-\infty}^{\infty}\iint E\left\{w\left(\boldsymbol{\zeta}',\xi'\right)w^*\left(\boldsymbol{\zeta}'',\xi''\right)\right\}\\ &\times\;h\left(\boldsymbol{\zeta}_1-\boldsymbol{\zeta}',\xi_1-\xi'\right)h^*\left(\boldsymbol{\zeta}_2-\boldsymbol{\zeta}'',\xi_2-\xi''\right)\;d\boldsymbol{\zeta}'\,d\boldsymbol{\zeta}''\,d\xi'\,d\xi'',\end{aligned} \tag{3.77}$$

where $h\left(\boldsymbol{\zeta},\xi\right)$ is the impulse response of the filter and $w\left(\boldsymbol{\zeta},\xi\right)$ is white noise. The auto-covariance of the white noise is given by

$$E\left\{w\left(\boldsymbol{\zeta}',\xi'\right)w^*\left(\boldsymbol{\zeta}'',\xi''\right)\right\}=\frac{N_0}{2}\delta\left(\boldsymbol{\zeta}''-\boldsymbol{\zeta}',\xi''-\xi'\right), \tag{3.78}$$

where $N_0/2$ is the (constant) power spectral density and δ is the Dirac delta function. Thus, upon substitution of (3.78) into (3.77),

$$\Gamma\left(\Delta\boldsymbol{\zeta},\Delta\xi\right)=-\frac{N_0}{2}\iiint_{-\infty}^{\infty}h\left(\boldsymbol{\zeta}',\xi'\right)h^*\left(\boldsymbol{\zeta}'+\Delta\boldsymbol{\zeta},\xi+\Delta\xi\right)\;d\boldsymbol{\zeta}'\,d\xi'. \tag{3.79}$$

Taking the Fourier transform of this expression and rearranging gives

$$\left|H\left(\mathbf{f}_\zeta,f_\xi\right)\right|^2=\frac{2}{N_0}\Lambda\left(\mathbf{f}_\zeta,f_\xi\right), \tag{3.80}$$

where $H\left(\mathbf{f}_\zeta,f_\xi\right)$ is the transfer function of the required filter and

$$\Lambda\left(\mathbf{f}_\zeta,f_\xi\right)=\iiint_{-\infty}^{\infty}\Gamma\left(\Delta\boldsymbol{\zeta},\Delta\xi\right)\exp\left(-j2\pi\left(\mathbf{f}_\zeta\cdot\Delta\boldsymbol{\zeta}+f_\xi\Delta\xi\right)\right)\;d\Delta\boldsymbol{\zeta}\,d\Delta\xi \tag{3.81}$$

is the power spectral density of the desired random process.

The filter is constructed from the power spectral density of the diffuse component using (3.80), (3.81), and (3.74), and the output is interpolated at the appropriate values,

$$\boldsymbol{\zeta}_i = \tfrac{f}{c}\mathbf{q}_x, \tag{3.82}$$

$$\xi_i = \tfrac{f}{c}q_z. \tag{3.83}$$

as illustrated in Figure 3.14. Realisation of the diffuse component is inefficient even

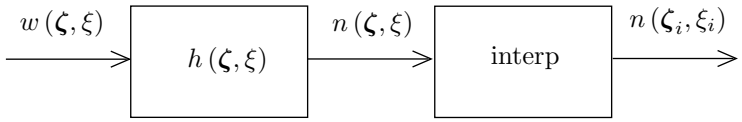

Figure 3.14 A diffuse beampattern component with stationary statistics can be realised by passing white noise through a linear filter. The filter is determined from the coherence function and the output of the filter is interpolated to give the realisation of the diffuse component.

when the statistics are stationary since a 3-D filtering operation, followed by a 3-D interpolation, is required. Moreover, the coherence function (3.74) is, in general, non-stationary and this approach is not valid.

3.6.2 Quasi-stationarity

Realisation of a non-stationary process is, in general, more difficult than realisation of a stationary process. Consequently it is less efficient. However, for a certain class of non-stationary processes, termed *quasi-stationary* [Bello 1963], the realisation can be more efficient. The term quasi-stationary is used loosely to describe any non-stationary process that is almost stationary. Here, the term refers to a windowed stationary process.

Suppose that the diffuse beampattern component is quasi-stationary and can be generated by passing white noise through two multipliers and a linear filter as shown in Figure 3.15(a). A two-dimensional white noise realisation, $w(\boldsymbol{\zeta})$, is windowed by a function, $b(\boldsymbol{\zeta})$. This is then passed through a linear filter, $h(\boldsymbol{\zeta})$, and the output is multiplied by a three-dimensional function, $d(\boldsymbol{\zeta},\xi)$. The resultant quasi-stationary process,

$$n(\boldsymbol{\zeta},\xi) = d(\boldsymbol{\zeta},\xi) \iint_{-\infty}^{\infty} b(\boldsymbol{\zeta}')\, w(\boldsymbol{\zeta}')\, h(\boldsymbol{\zeta}-\boldsymbol{\zeta}')\; d\boldsymbol{\zeta}, \tag{3.84}$$

is then interpolated at the appropriate values (3.82) and (3.83).

The auto-covariance of the filter output is given by

$$\Gamma(\boldsymbol{\zeta}_2,\xi_1,\boldsymbol{\zeta}_2,\xi_2) = d(\boldsymbol{\zeta}_1,\xi_1)\, d^*(\boldsymbol{\zeta}_2,\xi_2) \iiiint_{-\infty}^{\infty} b(\boldsymbol{\zeta}')\, b^*(\boldsymbol{\zeta}'')\, E\left\{ w(\boldsymbol{\zeta}')\, w^*(\boldsymbol{\zeta}'') \right\} \times\; h(\boldsymbol{\zeta}_1-\boldsymbol{\zeta}')\, h^*(\boldsymbol{\zeta}_2-\boldsymbol{\zeta}'')\; d\boldsymbol{\zeta}'\, d\boldsymbol{\zeta}'' \tag{3.85}$$

where the auto-covariance of the white noise is given by (3.78). This expression can

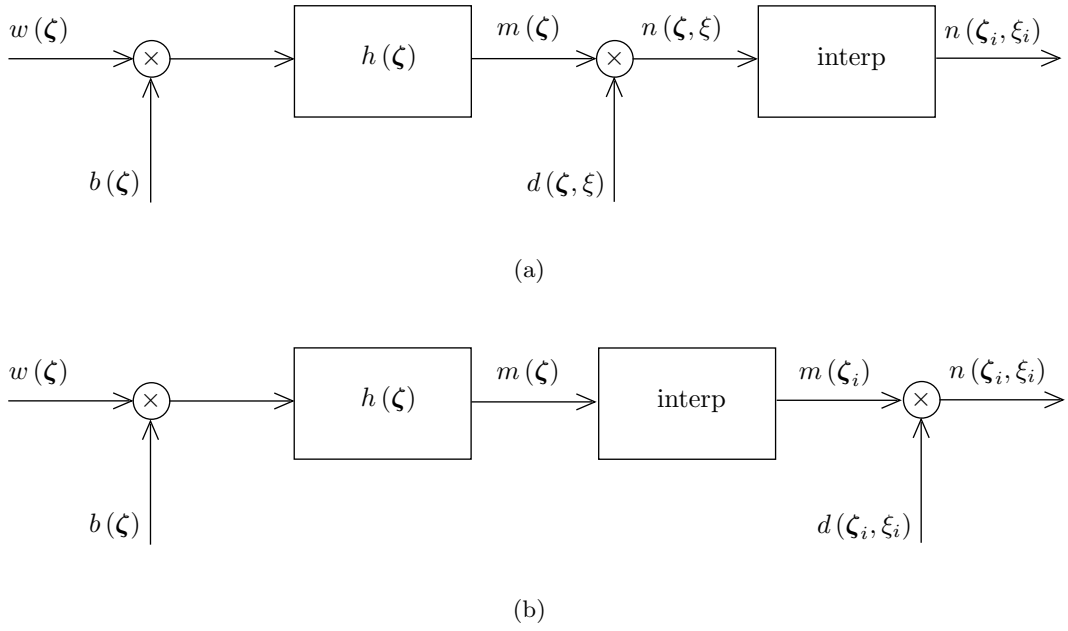

Figure 3.15 A diffuse beampattern component with quasi-stationary statistics can be realised by passing white noise through a linear filter and a pre and post-multiplier.

then be reduced to

$$\Gamma\left(\boldsymbol{\zeta}_2,\xi_1,\boldsymbol{\zeta}_2,\xi_2\right)=d\left(\boldsymbol{\zeta}_1,\xi_1\right)d^*\left(\boldsymbol{\zeta}_2,\xi_2\right)\iint_{-\infty}^{\infty}\left|b\left(\boldsymbol{\zeta}'\right)\right|^2 h\left(\boldsymbol{\zeta}_1-\boldsymbol{\zeta}'\right)h^*\left(\boldsymbol{\zeta}_2-\boldsymbol{\zeta}'\right)\,d\boldsymbol{\zeta}'. \quad (3.86)$$

The Weiner-Khinchine relation [Bahar 1990] is not valid here since the statistics are non-stationary. However, h, b, and d can be determined by comparison of (3.74) and (3.86), i.e.,

$$\begin{aligned}\iint_{-\infty}^{\infty}A\left(\mathbf{u}-\boldsymbol{\zeta}_1\right)A^*\left(\mathbf{u}-\boldsymbol{\zeta}_2\right)\chi\left(-\xi_1,\xi_2,\mathbf{u}\right)\,d\mathbf{u}=\\ d\left(\boldsymbol{\zeta}_1,\xi_1\right)d^*\left(\boldsymbol{\zeta}_2,\xi_2\right)\iint_{-\infty}^{\infty}\left|b\left(\boldsymbol{\zeta}'\right)\right|^2 h\left(\boldsymbol{\zeta}_1-\boldsymbol{\zeta}'\right)h^*\left(\boldsymbol{\zeta}_2-\boldsymbol{\zeta}'\right)\,d\boldsymbol{\zeta}'.\end{aligned} \quad (3.87)$$

Therefore,

$$h\left(\boldsymbol{\zeta}\right)=A\left(-\boldsymbol{\zeta}\right), \quad (3.88)$$

or equivalently,

$$H\left(\mathbf{f}_\zeta\right)=-a\left(-\mathbf{f}_\zeta\right), \quad (3.89)$$

and

$$\chi\left(-\xi_1,\xi_2,\boldsymbol{\zeta}\right)=d\left(\boldsymbol{\zeta}_1,\xi_1\right)d^*\left(\boldsymbol{\zeta}_2,\xi_2\right)\left|b\left(\boldsymbol{\zeta}\right)\right|^2. \quad (3.90)$$

Determination of the filter is simple using (3.88). However, this approach requires the Fourier transform of the characteristic function to be separable.

Although the quasi-stationary approach is only valid for a restricted class of characteristic functions, it is very efficient since it requires a 2-D, rather than 3-D, filtering operation. In fact, it can be made more efficient upon realisation that the order of the multiplier and the interpolater can be swapped as shown in Figure 3.15(b). This reduces the interpolation from three to two dimensions. The quasi-stationary approach is significantly faster; it has computational complexity of order N^2 compared with order N^3 for the other approaches.

3.7 ROUGHNESS STATISTICS

Natural underwater features have been shown to exhibit fractal characteristics. In particular, fractional Brownian motion (fBm) surfaces [Lane *et al.* 1992, Harding *et al.* 1999] have been shown suitable for describing the roughness [Goff and Jordan 1989]. However, it is common in the literature to model roughness using a Gaussian height-distribution with a particular correlation function, typically Gaussian or exponential. This is due to its simplicity compared with a fractal model. However, there has been more interest in scattering from fractal surfaces recently, e.g., [Franceschetti *et al.* 1999].

The expressions derived to this point are general (within the limits of the approximations) and, in theory, any statistical distribution can be employed. However, in the following sections Gaussian-distributed, Gaussian-correlated isotropic roughness is assumed for the rough facets, while fBm surfaces are used to model large-scale natural features such as the undulations in the seafloor. The choice of Gaussian statistics for the surface roughness is not the most suitable for modelling natural underwater features. However in practice, the effects of an incorrect choice of statistics is negligible compared to the lack of accurate ground-truth and the Gaussian statistics are sufficient. Future work should investigate facets with fractal roughness.

3.7.1 First-order Gaussian statistics

Consider a surface with a zero-mean, isotropic, Gaussian height distribution. The probability density function for the surface is given by

$$p(h) = \frac{1}{\sigma\sqrt{2\pi}} \exp\left(-\frac{h^2}{2\sigma^2}\right), \tag{3.91}$$

where σ^2 is the variance. The characteristic function for the height distribution is obtained by taking the Fourier transform of the probability density function, (3.91).

Thus, using the Fourier relation in Table A.2, the characteristic function is given by

$$\Phi(\nu) = \exp\left(-2\pi^2\sigma^2\nu^2\right). \tag{3.92}$$

The specular component of the beampattern is obtained from (3.53) and (3.92), giving

$$B_c(\hat{\mathbf{n}}_i, \hat{\mathbf{n}}_s, f) = j\frac{2\pi}{\lambda}\, R(\hat{\mathbf{n}}_s + \hat{\mathbf{n}}_r)\cdot\hat{\mathbf{n}}_k\, \exp\left(-2\pi^2\frac{\sigma^2 q_z^2}{\lambda^2}\right) A\left(\frac{f}{c}\mathbf{q}_x\right). \tag{3.93}$$

The specular component decreases to zero as the roughness increases, i.e., as $\sigma \to \infty$ or $f \to \infty$. Conversely, the specular component assumes the form of the beampattern for a smooth facet (3.33) as the roughness decreases, i.e., as $\sigma \to 0$. This is intuitively satisfying.

3.7.2 Second-order Gaussian statistics

The second-order (or bivariate) Gaussian probability distribution is given by

$$p(h_1, h_1, \Delta\mathbf{x}) = \frac{1}{2\pi\sigma^2\sqrt{1 - C(\Delta\mathbf{x})^2}} \exp\left(\frac{-1}{2\sigma^2\left(1 - C(\Delta\mathbf{x})\right)}\left[h_1^2 + h_2^2 - 2h_1h_2C(\Delta\mathbf{x})\right]\right) \tag{3.94}$$

and its characteristic function is given by

$$\Phi(\nu_1, \nu_2, \Delta\mathbf{x}) = \exp\left(-2\pi^2\sigma^2\left[\nu_1^2 + \nu_2^2 + 2\nu_1\nu_2\, C(\Delta\mathbf{x})\right]\right), \tag{3.95}$$

where C is the surface correlation function. The correlation function is given by

$$C(\Delta\mathbf{x}) = \exp\left(-\frac{|\Delta\mathbf{x}|^2}{l^2}\right) \tag{3.96}$$

for an isotropic, Gaussian-correlated surface, where l is the correlation length. Substitution of (3.96) into (3.95) yields the characteristic function,

$$\Phi(\nu_1, \nu_2, \Delta\mathbf{x}) = \exp\left(-2\pi^2\sigma^2\left(\nu_1^2 + \nu_2^2\right)\right) \exp\left(-4\pi^2\sigma^2\nu_1\nu_2\, \exp\left(-\frac{|\Delta\mathbf{x}|^2}{l^2}\right)\right). \tag{3.97}$$

An analytic expression for the Fourier transform is difficult to derive due to the nested exponential function. Nevertheless, the exponential function can be expanded using the exponential series,

$$\exp(x) = \sum_{n=0}^{\infty} \frac{1}{n!}x^n, \tag{3.98}$$

and it can be approximated by truncation of the series, i.e.,

$$\exp(x) \approx \sum_{n=0}^{N} \frac{1}{n!} x^n, \tag{3.99}$$

where N is the order of the approximation. The series converges quickly for $|x| < 1$ and the first few terms provide a good approximation. However, the series converges very slowly for $|x| > 1$ and a large number of terms must be retained.

The characteristic function can be approximated using an N^{th}-order approximation of the inner or outer exponential in (3.97). Approximating the outer exponential, which is denoted by the subscript, o, gives

$$\Phi_o^{(N)}(\nu_1, \nu_2, \Delta\mathbf{x}) = \exp\left(-2\pi^2\sigma^2\left(\nu_1^2 + \nu_2^2\right)\right)\left[1 + \sum_{n=1}^{N} \frac{(-4)^n}{n!}\pi^{2n}\sigma^{2n}\nu_1^n\nu_2^n \exp\left(-n\frac{|\Delta\mathbf{x}|^2}{l^2}\right)\right], \tag{3.100}$$

where the superscript, N, denotes the approximation order. This summation converges quickly when

$$\nu_1\nu_2 \ll \frac{1}{4\pi^2\sigma^2} \tag{3.101}$$

Consequently, the approximation is valid for smooth or slightly rough surfaces (small σ, large f) and at grazing incidence (small q_z). Taking the Fourier transform of the approximation over $\mathbf{x}$ gives,

$$\begin{aligned}\chi_o^{(N)}(\nu_1, \nu_2, \mathbf{u}) = {} & \exp\left(-2\pi^2\sigma^2\left(\nu_1^2 + \nu_2^2\right)\right) \\ & \times \left[\delta(\mathbf{u}) + \sqrt{\pi}l\sum_{n=1}^{N}\frac{(-4)^n}{n!\sqrt{n}}\pi^{2n}\sigma^{2n}\nu_1^n\nu_2^n \exp\left(-\frac{1}{n}\pi^2 l^2 |\mathbf{u}|^2\right)\right].\end{aligned} \tag{3.102}$$

Approximating the inner exponential, which is denoted by the subscript, i, gives

$$\Phi_i^{(N)}(\nu_1, \nu_2, \Delta\mathbf{x}) = \exp\left(-2\pi^2\sigma^2\left(\nu_1^2 + \nu_2^2\right)\right)\exp\left(-4\pi^2\sigma^2\nu_1\nu_2\left[1 + \sum_{n=1}^{N}\frac{(-1)^n}{n!}\frac{|\Delta\mathbf{x}|^{2n}}{l^{2n}}\right]\right). \tag{3.103}$$

This converges quickly for

$$\nu_1\nu_2 \gg \frac{1}{4\pi^2\sigma^2}, \tag{3.104}$$

i.e., when the surface is very rough. The Fourier transform of this expression is difficult to derive except for the first-order approximation. Discarding higher powers gives

$$\Phi_i^{(1)}\left(\nu_1,\nu_2,\Delta\mathbf{x}\right)=\exp\left(-2\pi^2\sigma^2\left(\nu_1+\nu_2\right)^2\right)\exp\left(\frac{4\pi^2\sigma^2\nu_1\nu_2}{l^2}\left|\Delta\mathbf{x}\right|^2\right) \tag{3.105}$$

and taking the Fourier transform yields

$$\chi_i^{(1)}\left(\nu_1,\nu_2,\mathbf{u}\right)=\frac{l}{2\sqrt{\pi}\sigma\sqrt{-\nu_1\nu_2}}\exp\left(-2\pi^2\sigma^2\left(\nu_1+\nu_2\right)^2\right)\exp\left(\frac{l^2}{4\sigma^2\nu_1\nu_2}\left|\mathbf{u}\right|^2\right). \tag{3.106}$$

The two approximations for the Fourier transform of the characteristic function are valid in two complementary regions; the *outer* approximation is valid for relatively smooth surfaces, while the *inner* approximation is valid for rough surfaces. A composite of the two approximations can be employed to provide a good overall approximation. The approximation error can be made arbitrarily small by retaining more terms in the approximation of the outer exponential. Figure 3.16 shows an example characteristic function and its Fourier transform along with the two approximations; the regions of validity are clearly obvious. Figure 3.16 shows the composite approximation.

Substitution of the outer approximation for the Fourier transform of the characteristic function (3.102) into the expression for the coherence function (3.74) yields

$$\begin{aligned}\Gamma_o\left(\boldsymbol{\zeta}_1,\xi_1,\boldsymbol{\zeta}_2,\xi_2\right)=&\exp\left(2\pi^2\sigma^2\left(\xi_1^2+\xi_2^2\right)\right)\sqrt{\pi}l\sum_{n=1}^{N}\frac{4^n}{n!\sqrt{n}}\pi^{2n}\sigma^{2n}\xi_1^n\xi_2^n\\&\times\iint_{-\infty}^{\infty}A\left(\mathbf{u}-\boldsymbol{\zeta}_1\right)A^*\left(\mathbf{u}-\boldsymbol{\zeta}_2\right)\exp\left(-\frac{1}{n}\pi^2l^2\left|\mathbf{u}\right|^2\right)\,d\mathbf{u}.\end{aligned} \tag{3.107}$$

This expression is not separable due to the summation and it does not fit the form for the quasi-stationary model (3.87). However, by assuming that the correlation length of the surface roughness is small compared to the facet extent, i.e., that the exponential inside the integral is wide compared to A, then it can be approximated as constant over the integral and

$$\begin{aligned}\Gamma_o\left(\boldsymbol{\zeta}_1,\xi_1,\boldsymbol{\zeta}_2,\xi_2\right)\approx&\exp\left(2\pi^2\sigma^2\left(\xi_1^2+\xi_2^2\right)\right)\sqrt{\pi}l\sum_{n=1}^{N}\frac{4^n}{n!\sqrt{n}}\pi^{2n}\sigma^{2n}\xi_1^n\xi_2^n\\&\times\exp\left(-\frac{1}{n}\pi^2l^2\frac{\left|\boldsymbol{\zeta}_1+\boldsymbol{\zeta}_2\right|^2}{4}\right)\iint_{-\infty}^{\infty}A\left(\mathbf{u}-\boldsymbol{\zeta}_1\right)A^*\left(\mathbf{u}-\boldsymbol{\zeta}_2\right)\,d\mathbf{u}.\end{aligned} \tag{3.108}$$

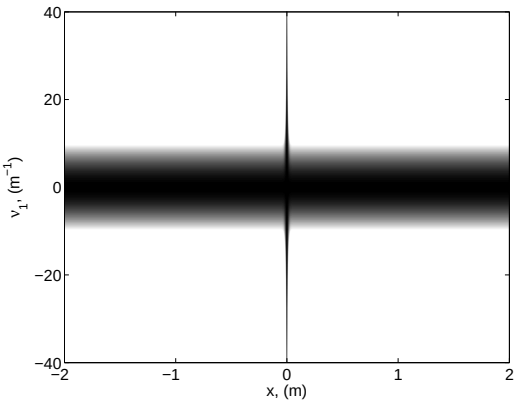

(a) ϕ, exact

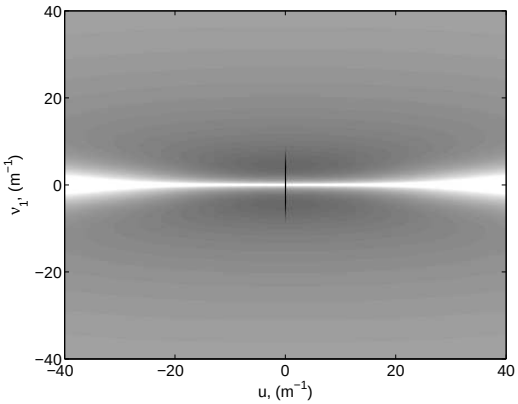

(b) χ, exact

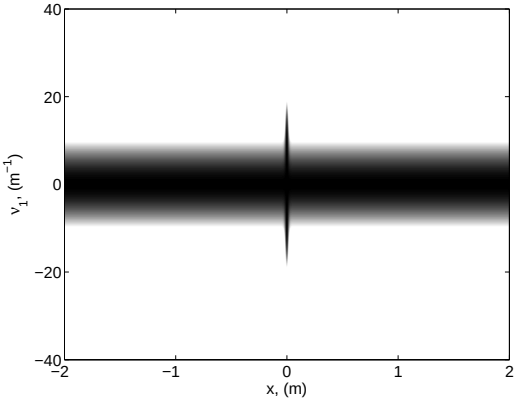

(c) ϕ, outer exp approximation (15^{th}-order)

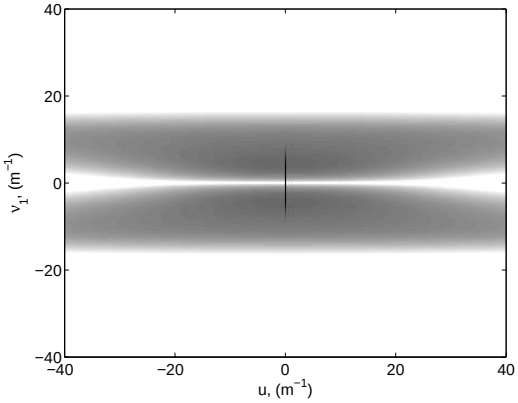

(d) χ, outer exp approximation (15^{th}-order)

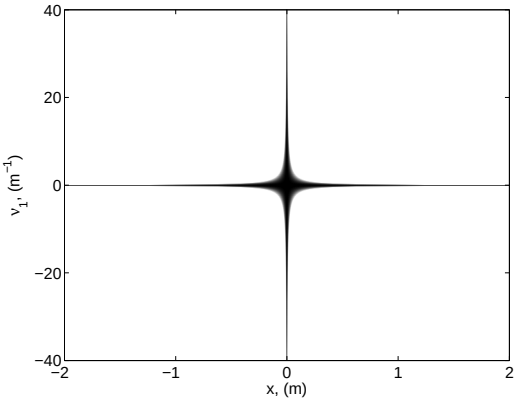

(e) ϕ, inner exp approximation

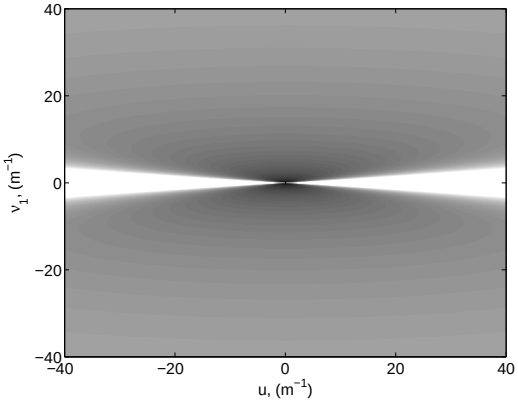

(f) χ, inner exp approximation

Figure 3.16 The inner and outer approximations for the Fourier transform of the characteristic function are valid for relatively smooth and very rough surfaces respectively. The exact function and the two approximations are shown here for roughness statistics of $\sigma = 0.05$ and $l = 0.02$.

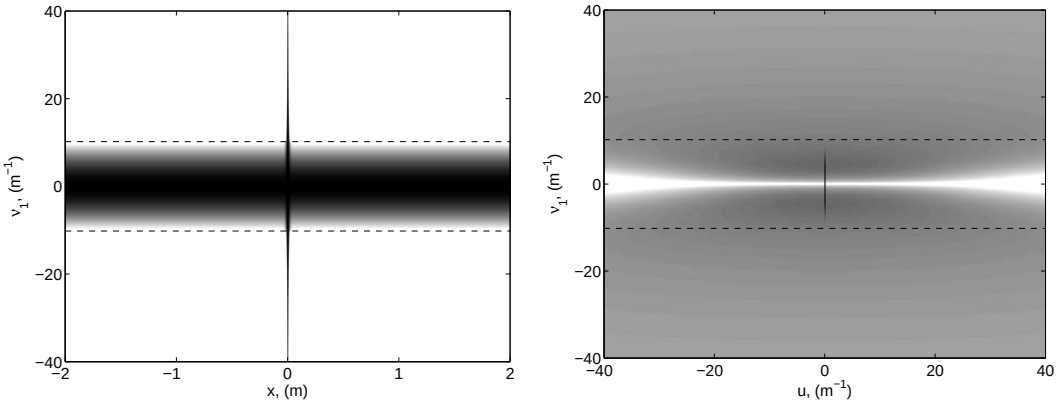

(a) ϕ, composite approximation

(b) χ, composite approximation

Figure 3.17 The complimentary regions of validity for the inner and outer approximations suggest a composite approximation. The transition between the two approximations is indicated by the dashed line.

Then, assuming that $\boldsymbol{\zeta}_1 \approx \boldsymbol{\zeta}_2$ and $\xi_1 \approx \xi_2$,

$$\begin{aligned}\Gamma_o\left(\boldsymbol{\zeta}_1, \xi_1, \boldsymbol{\zeta}_2, \xi_2\right) \approx & \exp\left(2\pi^2\sigma^2\left(\xi_1^2 + \xi_2^2\right)\right)\sqrt{\pi}l \\ & \times \left[\sum_{n=1}^{N} \frac{4^n}{n!\sqrt{n}}\pi^{2n}\sigma^{2n}\xi_1^{2n}\exp\left(-\frac{1}{n}\pi^2 l^2\left|\boldsymbol{\zeta}_1\right|^2\right)\right]^{\frac{1}{2}} \\ & \times \left[\sum_{n=1}^{N} \frac{4^n}{n!\sqrt{n}}\pi^{2n}\sigma^{2n}\xi_2^{2n}\exp\left(-\frac{1}{n}\pi^2 l^2\left|\boldsymbol{\zeta}_2\right|^2\right)\right]^{\frac{1}{2}} \\ & \times \iint_{-\infty}^{\infty} A\left(\mathbf{u} - \boldsymbol{\zeta}_1\right) A^*\left(\mathbf{u} - \boldsymbol{\zeta}_2\right)\, d\mathbf{u},\end{aligned} \tag{3.109}$$

and the components of the quasi-stationary filter are given by

$$b_o\left(\boldsymbol{\zeta}\right) = 1 \tag{3.110}$$

and

$$d_o\left(\boldsymbol{\zeta}, \xi\right) = \exp\left(-2\pi^2\sigma^2\xi^2\right)\left[\sqrt{\pi}l\sum_{n=1}^{N}\frac{4^n}{n!\sqrt{n}}\pi^{2n}\sigma^{2n}\xi^{2n}\exp\left(-\frac{1}{n}\pi^2 l^2\left|\boldsymbol{\zeta}\right|^2\right)\right]^{\frac{1}{2}}. \tag{3.111}$$

Substitution of the inner approximation for the Fourier transform of the characteristic function (3.106) into the expression for the coherence function (3.74) yields

$$\begin{aligned}\Gamma_i\left(\boldsymbol{\zeta}_1,\xi_1,\boldsymbol{\zeta}_2,\xi_2\right) =& \frac{l}{2\sqrt{\pi}\sigma}\left(\xi_1\xi_2\right)^{-\frac{1}{2}}\exp\left(-2\pi^2\sigma^2\left(\xi_2^2+\xi_1^2-2\xi_1\xi_2\right)\right) \\ &\times \iint_{-\infty}^{\infty} A\left(\mathbf{u}-\boldsymbol{\zeta}_1\right)A^*\left(\mathbf{u}-\boldsymbol{\zeta}_2\right)\exp\left(\frac{-l^2}{4\sigma^2\xi_1\xi_2}\left|\mathbf{u}\right|^2\right)\,d\mathbf{u}\end{aligned} \tag{3.112}$$

where the coherent component, B_c, is assumed zero, or at least very small since the approximation is valid for very rough surfaces only. Again, this expression does not fit the form of the quasi-stationary model since it is not separable. Making the same assumptions, i.e., that the correlation length of the surface roughness is small compared to the facet extent, and $\zeta_1 \approx \zeta_2$, $\xi_1 \approx \xi_2$, then the components of the quasi-stationary filter are given by

$$b_i\left(\boldsymbol{\zeta}\right) = 1, \tag{3.113}$$

$$d_i\left(\boldsymbol{\zeta},\xi\right) = \left(\frac{l}{2\sqrt{\pi}\sigma}\right)^{\frac{1}{2}}\xi^{-\frac{1}{2}}\exp\left(-\frac{l^2}{8\sigma^2\xi^2}\left|\boldsymbol{\zeta}\right|^2\right). \tag{3.114}$$

It is important to note that as the surface becomes rougher, i.e., as $\sigma \to \infty$ or as $l \to 0$ in (3.114), the diffuse beampattern component decreases to zero. This is due to a violation of the Kirchhoff approximation; the propagating field decreases to zero but the energy is not lost, it is contained in the (non-propagating) evanescent field. Although the validity of the result is questionable, the beampattern for a very rough surface can be calculated using a normalisation of the propagating field, whereby the energy lost to the evanescent field is retained [Harvey *et al.* 1999].

3.7.3 Example beampatterns

Some example beampatterns are shown here for a rectangular facet. Figure 3.18 shows the decomposition of the beampattern into its specular and diffuse components, where the diffuse component is represented by its root-mean-square value. In Figures 3.19 and 3.20, the characteristics of the surface roughness, σ and l, are varied; the ratio of the specular to diffuse components decreases as the standard deviation of the roughness is increased and the angular spread of the diffuse component increases with decorrelation of the surface roughness. In Figure 3.21, the angle of the incident field is varied. The specular direction changes with the angle of incidence and the specular component increases at grazing incidence. Figure 3.23 shows a particular beampattern realisation and its decomposition into specular and diffuse components. Figure 3.24 shows two different realisations of the beampattern and Figure 3.25 shows the variation of the realisation with increasing frequency.

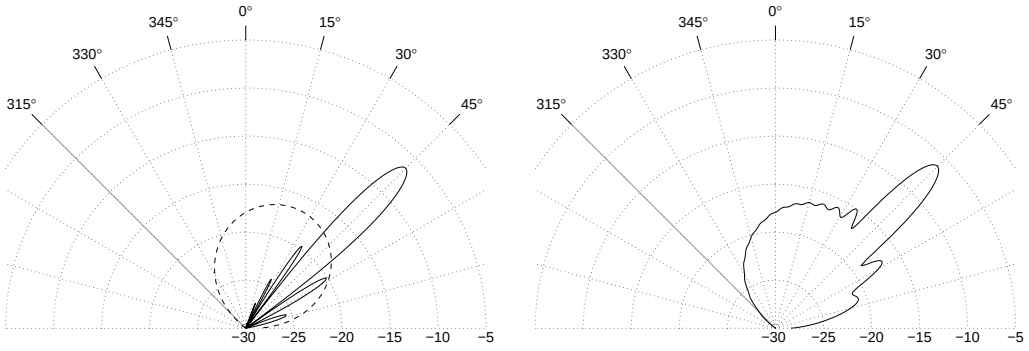

(a) specular and diffuse components (b) total beampattern

Figure 3.18 The mean intensity of the beampattern for a 0.5 m rough facet with a height variance of $\sigma = 5\,\text{mm}$ and a correlation length of $l = 20\,\text{mm}$. Figure (a) shows the decomposition of the field into its specular (solid line) and diffuse (dashed line) components, while Figure (b) shows the total beampattern intensity.

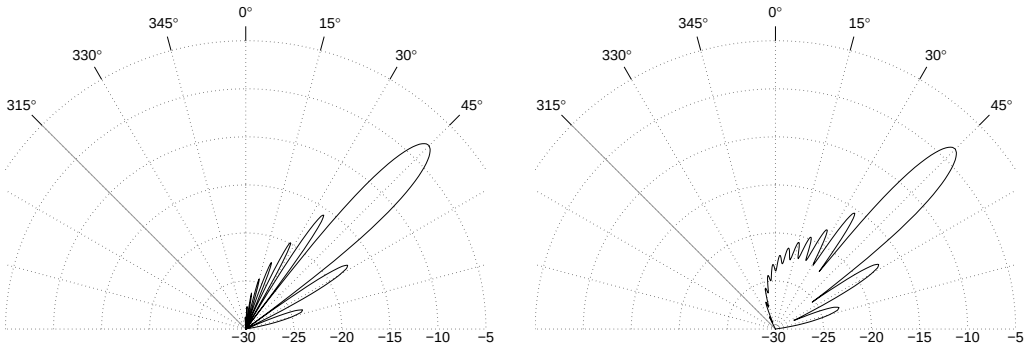

(a) $\sigma = 0\,\text{mm}$ (b) $\sigma = 2\,\text{mm}$

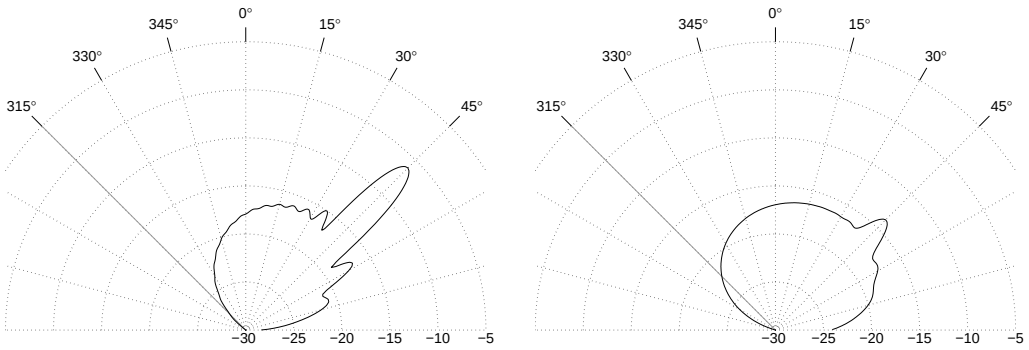

(c) $\sigma = 5\,\text{mm}$ (d) $\sigma = 10\,\text{mm}$

Figure 3.19 The height variance of the surface roughness is varied between $\sigma = 0\,\text{mm}$ and $\sigma = 10\,\text{mm}$ for a 0.5 m facet with a correlation length of $l = 20\,\text{mm}$.

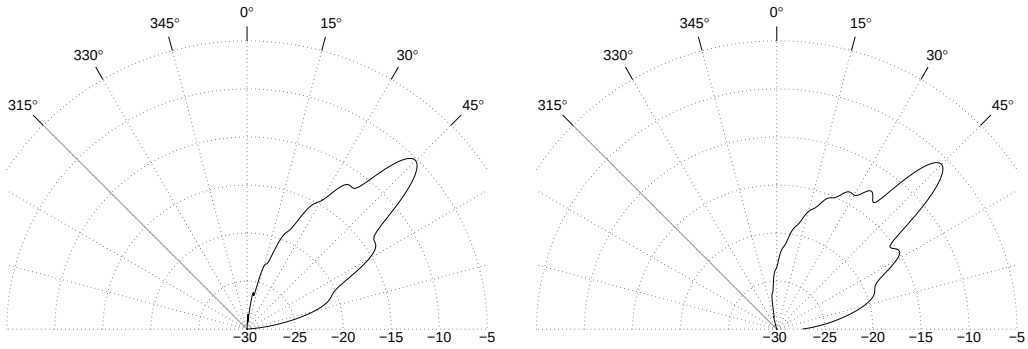

(a) $l = 0.1\,\mathrm{m}$

(b) $l = 0.05\,\mathrm{m}$

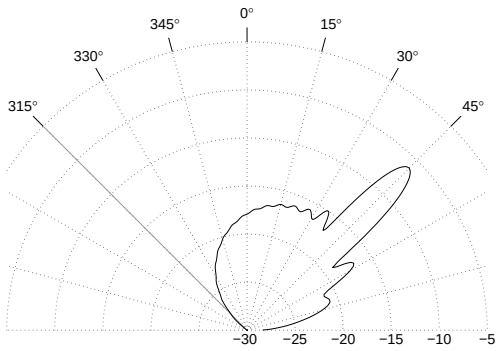

(c) $l = 0.02\,\mathrm{m}$

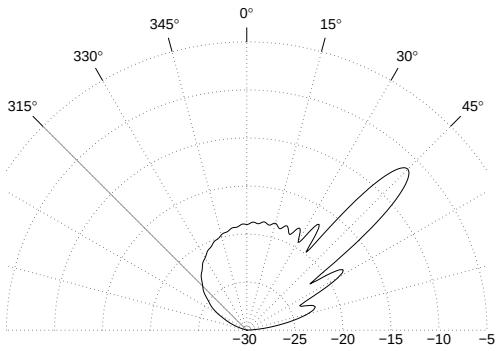

(d) $l = 0.01\,\mathrm{m}$

Figure 3.20 The correlation length of the surface roughness is varied between $l = 0.1\,\mathrm{m}$ and $l = 0.01\,\mathrm{m}$ for a $0.5\,\mathrm{m}$ facet with a height variance of $\sigma = 5\,\mathrm{mm}$.

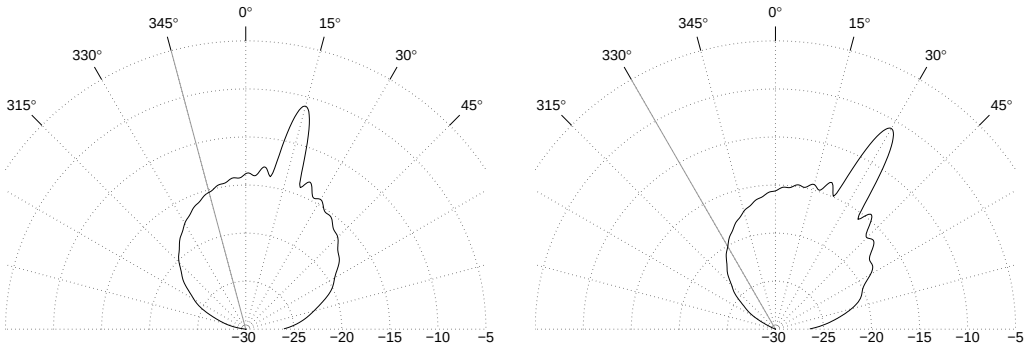

(a) $\theta_i = 15\,\text{deg}$ (b) $\theta_i = 30\,\text{deg}$

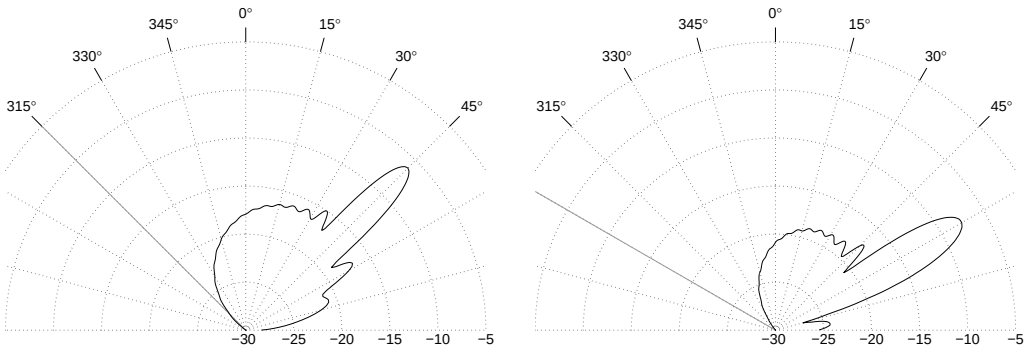

(c) $\theta_i = 45\,\text{deg}$ (d) $\theta_i = 60\,\text{deg}$

Figure 3.21 The angle of the incident wave is varied from 15 deg to 60 deg for the beampattern of a 0.5 m rough facet with a height variance of $\sigma = 5\,\text{mm}$ and a correlation length of $l = 20\,\text{mm}$.

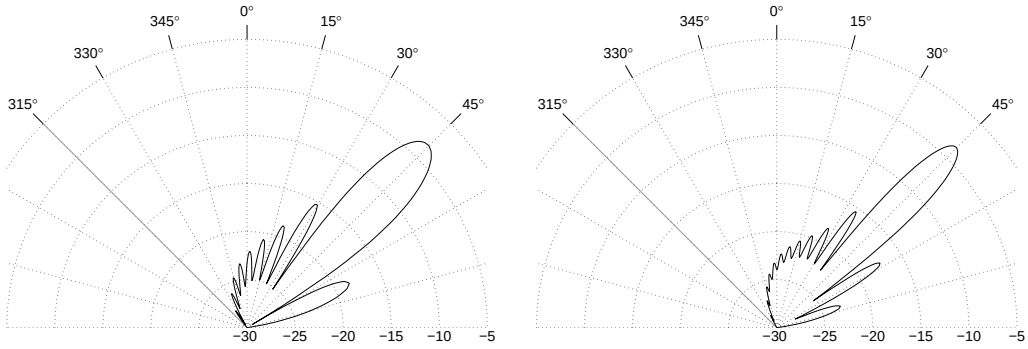

(a) $f = 20\,\text{kHz}$ (b) $f = 30\,\text{kHz}$

(c) $f = 50\,\text{kHz}$ (d) $f = 100\,\text{kHz}$

Figure 3.22 The frequency of the incident wave is varied from 20 kHz to 100 kHz for the beampattern of a 0.5 m rough facet with a height variance of $\sigma = 2\,\text{mm}$ and a correlation length of $l = 20\,\text{mm}$.

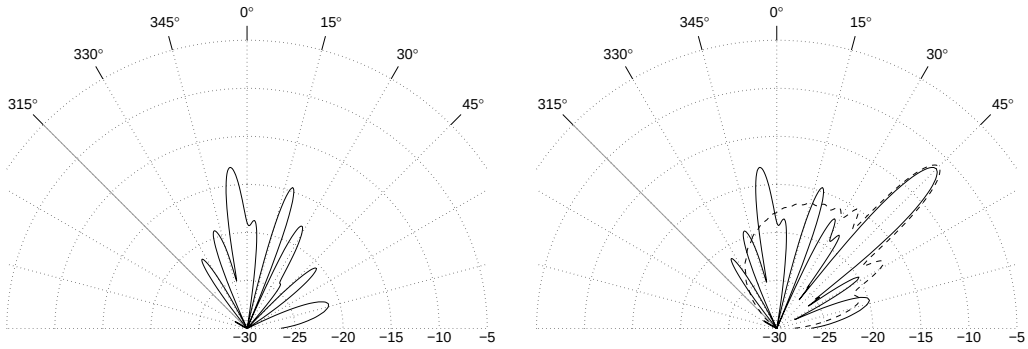

(a) diffuse component (b) total beampattern

Figure 3.23 A beampattern realisation is generated using the first and second-order statistics (the specular component and the mutual coherence function of the diffuse component) for a 0.5 m rough facet with a height variance of $\sigma = 5\,\text{mm}$ and a correlation length of $l = 20\,\text{mm}$. Figure (a) shows the realisation of the diffuse component and Figure (b) shows the realisation of the total beampattern.

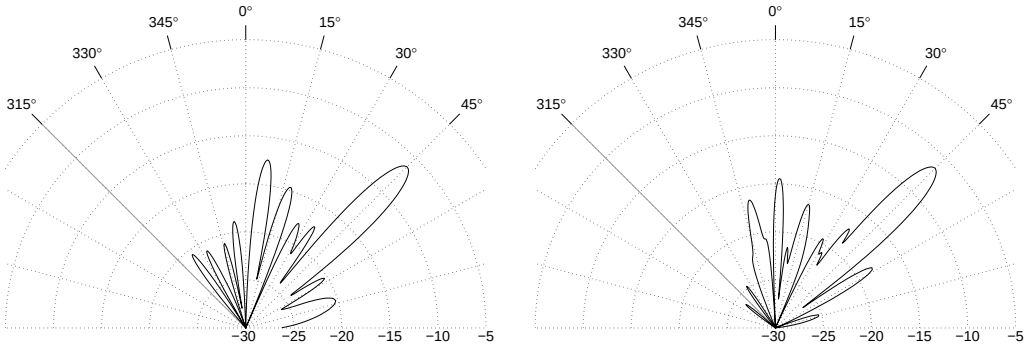

(a) (b)

Figure 3.24 Different realisations of the beampattern have the same statistics but each realisation is unique.

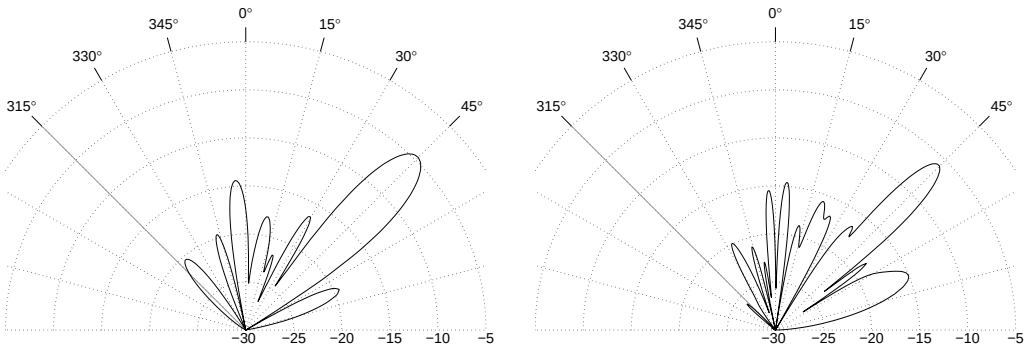

(a) $f = 20\,\text{kHz}$ (b) $f = 30\,\text{kHz}$

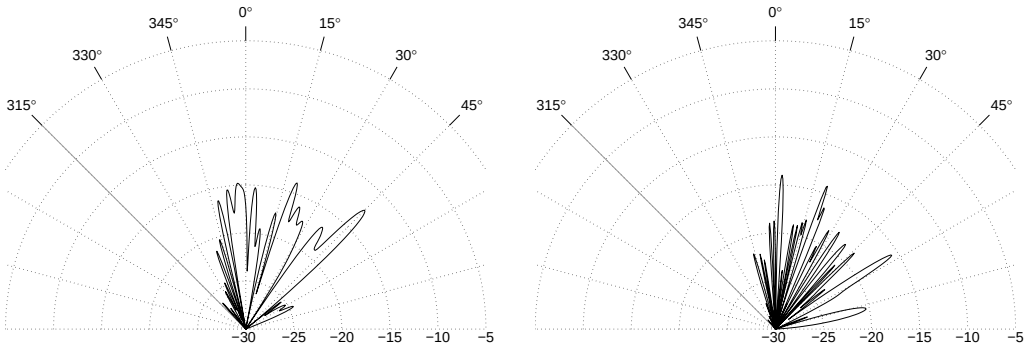

(c) $f = 50\,\text{kHz}$ (d) $f = 100\,\text{kHz}$

Figure 3.25 The frequency of the incident wave is varied between 20 kHz and 100 kHz, demonstrating the change in the correlation properties of the beampattern realisation due to the changing wavelength.

Chapter 4

MULTIPLE-RECEIVER INSAS SIMULATION

A simulator has been created to provide realistic data for development of the various SAS algorithms, including: reconstruction [Callow *et al.* 2002, Callow 2003, Hunter *et al.* 2003a], autofocus and motion-compensation [Callow 2003, Fortune 2005, Pilbrow 2007], interferometry [Barclay 2006], and target detection and classification [Hunter and Hayes 2005a]. Fast generation of the data is desirable and a trade-off between realism and efficiency is established. This is achieved using the rough facet scattering model described in the previous chapter and the techniques for improved efficiency described in this chapter. The simulator has been implemented for parallel use on a computing cluster in order to reduce simulation times.

The practical implementation of the scattering model and the simulator design is described in this chapter. First, the sonar specifications and imaging geometry are defined. Then, in Sections 4.2.1 and 4.2.2, efficient evaluation of the transducer and facet beampatterns is detailed. This method is extended for modelling time-variant facets, partially occluded facets, and temporal Doppler effects in Sections 4.3.3 to 4.3.5. The simulator uses ray-tracing to resolve occlusions and multiple-scattering; this is covered in Section 4.4. The simulator design and implementation is detailed in Section 4.5 and the parallel processing is discussed in Section 4.5.1.

4.1 IMAGING GEOMETRY

The previous chapter derived expressions for the scattering from points, smooth facets, and rough facets. These expressions are evaluated using the specifications and trajectory of the imaging platform. The platform considered here is a free-towed, remote-operated, or autonomous sonar.

The sonar has a single projector and N hydrophones that are fixed to the sonar body. The projector position is denoted by ${}^s\mathbf{x}_p$ and the hydrophone positions are denoted by ${}^s\mathbf{x}_{h1}, {}^s\mathbf{x}_{h2}, ..., {}^s\mathbf{x}_{hN}$. These are specified in local coordinates relative to the sonar position, $\mathbf{x}_s$, as illustrated in Figure 4.1; this is denoted by the superscript s. The sonar position is the origin of the local coordinate system and it can be chosen

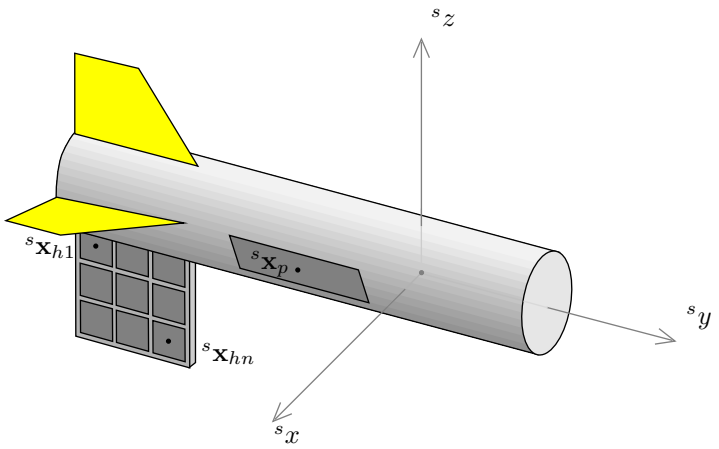

Figure 4.1 The locations and orientations of the transducers are specified in the coordinate system local to the sonar. The local coordinate system has an origin, $\mathbf{x}_s$, and orientation, $\mathbf{R}_s$, relative to the global coordinate system.

arbitrarily[1]. The orientation of the coordinate system is arbitrary also. Here the y-axis is aligned with the tail and nose of the sonar and the z-axis is in the upward direction.

The transducer beampattern expression (2.61) contains a 2-D Fourier transform over the plane containing the transducer aperture. It is convenient to define the aperture function in the x-y plane; this simplifies the calculation of the Fourier transform. The aperture function is defined in a coordinate system local to the transducer as shown in Figure 4.2. The origin is located at the aperture centre and the z axis is aligned with the transducer normal. The transducer normals are given by

$$^s\hat{\mathbf{n}}_p = {}^s\mathbf{R}_p {}^p\hat{\mathbf{n}}_p \tag{4.1}$$

and

$$^s\hat{\mathbf{n}}_{hn} = {}^s\mathbf{R}_{hn} {}^{hn}\hat{\mathbf{n}}_{hn} \tag{4.2}$$

in the sonar coordinate system, where ${}^p\hat{\mathbf{n}}_p = {}^{hn}\hat{\mathbf{n}}_{hn} = (0, 0, 1)$, and the superscripts p and hn denote the local coordinates of the projector and the n^{th} hydrophone. The rotation matrices ${}^s\mathbf{R}_p$, and ${}^s\mathbf{R}_{h1}$, ${}^s\mathbf{R}_{h2}$, ..., ${}^s\mathbf{R}_{hN}$ define the orientation of the projector and hydrophones relative to the sonar.

The sonar traverses a path in the global coordinate system as shown in Figure 4.3. The path is defined by the position and orientation of the sonar with respect to time, i.e., $\mathbf{x}_s = \mathbf{x}_s(t)$ and $\mathbf{R}_s = \mathbf{R}_s(t)$. The global coordinate system defined here has the y-axis aligned with the nominally straight path and the z-axis in the upward direction.

[1]It would be convenient to use the centre of rotation to define the sonar position. However, the centre of rotation is dependent on the forces acting upon the sonar and its position can vary. Instead, the centre of mass or centre of buoyancy can be used.

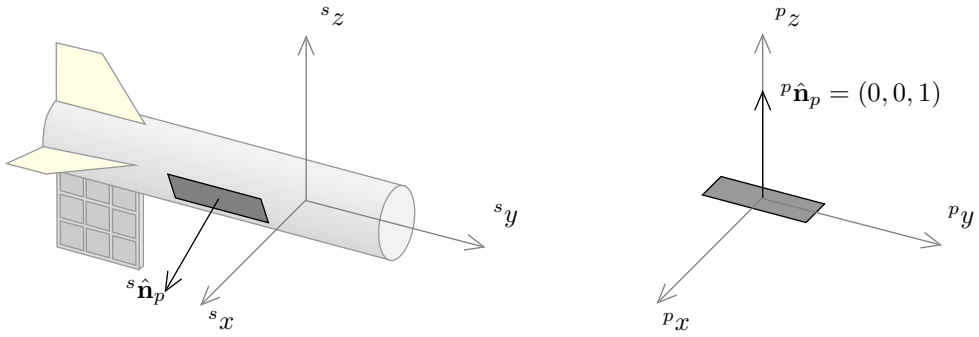

(a) sonar coordinates (b) transducer coordinates

Figure 4.2 The transducer aperture function is specified in a local coordinate system that is aligned with the plane containing the aperture. The origin of the coordinate system is at the aperture centre and the edges of the aperture are aligned with the x and y axes to simplify the Fourier transform.

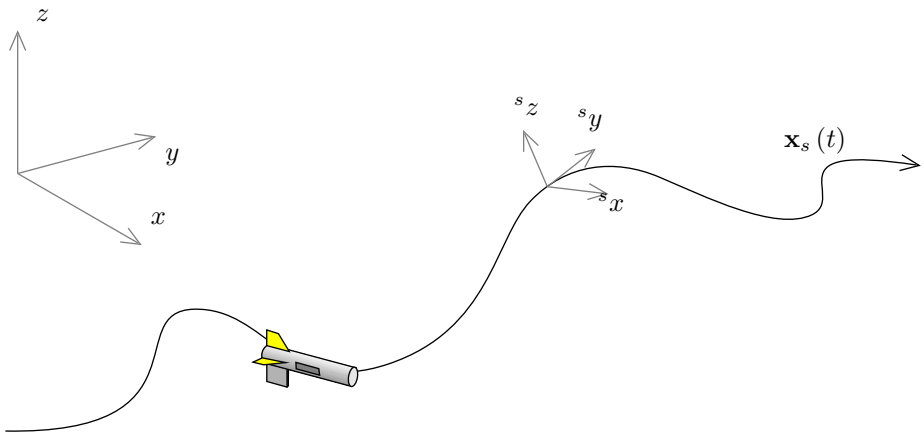

Figure 4.3 The sonar traverses a path in the global coordinate system. This is specified by the position and orientation of the sonar, $\mathbf{x}_s(t)$ and $\mathbf{R}_s(t)$.

In global coordinates, the position of the projector is given by

$$\mathbf{x}_p(t) = \mathbf{x}_s(t) + \mathbf{R}_s(t)\,{}^s\mathbf{x}_p \tag{4.3}$$

and its normal is given by

$$\hat{\mathbf{n}}_p(t) = \mathbf{R}_s(t)\,{}^s\hat{\mathbf{n}}_p. \tag{4.4}$$

Similarly, the positions and normals of the hydrophones are given by

$$\mathbf{x}_{hn}(t) = \mathbf{x}_s(t) + \mathbf{R}_s(t)\,{}^s\mathbf{x}_{hn} \tag{4.5}$$

and

$$\hat{\mathbf{n}}_{hn}(t) = \mathbf{R}_s(t)\,{}^s\hat{\mathbf{n}}_{hn}. \tag{4.6}$$

4.1.1 Sonar and transducer orientation

The orientation of the sonar and its transducers are specified by rotation matrices. It is common, however, to express the orientation using pitch, roll, and yaw (or heading) angles, θ_x, θ_y, and θ_z, that is, the angles of subsequent rotations about the x, y, and z axes. These are called Euler angles. The rotation matrix can be determined from the Euler angles using

$$\mathbf{R} = \mathbf{R}_z\mathbf{R}_y\mathbf{R}_x, \tag{4.7}$$

where

$$\mathbf{R}_x = \begin{pmatrix} 1 & 0 & 0 \\ 0 & \cos\theta_x & \sin\theta_x \\ 0 & -\sin\theta_x & \cos\theta_x \end{pmatrix}, \tag{4.8}$$

$$\mathbf{R}_y = \begin{pmatrix} \cos\theta_y & 0 & -\sin\theta_y \\ 0 & 1 & 0 \\ \sin\theta_y & 0 & \cos\theta_y \end{pmatrix}, \tag{4.9}$$

and

$$\mathbf{R}_z = \begin{pmatrix} \cos\theta_z & \sin\theta_z & 0 \\ -\sin\theta_z & \cos\theta_z & 0 \\ 0 & 0 & 1 \end{pmatrix} \tag{4.10}$$

are the subsequent rotation matrices. The rotations are usually performed in this order but any ordering can be used. Different orders of rotation result in different sets of Euler angles. Thus, the rotation order must be specified when using the Euler angles.

Quaternions are preferred over Euler angles for expressing orientation. A quaternion is a four-dimensional quantity (one real and three imaginary dimensions) and it is related to an axis and angle of rotation by

$$\mathbf{Q} = \begin{pmatrix} q_1 \\ q_2 \\ q_3 \\ q_4 \end{pmatrix} = \begin{pmatrix} \cos(\theta/2) \\ a_x \sin(\theta/2) \\ a_y \sin(\theta/2) \\ a_z \sin(\theta/2) \end{pmatrix}, \tag{4.11}$$

where $\mathbf{a} = (a_x, a_y, a_z)$ is the axis of rotation and θ is the angle. The quaternion is typically normalised, giving the unit quaternion,

$$\hat{\mathbf{Q}} = \frac{\mathbf{Q}}{|\mathbf{Q}|}, \tag{4.12}$$

where $|\mathbf{Q}| = \sqrt{q_1^2 + q_2^2 + q_3^2 + q_4^2}$ is the magnitude. The rotation matrix is obtained

from the quaternion by the relation

$$\mathbf{R} = \begin{pmatrix} q_1^2 + q_2^2 - q_3^2 - q_4^2 & 2q_2q_3 - 2q_1q_4 & 2q_1q_3 + 2q_2q_4 \\ 2q_1q_4 + 2q_2q_3 & q_1^2 - q_2^2 + q_3^2 - q_4^2 & 2q_3q_4 - 2q_1q_2 \\ 2q_2q_4 - 2q_1q_3 & 2q_1q_2 + 2q_3q_4 & q_1^2 - q_2^2 - q_3^2 + q_4^2 \end{pmatrix}. \tag{4.13}$$

The quaternion is a compact and convenient means of expressing orientation and it avoids the ambiguity associated with Euler angles.

4.2 FORMATION OF THE RAW DATA IMAGES

The echo data is organised into a collection of rows constituting a raw data image for each hydrophone. Each row in the image represents the echo from a subsequent ping. The times corresponding to the beginning of the transmitted signal are denoted by $t_m = t_1, t_2, ..., t_M$, where m is the ping number and the location of the sonar at these times is denoted by $\mathbf{u}_1, \mathbf{u}_2, ..., \mathbf{u}_M$. The raw data image for a given hydrophone is expressed as

$$e\left[t_m, t_n\right] = e\left[\mathbf{u}_m, t_n\right], \tag{4.14}$$

where $t_n = 0, \Delta t, 2\Delta t, ..., (N-1)\,\Delta t$ are the time samples for each ping,

$$\Delta t = \frac{1}{f_s} \tag{4.15}$$

is the sampling period and f_s is the sampling frequency. t_m and t_n are referred to as the *fast time* and *slow time* respectively. The fast time can be expressed as a range by assuming a constant sound speed profile, i.e.,

$$r_n = \frac{t_n}{c}, \tag{4.16}$$

and, for a linear path, the slow time can be expressed as an along-track position, i.e.,

$$\mathbf{u}_m = \begin{pmatrix} 0 \\ y_m \\ D \end{pmatrix}, \tag{4.17}$$

where D is the (constant) sonar depth and

$$y_m = t_m f_p v \tag{4.18}$$

for a constant ping rate, f_p, and velocity, v.

The raw data image is generated by a summation of the responses from the visible scatterers, where the visibility of each scatterer is determined by ray-tracing as

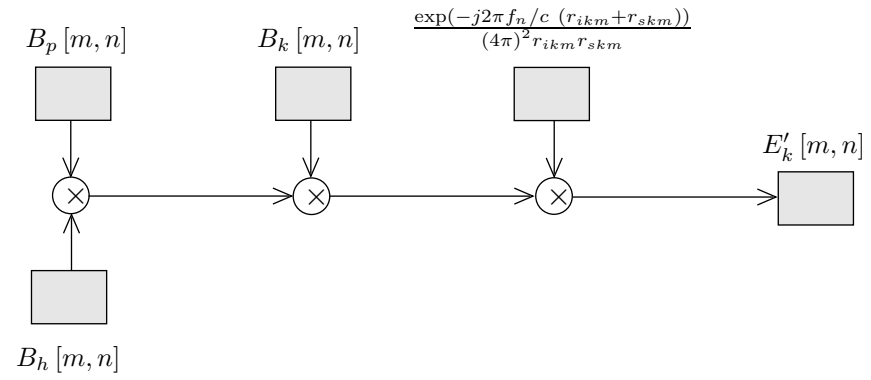

(a) k^{th} scatterer response

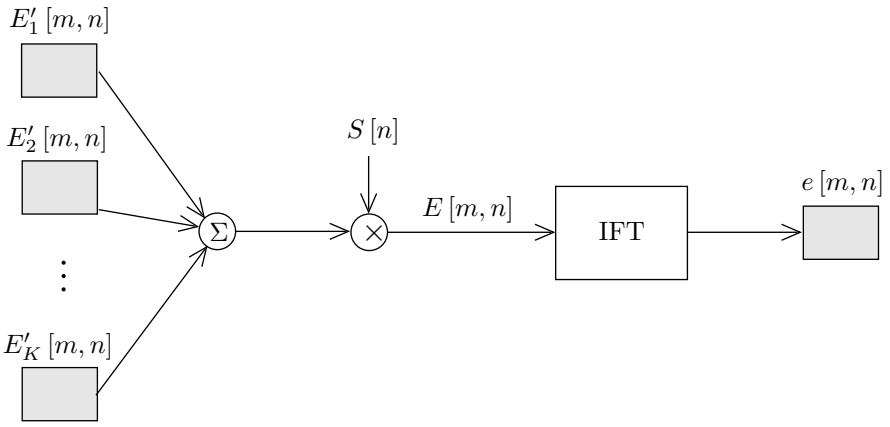

(b) raw data image

Figure 4.4 The raw data images are formed in the temporal frequency domain using a summation of the responses from each of the scatterers, where the scatterer is denoted by the subscript, k. The signal spectrum, S, can be applied after the summation if Doppler effects are ignored.

described in Section 4.4. The raw data image is given by

$$e\left[\mathbf{u}_m, t_n\right] = \sum_{k=1}^{K} e_k\left[\mathbf{u}_m, t_n\right] \tag{4.19}$$

or, in the temporal frequency domain,

$$E\left[\mathbf{u}_m, f_n\right] = \sum_{k=1}^{K} E_k\left[\mathbf{u}_m, f_n\right], \tag{4.20}$$

where f_n is the temporal frequency with respect to the fast time and

$$E_k\left[\mathbf{u}_m, f_n\right] = \frac{1}{f_s}\sum_{n=0}^{N-1} e_k\left[\mathbf{u}_m, t_n\right]\exp\left(-j2\pi f_n t_n\right) \tag{4.21}$$

is the response from the k^{th} scatterer. Using the expression for the scattered field, (3.1) or (3.32),

$$\begin{aligned} E_k\left[\mathbf{u}_m, f_n\right] =& S\left[f_n\right]\frac{\exp\left(-j\ 2\pi f_n/c\left(r_{ikm}+r_{skm}\right)\right)}{\left(4\pi\right)^2 r_{ikm}r_{skm}} \\ &\times B_p\left[\hat{\mathbf{n}}_{ikm}, f_n\right] B_h\left[\hat{\mathbf{n}}_{skm}, f_n\right] B_k\left[\hat{\mathbf{n}}_{ikm}, \hat{\mathbf{n}}_{skm}, f_n\right], \end{aligned} \tag{4.22}$$

where

$$\mathbf{r}_{ikm} = \mathbf{x}_k - \mathbf{x}_{pm}, \tag{4.23}$$

$$r_{ikm} = \left|\mathbf{r}_{ikm}\right|, \tag{4.24}$$

$$\hat{\mathbf{n}}_{ikm} = \frac{\mathbf{r}_{ikm}}{r_{ikm}}, \tag{4.25}$$

$$\mathbf{r}_{skm} = \mathbf{x}_{hm} - \mathbf{x}_k, \tag{4.26}$$

$$r_{skm} = \left|\mathbf{r}_{skm}\right|, \tag{4.27}$$

$$\hat{\mathbf{n}}_{skm} = \frac{\mathbf{r}_{skm}}{r_{skm}}, \tag{4.28}$$

$\mathbf{x}_{pm}$ and $\mathbf{x}_{hm}$ are the projector and hydrophone locations for the m^{th} ping, $\mathbf{x}_k$ is the location of the k^{th} scatterer, and B_k is the scatterer beampattern. Figure 4.4 illustrates the formation of the raw data images.

The subscript k denoting the k^{th} scatterer is suppressed in the following sections and a single scatterer is considered. The raw data images are discrete. However, they are considered continuous in the following sections for notational convenience.

4.2.1 Transducer beampattern evaluation

The transducer beampattern expression (2.61) is evaluated in the coordinate system local to the transducer. A change of variables can be used to obtain the expression for the beampattern of an arbitrarily oriented transducer in the global coordinate system. For the projector,

$$B_p\left(\hat{\mathbf{n}}_i, f\right) = j\frac{2\pi}{\lambda}\left(1+{}^p n_{iz}\right) A_p\left(\frac{1}{\lambda}\,{}^p n_{ix}, \frac{1}{\lambda}\,{}^p n_{iy}\right), \tag{4.29}$$

where the aperture function, $a_p\left({}^p x, {}^p y\right)$, is defined in the x-y plane of the projector coordinates. The direction of the incident field, ${}^p\hat{\mathbf{n}}_i$, is given in the projector coordinates

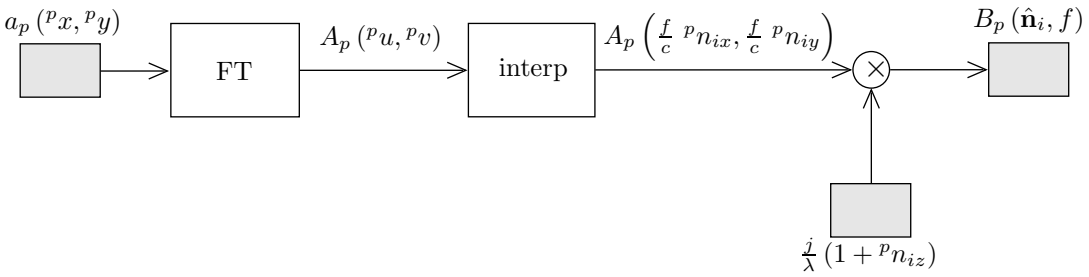

Figure 4.5 Evaluation of the transducer beampattern involves a Fourier transform of the aperture function and an interpolation, followed by application of the obliquity factor. The interpolation is dependent on the sonar trajectory and the temporal bandwidth.

and it is related to the global coordinate system by

$$ {}^p\hat{\mathbf{n}}_i\left(t\right) = \begin{pmatrix} {}^p n_{ix} \\ {}^p n_{iy} \\ {}^p n_{iz} \end{pmatrix} = {}^s\mathbf{R}_p^{-1}\mathbf{R}_s^{-1}\left(t\right)\hat{\mathbf{n}}_i\left(t\right), \tag{4.30} $$

where

$$ \hat{\mathbf{n}}_i\left(t\right) = \frac{\mathbf{x}_k - \mathbf{x}_p\left(t\right)}{\left|\mathbf{x}_k - \mathbf{x}_p\left(t\right)\right|} \tag{4.31} $$

and $\mathbf{x}_k$ is the location of the scatterer. Here t is the slow time and f is the temporal frequency with respect to the fast time. Similarly,

$$ B_h\left(\hat{\mathbf{n}}_s, f\right) = j\frac{2\pi}{\lambda}\left(1 + {}^h n_{sz}\right) A_h\left(\frac{1}{\lambda}\ {}^h n_{sx}, \frac{1}{\lambda}\ {}^h n_{sy}\right) \tag{4.32} $$

for the hydrophones, where the aperture function, $a_h\left({}^h x, {}^h y\right)$ is defined in the x-y plane of the hydrophone coordinates,

$$ {}^h\hat{\mathbf{n}}_s\left(t\right) = \begin{pmatrix} {}^h n_{sx} \\ {}^h n_{sy} \\ {}^h n_{sz} \end{pmatrix} = {}^s\mathbf{R}_h^{-1}\mathbf{R}_s^{-1}\left(t\right)\hat{\mathbf{n}}_s\left(t\right), \tag{4.33} $$

and

$$ \hat{\mathbf{n}}_s\left(t\right) = \frac{\mathbf{x}_h\left(t\right) - \mathbf{x}_k}{\left|\mathbf{x}_h\left(t\right) - \mathbf{x}_k\right|}. \tag{4.34} $$

The beampattern of an arbitrarily oriented facet is evaluated in a similar way; this is detailed in the next section. Figure 4.5 illustrates the evaluation of the transducer beampattern and Figure 4.6 shows examples of each stage.

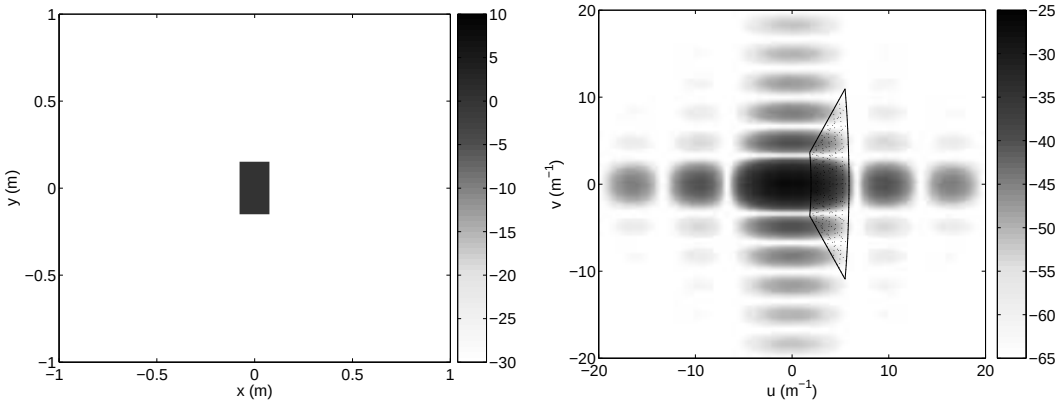

(a) projector aperture function

(b) Fourier transform (magnitude)

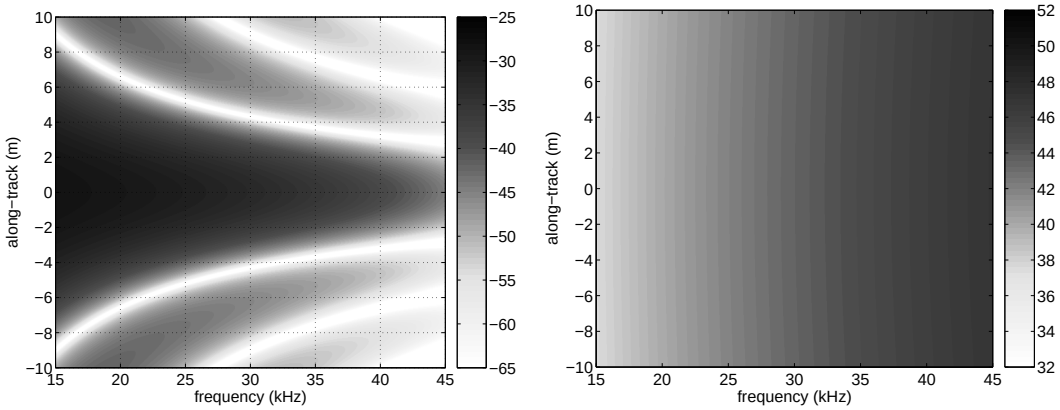

(c) interpolated Fourier transform

(d) obliquity factor

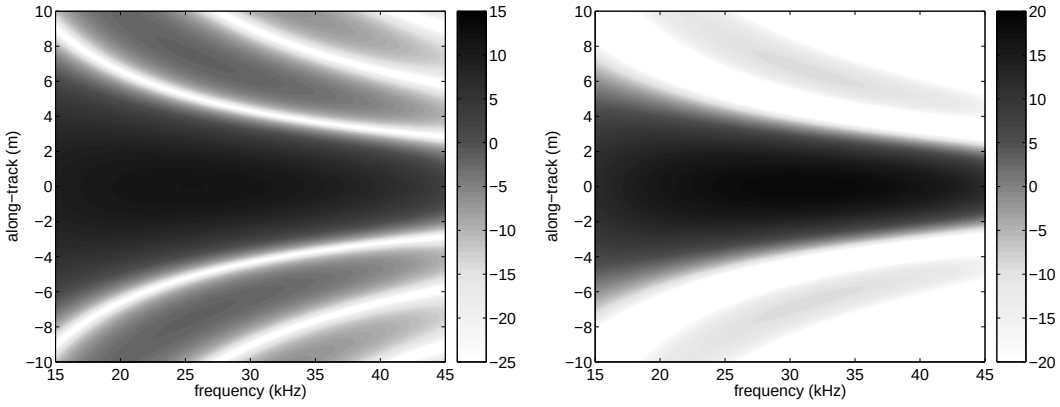

(e) projector response

(f) projector and hydrophone response

Figure 4.6 Evaluation of the transducer response is illustrated in Figure 4.5. Examples of the various stages are shown here for a scatterer located at an across-track distance of 25 m, and 5 m below the sonar. The specifications of the KiwiSAS-IV are used (see Section 5.1) and the 30 kHz chirp is considered.

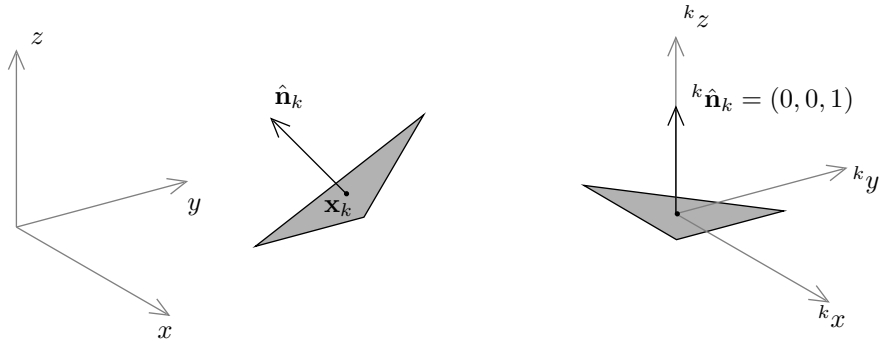

(a) global coordinates (b) facet coordinates

Figure 4.7 The facet aperture function is defined in a local coordinate system that is aligned with the plane containing the aperture. The origin of the coordinate system is at the facet centroid.

4.2.2 Facet beampattern evaluation

The expressions for the specular and diffuse components of the facet beampattern (given in Sections 3.4 and 3.5) are evaluated in the coordinate system local to the facet. The specular component of the facet beampattern is given by

$$B_c\left(\hat{\mathbf{n}}_i, \hat{\mathbf{n}}_s, f\right) = j\frac{2\pi}{\lambda} R \left({}^k n_{rz} + {}^k n_{sz}\right) \exp\left(-2\pi^2 \frac{\sigma^2}{\lambda^2}\left({}^k q_z\right)^2\right) A\left(\frac{1}{\lambda}\,{}^k q_x, \frac{1}{\lambda}\,{}^k q_y\right), \tag{4.35}$$

where the aperture function, $a\left({}^k x, {}^k y\right)$, is defined in the x-y plane of the facet coordinates as shown in Figure 4.7,

$${}^k\mathbf{q}\left(t\right) = \begin{pmatrix} {}^k q_x \\ {}^k q_y \\ {}^k q_z \end{pmatrix} = {}^k\hat{\mathbf{n}}_r\left(t\right) - {}^k\hat{\mathbf{n}}_s\left(t\right), \tag{4.36}$$

$$\begin{aligned} {}^k\hat{\mathbf{n}}_r\left(t\right) &= \mathbf{R}_k^{-1}\hat{\mathbf{n}}_r\left(t\right), & (4.37)\\ {}^k\hat{\mathbf{n}}_s\left(t\right) &= \mathbf{R}_k^{-1}\hat{\mathbf{n}}_s\left(t\right), & (4.38) \end{aligned}$$

and the orientation of the facet with respect to the global coordinates is defined by the rotation matrix $\mathbf{R}_k$. Similarly for the diffuse component,

$$\begin{aligned} B_d\left(\hat{\mathbf{n}}_i, \hat{\mathbf{n}}_s, f\right) =& j\frac{2\pi}{\lambda} R \left({}^k n_{rz} + {}^k n_{sz}\right) d\left(\frac{1}{\lambda}{}^k q_x, \frac{1}{\lambda}{}^k q_y, \frac{1}{\lambda}{}^k q_z\right) \\ &\times \int_{-\infty}^{\infty}\!\!\int b\left(u,v\right) w\left(u,v\right) h\left(\frac{1}{\lambda}{}^k q_x - u, \frac{1}{\lambda}{}^k q_y - v\right) du\, dv, \end{aligned} \tag{4.39}$$

where b, d, and h are defined in Section 3.7.2.

Figure 4.8 illustrates the evaluation of the facet beampattern, where the convolution (4.39) is performed using the Fourier transform and the obliquity factor is applied after combination of the specular and diffuse components as shown in Figure 4.9. Examples of each stage in evaluating the facet beampattern are shown in Figures 4.10, 4.11 and 4.12. Figure 4.13 shows the combination of the transducer and facet beampatterns and application of the phase delays and spreading losses. Figure 4.14 shows the application of the signal spectrum and the resultant raw data imagery.

4.3 FOURIER WARPING

Evaluation of the transducer and facet beampatterns requires a Fourier transform of the aperture function. The Fourier transform of an arbitrary rectangular or triangular aperture function can be determined analytically (see Appendix A). However, this requires a general expression, which can be cumbersome; this is particularly true for a triangular aperture. Instead, the Fourier warping theorem, which is derived in Appendix A, can be used to evaluate the Fourier transform of an arbitrary aperture using the expression for a simple reference aperture. The Fourier transform of an arbitrary parallelogram can be obtained from the expression for a square and the Fourier transform of an arbitrary triangle can be obtained from the expression for a right-angle triangle.

The Fourier warping theorem states that a transformation (or warping) in one domain results in an inverse transformation in the other domain; this is a generalisation of the scaling property of the Fourier transform [Bracewell 1986]. Consider the Fourier transform pair

$$a(\mathbf{x}) \longleftrightarrow A(\mathbf{u}). \tag{4.40}$$

By the warping property of the Fourier transform,

$$a(\mathbf{R}\mathbf{x}) \longleftrightarrow \frac{1}{\det(\mathbf{R})} A\left(\left(\mathbf{R}^{-1}\right)^{T}\mathbf{u}\right), \tag{4.41}$$

where $\mathbf{R}$ is a matrix that describes a warping of points, $\mathbf{x}$ to $\mathbf{x}' = \mathbf{R}\mathbf{x}$, and $\det(\mathbf{R})$ is the determinant of $\mathbf{R}$. The superscript, T, denotes the matrix transpose operation.

A reference aperture function is selected and the appropriate transformation, which warps the desired aperture to the reference aperture, is determined. The Fourier warping property is then used to determine the Fourier transform of the desired aperture function using the transformation matrix $\mathbf{R}$ and the Fourier transform expression for the reference aperture. The 3×3 transformation matrix describes an affine transformation, that is, scaling, rotation, and shear [Anton and Rorres 1994]. An affine transformation can warp an arbitrary parallelogram to a unit square and an arbitrary

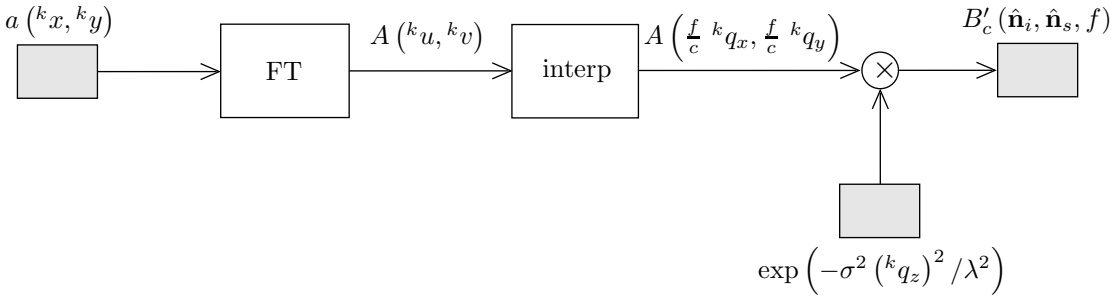

(a) specular beampattern component

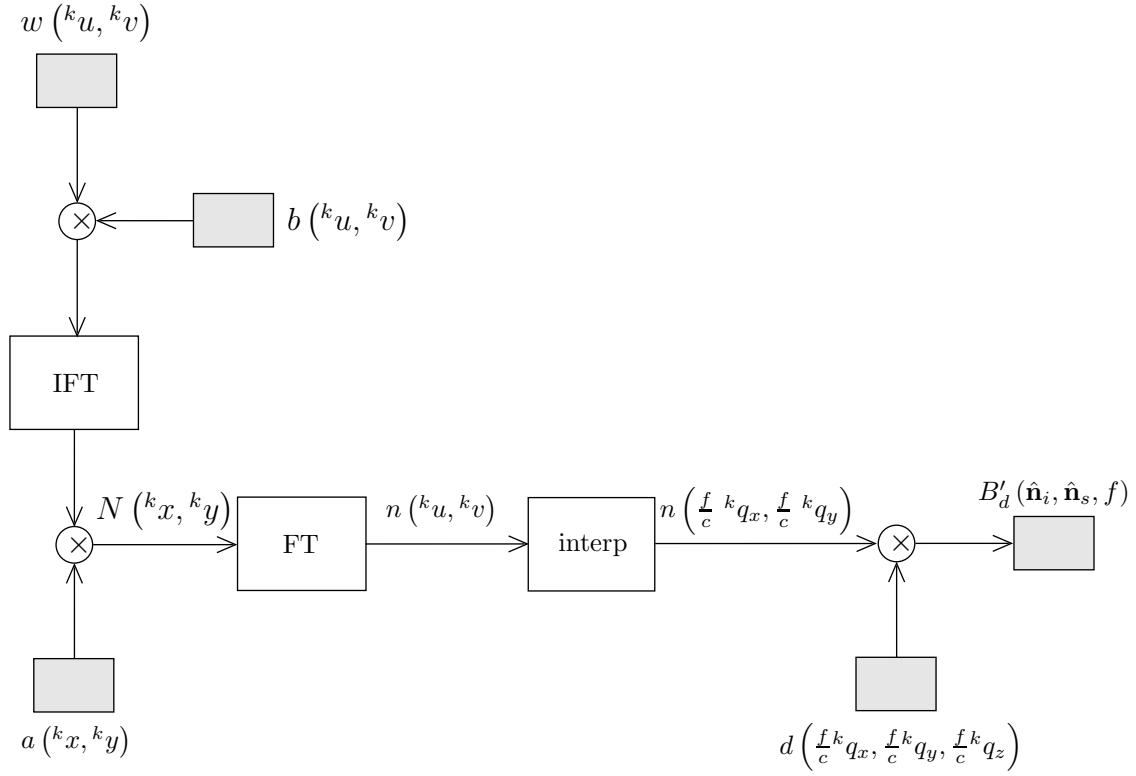

(b) diffuse beampattern component

Figure 4.8 The beampattern of a rough facet is generated from the weighted sum of a specular component and a realisation of the diffuse component. The specular component is generated by interpolating the Fourier transform of the facet aperture function. The diffuse component is generated by interpolating white noise that has been passed through a quasi-stationary filter.

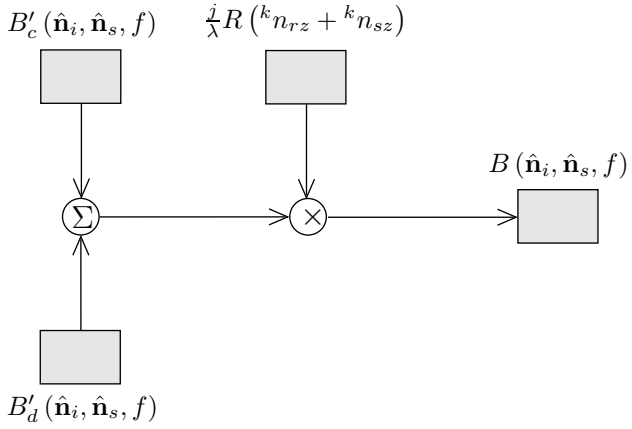

Figure 4.9 The facet beampattern is the sum of a specular component and a diffuse component. The obliquity factor, which is common to both components, can be applied after the summation.

triangle to a unit right-angle triangle. The Fourier transform expressions for these reference aperture functions are given by (3.37) and (3.40).

4.3.1 Triangular facets

A triangle is defined by its three vertices: $\mathbf{x}_0$, $\mathbf{x}_1$, and $\mathbf{x}_2$. These vectors can be combined to create a matrix,

$$\mathbf{T} = \begin{pmatrix} x_0 & x_1 & x_2 & n_x \\ y_0 & y_1 & y_2 & n_y \\ z_0 & z_1 & z_2 & n_z \end{pmatrix}, \tag{4.42}$$

where $\mathbf{x}_0 = (x_0, y_0, z_0)$, etc., and $\hat{\mathbf{n}} = (n_x, n_y, n_z)$ is the surface normal. Similarly, a reference unit right-angle triangle (centred about its centroid) is described by the matrix,

$$\mathbf{T}_u = \begin{pmatrix} \frac{1}{3} & \frac{1}{3} & -\frac{2}{3} & 0 \\ -\frac{1}{3} & \frac{2}{3} & -\frac{1}{3} & 0 \\ 0 & 0 & 0 & 1 \end{pmatrix}. \tag{4.43}$$

The matrix, $\mathbf{R}$, describing the transformation from $\mathbf{T}$ to $\mathbf{T}_u$ is determined from the matrices, (4.42) and (4.43), using the relation

$$\mathbf{T}_u = \mathbf{R}\mathbf{T}. \tag{4.44}$$

Thus,

$$\mathbf{R} = \mathbf{T}_u \left(\mathbf{T}^T\mathbf{T}\right)^{-1} \mathbf{T}^T, \tag{4.45}$$

where $\left(\mathbf{T}^T\mathbf{T}\right)^{-1} \mathbf{T}^T$ is the pseudo-inverse of $\mathbf{T}$ [Anton and Rorres 1994].

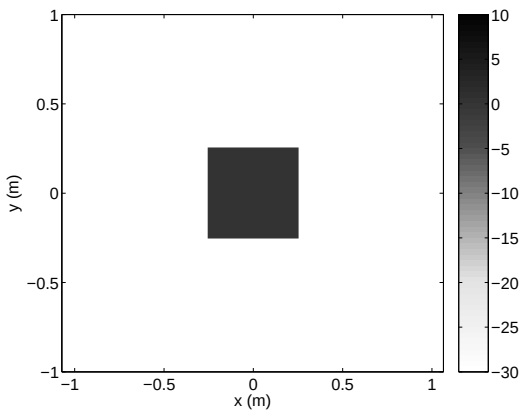

(a) facet aperture function

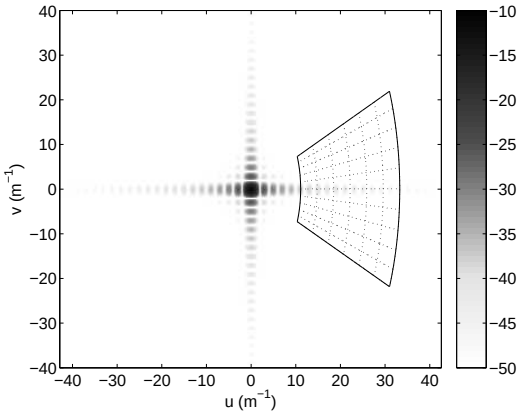

(b) Fourier transform (magnitude)

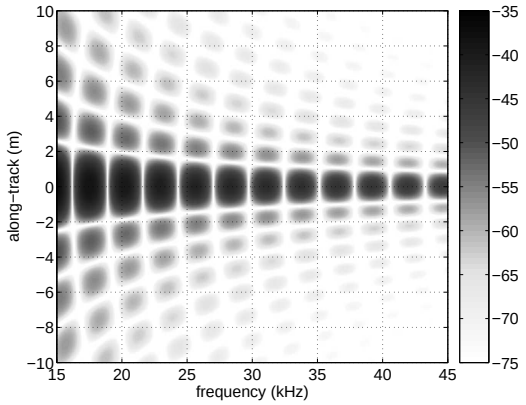

(c) interpolated Fourier transform

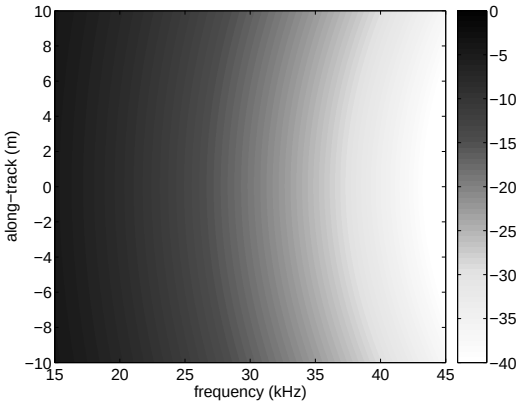

(d) specular weighting

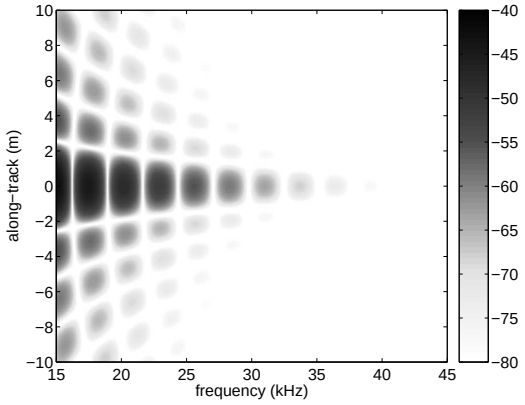

(e) specular component

Figure 4.10 Evaluation of the specular facet response is illustrated in Figure 4.8(a). Examples of the various stages are shown here for a 0.5×0.5 m rough facet located at an across-track distance of 25 m, and 5 m below the sonar. The facet roughness has a height variance of 5 mm and a correlation length of 10 mm.

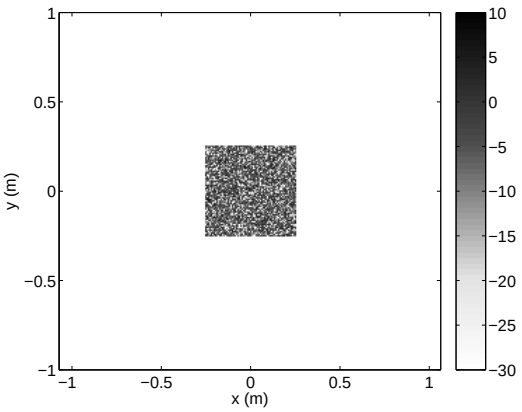

(a) noise spectrum (magnitude)

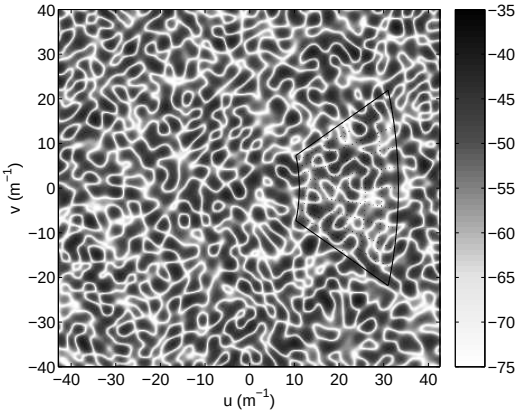

(b) noise (magnitude)

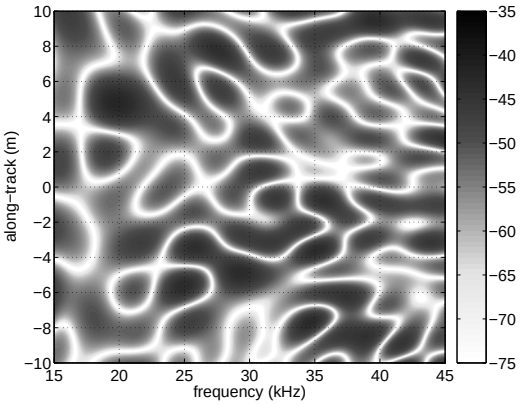

(c) interpolated noise

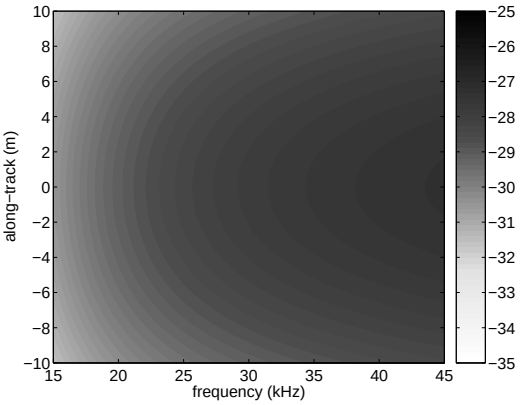

(d) diffuse weighting

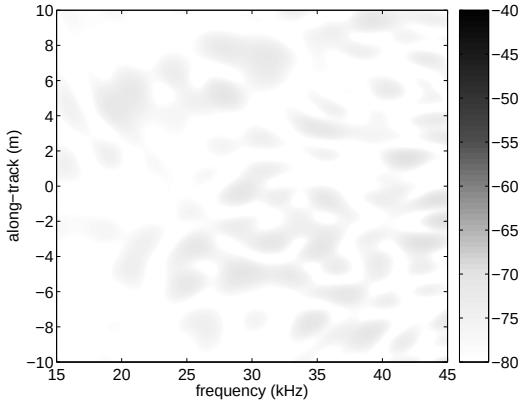

(e) diffuse component

Figure 4.11 Evaluation of the diffuse facet response is illustrated in Figure 4.8(b). Examples of the various stages are shown here for a 0.5×0.5 m rough facet located at an across-track distance of 25 m, and 5 m below the sonar. The facet roughness has a height variance of 5 mm and a correlation length of 10 mm.

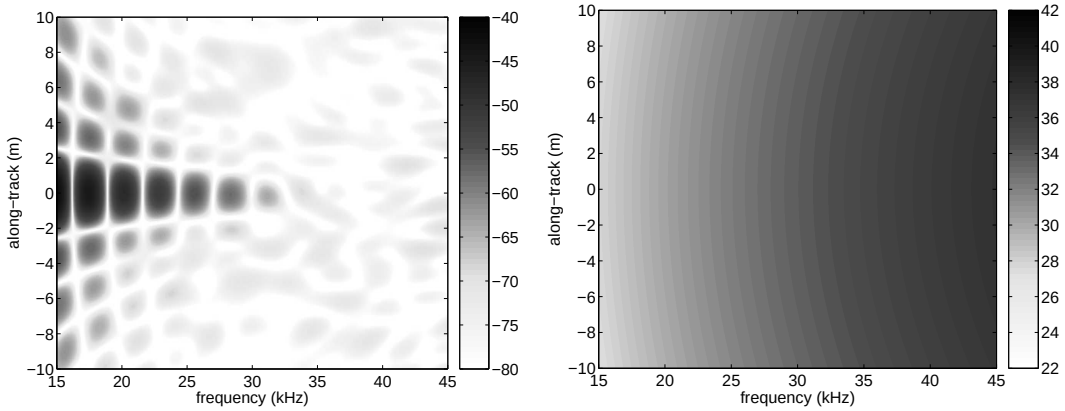

(a) specular and diffuse components

(b) obliquity factor

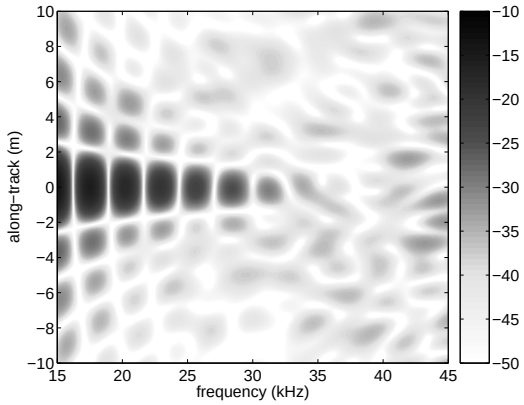

(c) facet response

Figure 4.12 The total facet response is the sum of the specular and diffuse components; this is illustrated in Figure 4.9. The obliquity factor, which is common to both components, is applied after the summation.

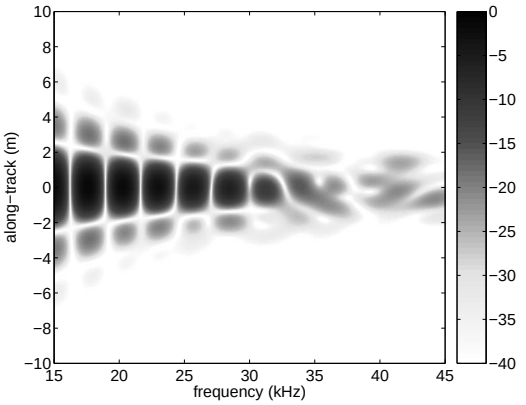

(a) projector, hydrophone, and facet response (magnitude)

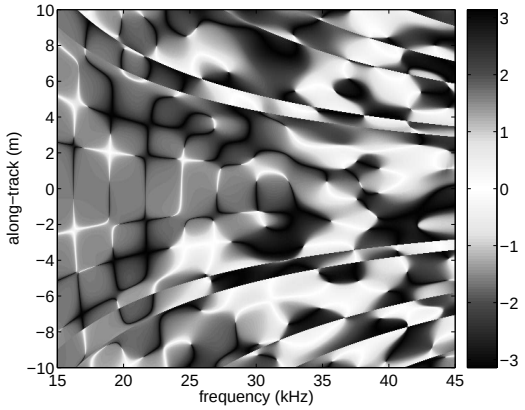

(b) phase response

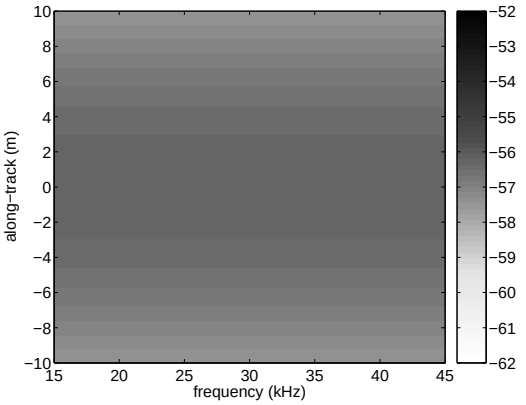

(c) spreading loss

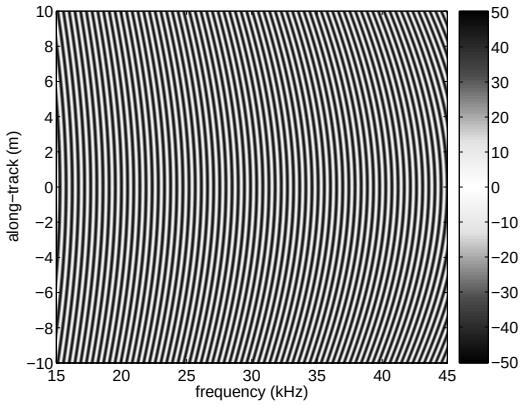

(d) phase migration

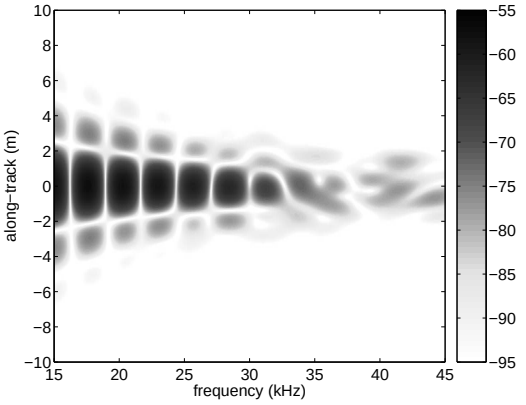

(e) total magnitude response

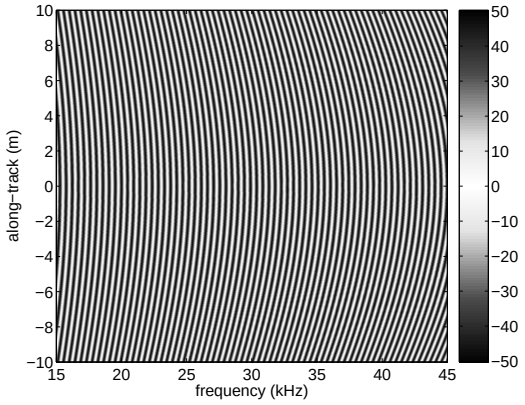

(f) total phase response

Figure 4.13 The total response is obtained by combining the transducer and facet responses as illustrated in Figure 4.4(a). The spreading loss and phase migration is then applied.

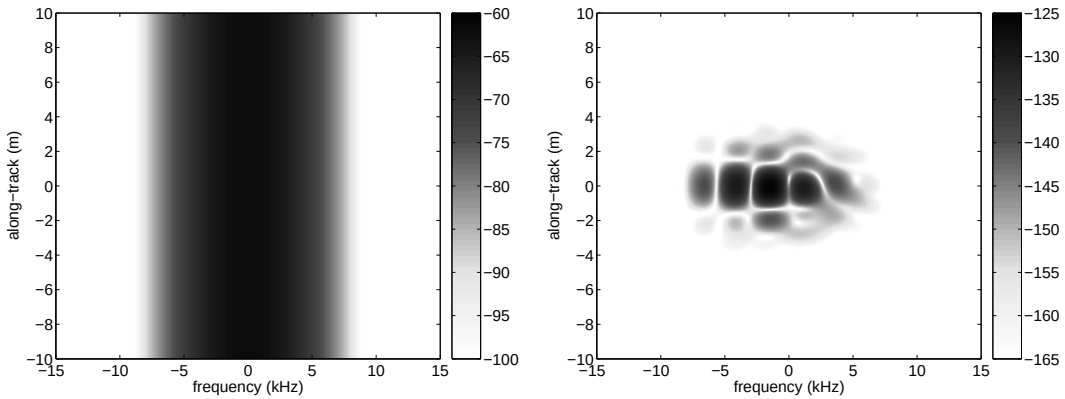

(a) baseband chirp spectrum with Blackman window (magnitude)

(b) baseband chirp response

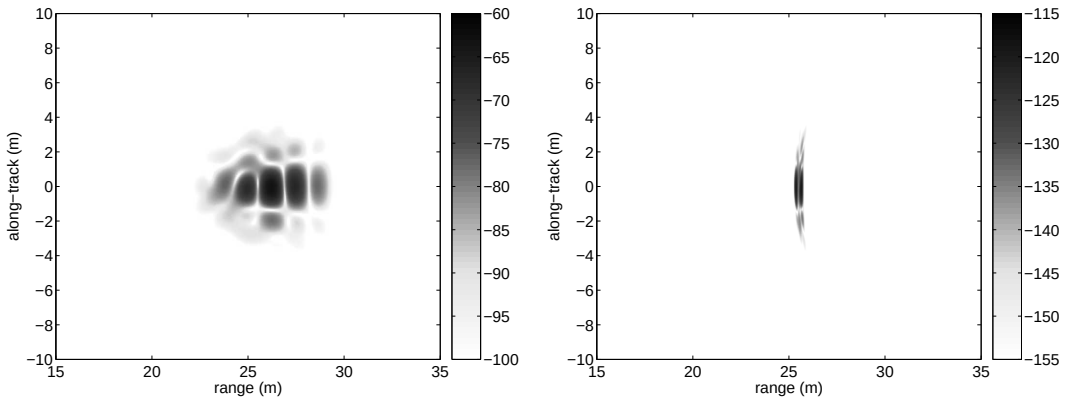

(c) baseband raw data

(d) pulse-compressed data

Figure 4.14 Once the responses from all the facets have been summed (in this case only one), the chirp spectrum is applied and the raw data is obtained by an inverse Fourier transform; this is illustrated in Figure 4.4(b).

The Fourier transform of the unit right-angle triangle is shown in Figure 4.15(c). The spatial frequencies corresponding to a particular path and facet orientation are illustrated and the interpolated values are shown in Figure 4.15(e). The Fourier transform of an example arbitrary triangular aperture is shown in Figure 4.15(d) and the interpolated values are shown in Figure 4.15(f) for the same path and facet orientation. Alternatively, the same values can be obtained by interpolating the Fourier transform of the unit right-angle triangle at spatial frequencies warped by the matrix, $\left(\mathbf{R}^{-1}\right)^T$, where $\mathbf{R}$ is the transformation from the arbitrary triangle to the unit right-angle triangle; this is shown in Figure 4.16. The same approach is used to determine the Fourier transform of an arbitrary parallelogram (a sheared rectangle) from the Fourier transform of the unit square.

The advantage of the warping technique is that only a single lookup table needs to be calculated and stored; this is then interpolated as required [2]. In addition, the transformation from global to local coordinates can be incorporated in the matrix, $\mathbf{R}$.

4.3.2 Non-triangular facets

A quadrilateral aperture can be constructed from two triangular apertures, i.e.,

$$a_Q(\mathbf{x}) = a_{T1}(\mathbf{x} - \mathbf{x}_1) + a_{T2}(\mathbf{x} - \mathbf{x}_2), \tag{4.46}$$

where $\mathbf{x}_1$ and $\mathbf{x}_2$ are the centroids. The Fourier transform of the quadrilateral aperture can then be determined using the linearity and shift theorems of the Fourier transform, i.e.,

$$A_Q(\mathbf{u}) = A_{T1}(\mathbf{u}) \exp(-j2\pi\ \mathbf{x}_1 \cdot \mathbf{u}) + A_{T2}(\mathbf{u}) \exp(-j2\pi\ \mathbf{x}_2 \cdot \mathbf{u}). \tag{4.47}$$

Expressing the triangles using the unit right-angle triangle and the appropriate transformations,

$$\begin{aligned} a_{T1}(\mathbf{x}) &= a_T(\mathbf{R}_1\mathbf{x}) && (4.48)\\ a_{T2}(\mathbf{x}) &= a_T(\mathbf{R}_2\mathbf{x}), && (4.49) \end{aligned}$$

and invoking the warping theorem of the Fourier transform yields the Fourier transform of the quadrilateral aperture;

$$\begin{aligned} A_Q(\mathbf{u}) = &\frac{1}{\det(\mathbf{R}_1)} A_T\left(\left(\mathbf{R}_1^{-1}\right)^T \mathbf{u}\right) \exp(-j2\pi\ \mathbf{x}_1 \cdot \mathbf{u}) \\ &+ \frac{1}{\det(\mathbf{R}_2)} A_T\left(\left(\mathbf{R}_2^{-1}\right)^T \mathbf{u}\right) \exp(-j2\pi\ \mathbf{x}_2 \cdot \mathbf{u}). \end{aligned} \tag{4.50}$$

[2] Separate lookup tables are required for parallelograms and triangles. A projective transformation [Foley *et al.* 1997] can be used to warp an arbitrary quadrilateral to the unit right-angle triangle. However, the Fourier relationship for a projective transformation is difficult to determine.

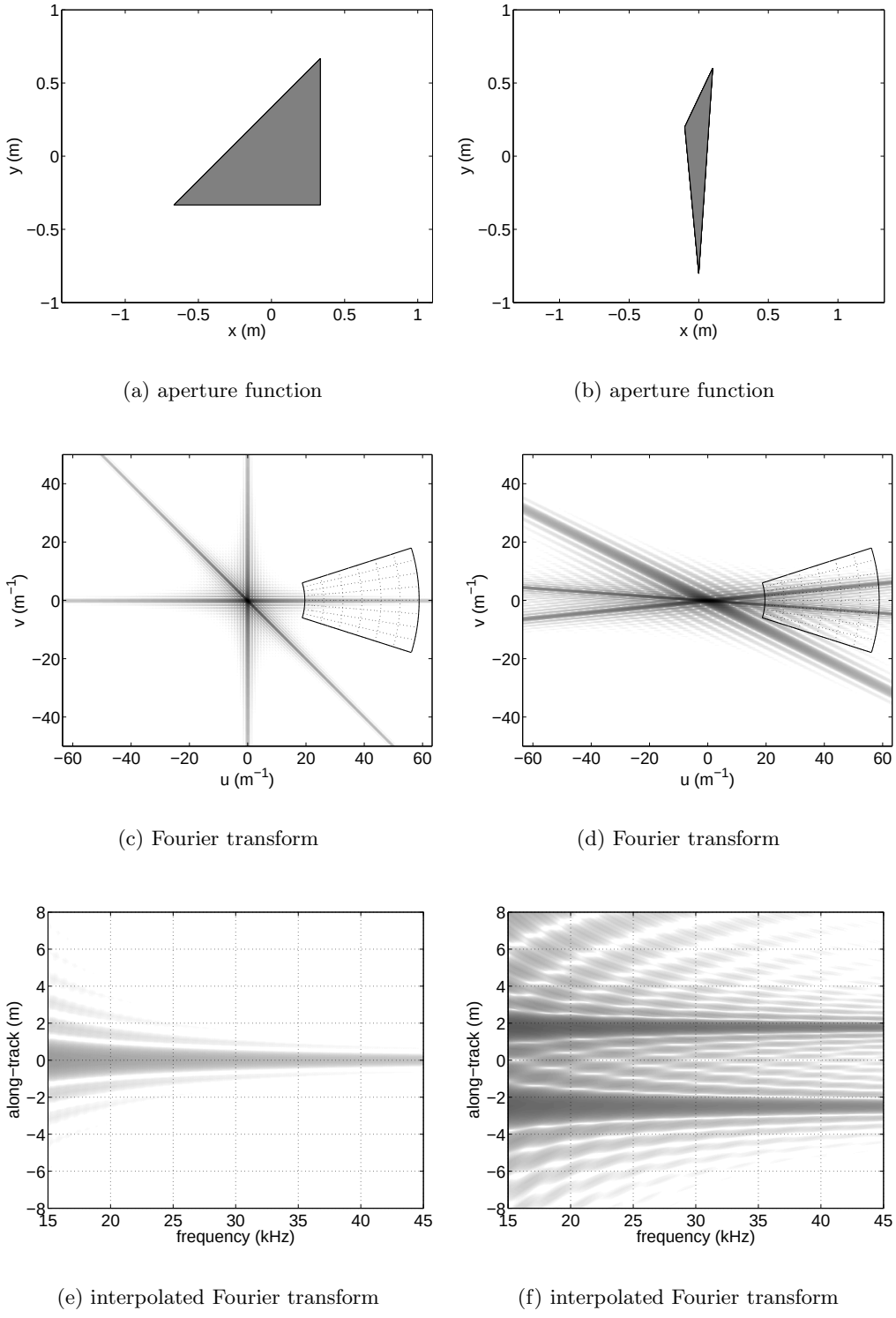

(a) aperture function

(b) aperture function

(c) Fourier transform

(d) Fourier transform

(e) interpolated Fourier transform

(f) interpolated Fourier transform

Figure 4.15 The Fourier transform of the facet aperture function is evaluated at spatial frequencies that are dependent on the sonar trajectory, the facet location and orientation, the temporal bandwidth, and the medium properties. The boxed regions in (c) and (d) illustrate the interpolated spatial frequencies.

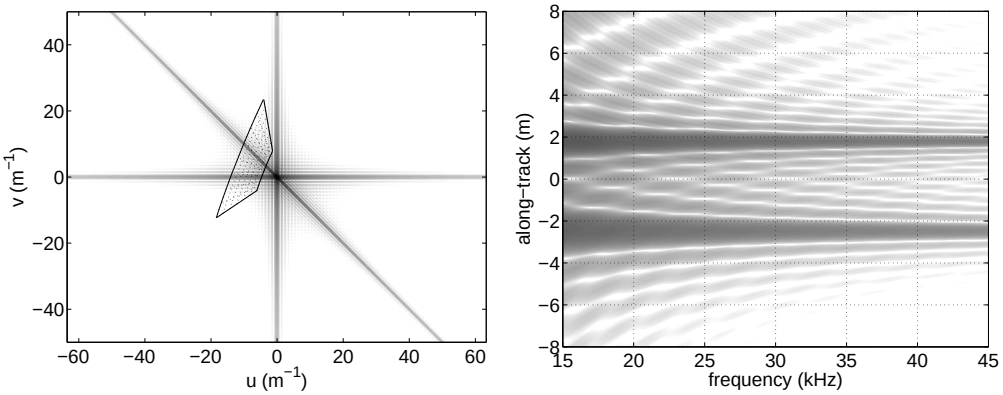

(a) Fourier transform of the aperture function

(b) interpolated Fourier transform

Figure 4.16 The beampattern of an arbitrary triangular facet can be evaluated using the Fourier transform of the unit right-angle triangle aperture function. The interpolated spatial frequencies are warped using the matrix $\left(\mathbf{R}^{-1}\right)^T$, where $\mathbf{R}$ is a matrix describing the affine transformation required to map the arbitrary triangle to the unit right-angle triangle.

In general, an arbitrary polygonal aperture can be constructed from N conjoined triangular apertures. Using the warping and shifting properties, the Fourier transform of an arbitrary aperture is given by

$$A\left(\mathbf{u}\right) = \sum_{n=1}^{N} \frac{1}{\det\left(\mathbf{R}_n\right)} A_T\left(\left(\mathbf{R}_n^{-1}\right)^T \mathbf{u}\right) \exp\left(-j2\pi\ \mathbf{x}_n \cdot \mathbf{u}\right), \tag{4.51}$$

where $\mathbf{x}_n$ and $\mathbf{R}_n$ are the centroid and transformation matrix for the n^{th} triangular aperture.

4.3.3 Time-variant facets

The shape, position, and orientation of a facet can change with time. For example, a moving sea surface can be modelled using time-variant facets [Davis 2001]. A time-variant facet has a time-variant beampattern and determination of the beampattern requires calculation and interpolation of the Fourier transform of the (time-variant) aperture function for each unique facet shape, i.e., for each along-track sample, y_p. While the beampattern changes continuously with time, here it is assumed constant for the duration of each scattering event.

Calculation of the Fourier transform for each unique facet shape is inefficient. Instead, the Fourier warping theorem can be employed and the beampattern of the time-variant facet can be obtained using only the Fourier transform of the unit right-

angle triangle. The required transformations are obtained from

$$\mathbf{T}_u = \mathbf{R}(t)\,\mathbf{T}(t), \tag{4.52}$$

where $\mathbf{T}(t)$ describes the aperture of the triangle for each along-track sample and the transformation matrices, $\mathbf{R}(t)$, map the triangles to the unit right-angle triangle (refer (4.45)). The time-variant Fourier transform is then given by

$$A(\mathbf{u},t) = \frac{1}{\det(\mathbf{R}(t))} A_T\left(\left(\mathbf{R}^{-1}(t)\right)^T \mathbf{u}\right). \tag{4.53}$$

An example time-variant facet is illustrated in Figure 4.17 for four instances of time. The Fourier transforms of the aperture functions are shown and the interpolated spatial frequencies are indicated along with the equivalent (warped) spatial frequencies required for interpolation of the expression for the unit right-angle triangle. The interpolated values are illustrated in Figure 4.18.

4.3.4 Partially occluded facets

A facet is occluded when it is in the shadow region of an opaque object. If a facet is completely occluded, then it does not contribute to the scattered field and can be ignored. If it is not occluded, the scattered field can be determined using the facet beampattern. When a facet is partially occluded, however, its beampattern is determined using the effective shape of the facet, which is dependent on the shadows cast across the facet. Moreover as the illumination point is changed, the shadows move and, thus, the effective shape changes.

A first-order, linear shadow boundary is considered here. For a triangular facet this results in an effective facet that is a triangular or quadrilateral shape. An iterative ray-tracing approach can be used to find the visible region of a facet occluded by a linear shadow. Rays are traced to the corners of the facet to find the visible vertices. Then additional rays are traced for each partly occluded edge using a bisection search. This is illustrated in Figure 4.19 and ray-tracing is covered in Section 4.4.

The effective aperture of a partly occluded triangular facet can be decomposed into two time-variant triangular apertures for a linear shadow boundary. The Fourier transforms are computed as described in Section 4.3.3 and combined as described in Section 4.3.2. More complicated shadows can be modelled in a similar manner by partitioning the effective aperture into a number of triangular apertures.

A naive approach to modelling an occluded facet (an approach that was employed previously) is to use a simple binary shadow mask. A single ray is traced to the facet centroid to determine its visibility for each along-track sample. The facet is considered either fully visible or not visible. This results in a discontinuity in the facet response

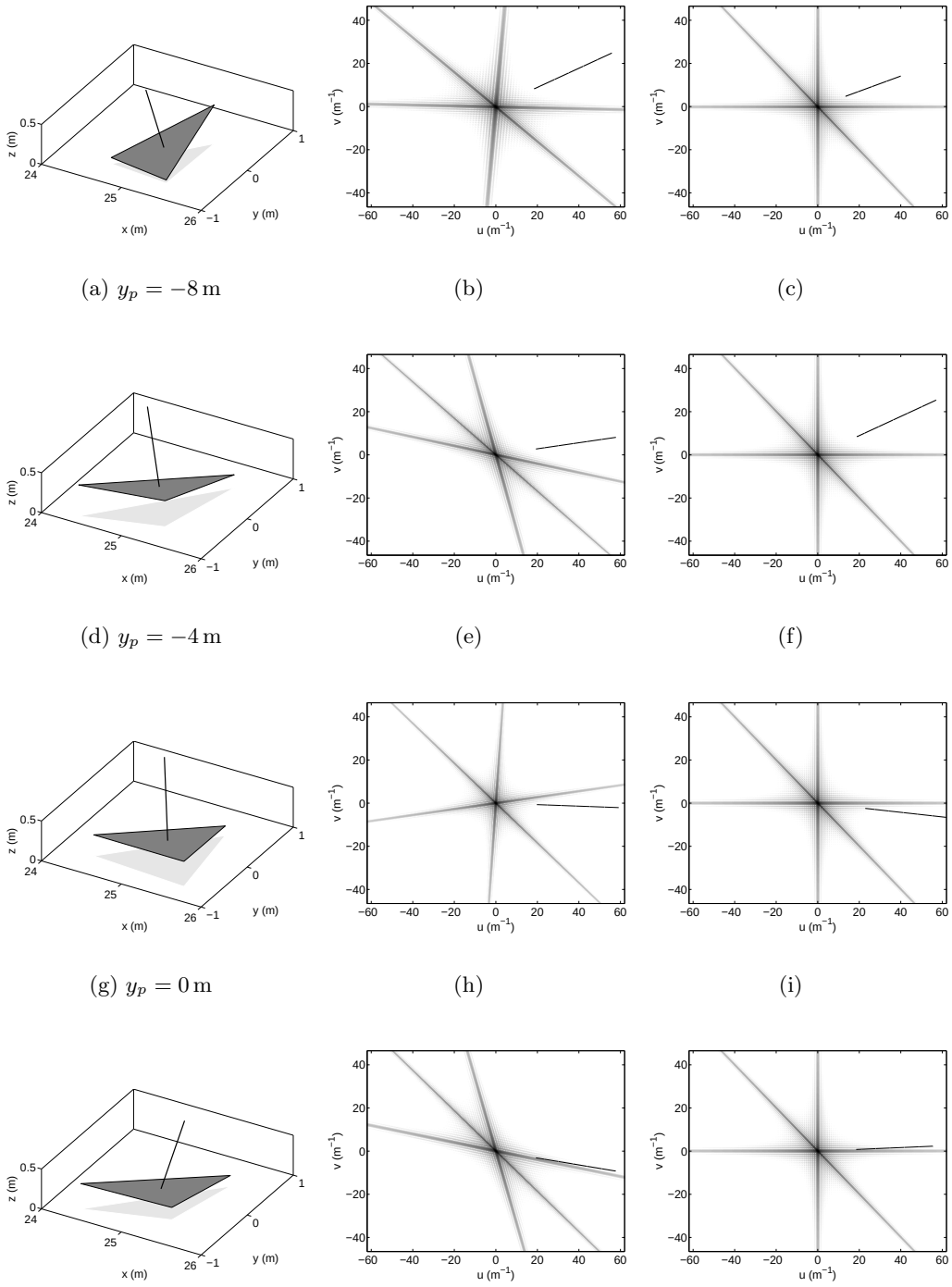

(a) $y_p = -8\,\mathrm{m}$ (b) (c)

(d) $y_p = -4\,\mathrm{m}$ (e) (f)

(g) $y_p = 0\,\mathrm{m}$ (h) (i)

(j) $y_p = +4\,\mathrm{m}$ (k) (l)

Figure 4.17 A time-variant facet has a time-variant beampattern. Determination of the beampattern requires calculation and interpolation of the Fourier transform of the aperture function for each unique aperture shape. A more efficient approach is to interpolate the Fourier transform of a unit right-angle triangle using the spatial frequencies warped by the appropriate time-variant transformation, $\left(\mathbf{R}^{-1}\left(t\right)\right)^{T}$. The lines indicate the interpolated spatial frequencies for the particular along-track samples.

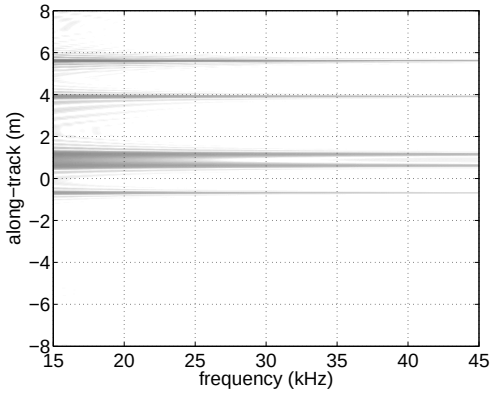

Figure 4.18 The beampattern of a time-variant facet is evaluated by interpolating the Fourier transform of the (time-variant) aperture function at the appropriate (warped) spatial frequencies. This is shown in Figure 4.17.

that introduces undesirable artefacts in the simulated data. The severity of the artefacts increase with the facet size. Correct modelling of the partial occlusion has alleviated this problem.

A partially occluded triangular facet is considered in Figure 4.20. The facet is located at an across-track distance of 25 m, and 5 m below the sonar. The facet is occluded by a 1 m diameter sphere located at an across-track distance of 10 m, and 2 m below the sonar. Figure 4.20(a),(d),(g), and (j) show the decomposition of the effective aperture function as the facet becomes occluded. Figure 4.20(b),(e),(h), and (k) show the Fourier transform of the effective aperture function and the interpolated spatial frequencies and Figure 4.20(c),(f),(i), and (l) show the (more efficient) interpolation using the Fourier transform of the unit right-angle triangle. The interpolated values are shown in Figure 4.21(a) and the values obtained using a binary shadow mask are shown in Figure 4.21(b). The discontinuity is clearly evident for the binary mask.

4.3.5 Temporal Doppler effects

The expressions derived in the previous chapters consider stationary transducers and scattering objects. However, the sonar transmits a signal at regular intervals as it moves continuously along its path. The sonar location changes during the time taken for the signal to travel to the scatterers and back as shown in Figure 4.22(a). Moreover, the locations of the transducers change during the periods of transmission and reception resulting in a temporal Doppler shift of the transmitted signal and received echoes [Hawkins and Gough 2004]. Similar effects occur for scattering objects that are not stationary.

For a slow-moving sonar, the stop-and-hop approximation can be employed. That is, the sonar is assumed stationary during the transmission of the signal and reception

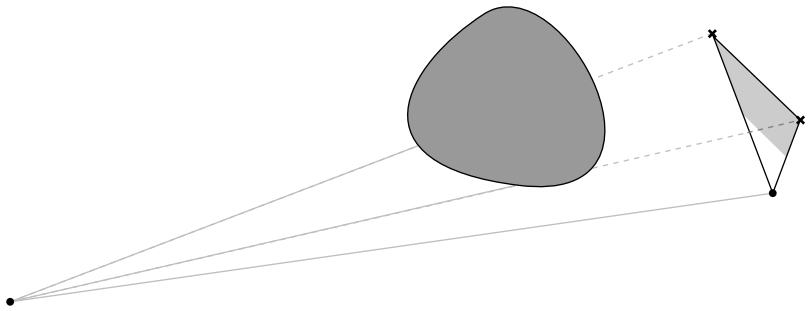

(a) first iteration

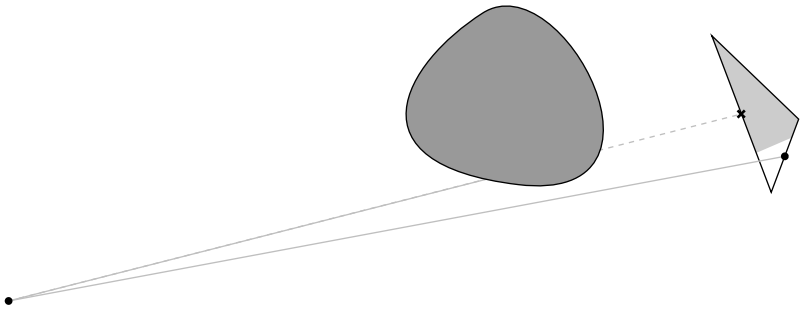

(b) second iteration

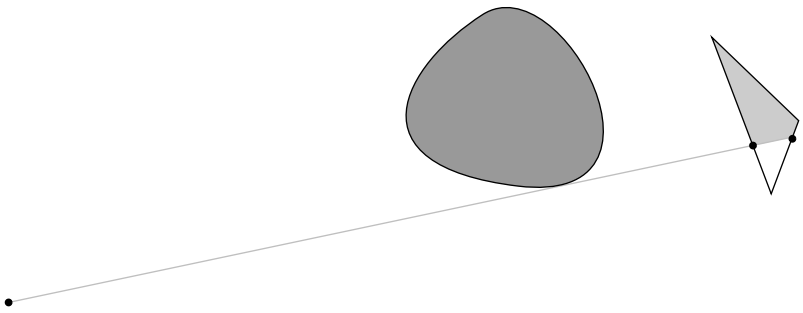

(c) n^{th} iteration

Figure 4.19 A first-order approximation to the shadow boundary can be determined using an iterative ray-tracing technique.

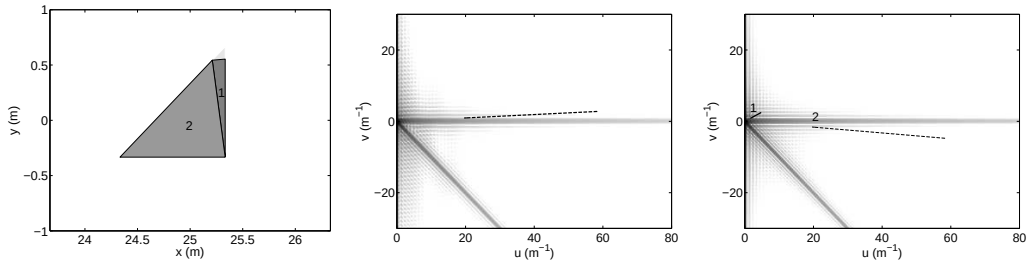

(a) $y_p = -1.28\,\mathrm{m}$ (b) (c)

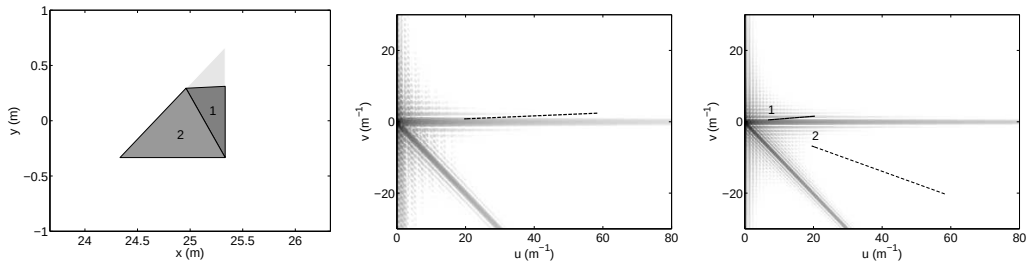

(d) $y_p = -0.97\,\mathrm{m}$ (e) (f)

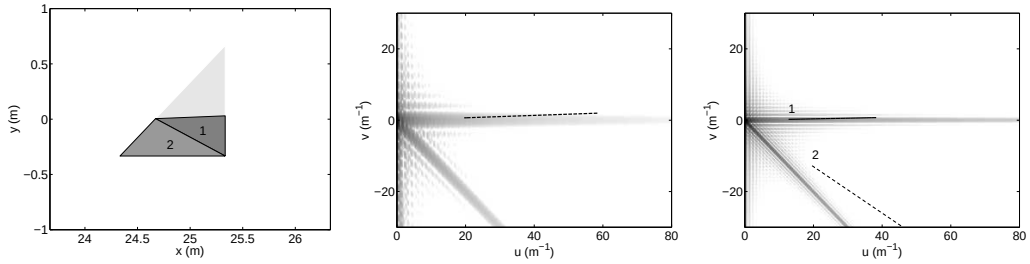

(g) $y_p = -0.66\,\mathrm{m}$ (h) (i)

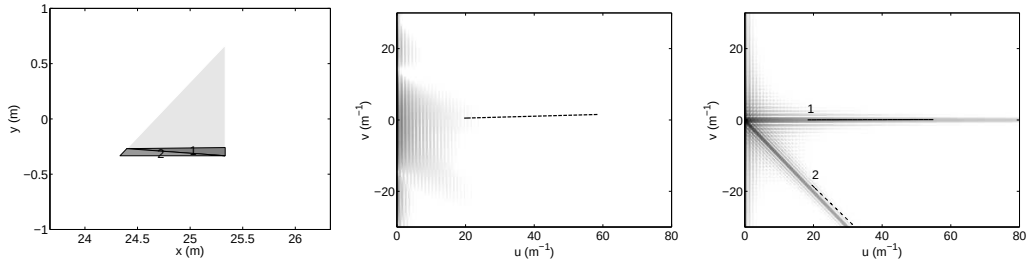

(j) $y_p = -0.34\,\mathrm{m}$ (k) (l)

Figure 4.20 The effective shape of a facet changes as it becomes occluded. For a linear shadow the effective shape is a parallelogram or a triangle and the effective facet can be decomposed into one or two triangles. Figures (a),(d),(g), and (j) show the effective facet shape and its decomposition into triangles as the facet becomes occluded. Figures (b),(e),(h), and (k) show the Fourier transform of the effective aperture, where the dotted line indicates the interpolated spatial frequencies. Alternatively the interpolations can be performed using the Fourier transform of the unit right-angle triangle and the appropriate warping as shown in Figures (c),(f),(i), and (l).

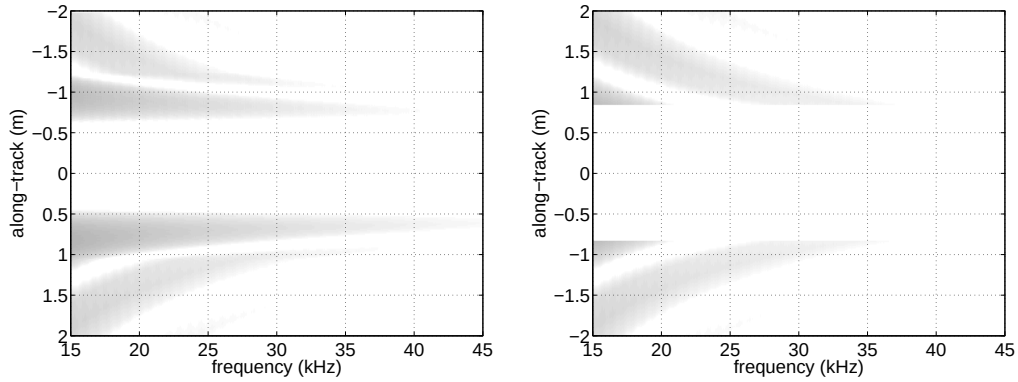

(a) first-order occlusion (b) binary shadow mask

Figure 4.21 The beampattern of a partially occluded facet is determined by evaluation of the Fourier transform of the effective aperture function. This is shown in Figure (a). A naive approach employs a simple binary shadow mask as shown in Figure (b); this introduces artefacts in the simulated data due to the sharp discontinuity.

of the echoes; its location is constant for each ping. It then instantaneously moves to the location of the next ping. This is illustrated in Figure 4.22(b). The stop-and-hop approximation ignores the change in the sonar location between transmission and reception and it ignores temporal Doppler effects. Neglecting these effects in the SAS reconstruction results in image corruption. Geometric distortion is introduced due to the different transmit and receive locations [Callow 2003], and the imagery is de-focused due to the Doppler effects [Hawkins and Gough 2004].

The simulator does not employ the stop-and-hop approximation. Geometric effects are incorporated using ray-tracing, which is described in Section 4.4, and temporal Doppler effects are modelled using the Fourier warping theorem.

Consider a transmitted band-limited signal,

$$s\left(t\right) = \tilde{s}\left(t\right) \exp\left(-j2\pi f_c t\right), \tag{4.54}$$

with a Fourier transform,

$$S\left(f\right) = \tilde{S}\left(f - f_c\right), \tag{4.55}$$

where f_c is the centre frequency and $s\left(t\right)$ has a bandwidth $B < 2f_c$. Temporal Doppler causes a compression or dilation of the received signal, i.e.,

$$\begin{aligned} s_d\left(t\right) &= \sqrt{\eta}\; s\left(\eta t\right) & (4.56)\\ &= \sqrt{\eta}\; \tilde{s}\left(\eta t\right) \exp\left(-j2\pi\; \eta f_c t\right), & (4.57) \end{aligned}$$

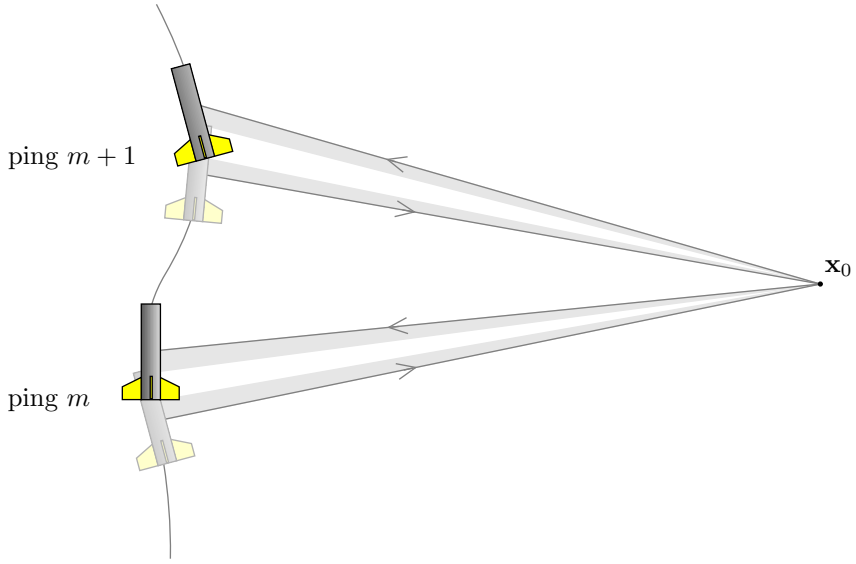

(a) continuously moving sonar

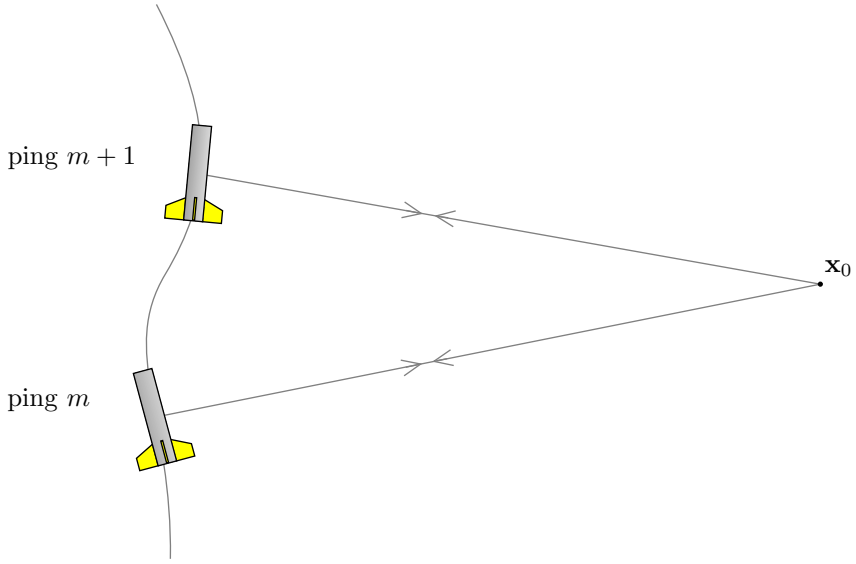

(b) stop-and-hop approximation

Figure 4.22 The sonar moves during the periods of transmission and reception, and during the period that the signal is traveling to and from the scatterer. This is illustrated in Figure (a), where the arrows indicate the paths of the signal at the beginning of transmission and at the end of reception. The grey regions indicate the signal paths during transmission and reception. For a slow-moving sonar, the stop-and-hop approximation can be employed. The sonar is assumed stationary for each ping and then moves instantaneously to the location of the next ping. This is illustrated in Figure (b).

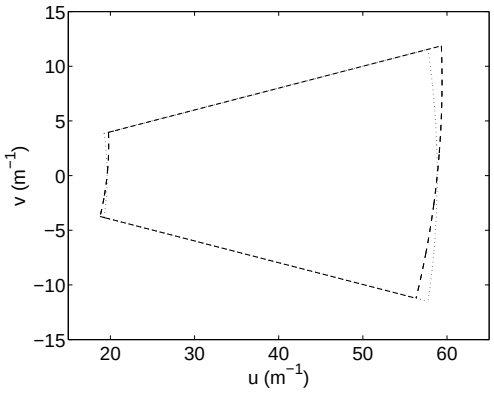

Figure 4.23 Movement of the imaging platform induces Doppler effects. This results in an apparent change in temporal frequency and causes a warping of the interpolated spatial frequencies. The dotted and dashed lines indicate the region of interpolated values with and without Doppler effects respectively.

or in the temporal frequency domain,

$$S_d(f) = \frac{1}{\sqrt{\eta}}\,\tilde{S}\left(\frac{1}{\eta}\left(f - \eta f_c\right)\right). \tag{4.58}$$

The signal spectrum is compressed by $1/\eta$ and shifted by $(\eta - 1)\, f_c$. The Doppler scaling factor, η, is given by

$$\eta = \eta_1 \eta_2, \tag{4.59}$$

where

$$\eta_1 = 1 + v_p/c, \tag{4.60}$$

$$\eta_2 = \frac{1}{1 - v_h/c}, \tag{4.61}$$

and v_p and v_h are the projections of the projector and hydrophone velocities onto the axis between the transducer and the target [Hawkins and Gough 2004].

The signal reaching the target is compressed/dilated by η_1. Thus, the interpolation of the Fourier transform must be scaled and shifted using this factor, i.e.,

$$A_d\left(\frac{f}{c}\mathbf{q}_x\right) = A\left(\frac{f_{d1}}{c}\mathbf{q}_x\right), \tag{4.62}$$

where

$$f_{d1} = \frac{1}{\eta_1}\left(f - (\eta_1 - 1)\, f_c\right) \tag{4.63}$$

are the warped frequencies for the outgoing Doppler effect. This is illustrated in Figure 4.23. A similar effect occurs at each transducer using f_{d1} for the projector and

$$f_d = \frac{1}{\eta}\left(f - (\eta - 1)\, f_c\right) \tag{4.64}$$

for the hydrophone. Therefore, the received echo signal is given by

$$E\left(y_p, f\right) = \frac{1}{\sqrt{\eta}} S\left(f_d\right) B_p\left(\hat{\mathbf{n}}_i, f_{d1}\right) B_h\left(\hat{\mathbf{n}}_s, f_d\right) B\left(\hat{\mathbf{n}}_i, \hat{\mathbf{n}}_s, f_{d1}\right), \tag{4.65}$$

where B_p and B_h are the projector and hydrophone beampatterns, and B is the facet beampattern.

4.4 RAY-TRACING

The simulator uses the ray-tracing technique to determine the distance to each of the primitives, to resolve occlusions, and to model multiple-scattering between primitives. Ray theory is a high-frequency approximation for wave propagation, which is detailed in Section 2.4.3. Here, the practical implementation of an acoustic ray-tracer is considered.

Ray-tracing is well-established for the generation of synthetic non-coherent visible light imagery, commonly referred to as computer graphics or CG [Foley *et al.* 1997], where the high-frequency approximation is well satisfied. Ray-tracing has been applied to acoustic and electromagnetic wave propagation [Jensen *et al.* 1993, Rohan 1991]. However, the region of validity is limited since the diffraction of low-frequency waves around the edges of objects is neglected. While diffraction can be approximated using the geometrical theory of diffraction [Hansen 1981], here the operating frequencies are considered high enough that diffraction can be ignored. This assumption is not necessarily valid and should be investigated in future work.

In CG, the electromagnetic rays are assumed linear since the electromagnetic properties of the medium, which is typically air, do not vary significantly with space or time. However for acoustic waves in the underwater environment, it is common for the rays to bend due to the variable sound speed profile as discussed in Section 2.4.1. The ray bending is significant over large distances but for small distances, such as those considered in the shallow water environment, the rays can be assumed linear.

4.4.1 Occlusions

Rays are traced from the projector, to the scatterers, and back to each hydrophone as shown in Figure 4.24. The visibility of the scatterers are determined by calculating the intersection of the rays with the opaque objects, i.e., the other scatterers. The scatterer is considered occluded if the rays are intersected and it is removed from the scattered field calculation. In the case of a facet scatterer, which can be partially occluded, the rays are traced to determine the effective facet shape as described in Section 4.3.4.

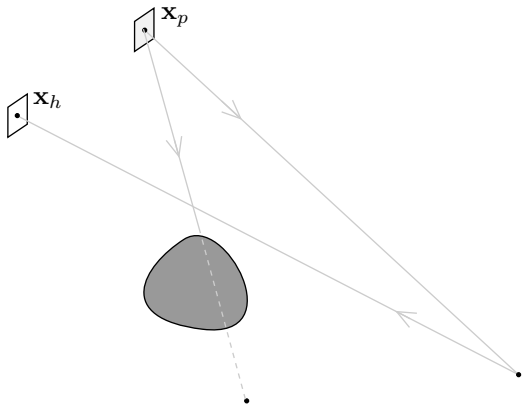

Figure 4.24 Rays are traced from the projector, to the scatterers, and back to each hydrophone. The visibility of the scatterers are determined by calculating the intersection of the rays with the opaque objects.

Semi-opaque targets are considered opaque for the occlusion determination, and the transmitted field is modelled by multiple-scattering, which is covered in Section 4.4.2.

4.4.2 Multiple scattering

A recursive ray-tracing technique is employed to model the higher orders of scattering [Foley *et al.* 1997]. After the first-order scattering has been resolved, the second-order scattering is determined. Rays are traced from each visible scatterer, as if it were a projector, to the other scatterers in the scene. Rays are then traced from the scatterers that are visible to the secondary scattering source back to each of the hydrophones. This is illustrated in Figure 4.25. The third and higher order scattering is resolved in a similar manner. Recursive ray-tracing has a high computational cost with order N^M calculations required for a scene of N scatterers and for M orders of multiple scattering.

Multiple scattering can play an important role in the formation of sonar imagery. It is particularly important in the shallow water environment where multipath scattering from the sea surface is a significant problem [Hayes 2004]. The method of images [Kinsler *et al.* 2000] can be used to model multipath from a smooth sea surface. However, the recursive ray-tracing technique must be employed when the sea surface is rough since the facets comprising the surface are in a non-planar geometry (and time-varying). The seafloor can also give rise to multipath interactions, as well as multiple scattering within complicated targets. Sea surface and sea floor multipath scattering are illustrated in Figures 4.26 and 4.27.

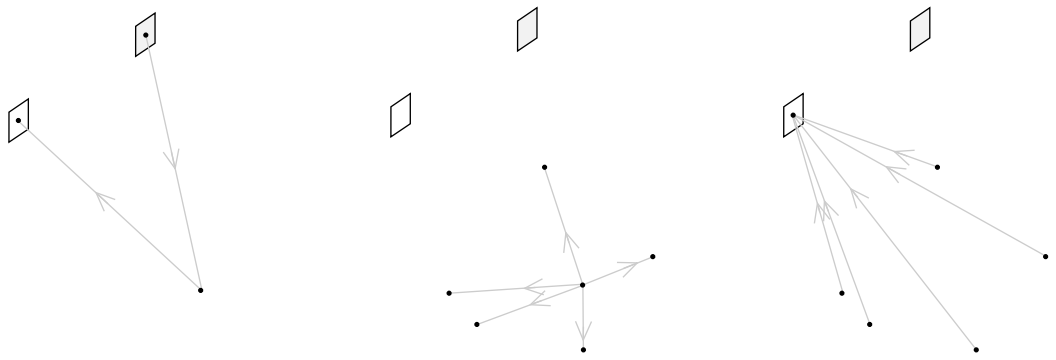

(a) first-order propagation and scattering

(b) second-order propagation

(c) second-order scattering

Figure 4.25 For second-order scattering, rays are traced from each visible scatterer to the other scatterers and then back to each of the hydrophones.

4.4.3 Ray-sphere intersection

The simplest ray intersection test is for a sphere. Consider a ray originating from the point $\mathbf{x}_p$, in the direction of a point $\mathbf{x}_k$. The ray is defined by the equation

$$\mathbf{r}(t) = \mathbf{x}_p + \hat{\mathbf{n}}_i t, \quad t \geq 0, \tag{4.66}$$

where

$$\hat{\mathbf{n}}_i = \frac{\mathbf{x}_k - \mathbf{x}_p}{|\mathbf{x}_k - \mathbf{x}_p|} \tag{4.67}$$

is the direction of propagation and t is an arbitrary variable. The sphere is defined by the equation

$$|\mathbf{x} - \mathbf{x}_0|^2 = a^2, \tag{4.68}$$

where a is the radius and $\mathbf{x}_0$ is the centre of the sphere. The intersection of the ray and the sphere is found by solving the simultaneous equations (4.66) and (4.68). This results in a quadratic equation,

$$At^2 + Bt + C = 0, \tag{4.69}$$

where

$$A = |\hat{\mathbf{n}}_i|^2 \tag{4.70}$$

$$B = 2(\mathbf{x}_p - \mathbf{x}_0) \cdot \hat{\mathbf{n}}_i \tag{4.71}$$

$$C = |\mathbf{x}_p - \mathbf{x}_0|^2 - a^2, \tag{4.72}$$

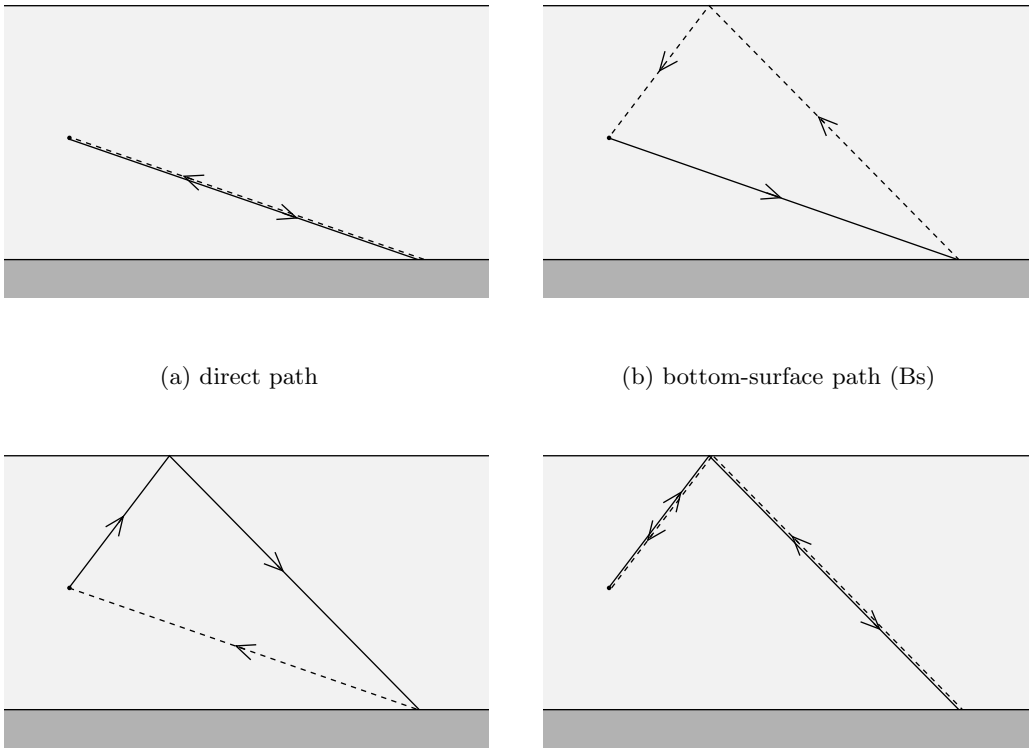

(a) direct path

(b) bottom-surface path (Bs)

(c) surface-bottom path (sB)

(d) surface-bottom-surface path (sBs)

Figure 4.26 The close proximity of the sea surface in shallow water results in significant multipath scattering. The first few modes of sea surface multipath are illustrated here. Specular sea surface scattering (denoted by the lower-case s) and diffuse sea floor, or bottom, scattering (denoted by the upper-case B) are considered [Pinto *et al.* 2004].

which can be solved using the quadratic formula,

$$t = \frac{-B \pm \sqrt{B^2 - 4AC}}{2A}. \tag{4.73}$$

The ray intersects the sphere when t is real and greater than zero and the point of intersection can be found by substituting (4.73) into (4.66).

4.4.4 Ray-polygon intersection

The simulator uses a facet decomposition of the objects in the scene. Therefore, the ray-polygon intersection test is the most important. First, the ray is tested for intersection with the plane containing the facet. Then, if the ray intersects the plane, the point of intersection is determined to be inside or outside the polygon; this is referred to as a point-in-polygon test.

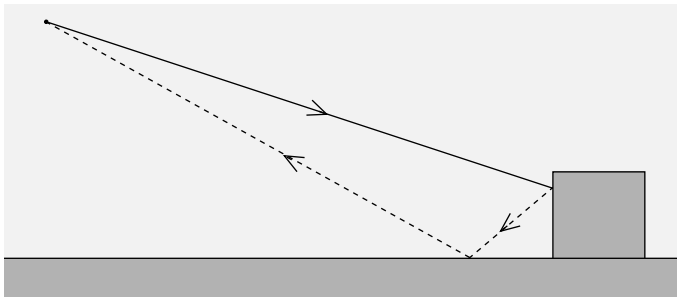

Figure 4.27 A proud object can give rise to multipath scattering from the seafloor.

The plane is defined by the equation

$$\hat{\mathbf{n}}_k \cdot (\mathbf{x} - \mathbf{x}_0) = 0, \tag{4.74}$$

where $\hat{\mathbf{n}}_k$ is the normal and $\mathbf{x}_0$ is a point in the plane, e.g., a vertex of the polygon. The point of intersection is determined by solving the simultaneous equations (4.66) and (4.74). This results in the equation

$$t = \frac{\hat{\mathbf{n}}_k \cdot (\mathbf{x}_0 - \mathbf{x}_p)}{\hat{\mathbf{n}}_i \cdot \hat{\mathbf{n}}_k}. \tag{4.75}$$

The ray intersects the plane when t is finite and greater than or equal to zero and the point of intersection can be found by substituting (4.75) into (4.66).

To determine if the point of intersection is inside the polygon, a ray is traced from the point along the plane. If the ray crosses a polygon edge an odd number of times then the point of intersection is inside the polygon, if the ray does not cross any edges or it crosses an even number of edges then it is outside. This is illustrated in Figure 4.28.

4.4.5 Bounding volumes

Facets or collections of facets can be enclosed in a bounding volume. The bounding volume approximates the region of space occupied by the facets and it is chosen such that intersection tests with the bounding surface are simple. Intersection tests with the facets contained within the bounding volume are only performed if the bounding surface is intersected. This greatly reduces the computational requirements for ray-tracing. Possible bounding volumes include boxes, cylinders, spheres, ellipsoids, and discrete oriented polytopes (DOPs) [Foley *et al.* 1997].

In the simulator, each object and each facet comprising the object is enclosed within a bounding sphere. If an object's bounding sphere is intersected, then intersection tests are performed for each of the bounding spheres for the facets. For each of these that is intersected, a full polygon intersection test is performed. A hierarchy of bounding

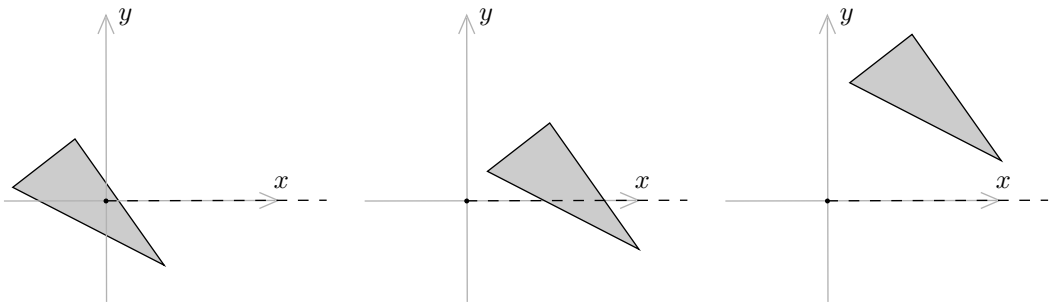

(a) odd number of crossings (b) even number of crossings (c) no crossings

Figure 4.28 A point-in-polygon test is used to determine if the point of intersection with the ray and the plane is inside the polygon. The polygon is rotated to the x–y plane and shifted so that the point of intersection is at the origin. A line is traced outward from the origin (in any direction). The point of intersection is inside the polygon if the line crosses an even number of polygon edges. Otherwise it is outside the polygon.

volumes can be employed to further reduce the ray intersection computations [Foley *et al.* 1997].

The bounding sphere for an object can be found using Welzl's algorithm [Welzl 1991]. The algorithm is used to find the minimal bounding (hyper) sphere for an arbitrary collection of points in an arbitrary number of dimensions. Here Welzl's algorithm is used to find the minimal bounding sphere for the vertices of a 3-D object. The bounding sphere for a triangular facet can be found by using Welzl's algorithm or, more efficiently, using a simplified form of the Elzinga-Hearn algorithm [Elzinga and Hearn 1972]. For an obtuse or right-angle triangle, the centre of the sphere is at the middle of the longest edge and the radius is half the length of the longest edge. For an acute triangle, the centre of the sphere is at the intersection of the internal angle bisectors. This is shown in Figure 4.29.

4.5 KIWI SAS SIMULATOR

The multiple-receiver InSAS simulator, referred to as the Kiwi SAS Simulator, has been implemented in the Python [van Rossum 2003] and C [Kernighan and Ritchie 1988] programming languages. Python is a high-level scripting language. It is used in the simulator to interface the various low-level C modules that implement the computationally expensive code, i.e., the Fourier transforms (FFT), interpolation, and ray-tracing. The FFT and array manipulation code is implemented in the Numeric/Numarray Python package [Ascher *et al.* 2001, Greenfield *et al.* 2004], while the interpolation and ray-tracing code was developed specifically for the simulator.

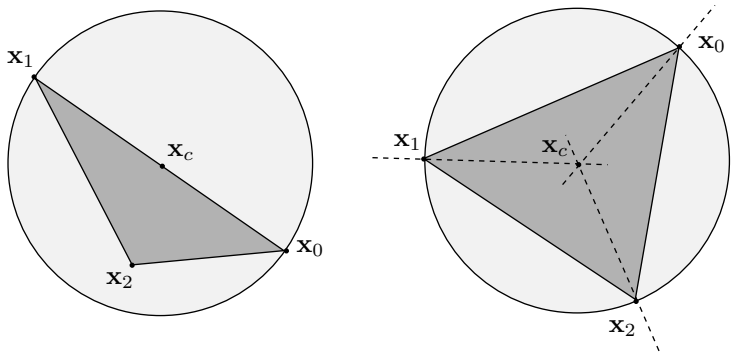

(a) obtuse triangle (b) acute triangle

Figure 4.29 For an obtuse or right-angle triangle, the minimal bounding sphere is centred at the middle of the longest edge. For an acute triangle, it is centred at the intersection of the internal angle bisectors.

The specifications for each simulation are defined in a configuration file that is parsed using the Zope ZConfig format [Latteier *et al.* 2005]. ZConfig is an XML (Extensible Markup Language) [Bray *et al.* 2004] based application configuration package for Python, which supports hierarchical schema. The configuration file specifies the simulation parameters including the sound speed profile, the sonar specifications, the sonar trajectory, and the objects in the scene.

Each object is characterised by a vertex array that defines the facets, its acoustic properties (density and sound speed), and its roughness statistics. The vertex arrays are specified in VRML (Virtual Reality Modelling/Markup Language). VRML is a file format similar to XML for specifying 3-D objects [Carey *et al.* 1997]. The vertex arrays are tessellated until the Rayleigh criterion (2.60) is met. Each facet is then processed using the methods described in this chapter. Figure 4.30 shows the data flow diagram for the simulator code.

4.5.1 Parallel implementation

On order of 10,000 to 1 million facets are required for a typical simulated scene. While the processing time for each facet is small, the total simulation time can be on the order of days for this number of facets. This is compounded severely when multiple scattering is introduced. To alleviate this, the simulator has been implemented for parallel operation on a computing cluster.

The Local Area Multiprocessor (LAM) implementation [Burns *et al.* 1994, Squyres and Lumsdaine 2003] of the Message Passing Interface (MPI) standard [Otto 1995, Huss-Lederman 1997] was employed for the parallel processing. The configuration file is sent from the local computer to a master node in the computing cluster (this could be

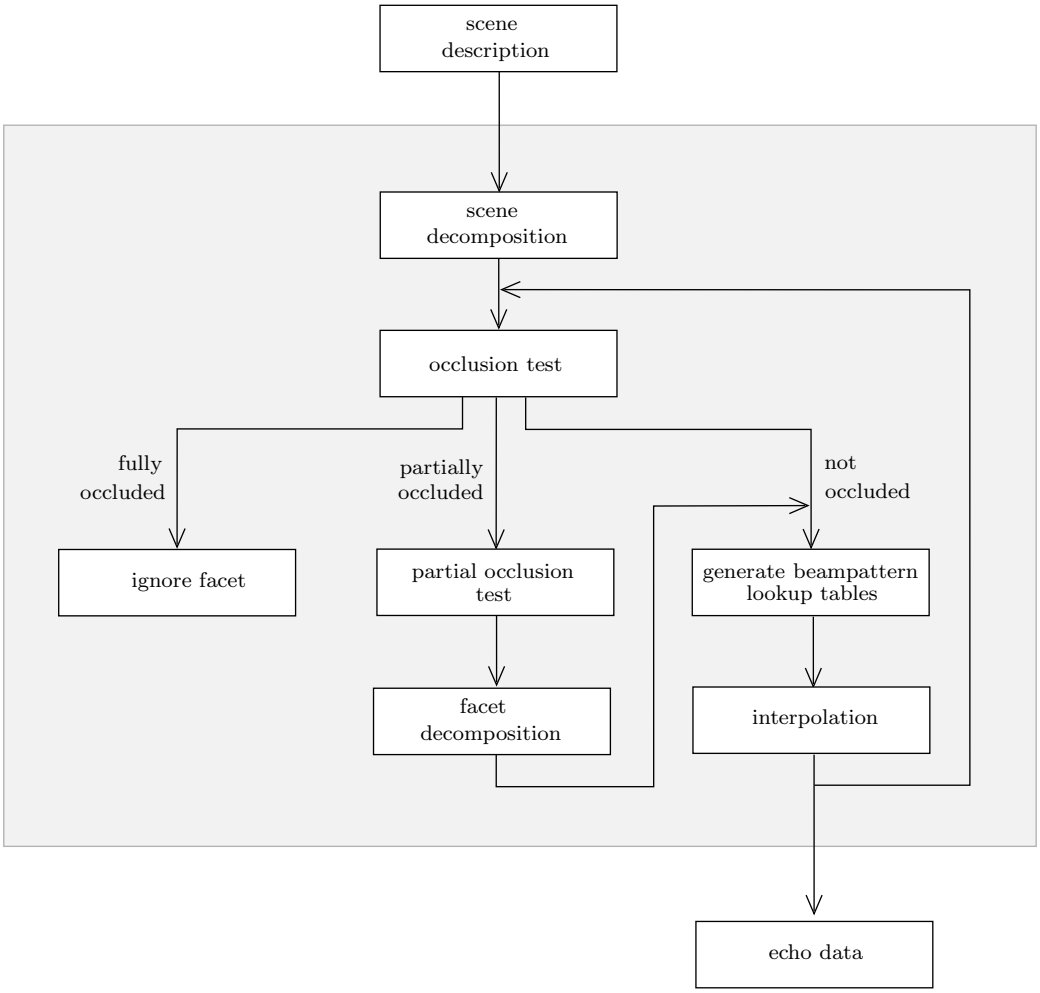

Figure 4.30 Data flow diagram for the simulator code.

the the same computer). The master node processes the configuration file and initiates the simulation. Packets of facets are then sent by the master node to the slave nodes in the cluster for processing; these communications are handled transparently via the LAM API (Application Programming Interface) as shown in Figure 4.31. Once a slave has processed the packet, the simulated data is sent back to the master (via the LAM API) where it is combined with the results from the other slaves. This cycle repeats until all of the facets have been processed.

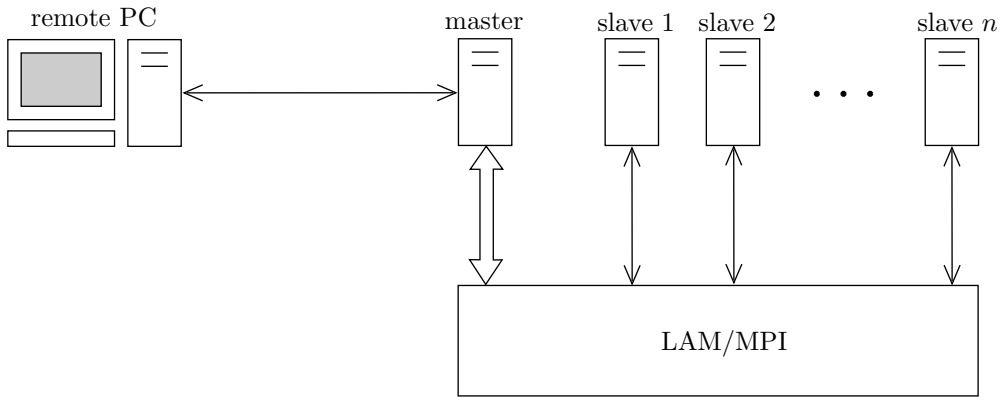

Figure 4.31 Topography of the parallel implementation of the simulator.

Chapter 5

RESULTS FROM SIMULATED DATA

Some example simulations are presented in this chapter to illustrate the performance of the simulator. The simulated data is then used to demonstrate some important aspects of SAS, including the advantages of SAS over conventional sidescan sonar and the current research problems.

The specifications of the simulated SAS platform, the KiwiSAS IV, are given in Section 5.1. Then, two example scenes are simulated. The first scene is typical of a sea-trial and consists of two mine-like objects on an undulating seafloor. The second scene, a plane wreck, is more elaborate and demonstrates the flexibility of the simulator for modelling arbitrary scenes. In Section 5.5, simulated data is compared with real data collected on a sea-trial in Lyttelton Harbour. Finally, the computational performance of the simulator is assessed in Section 5.6.

5.1 KIWISAS IV SPECIFICATIONS

The simulator is demonstrated using the specifications of the SAS platform designed, built, and operated by the Acoustics Research Group at the University of Canterbury – the KiwiSAS IV [Barclay *et al.* 2006]. The KiwiSAS IV differs from the previous models [Hayes 1989, Hawkins 1996, Hayes *et al.* 2001] in its use of digital data acquisition and storage hardware inside the towfish [Hayes *et al.* 2002, Barclay *et al.* 2002]; the previous sonars sent the analogue data via the tow-cable to the boat where the digital data acquisition and storage was performed. The KiwiSAS III was the first model capable of interferometric processing by use of a 3-element vertical hydrophone array. The KiwiSAS IV has provision for up to 18 hydrophones and independent operation of 12 projector elements, where previously all projector elements were driven using the same signal.

The KiwiSAS is a neutrally buoyant, nose-towed sonar. It has a blunt-nose design (for stability) with rear stabilising fins as shown in Figure 4.1. The towfish is weighed down by a depressor weight on the tow cable near the nose of the towfish and the altitude above the seafloor is controlled by the tow speed.

transducer	**dimensions** (m)		**position** (m)			**declination**
	y	z	x	y	z	(deg)
projector	0.336	0.0840	0.0950	-0.1930	-0.0250	12
hydrophone 1	0.0774	0.0774	0.0140	-0.7754	-0.2346	0
hydrophone 2				-0.6980	-0.2346	
hydrophone 3				-0.6206	-0.2346	
hydrophone 4				-0.7754	-0.3120	
hydrophone 5				-0.6980	-0.3120	
hydrophone 6	⋮	⋮	⋮	-0.6206	-0.3120	⋮
hydrophone 7				-0.7754	-0.3894	
hydrophone 8				-0.6980	-0.3894	
hydrophone 9				-0.6206	-0.3894	
top array	0.2322	0.0774	0.0140	-0.6980	-0.2346	0
middle array					-0.3120	
bottom array	⋮	⋮	⋮	⋮	-0.3894	⋮

Table 5.1 The KiwiSAS-IV has a single projector and a 3×3 hydrophone array. The rows of the hydrophone array are typically combined into a vertical array of 3 receivers for interferometry.

A single projector is located on the starboard side of the towfish midway between the nose and tail. It is tilted down by 12 deg in an effort to reduce multipath reflections from the sea-surface. The projector is composed of 12 independently driven Tonpilz elements [Hawkins and Gough 1995a]. This allows for beam shaping and beam steering [Hayes 2002], e.g., for spotlight mode operation [Carrera *et al.* 1995, Jakowatz *et al.* 1996], which will be considered in future research. A starboard-facing 3×3 hydrophone array is located at the stern, below the towfish body. The hydrophones are constructed from the piezoelectric material – PVDF (polyvinylidene fluoride). This array utilises 9 of the 18 available receiver channels. The remaining 9 channels will be utilised in future research for improved mapping rates using either a linear along-track array, or a port-side array. The dimensions and locations of the transducers are given in Table 5.1.

The KiwiSAS transmits a pulsed signal at regular time intervals. An arbitrary waveform can be transmitted, e.g., a hyperbolic chirp or a pseudo-random noise sequence [Cook and Bernfeld 1967]. However, a linear FM chirp is usually employed. Two linear FM chirp signals are transmitted simultaneously, utilising the two resonant regions of the projector frequency response [Hawkins 1996]. The two chirp signals have centre frequencies of 30 kHz and 100 kHz, each with a 20 kHz bandwidth. The signal specifications are given in Table 5.2.

5.1.1 Navigation systems

The towfish navigation data is recorded by two independent systems. The first is an inertial navigation system (INS) within the towfish. The INS for the KiwiSAS-III

centre frequency,	f_c	(kHz)	30	100
bandwidth,	B	(kHz)	20	
wavelength,	λ	(cm)	3.75–7.5	1.36–1.67
pulse length,	t_c	(ms)	12.5	
sampling frequency,	f_s	(kHz)	30	
signal resolution,			16 bit	
ping rate,	f_p	(Hz)	15	

Table 5.2 The KiwiSAS-IV transmits two simultaneous chirp signals – one at 30 kHz and another at 100 kHz.

consisted of 3 accelerometers and 3 magnetometers in a perpendicular configuration [Pilbrow *et al.* 2002]; the orientation of the towfish is determined from the apparent change in the Earth's gravitational and magnetic field as detected by the 6 sensors. This approach is quite crude and it ignores the coupling of translational motion, which affects the accelerometers. The INS for the KiwiSAS-IV includes an additional 3 gyroscopes that will provide a better estimate of the towfish orientation.

The second navigation system employs a number of active beacons that are deployed prior to each experiment [Pilbrow 2007]. The beacons are deployed on the seafloor in a long baseline configuration. The beacons respond to each sonar ping with a 70 kHz chirp, which is then detected by the sonar. The benefit of this system is twofold: 1) The time-of-flight information for each beacon ping can be used to triangulate the position of the sonar – this requires at least three beacons in a non-colinear arrangement. 2) The beacons act as very good point sources, providing imagery of the points that is relatively free from reverberation. This is particularly useful for autofocus.

At the time of this thesis, neither navigation system was completely operational and navigation data was unavailable. In future work, a Kalman filter [Kalman 1960, Brown and Hwang 1997] will be employed to combine the data from the 9 INS sensors, a pressure sensor (for determining the depth), and the beacons to provide a much improved estimate of the towfish position and orientation.

5.2 SIMULATED SAS IMAGERY OF A TYPICAL SCENE

The first simulated scene is typical of an actual sea-trial where individual targets are deployed on a relatively featureless sea floor. The scene has been constructed to resemble actual SAS imagery of a spherical target and a cylindrical target from a 1999 rail-mounted experiment by QINETIQ [Banks 2002]. The simulated scene consists of a sphere-like target[1] of approximately 1.5 m diameter and a 3 m long cylindrical target of 1 m diameter. The two targets are resting on the seafloor, which is 5 m below the sonar.

[1]The *Utah* or *Newell teapot* is a popular 3-D reference object in the computer graphics community. It is a standard primitive in most modern 3-D modelling packages.

The sea floor is a fractal surface with 0.5 m peak-peak undulations and a correlation length of approximately 5 m. The spherical target is composed of 552 triangular facets, the cylindrical target is composed of 720 and the sea floor is composed of 38442. The scene is imaged along a linear trajectory at a speed of 1 m/s. The seafloor is composed of medium sand and the targets are air-filled (see Tables 2.1 and 2.2).

The simulated raw data and the SAS imagery of the scene are shown in Figure 5.1 and Figure 5.2 for the 30 kHz and 100 kHz bands respectively. The SAS imagery is reconstructed using a Matlab implementation of the wavenumber algorithm (see Section 1.3.3). The data is filtered in the spatial and temporal frequency domain using a Blackman window and the Stolt mapping is performed using a 4× sinc interpolation followed by linear interpolation.

5.2.1 Shadows cast by proud objects

A feature that is of great interest in SAS imagery (or any high-resolution sonar imagery) are the shadow regions. Objects that are proud of the sea floor prevent the incident acoustic energy from reaching the region of seafloor behind the object, thus, casting a shadow. This is particularly true for the sidescan imaging geometry in shallow water where the imaging angle is very shallow. The shadow cast by a proud object is often more obvious than the object itself and the shape of the shadow can be used to assist with target classification [Bell *et al.* 2004].

Two proud objects are present in the scene. These cast significant shadows in the SAS imagery. The shadows give an indication of the object profiles and can be used to estimate the heights of the objects. It is important to note that the shadows in the 100 kHz imagery are sharper than those in the 30 kHz imagery. This is due to the wider beampatterns at the lower frequencies. A wider beampattern covers a larger area of sea floor at each along-track position. This allows the acoustic energy from subsequent pings to image inside the geometrical shadow region, resulting in a penumbra, or blurring of the shadow boundary. The penumbra is more prominent for a wider beampattern, i.e., at lower frequencies [Hunter and Hayes 2005a].

In practice the shadows are degraded by a number of factors. A dominant factor in shallow water is multipath scattering from the sea surface (see Section 4.4.2). The shadows are also degraded due to reconstruction artefacts caused by deviations from a linear trajectory, diffraction into the shadow region, and due to acoustic noise.

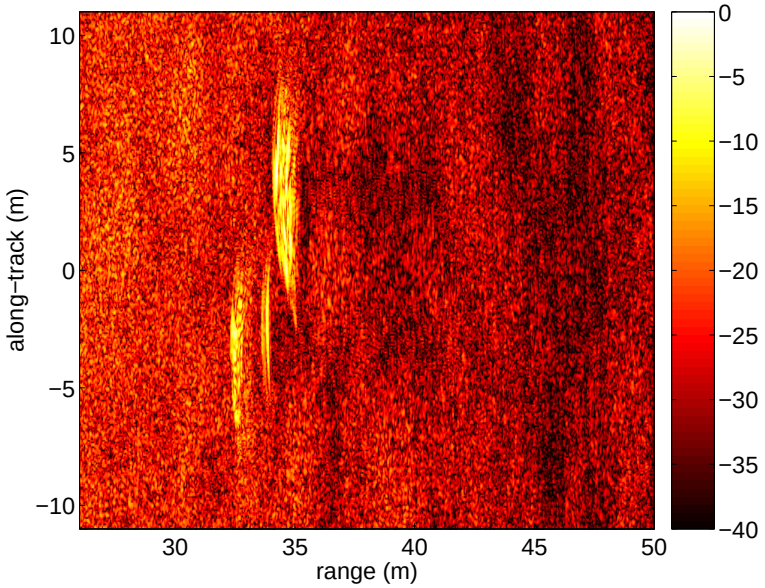

(a) pulse-compressed data (30 kHz)

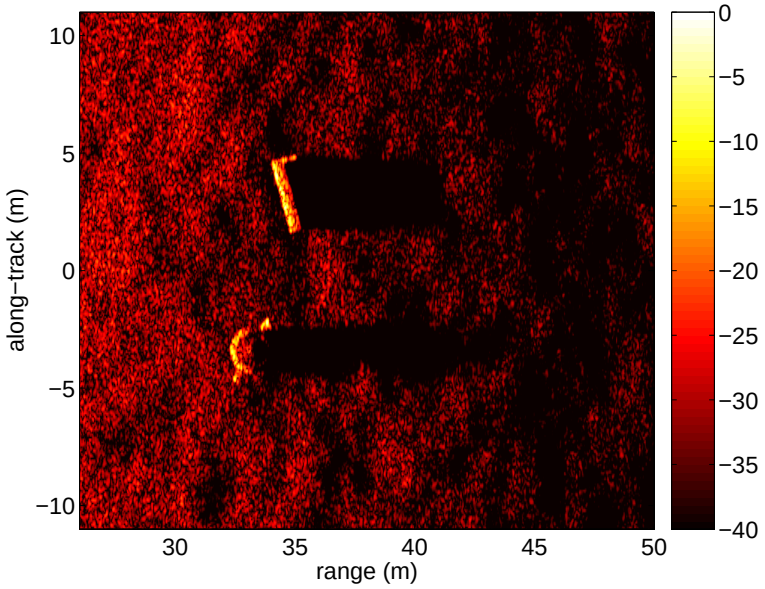

(b) SAS imagery (30 kHz)

Figure 5.1 30 kHz simulated SAS imagery of spherical and cylindrical targets on an undulating seafloor.

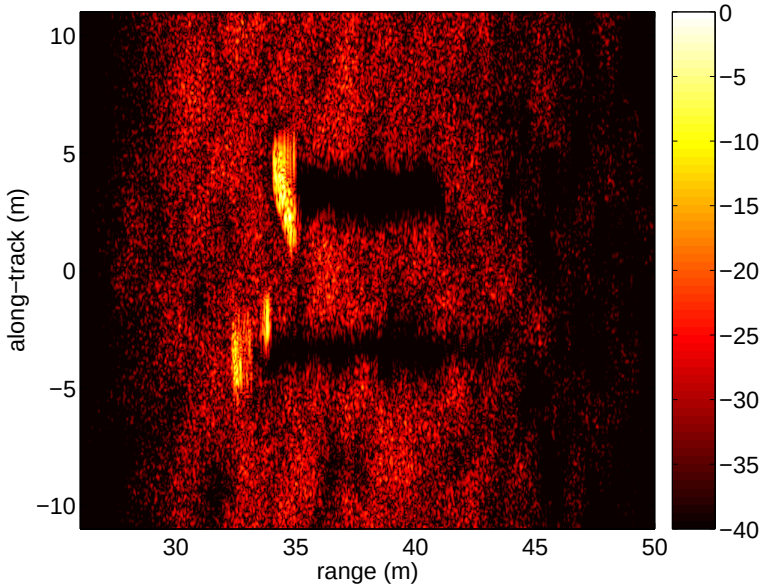

(a) pulse-compressed data (100 kHz)

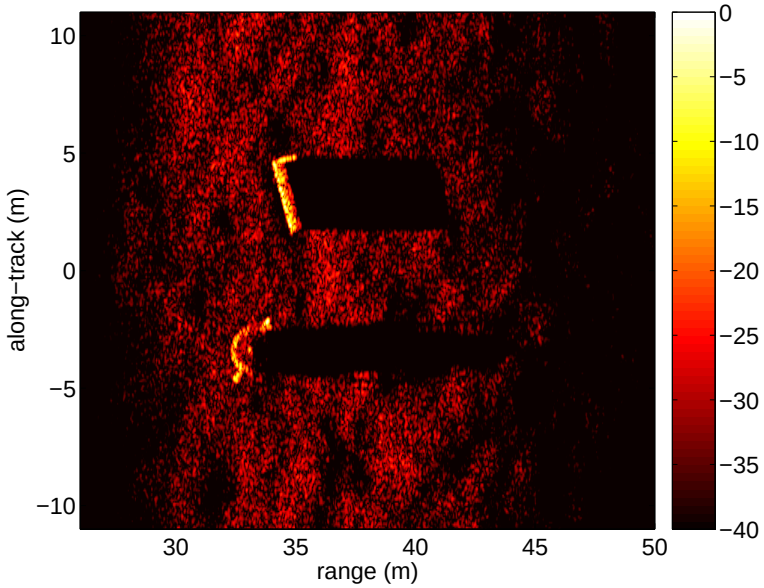

(b) SAS imagery (100 kHz)

Figure 5.2 100 kHz simulated SAS imagery of spherical and cylindrical targets on an undulating seafloor.

5.2.2 Aspect-dependence

A SAS differs from a conventional side-scan sonar in its use of coherent processing; this facilitates lower frequencies and/or a smaller physical aperture, which results in a wider physical beam. A conventional high-resolution sonar has a very narrow beam and objects are illuminated over a very narrow range of angles. In SAS, although the synthesised beam is narrow, the physical beam is typically wide and objects are illuminated over a range of angles.

The synthetic aperture processing algorithms assume that the scattering is aspect-independent, that is, the response from the scatterers is independent of angle. However, in general, this is not the case. In particular, points of specular reflection and shadow regions change with the angle of illumination.

To illustrate the aspect-dependence of the simulated imagery, synthetic sub-apertures are formed at different positions along the sonar trajectory. A smaller physical aperture is employed to obtain a wider beampattern and to accentuate the aspect-dependence. Consequently, a slower speed of 0.25 m/s is used to satisfy the sampling constraints. Formation of the sub-aperture imagery is described in Appendix B. The sub-aperture imagery is shown in Figure 5.3 for along-track positions of −8 m, 0 m, and +8 m. The shadow regions are shown to change as the path is traversed; upon combining the sub-aperture imagery to obtain the full-resolution SAS image, the aspect-dependent shadows will combine to produce a penumbra region that blurs the shadow boundaries [Hunter and Hayes 2005a].

5.3 SOURCES OF IMAGE CORRUPTION

The simulated data presented in Section 5.2 is ideal; it is free from many of the corrupting sources that are present in a real sea trial. These include unknown deviations from a linear trajectory, multipath scattering, scattering within the water column, e.g., from bubbles, fish, etc. and a large number of acoustic noise sources, e.g., biological noise, shipping noise, etc.

The ideal nature of simulated data is useful for the early development of SAS algorithms since the sources of data corruption can be ignored. However, often an algorithm performs well on simulated data but fails on real data. The inclusion or exclusion of the major sources of data corruption is important for these reasons. Two sources of image corruption are considered here: uncompensated deviations from a linear trajectory and multipath scattering from the sea surface.

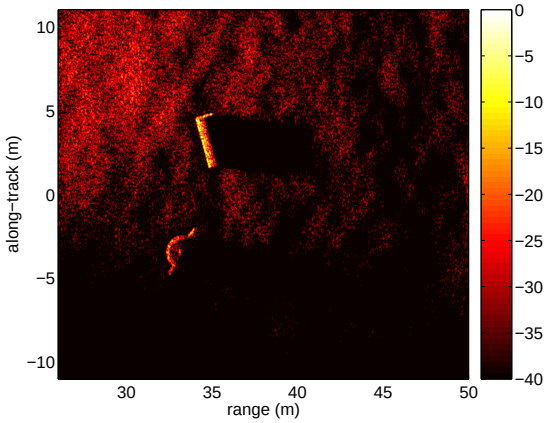

(a) trailing sub-aperture

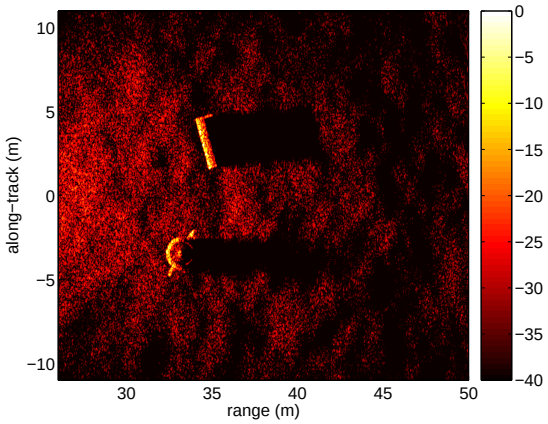

(b) broadside sub-aperture

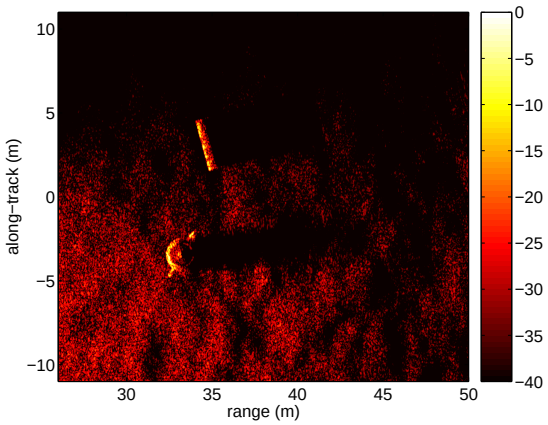

(c) leading sub-aperture

Figure 5.3 Aspect-dependent SAS imagery of the targets shows the migration of shadows as the synthetic aperture is traversed.

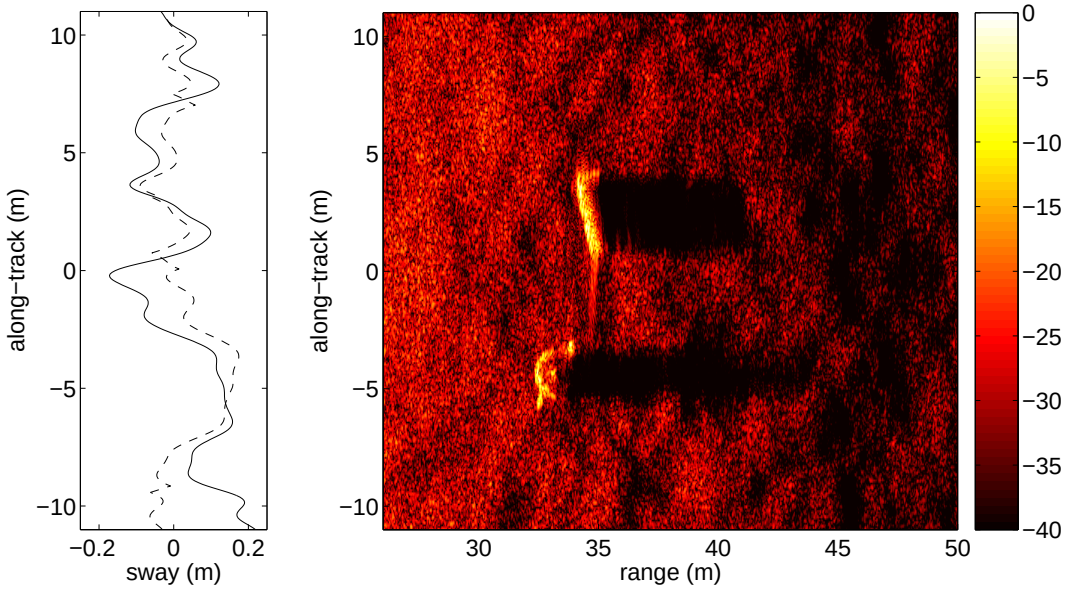

(a) sway path

(b) SAS imagery (30 kHz)

Figure 5.4 A Gaussian-distributed and Gaussian-correlated sway with a 10 cm RMS amplitude and a correlation length of 0.5 m is shown in (a) (the solid line). The sway is estimated using the shear average autofocus algorithm, giving an estimate of the sway (the dotted line). The residual uncompensated sway causes blurring and artefacts in the reconstructed SAS imagery in (b).

5.3.1 Deviations from a linear trajectory

Deviations from a linear trajectory are inevitable for a free-towed sonar. While the reconstruction algorithms can accommodate these deviations, often they are unknown or they are not measured with sufficient accuracy and autofocus or micro-navigation techniques must be employed. The deviations can be decomposed into six motions: sway, surge, heave, pitch, roll, and yaw. These correspond to the three translational and three rotational motions respectively. The six motions affect the imagery in different ways. Some affect the imagery more severely than others, for example, uncompensated sway causes image blurring, while roll causes errors in the bathymetric reconstruction. Typically a combination of the motions is present, for example, a *cork-screw* trajectory [Gough 2003].

To illustrate the effects of uncompensated deviations, the scene is simulated with random variations on the nominally linear sonar trajectory. An example sway is shown in Figure 5.4(a). The sway is Gaussian-distributed and Gaussian-correlated with a 10 cm RMS amplitude and a correlation length of 0.5 m. The shear average autofocus algorithm [Fienup 1989, Johnson *et al.* 1995] is employed to estimate the sway and the motion is compensated using a narrow-beam approximation [Callow 2003]. The estimated sway differs from the actual sway and the (uncompensated) residual error

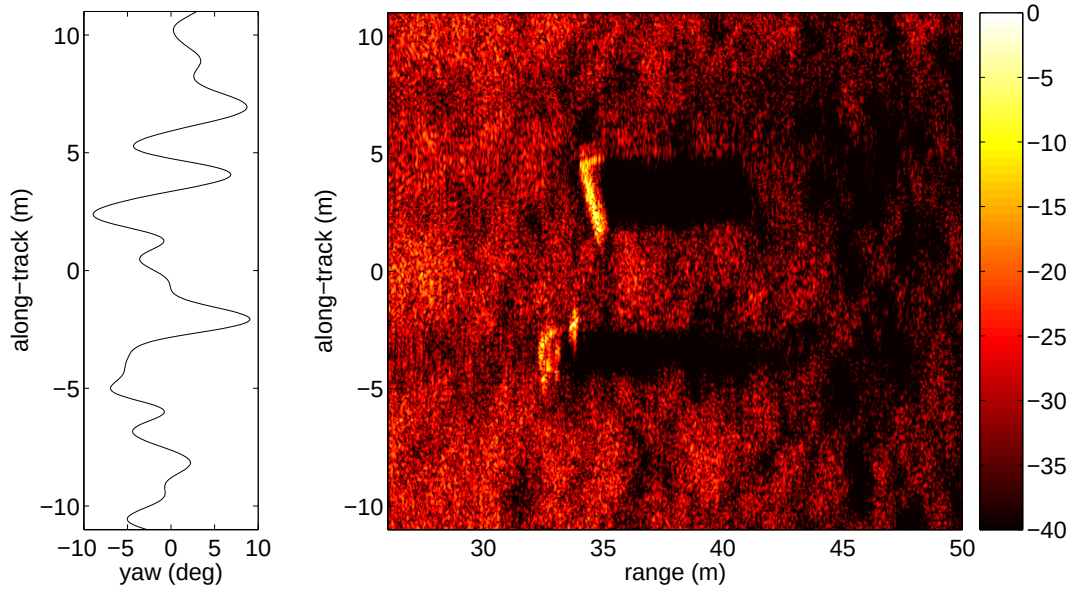

(a) yaw path

(b) SAS imagery (30 kHz)

Figure 5.5 A Gaussian-distributed and Gaussian-correlated yaw with a 4 deg RMS amplitude and a correlation length of 0.5 m is shown in (a). The yaw is difficult to estimate and correct and it causes blurring and artefacts in the reconstructed SAS imagery in (b).

results in corruption of the SAS imagery. The narrow-beam approximation introduces errors also. The resultant SAS imagery is shown in Figure 5.4(b). The uncompensated sway causes blurring of the imagery, which results in resolution loss and reconstruction artefacts.

An example yaw is shown in Figure 5.5(a). The yaw is Gaussian-distributed and Gaussian-correlated with a 4 deg RMS amplitude and a correlation length of 0.5 m. For a single along-track receiver, an arbitrarily yawed path is not easily estimated. Moreover, it is not easily compensated when it is known. The SAS imagery is reconstructed without any compensation as shown in Figure 5.5(b), which results in corruption of the SAS imagery.

5.3.2 Sea surface multipath

Multipath scattering from the sea surface is a problem for sonar imaging in shallow water. The close proximity of the sea surface results in significant multipath reflections that corrupt the echo data. Sea surface multipath scattering degrades SAS imagery and affects bathymetric processing [Hayes *et al.* 2006].

Sea surface multipath is illustrated here for a flat sea surface, corresponding to calm sea conditions, and a time-varying sea surface, corresponding to rough sea conditions.

The sea surface is 10 m above the sonar. The first three dominant multipath modes are simulated, that is, the bottom-surface, surface-bottom, and surface-bottom-surface paths, in addition to the direct path as illustrated in Figure 4.26. Figure 5.6 shows the effects of the multipath corruption on the simulated SAS imagery.

For the smooth sea surface, the multipath reflections manifest as delayed replica images in range[2]. For the rough sea surface the coherence of the multipath reflections is reduced and the delayed replicas are blurred due to the coherent SAS processing. The delayed replica images of the objects appear as extra objects in the imagery, particularly for multipath scattering from a smooth sea surface. The multipath reverberation reduces the overall contrast of the imagery.

5.4 SIMULATED INSAS IMAGERY OF A PLANE WRECK

A Stuka WWII bomber[3] is used as the target of interest in the second simulated scene. A VRML model of this aircraft, which is shown in Figure 5.7, was freely available. It is an interesting target and it illustrates the flexibility of the simulator for simulating arbitrary scenes. The Stuka is a useful target for studying bathymetric reconstruction algorithms due to its large extent, distinctive height variations, and complicated structure.

The Stuka is resting (partially buried) on the same undulating seafloor used in the first simulated scene. Although unlikely, it is assumed to be air-filled for lack of a model of the internal structure. The Stuka has a 15 m wingspan, a length of 11.5 m, and a height of 3.9 m. It is buried by approximately 0.5 m and orientated at 45 deg with respect to the sonar path. The VRML model is composed of 3995 triangular facets, which are tessellated to a maximum facet dimension of 0.2 m yielding 47512 facets.

A big advantage of using simulated data is the availability of the scene model used to generate the data. This can be used to validate the SAS algorithms. The ideal imagery of the scene can be obtained from the scene model and this can be compared with the SAS imagery. Figure 5.8 shows the ensemble imagery from a sidescan sonar with an infinitesimally narrow beam in the along-track direction, i.e., a vertical *fan* beam. This ideal imagery is obtained by ray-tracing within a vertical 2-D plane perpendicular to the sonar trajectory. The ensemble average is determined by assuming diffuse Lambertian scattering, i.e., a cosine beampattern for the scattered field. However, the

[2]The delayed images are not exact replicas since the vertical angle of incidence is different for each multipath mode.

[3]The Junkers JU 87, or "Stuka", was a notable German dive bomber in World War II. It is distinguished by its inverted gull wings and the notorious wail of its wind-powered siren. The siren would wail as the bomber dived in a form of psychological warfare to scare ground troops. More than six thousand Stukas were built during WWII, so it stands to reason that there are at least a few buried beneath the ocean due to its dive bombing tactic. However, it is doubtful that they would be in a preserved state similar to the model, particularly after more than 50 years of corrosion in the sea.

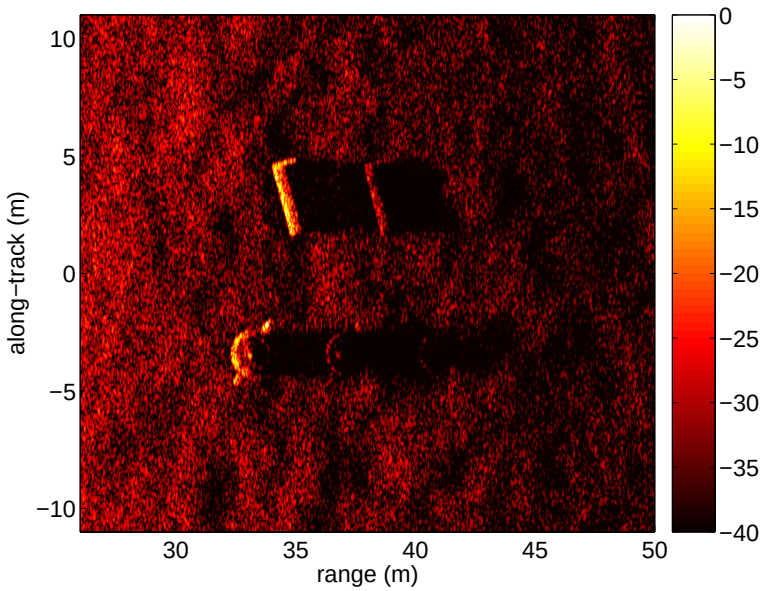

(a) smooth sea surface

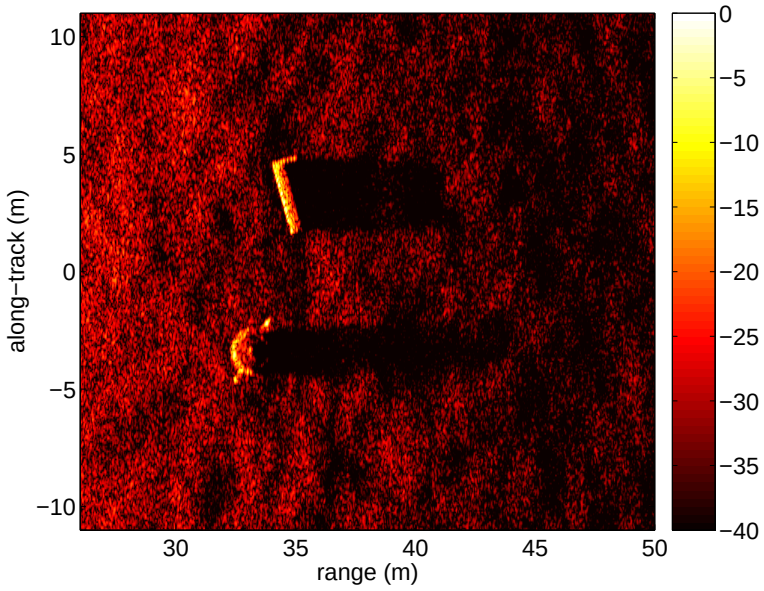

(b) rough sea surface

Figure 5.6 The simulated sea-surface is 15 m above the seafloor and 10 m above the sonar path. A smooth sea-surface causes coherent replica targets to appear in the imagery as shown in (a). For a rough sea-surface, the multipath replicas are blurred by the coherent SAS processing.

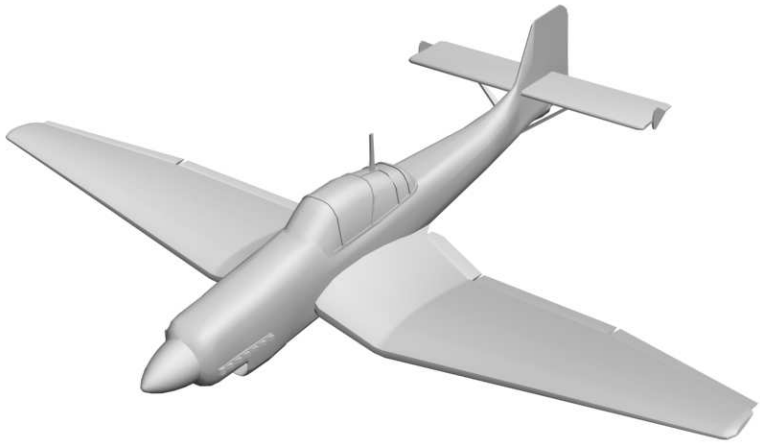

Figure 5.7 A VRML model of the Junkers JU 87 "Stuka" WWII bomber was freely available.

assumption of Lambertian scattering is not necessarily correct. The ideal imagery has unlimited resolution and it is speckle-free.

The simulated SAS imagery is shown in Figures 5.9 and 5.10. It differs from the ideal imagery in three respects: 1) the simulated imagery has finite resolution determined by the bandwidth of the chirp and the along-track dimensions of the transducers, 2) the speckle noise is not present in the ideal imagery, and 3) the aspect dependence of the transducers and the scene is not included in the ideal imagery, i.e., there are no transducer beampattern variations across the scene and the shadows are very sharp.

5.4.1 Bathymetry

The KiwiSAS hydrophone array provides a vertically separated set of 3 hydrophones for interferometry. The KiwiSAS uses wide-band signals (a quality factor, or Q, of 1.5 for the 30 kHz band and 5 for the 100 kHz band) so simple narrow-band interferometry does not suffice. For wide-band signals, the time delay between the hydrophones is used to estimate the angle of arrival and infer the seafloor topography. A maximum likelihood estimate of the seafloor topography is obtained using the imagery from the 3 hydrophones and 2 frequency bands [Hayes *et al.* 2006]. The variance of the height estimates is reduced using multiple frequency sub-bands and azimuth looks at the sacrifice of resolution [Barclay 2006]. The bathymetric reconstruction of the scene using 9 frequency sub-bands and 5 azimuth looks is shown in Figure 5.11(b). The regions of low coherence, which are mainly within the shadow region, have been removed.

A comparison of the ideal heightmap in Figure 5.11(a) with the heightmap obtained from the SAS imagery identifies the problems with the bathymetric reconstruction

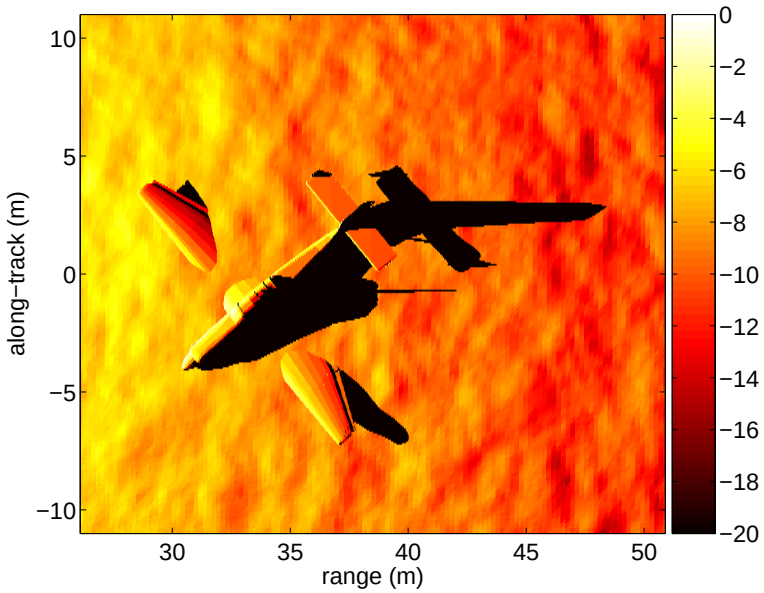

Figure 5.8 The simulator can be used to generate an ideal intensity map of the scene, i.e., the ensemble averaged imagery for a very narrow-beam sonar.

algorithm. As expected, the resolution of the reconstructed heightmap is lower than the ideal heightmap and the heights within the shadow regions are unknown due to low coherence. However, the major problem occurs at regions of layover; that is, in regions where two or more scattering objects occupy the same position in range [Hayes *et al.* 2005]. The bathymetric reconstruction algorithm assumes that a single scattering object is present at each range; this assumption is violated at regions of layover. Consequently, the height is estimated as the average height of the scatterers. This can be seen Figure 5.11(b); it is particularly obvious for regions of the plane that do not coincide with a shadowed region of seafloor, for example, the portion of the tail that coincides with the shadow is the correct height, while the remaining portion is lower. The same effect occurs when multipath scattering is present. Attempts to correct the layover problem use super resolution techniques such as the RELAX algorithm [Hayes *et al.* 2005, Hayes *et al.* 2006].

Augmentation of the intensity imagery and the bathymetric heightmap is a good method of visualising the SAS data. The intensity imagery is used as a texture for rendering the heightmap. The result is a 3-D model of the scene that is *illuminated* by the sonar. The augmented data is shown in Figure 5.12 for the ideal and simulated imagery of the Stuka scene. The simulated imagery is clearly of lower quality than the ideal imagery. The speckle reduces the fidelity and the layover causes the plane to meld with the seafloor. Speckle reduction [Courmontagne *et al.* 2006] and layover estimation could be used to improve this disparity.

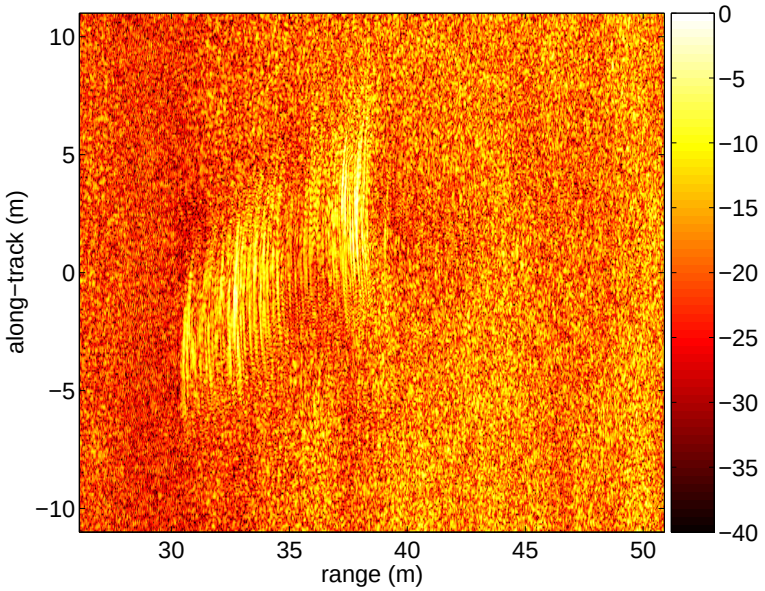

(a) pulse-compressed data (30 kHz)

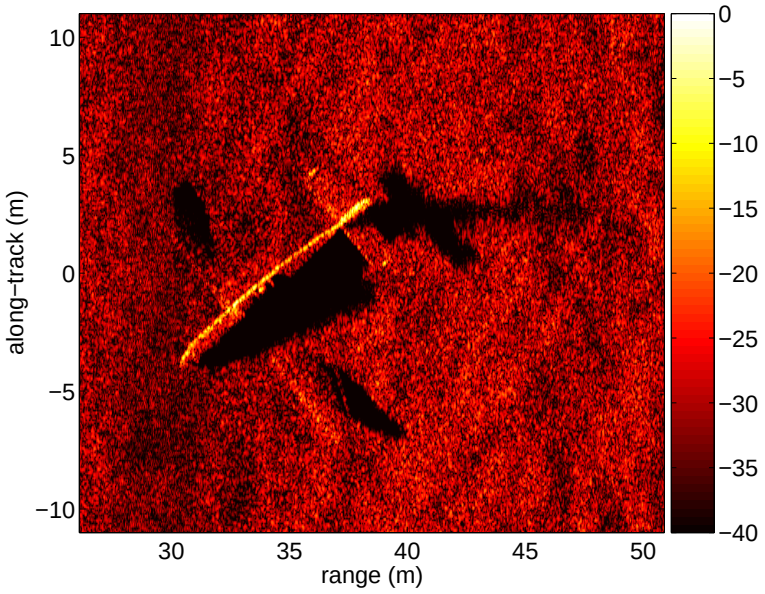

(b) SAS imagery (30 kHz)

Figure 5.9 30 kHz simulated SAS imagery of a Stuka WWII bomber on an undulating seafloor.

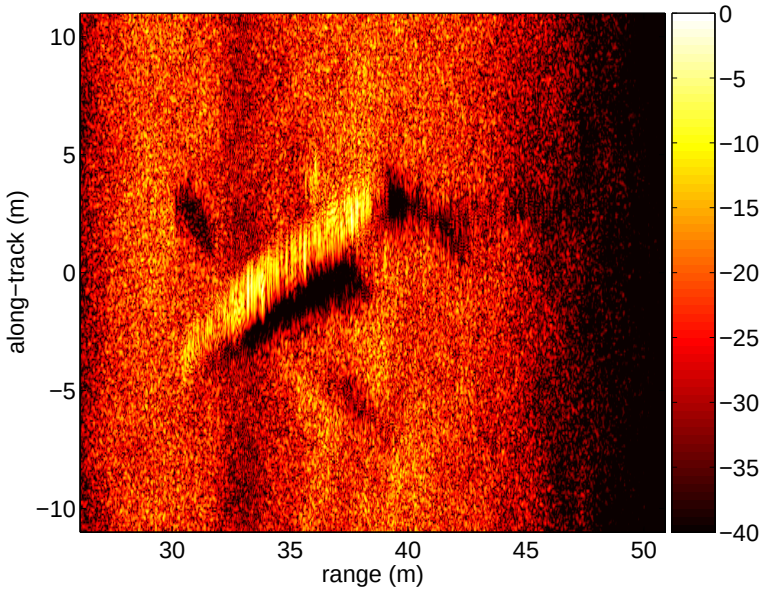

(a) pulse-compressed data (100 kHz)

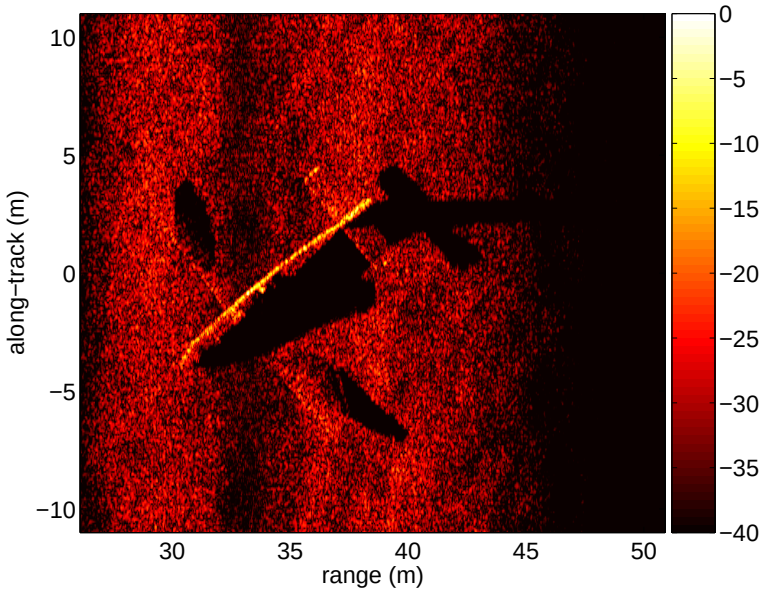

(b) SAS imagery (100 kHz)

Figure 5.10 100 kHz simulated SAS imagery of a Stuka WWII bomber on an undulating seafloor.

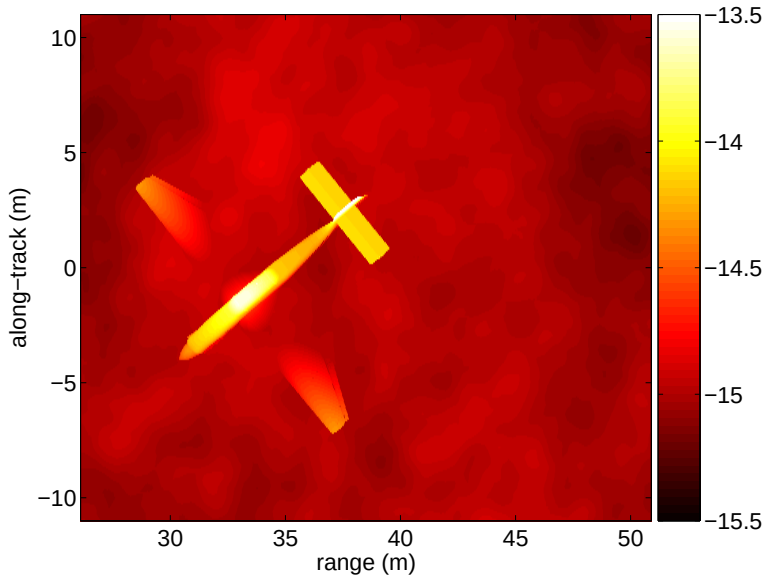

(a) ideal heightmap

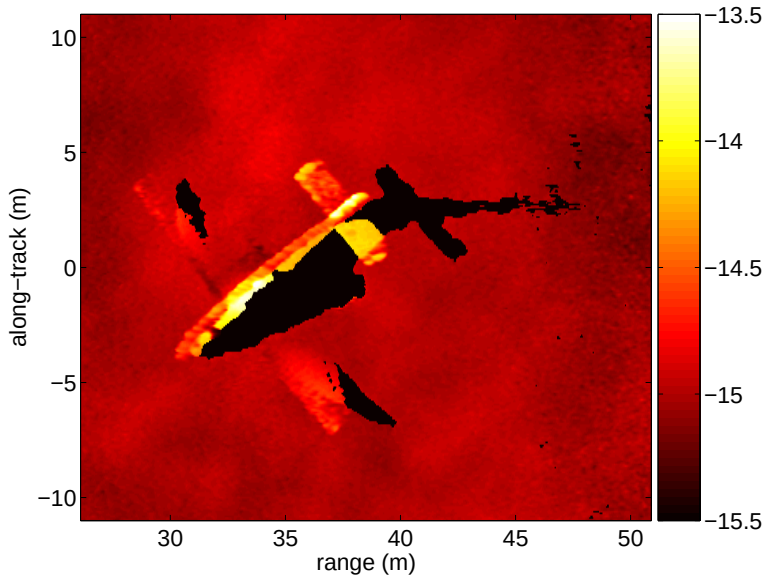

(b) reconstructed heightmap

Figure 5.11 The ideal heightmap of the Stuka scene can be compared with the heightmap reconstructed from the simulated SAS imagery. The estimated heightmap is incorrect in regions of layover.

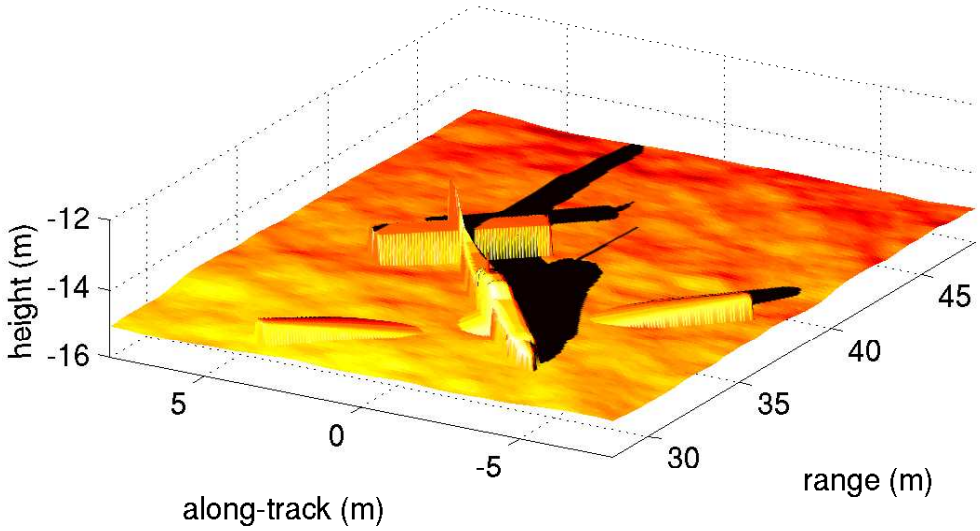

(a) ideal render

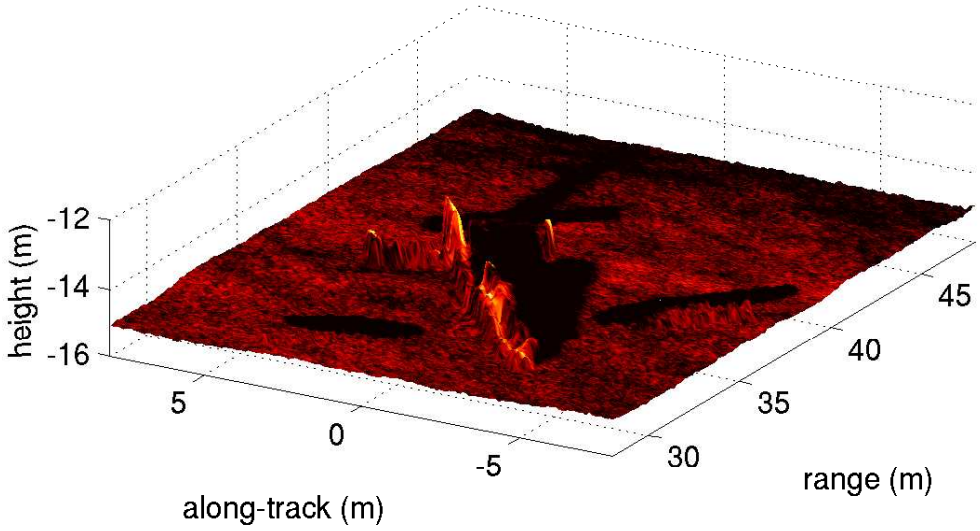

(b) render

Figure 5.12 Augmentation of the intensity imagery and the bathymetric heightmap is a good method of visualising the SAS data.

5.5 LYTTELTON HARBOUR SEA-TRIAL

To validate the data produced by the simulator, the simulated imagery is compared with imagery obtained by the KiwiSAS in an actual sea-trial. Two sea-trials were conducted in February and March of 2006 using the KiwiSAS-IV in Lyttelton Harbour, Canterbury, New Zealand. Parson's Rock is a feature of interest in the imagery from these trials. It is a volcanic rock mass that protrudes up to 6 m from the surrounding silt/sand seafloor at an average depth of 10 m. While ground-truth for the region is unavailable, the protruding rock appears to be some 50 m by 50 m in extent. The rock was imaged at a range of approximately 15–25 m with the towfish traveling roughly mid-water.

The SAS imagery from a run during the February sea-trial is shown in Figure 5.13. The imagery was reconstructed assuming a linear trajectory and a constant speed of 1 m/s. Navigation data was unavailable for the trials and any deviations from the linear trajectory are left uncorrected. Localised along-track blurring is evident in the imagery; this is thought to be due to variations in the towfish speed. The along-track *banding*, which is evident in the 100 kHz imagery, is an indication of roll; this has an affect on the interferometric phase estimation. It is likely that other deviations are also present. These uncompensated motions reduce the image resolution, introduce geometrical distortions, and cause reconstruction artefacts. It is important to note that the 30 kHz imagery appears noisier than the 100 kHz imagery. This could be due to multipath scattering from the sea surface and/or due to sub-surface penetration and volume scattering.

A bathymetric reconstruction of the experimental data was performed using 9 frequency sub-bands and 5 azimuth looks. Erroneous spikes in the heightmap due to phase wrapping and low coherence were removed by thresholding and the heightmap was repaired using Delaunay triangulation [Preparata and Shamos 1985]. The resultant heightmap is shown in Figure 5.14(a); the resolution is approximately 50 cm by 75 cm (across-track × along-track). Parson's Rock is evident on the left hand side, reaching a height of approximately 6 m above the seafloor.

The heightmap exhibits a series of ridges; these correlate with the banding in the 100 kHz imagery. It is probable that these ridges are not a feature of the seafloor but an artefact due to interferometric phase errors from the uncompensated roll. The heightmap also exhibits high-frequency variations that are commensurate with the speckle in the imagery (after filtering). It is unlikely that these variations are an actual feature of the seafloor.

The bathymetric heightmap is used as an input mesh for the simulator. The heightmap is tessellated into a collection of triangles with along/across-track dimensions of 15 cm by 15 cm, yielding a mesh of approximately 50000 facets. The properties of rock are assumed for the seafloor (see Table 2.1) and the simulated echo data is generated

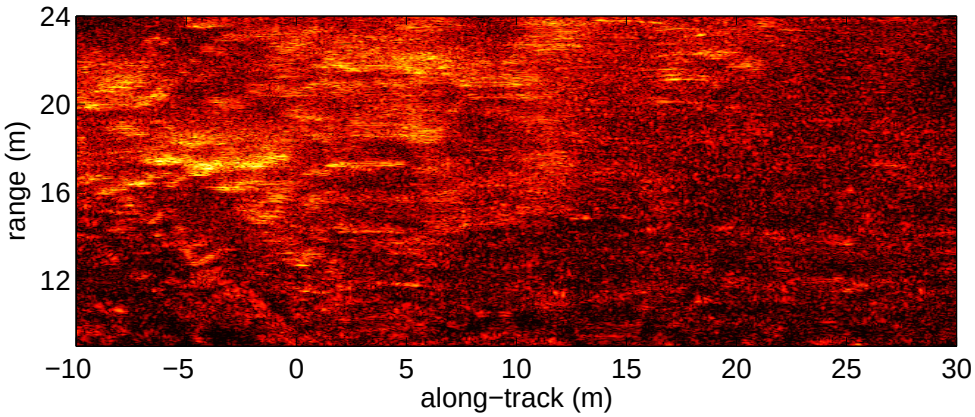

(a) SAS imagery (30 kHz)

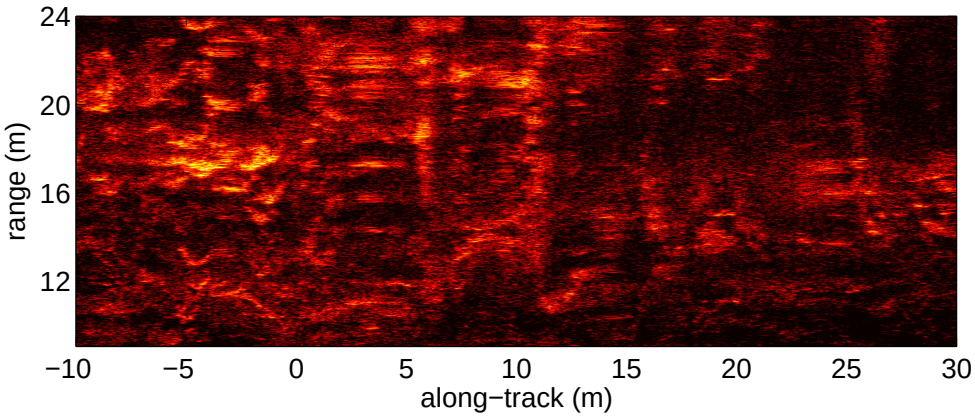

(b) SAS imagery (100 kHz)

Figure 5.13 Reconstructed SAS imagery of Parson's Rock in Lyttelton Harbour.

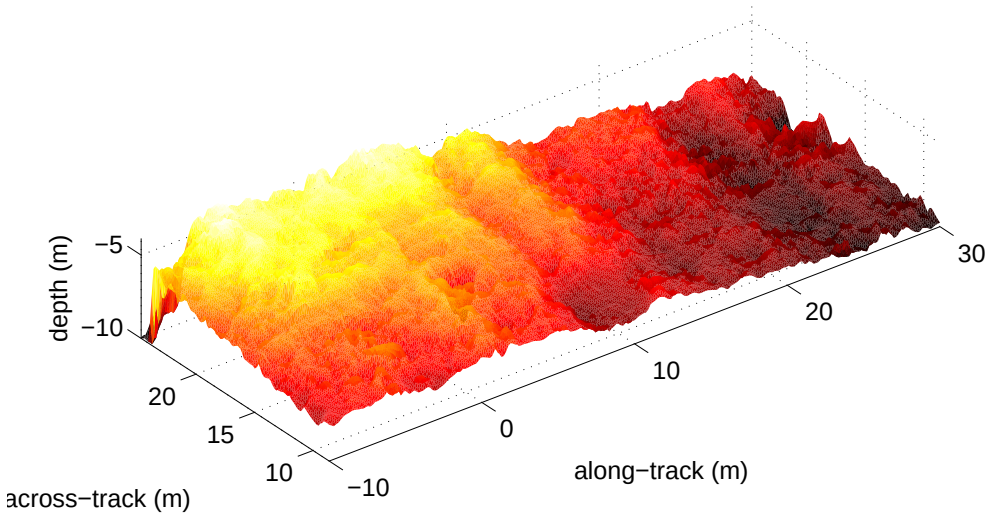

(a) full-resolution heightmap

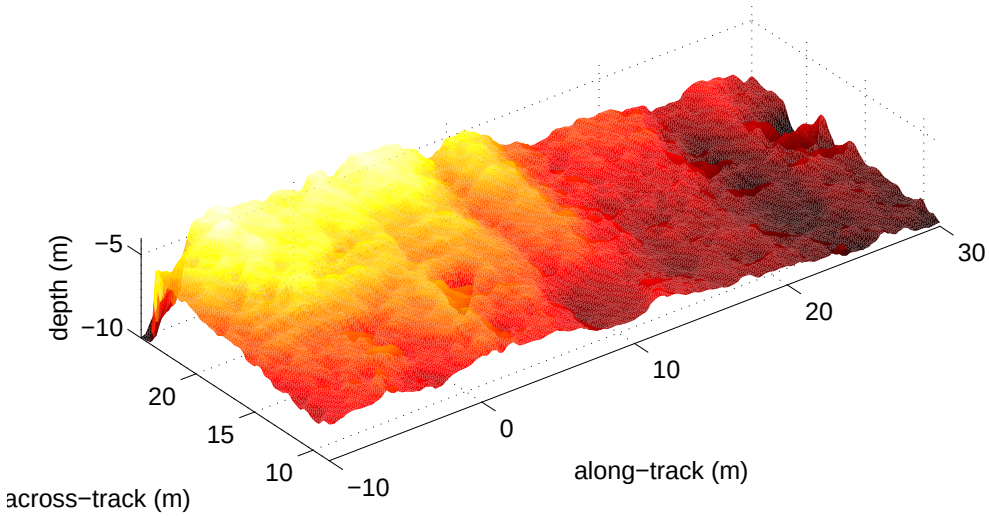

(b) median filtered heightmap

Figure 5.14 Bathymetric heightmaps of Parson's Rock in Lyttelton Harbour. The full-resolution heightmap shown in (a) exhibits speckle artefacts. The heightmap is median filtered in (b) to remove the artefacts.

using a linear towpath at a speed 1 m/s and a depth of 5 m.

The simulated SAS imagery is shown in Figure 5.15. A comparison with the experimental imagery in Figure 5.13 shows significant differences. Most notably, the simulated imagery has a higher resolution and the seafloor appears to have higher spatial frequency content. The simulated data does not exhibit the same artefacts due to uncompensated towpath deviations and the experimental data appears noisier. However, the beampattern nulls in the simulated and experimental imagery appear in the same locations; this indicates that the underlying structure of bathymetric heightmap is correct.

The heightmap is filtered to remove the speckle artefacts using a $0.5\,\mathrm{m} \times 0.5\,\mathrm{m}$ median filter. The simulated imagery using the filtered heightmap is shown in Figure 5.16(b). This imagery resembles the experimental data more closely. However, the simulated and experimental imagery are far from identical.

The disparity between the experimental and simulated imagery indicates an inconsistency between the forward and inverse models. Both the forward and inverse models employ simplifying assumptions that will contribute to these differences. The towfish navigation data was unavailable and, consequently, the unknown deviations from an assumed linear towpath were left uncompensated; this is thought to be the biggest source of error. In addition, certain aspects were neglected in the simulations including multipath scattering, sub-surface penetration, and volume scattering.

5.6 COMPUTATIONAL PERFORMANCE

The simulator is implemented for parallel operation on a computing cluster. It has been tested on several clusters, including two clusters within the Electrical and Computer Engineering department at the University of Canterbury, an ad-hoc cluster of University workstations, and a small inhomogeneous cluster of Mac and Linux computers. The cluster used to generate the imagery for this thesis consisted of ten 2.35 GHz dual-processor 64-bit Opterons (20 processors in total) with 4GB of RAM each. The computers ran the Linux operating system and were managed by the Sun Grid Engine [Sun Microsystems 2002].

The computational performance of the simulator is highly dependent on the complexity and size of the simulated scene and the specifications and number of nodes in the computing cluster. A simple benchmark scene is simulated to give an indication of the simulator performance and the computational gain achieved through parallel computing. The scene consists of a single target that is composed of 552 triangular facets. The simulated imagery has dimensions of 512×1024 pixels. The scene is simulated on an ad-hoc cluster of up to 50 1.8 GHz computers with 1 GB of RAM each. The benchmark results are shown in Figure 5.17.

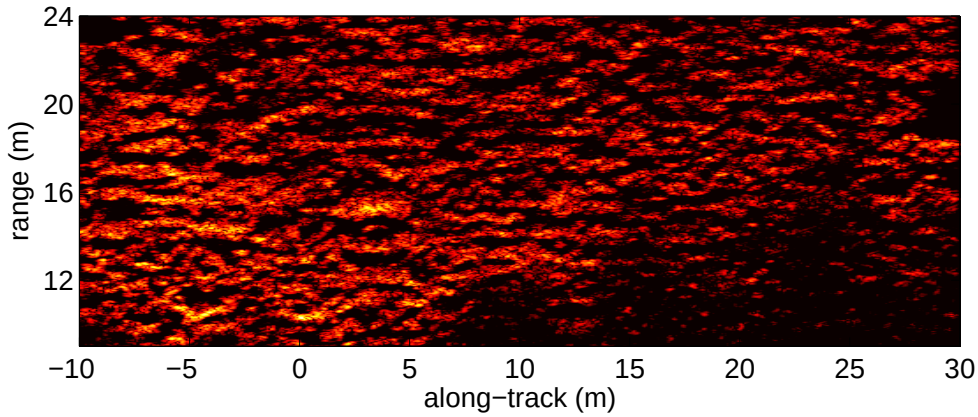

(a) simulated SAS imagery (30 kHz)

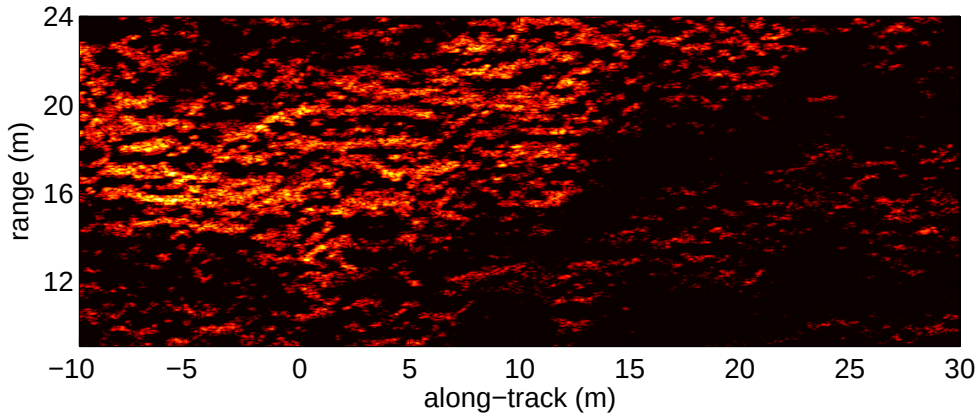

(b) simulated SAS imagery (100 kHz)

Figure 5.15 Simulated SAS imagery of Parson's Rock.

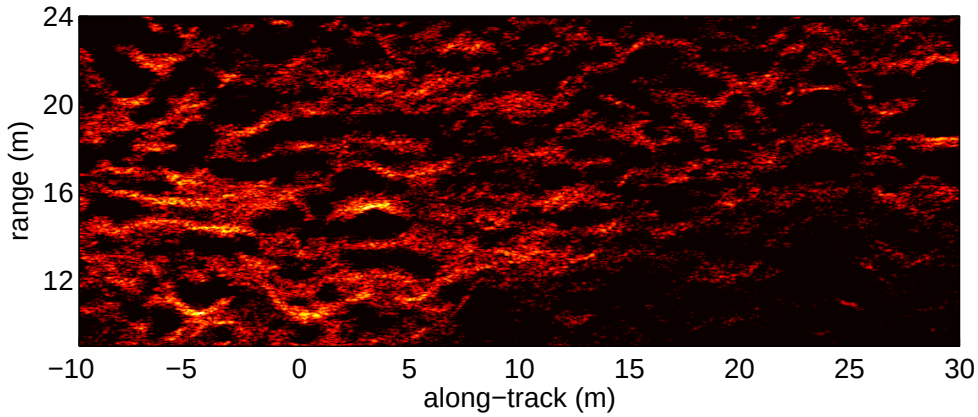

(a) simulated SAS imagery (30 kHz)

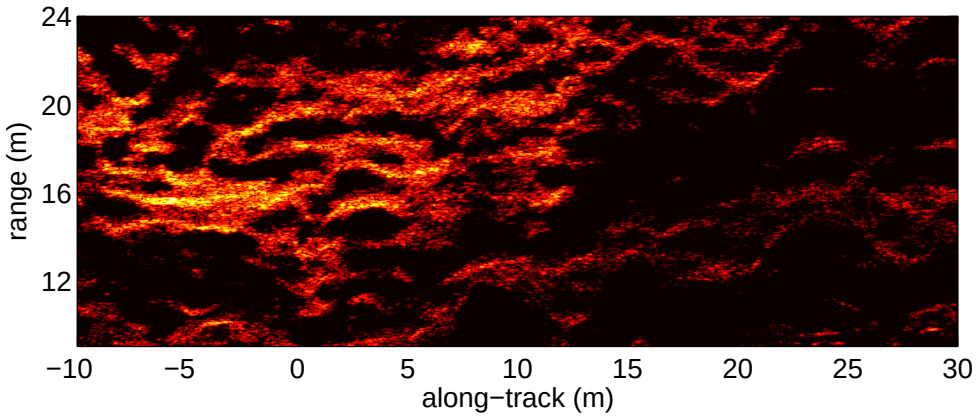

(b) simulated SAS imagery (100 kHz)

Figure 5.16 Simulated SAS imagery of Parson's Rock.

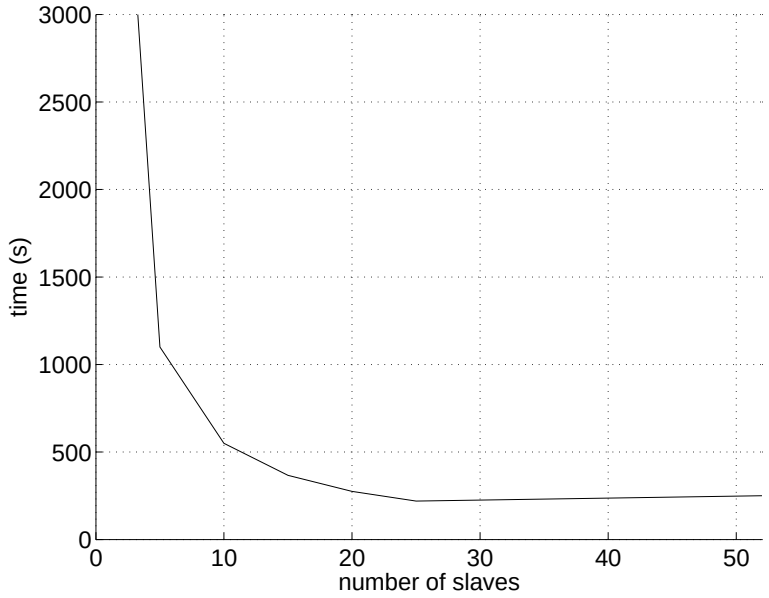

Figure 5.17 Computation times for a benchmark scene of 552 facets.

The computation times for the scene indicates that each facet is simulated in approximately 5 s on a single node. However, this is highly scene-specific since it depends on the ray-tracing requirements and the dimensions of the imagery. It is also dependent on the specifications of the cluster nodes. The simulation time scales linearly with the number of hydrophones and the number of transmitted signals. An exponential decrease in computation time with respect to the number of nodes is achieved through use of parallel computing. However, overhead costs become significant for approximately 25 nodes or more and the computation time actually increases with more nodes; this value varies with the specifications of the nodes and the network connection between the nodes.

Chapter 6

CONCLUSIONS

The acoustic scattering model presented in this thesis is more computationally efficient than the standard Kirchhoff scattering model employed by most SAS and SAR simulators. The scattering model presented here extends the Kirchhoff model by incorporating facet roughness. A scene can be decomposed into fewer rough (rather than smooth) facets since the small-scale roughness does not need to be modelled explicitly. Although the scattering from a rough facet is more complicated and, hence, requires more computation, the number of facets is significantly reduced and the model is more efficient overall.

The extended Kirchhoff model is limited by the same constraints on the roughness as the standard Kirchhoff model; the surface curvature is assumed large compared to a wavelength. The model is restricted to far-field scattering problems. Scattering from a rough facet is determined using an analytic expression for the far-field beampattern statistics. Therefore, the facets and the physical (as opposed to synthetic) transducers are assumed to be within mutual Fraunhoffer regions. The same restriction applies for multiple scattering between facets. The far-field requirement is satisfied for typical SAS imaging geometries and for sea-surface multipath. However, it does put a restriction on short-range multiple scattering, e.g., it is not advantageous to use the model for multiple scattering within an object or for sub-surface penetration.

The analytic expressions for the beampattern statistics have been derived for rectangular and triangular facets and Gaussian roughness statistics. Arbitrary facet shapes can be modelled analytically or by using conjoined triangular facets. The beampattern expressions for non-Gaussian roughness statistics have not been derived, although this should be possible.

The beampattern expressions can be evaluated more efficiently using the Fourier warping theorem (this also applies for the standard Kirchhoff model). Determination of the beampattern expression requires the evaluation of a Fourier transform of the 2-D facet aperture function. The Fourier transform of an arbitrary triangular aperture function can be obtained using the Fourier transform of a reference triangular aperture function and the appropriate transformation, or warping, of interpolated spatial fre-

quencies. Therefore, only a single Fourier transform needs to be calculated and stored; this is then interpolated as required. This technique offers a significant improvement in efficiency since the Fourier transform of each unique facet does not need to be calculated. The Fourier warping theorem can also be employed for efficient modelling of time-variant facets (such as the facets of a moving sea-surface), partially occluded facets, and for modelling temporal Doppler effects.

A SAS simulator has been implemented using the proposed scattering model. The simulator can generate raw echo data for arbitrary scenes and sonar trajectories. The echo data is generated by the sum of responses from each visible facet, where occlusions and multiple scattering are resolved by ray-tracing. Ray theory employs a high-frequency approximation and, consequently, diffraction effects are ignored. Nevertheless, the simulated imagery incorporates many important features, including coherent speckle noise, shadows cast by proud objects, aspect-dependent scattering and shadowing, and sea-surface multipath.

The simulator is capable of simulating larger and more complicated scenes than simulators employing the standard Kirchhoff scattering model. However, a computing cluster or supercomputer is recommended to simulate realistic scenes in a reasonable time-frame. A typical scene consists of between 10,000 and 1 million facets (this is likely to increase as computing power advances and as more complicated scenes become available). The simulation time for a scene of this size is on the order of hours when simulated in parallel rather than days when simulated on a single computer.

The SAS imagery produced by the simulator resembles imagery from experimental data collected by the KiwiSAS and data collected elsewhere. However, a rigorous validation of the simulated data has not been performed since accurate ground-truth for the KiwiSAS data is unavailable. Regardless, the simulated imagery has been used to assess the performance of SAS algorithms. In particular, the simulator has been very useful for testing and developing the bathymetric reconstruction algorithms.

Preliminary results show that a simulator could be used as a feedback path in an iterative, closed-loop reconstructor. A comparison between the simulated and experimental data provides a metric for the quality of the reconstruction. If the two data sets are identical then the reconstruction is consistent with the simulation and, assuming the simulator is perfect, the reconstruction is correct. At present this approach is not feasible for two main reasons: 1) the simulator employs too many simplifying assumptions to justify the neglection of simulation errors, and 2) the computational requirements for the simulation stage are too prohibitive for an iterative scheme.

In summary, the acoustic scattering model and its implementation in the SAS simulator are valuable tools for the development and testing of SAS algorithms. The mathematical development of the scattering model provides insight into the SAS imaging process and the simulator provides a means of obtaining ideal echo data that can

be used to develop and validate SAS algorithms. Moreover, the simulator can provide echo data for arbitrary scenes reducing the need for expensive and time-consuming sea trials.

6.1 RECOMMENDATIONS FOR FUTURE RESEARCH

Many improvements and extensions could be made to the research presented in this thesis. Throughout the course of research a number of possible paths for future research have become apparent:

Non-Gaussian roughness statistics – The analytic expressions for the statistics of the facet beampattern have been derived for Gaussian statistics. However, research has shown that the statistics of the seafloor roughness are actually fractal. Although Gaussian statistics are commonly assumed, the beampattern expressions for other statistical distributions, such as fractal statistics, should be derived.

Alternative scattering models – The Kirchhoff approximation has a number of inherent weaknesses, primarily its limited region of validity. The proposed scattering model does not account for shadowing and multiple scattering for the small-scale roughness. Its validity is reduced for grazing angles, which are common in the shallow-water side-scan geometry, and the enhanced back-scattering phenomenon [Phu *et al.* 1993] is not modelled. It is also restricted to surface scattering problems. The far-field approximation restricts the modelling of short-range multiple scattering and the high-frequency ray assumption neglects diffraction. Generalisations of the Kirchhoff approximation, such as the small-slope approximation, should be investigated. Alternatively, a numerical model, such as the finite element method, could be employed. However, this would require significant computing power.

Sub-surface penetration – There is significant interest at present in SAS imaging of buried objects. SAS processing allows lower frequencies to be used whilst retaining a high resolution. This is useful since lower frequencies propagate further into the sediment. Therefore, SAS has potential for buried object imaging. The proposed scattering model is not well suited for modelling penetration into the sediment due to the far-field approximation. If sub-surface penetration is to be investigated then a numerical model will probably be required, i.e., finite difference or finite element methods.

Further comparison with experimental data – The comparison between experimental data from the KiwiSAS and simulated data was unconclusive due to the lack of accurate ground-truth and navigation data. Further comparison between experimental

and simulated data is required to validate the simulated imagery and to identify areas for improvement. An inertial navigation system and an active beacon system are currently being developed. These should be employed in future sea-trials, perhaps in conjunction with autofocus algorithms, to improve the SAS imagery and bathymetric heightmap before generating the mesh for the simulator. Ideally, a known scene with accurate ground-truth would be imaged.

Ground-truth measurements – Although accurate ground-truth is difficult to obtain, it would be useful to know more about the properties of the sea floor and water column in the vicinity of Lyttelton Habour. Bottom samples should be taken and the properties such as density, sound-speed, absorption, etc., should be measured and documented. A sound-speed profile of the water column would be useful for long range imaging where refraction effects will become important. Underwater photography and video would give an indication of the seafloor structure (it would be particularly interesting for Parson's Rock). However, this would require a dive survey.

Benchmarking against other simulators – It would be interesting to compare the output of the Kiwi SAS simulator with the output of another simulator, e.g., SWAT, for an identical scene. Unfortunately, SWAT is the property of the U.S. Navy and has restricted availability. However, comparisons using other simulators could be performed.

Iterative closed-loop reconstruction – The comparison between simulated and experimental imagery indicates that an iterative, closed-loop reconstructor is feasible. An investigation of possible image comparison metrics and methods of using the metric to adjust the reconstruction and simulation parameters is required. At present the simulation errors and computational requirements restrict this path of research. However with the constant advance in computing power [Moore 1965], this should become possible in the near future.

Improved parallel implementation – The parallel implementation of the simulator dramatically increases the computational efficiency. However, the efficiency is directly related to the number of nodes in the computing cluster. The cost to set up and maintain a cluster is not small and, consequently, the simulator is not always a viable option. Existing workstations could be utilised to create an ad-hoc cluster, utilising otherwise idle CPU cycles. This has been implemented for a number of computation-intensive research projects including the search for extraterrestrial life (SETI) [Anderson *et al.* 2002], mapping the human genome [Larson *et al.* 2002], and climate prediction [Christensen *et al.* 2005]. These projects use the Berkeley Open Infrastructure for Network Computing (BOINC) [Anderson 2004, Anderson *et al.* 2005, Anderson and

Fedak 2006]. The implementation of a numerical model, such as the finite element method, may require this approach due to the heavy computational cost.

GPU/PPU implementation – The simulator currently operates on general purpose CPUs. However, the recent use of GPUs (graphics processing units) for physics applications [Thompson *et al.* 2002] suggests that this could be an option for better computational performance. More recently PPUs (physics processing units) have become available, which could be more suited for the task.

Appendix A

THE FOURIER TRANSFORM

The Fourier transform [Bracewell 1986] is used extensively throughout this thesis. The Fourier transform and a number of useful identities and transform pairs are defined here.

The Fourier transform of a function, $g(t)$, is given by

$$G(f) = \int_{-\infty}^{\infty} g(t) \exp(-j2\pi ft)\ dt \tag{A.1}$$

and its inverse Fourier transform is given by

$$g(t) = \int_{-\infty}^{\infty} G(f) \exp(j2\pi ft)\ df, \tag{A.2}$$

where f is the Fourier variable, usually referred to as the frequency. Extension of the Fourier transform to multiple dimensions is trivial.

A.1 PROPERTIES OF THE FOURIER TRANSFORM

A summary of useful properties of the Fourier transform are given in Table A.1.

A.1.1 Fourier warping theorem

The transformation, or warping, of a function results in an inverse warping of the Fourier transform. This is a generalisation of the scaling and shifting properties (see Table A.1). The warping theorem is derived here for the affine transformation of a 2-D function.

Consider a 2-D function, $a(\mathbf{x})$, with a Fourier transform, $A(\mathbf{u})$. Then, consider the affine transformation of the function,

$$a'(\mathbf{x}) = a(\mathbf{R}\mathbf{x}), \tag{A.3}$$

property	**description**
1) linearity	$Ag_1(t) + Bg_2(t) \longleftrightarrow AG_1(f) + BG_2(f)$
2) time scaling	$g(At) \longleftrightarrow \frac{1}{\lvert A\rvert}\, G\left(\frac{1}{A}f\right)$
3) duality	$G(t) \longleftrightarrow g(-f)$
4) time shifting	$g(t-t_0) \longleftrightarrow G(f)\exp(-j2\pi f t_0)$
5) frequency shifting	$g(t)\exp(j2\pi f_0 t) \longleftrightarrow G(f-f_0)$
6) area under $g(t)$	$\int_{-\infty}^{\infty} g(t)\ dt = G(0)$
7) area under $G(f)$	$g(0) = \int_{-\infty}^{\infty} G(f)\ df$
8) differentiation in the time domain	$\frac{d}{dt}g(t) \longleftrightarrow j2\pi f\ G(f)$
9) integration in the time domain	$\int_{-\infty}^{t} g(\tau)\ d\tau \longleftrightarrow \frac{1}{j2\pi f}\, G(f) + \frac{1}{2}\, G(0)\,\delta(f)$
10) conjugate functions	$g^*(t) \longleftrightarrow G^*(-f)$
11) multiplication in the time domain	$g_1(t)\, g_2(t) \longleftrightarrow \int_{-\infty}^{\infty} G_1(\lambda)\, G_2(f-\lambda)\ d\lambda$
12) convolution in the time domain	$\int_{-\infty}^{\infty} g_1(\tau)\, g_2(t-\tau)\ d\tau \longleftrightarrow G_1(f)\, G_2(f)$
13) correlation in the time domain	$\int_{-\infty}^{\infty} g_1(\tau)\, g_2(t+\tau)\ d\tau \longleftrightarrow G_1(f)\, G_2^*(f)$

Table A.1 A summary of Fourier transform properties. This table is modified from [Haykin 1994].

where

$$\mathbf{R} = \begin{pmatrix} r_{11} & r_{12} & r_{13} \\ r_{21} & r_{22} & r_{23} \\ r_{31} & r_{32} & r_{33} \end{pmatrix} \tag{A.4}$$

is a matrix[1] describing the transformation of points $\mathbf{x}$ to $\mathbf{x}' = \mathbf{R}\mathbf{x}$. The Fourier Transform of $a'(\mathbf{x})$ is given by

$$A'(\mathbf{u}) = \int\!\!\int_{-\infty}^{\infty} a(\mathbf{R}\mathbf{x}) \exp(-j2\pi\ \mathbf{x}\cdot\mathbf{u})\ d\mathbf{x}. \tag{A.5}$$

Making the substitution, $\boldsymbol{\lambda} = \mathbf{R}\mathbf{x}$, gives

$$A'(\mathbf{u}) = \frac{1}{\det(\mathbf{R})} \int\!\!\int_{-\infty}^{\infty} a(\boldsymbol{\lambda}) \exp\left(-j2\pi\ \mathbf{R}^{-1}\boldsymbol{\lambda}\cdot\mathbf{u}\right)\ d\boldsymbol{\lambda}, \tag{A.6}$$

where $1/\det(\mathbf{R})$ is the Jacobian and $\det(\mathbf{R})$ is the determinant of $\mathbf{R}$. Re-arranging

[1]The matrix, $\mathbf{R}$, is often termed the rotation matrix but it describes a more general transformation than a simple rotation; it can describe rotation, scaling, and shear.

function	**Fourier transform**
$\text{rect}\left(\frac{t}{T}\right)$	$T\ \text{sinc}\left(Tf\right)$
$\text{sinc}\left(2Bt\right)$	$\frac{1}{2B}\text{rect}\left(\frac{1}{2B}f\right)$
$\exp\left(-A\left\|t\right\|\right)u\left(t\right),\ A>0$	$\frac{1}{A+j2\pi f}$
$\exp\left(-A\left\|t\right\|\right),\ A>0$	$\frac{2A}{A^2+\left(2\pi f\right)^2}$
$\exp\left(-At^2\right),\ A>0$	$\sqrt{\frac{\pi}{A}}\exp\left(-\frac{\pi^2}{A}f^2\right)$
$\begin{cases} 1-\frac{\left\|t\right\|}{T}, & \left\|t\right\|<T \\ 0, & \left\|t\right\|\geq T \end{cases}$	$T\text{sinc}^2\left(fT\right)$
$\delta\left(t\right)$	1
1	$\delta\left(f\right)$
$\delta\left(t-t_0\right)$	$\exp\left(-j2\pi ft_0\right)$
$\exp\left(j2\pi f_0t\right)$	$\delta\left(f-f_0\right)$
$\cos\left(2\pi f_0t\right)$	$\frac{1}{2}\left[\delta\left(f-f_0\right)+\delta\left(f+f_0\right)\right]$
$\sin\left(2\pi f_0t\right)$	$\frac{1}{2j}\left[\delta\left(f-f_0\right)-\delta\left(f+f_0\right)\right]$
$\text{sgn}\left(t\right)$	$\frac{1}{j\pi f}$
$\frac{1}{\pi t}$	$-j\ \text{sgn}\left(f\right)$
$u\left(t\right)$	$\frac{1}{2}\delta\left(f\right)+\frac{1}{j2\pi f}$
$\sum_{n=-\infty}^{\infty}\delta\left(t-nT\right)$	$\frac{1}{T}\sum_{n=-\infty}^{\infty}\delta\left(f-n\frac{1}{T}\right)$

Table A.2 A collection of useful Fourier transform pairs. This table is modified from [Haykin 1994]

the expression (A.6), gives

$$A'\left(\mathbf{u}\right)=\frac{1}{\det\left(\mathbf{R}\right)}\iint_{-\infty}^{\infty}a\left(\boldsymbol{\lambda}\right)\exp\left(-j2\pi\ \boldsymbol{\lambda}\cdot\left(\mathbf{R}^{-1}\right)^T\mathbf{u}\right)\ d\boldsymbol{\lambda}, \tag{A.7}$$

which yields the Fourier relation:

$$a\left(\mathbf{Rx}\right)\longleftrightarrow\frac{1}{\det\left(\mathbf{R}\right)}\ A\left(\left(\mathbf{R}^{-1}\right)^T\mathbf{u}\right). \tag{A.8}$$

Thus, a transformation $\mathbf{R}$ in one domain results in a transformation $\left(\mathbf{R}^{-1}\right)^T$ in the other domain. This is the Fourier warping theorem.

It would be convenient to define the Fourier relation for a projective transformation in homogeneous coordinates [Foley *et al.* 1997]. However, the projective transformation is non-linear and the relation is not easily derived.

A.2 USEFUL FOURIER TRANSFORMS

A collection of useful Fourier transform pairs is given in Table A.2.

A.2.1 Fourier transform of a triangular aperture

Consider a right-angle triangular aperture defined by

$$\mathrm{tri}'(x,y) = \begin{cases} 1, & -\frac{1}{2} > (x,y) > \frac{1}{2}, \quad y < x \\ 0, & \text{elsewhere} \end{cases} . \tag{A.9}$$

The Fourier transform of the aperture is given by

$$\mathrm{TRI}'(u,v) = \iint_{-\infty}^{\infty} \mathrm{tri}'(x,y) \exp\left(-j2\pi\left(ux+vy\right)\right)\, dx\, dy. \tag{A.10}$$

Substituting for the aperture expression (A.9) gives

$$\mathrm{TRI}'(u,v) = \int_{-\frac{1}{2}}^{\frac{1}{2}} \exp\left(-j2\pi\ vy\right) \left[\int_{y}^{\frac{1}{2}} \exp\left(-j2\pi\ ux\right)\, dx\right]\, dy \tag{A.11}$$

and evaluating the integrals gives

$$\begin{aligned} \mathrm{TRI}'(u,v) = \frac{-1}{j2\pi u} \Bigg[& \frac{1}{j2\pi v} \exp\left(-j\pi u\right) \Big(\exp\left(j\pi v\right) - \exp\left(-j\pi v\right) \Big) \\ & - \frac{1}{j2\pi\left(u+v\right)} \Big(\exp\left(j\pi\left(u+v\right)\right) - \exp\left(-j\pi\left(u+v\right)\right) \Big) \Bigg], \end{aligned} \tag{A.12}$$

where the exponential functions can be replaced by sinc functions. Thus,

$$\mathrm{TRI}'(u,v) = \frac{j}{2\pi u} \Big[\exp\left(-j\pi u\right) \mathrm{sinc}\left(v\right) - \mathrm{sinc}\left(u+v\right) \Big]. \tag{A.13}$$

The Fourier transform of an arbitrary triangular aperture can be obtained using the properties of Table A.1 and/or the Fourier warping theorem. For example, the Fourier transform of the right-angle triangular aperture (A.9) centred about its centroid,

$$\mathrm{tri}(x,y) = \mathrm{tri}'\left(x + \frac{1}{6}, y - \frac{1}{6}\right), \tag{A.14}$$

is given by

$$\mathrm{TRI}(u,v) = \frac{j}{2\pi u} \exp\left(j\pi\left(\frac{1}{3}u - \frac{1}{3}v\right)\right) \Big[\exp\left(-j\pi u\right) \mathrm{sinc}\left(v\right) - \mathrm{sinc}\left(u+v\right) \Big] \tag{A.15}$$

using the shifting property of the Fourier transform.

Appendix B

ASPECT-DEPENDENT SAS RECONSTRUCTION

Synthetic aperture sonars employ wide beams to achieve greater spatial frequency coverage; this facilitates higher along-track resolution. A wide beam *illuminates* the scene over a wide range of angles for each along-track position. While the SAS reconstruction algorithms assume the scene reflectivity is independent of angle, in general, this is not the case. The aspect-dependence of SAS imagery can be useful for characterising objects based on the movement of specular reflections and shadows between pings.

In this appendix, an aspect-dependent reconstruction algorithm is described. It is a simple extension of the wavenumber algorithm, incorporating an azimuth filtering stage to isolate the aspect-dependence at the sacrifice of spatial resolution. The aspect-dependence adds an additional dimension to the imagery, yielding data in two spatial dimensions, reflectivity, and aspect. The 4-D data can be interpreted by mapping the aspect-dependence using colour, or more naturally, utilising the time-dimension to produce a *movie*.

Consider the echo data, $e(x, y)$, and its Fourier transform in along-track,

$$E(x, k_y) = \int_{-\infty}^{\infty} e(x, y) \exp(-jk_y y)\ dy, \tag{B.1}$$

where x is the range, y is the along-track position,

$$k_y = 2\pi f_y \tag{B.2}$$

is the along-track angular wavenumber, and f_y is the spatial frequency. The data is sampled with an along-track spacing of

$$\Delta y = \frac{v}{f_p}, \tag{B.3}$$

giving an along-track sample rate of $1/\Delta y$, where v is the (constant) speed of the sonar and f_p is the ping rate. It is assumed that the aperture is sampled adequately (to avoid

aliasing), i.e.,

$$\Delta y \leq \frac{D}{2}, \tag{B.4}$$

where D is the extent of the smallest transducer. Often a more conservative constraint of D/4 is assumed.

In the far-field, the wavenumber k_y can be related to the angle of the incident plane waves by the relation:

$$k_y \approx k \sin\theta, \tag{B.5}$$

where

$$k = \frac{2\pi f}{c} \tag{B.6}$$

is the temporal wavenumber, f is the temporal frequency, c is the propagation speed, and θ is the angle of the incident wave. By windowing the data in the along-track wavenumber domain, different angles of incidence can be isolated. However, windowing the data reduces the image resolution.

The echo data is defined for along-track wavenumbers extending from $-\pi/\Delta y$ to $\pi/\Delta y$ by the Nyquist theorem. This corresponds to resolvable angles extending from

$$\theta_{\min} = -\sin^{-1}\left(\frac{\pi}{k\Delta y}\right) \tag{B.7}$$

to

$$\theta_{\max} = \sin^{-1}\left(\frac{\pi}{k\Delta y}\right). \tag{B.8}$$

However, the data is windowed by the transducer beampattern, which for a rectangular aperture,

$$a(y) = \text{rect}\left(\frac{y}{D}\right), \tag{B.9}$$

is given by[1]

$$A(k_y) = D\ \text{sinc}\left(\frac{D}{2\pi}k_y\right) \tag{B.10}$$

and has a null–null beamwidth of

$$\theta_{\text{null}} = \sin^{-1}\left(\frac{4\pi}{Dk}\right) \tag{B.11}$$

$$\approx \frac{2\lambda}{D}, \tag{B.12}$$

where λ is the wavelength. This is illustrated in Figure B.1(a).

[1]The expression for the beampattern differs from the expression given in Chapter 2. The obliquity term is neglected here.

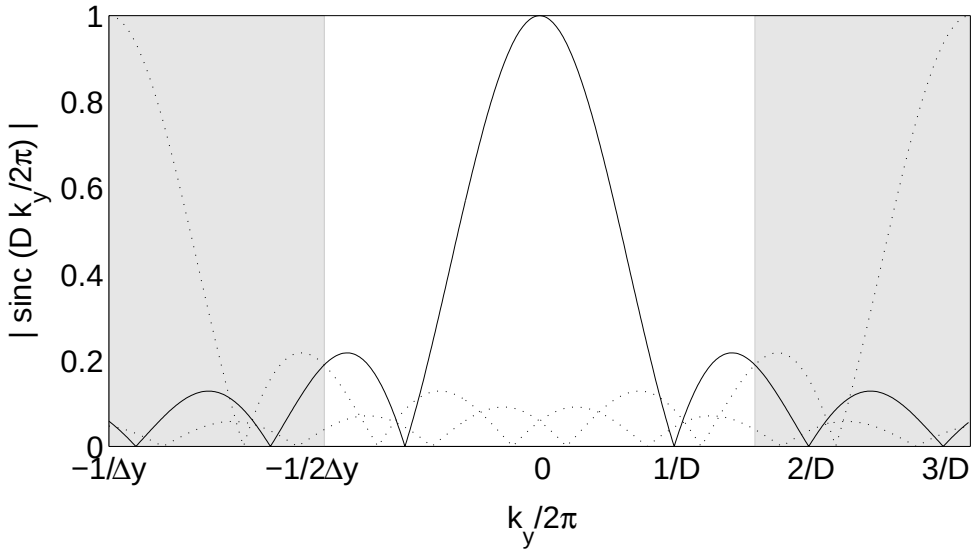

(a) transducer beampattern

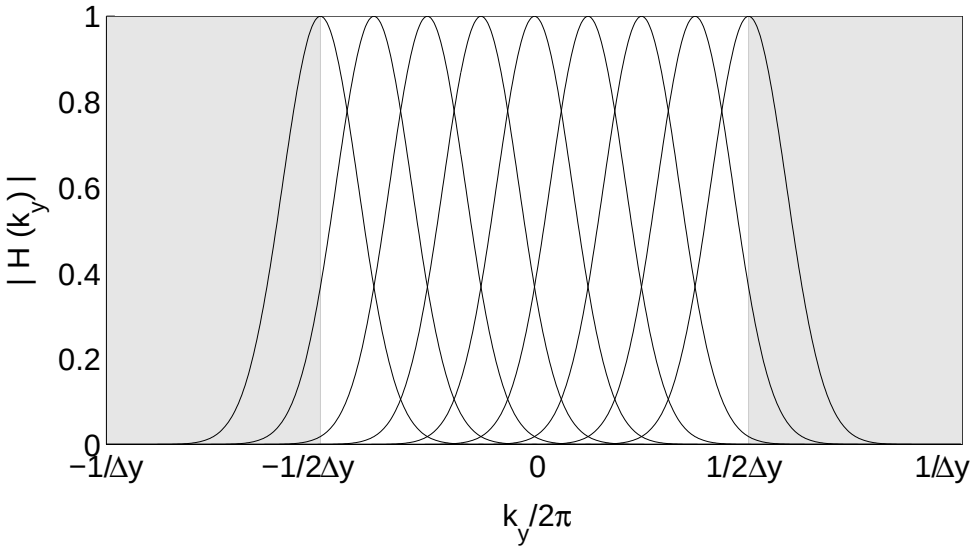

(b) aspect filters

Figure B.1 The spatial frequencies extending from $-1/2\Delta y$ to $1/2\Delta y$ are collected by the sonar. However, this region is windowed by the transducer beampattern. The dotted plots show the aliased beampatterns. Different angles of incidence can be isolated by windowing the data in the along-track spatial frequency domain. Figure (b) illustrates 9 example aspect filters. The spatial frequencies $\pm 1/\lambda$ correspond to angles of ± 90 deg.

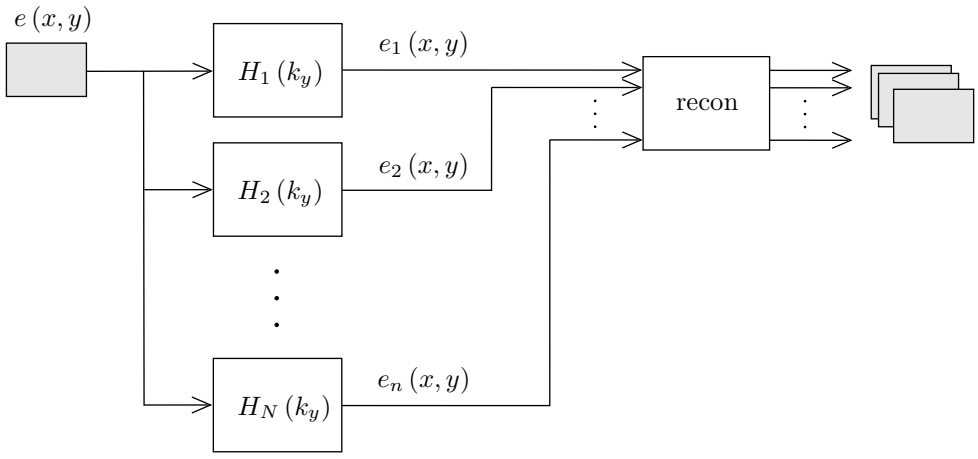

Figure B.2 The echo data is passed through a set of filters with different spatial frequency bandwidths; these correspond to different aspect angles. The filtered data sets are reconstructed, yielding a 3-D array of aspect-dependent SAS images.

The data is windowed about wavenumbers that correspond to different angles as shown in Figure B.1(b), i.e.,

$$E_n(x,k_y) = H_n(k_y)\,E(x,k_y)\,, \tag{B.13}$$

where

$$H_n(k_y) = \text{win}\left(\frac{k_y - k_{yn}}{L}\right), \tag{B.14}$$

k_{yn} is the wavenumber at the centre of the window, and win is the window function. Each windowed data set,

$$e_n(x,y) = \frac{1}{2\pi}\int_{-\infty}^{\infty} E(x,k_y)\exp(jk_y y)\;dk_y \tag{B.15}$$

is reconstructed and the result is a 3-D array of SAS images corresponding to different aspects. This process is illustrated in Figure B.2

There are a number of methods for interpreting the array of aspect-dependent imagery. One method is to colour-code each pixel based on the aspect-dependence [Callow 2005]. Normally each pixel in a SAS image is assigned a value (V) in the HSV colour-space [Foley *et al.* 1997], the saturation (S) is set to zero, and the hue (H) is not used. Instead the different aspects can be assigned different hues. For example, blue for forward ($0 < \theta < 90\,\text{deg}$) and red for aft ($-90 < \theta < 0\,\text{deg}$) aspect-dependence. The saturation can then be used to express the strength of the dependence. This particular mapping is illustrated in Figure B.3. The migration of the specular reflection will change from blue, through white, to red as the sphere is forward, broadside, and then aft of the sonar. Alternatively, each angle can be mapped to a unique hue.

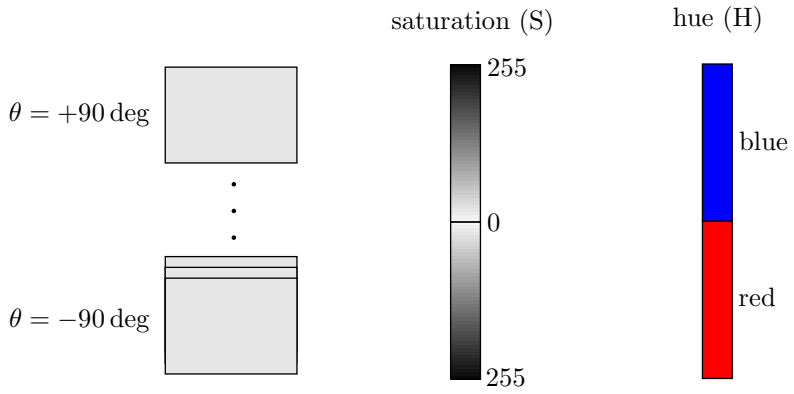

Figure B.3 The aspect-dependence of the 3-D array can be visualised by assigning the forward and aft reflections different hues of blue and red respectively.

Another method of visualising the aspect-dependence is to utilise the time-dimension instead of colour. A series of frames are created corresponding to different along-track positions of the sonar. For each along-track position, y_p, the values of the pixels in the frame are determined by interpolating the 3-D array at the corresponding x, y positions, and at the appropriate wavenumbers corresponding to the angles

$$\theta = \sin^{-1}\left(\frac{y - y_p}{\sqrt{x^2 + (y - y_p)^2}}\right), \tag{B.16}$$

as illustrated in Figure B.4. The result is a movie of the reflectivity as the sonar traverses the scene. The movement of shadows and specular reflections are very apparent using this visualisation technique.

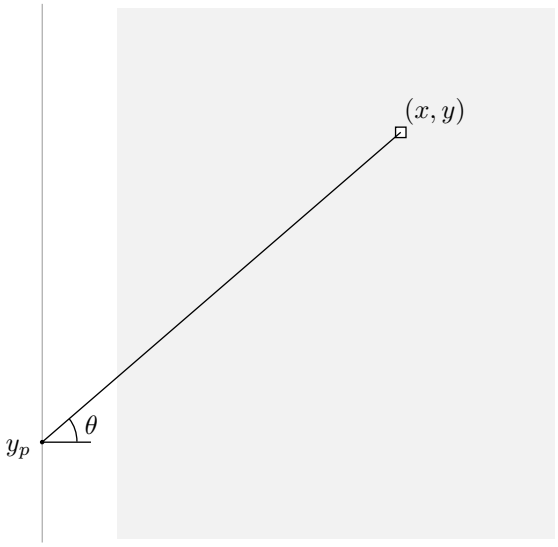

Figure B.4 For an along-track position, y_p, different pixels in the frame correspond to different aspects.

REFERENCES

Anderson, D.P. (2004), 'BOINC: A system for public-resource computing and storage', In *5th IEEE/ACM International Workshop on Grid Computing*, IEEE/ACM, Pittsburg, USA, November.

Anderson, D.P. and Fedak, G. (2006), 'The computational and storage potential of volunteer computing', In *IEEE/ACM International Symposium on Cluster Computing and the Grid*, IEEE/ACM, Singapore, May.

Anderson, D.P., Cobb, J., Korpela, E., Lebofsky, M. and Werthimer, D. (2002), 'SETI@home: An experiment in public-resource computing', In *Communications of the ACM*, ACM, November, pp. 56–61.

Anderson, D.P., Korpela, E. and Walton, R. (2005), 'High-performance task distribution for volunteer computing', In *1st IEEE International Conference on e-Science and Grid Technologies*, IEEE, Melbourne, Australia, December.

Anton, H. and Rorres, C. (1994), *Elementary Linear Algebra: Applications Version*, John Wiley and Sons Inc., 7th ed.

Ascher, D., Dubois, P.F., Hinsen, K., Hugunin, J. and Oliphant, T. (2001), *Numerical Python*, Lawrence Livermore National Laboratory, Livermore, California, September.

Axelsson, S.R.J. (2001), 'Suppressed ambiguity in range by phase-coded waveforms', In *International Geoscience and Remote Sensing Symposium 2001*, June, pp. 2006–2009.

Bahar, H. (1990), *Analog and Digital Signal Processing*, John Wiley and Sons.

Bamler, R. (1992), 'A comparison of range-Doppler and wavenumber domain SAR focusing algorithms', *IEEE Trans. Geosci. Remote Sensing*, Vol. 30, No. 4, July, pp. 706–713.

Banks, S. (2002), *Studies in High Resolution Synthetic Aperture Sonar*, PhD thesis, Department of Electronic and Electrical Engineering, University College London, September.

Barclay, P.J. (2006), *Interferometric Synthetic Aperture Sonar*, PhD thesis, Department of Electrical and Computer Engineering, University of Canterbury, New Zealand, August.

Barclay, P.J., Hayes, M.P. and Gough, P.T. (2002), 'Multi-channel data acquisition for a free-towed synthetic aperture sonar', In *Proceedings of Electronics New Zealand Conference, ENZCON 2002*, ENZCON, Dunedin, New Zealand, November.

Barclay, P.J., Hayes, M.P. and Gough, P.T. (2006), 'Bathymetric results from a multi-frequency InSAS sea-trial', In *Oceans 2006 Asia-Pacific*, IEEE, Singapore, May.

Basu, S. and Bresler, Y. (2000), '$O\left(N^2 \log_2 N\right)$ filtered backprojection reconstruction algorithm for tomography', *IEEE Trans. Image Processing*, Vol. 9, No. 10, October, pp. 1760–1773.

Basu, S. and Bresler, Y. (2002), '$O\left(N^3 \log N\right)$ backprojection algorithm for the 3-D Radon transform', *IEEE Trans. Med. Imag.*, Vol. 21, No. 2, February, pp. 76–88.

Beckmann, P. and Spizzichino, A. (1987), *The Scattering of Electromagnetic Waves from Rough Surfaces*, Artech House.

Bell, J.M. (1995), *A Model for the Simulation of Sidescan Sonar*, PhD thesis, Heriot-Watt University, Edinburgh, Scotland.

Bell, J.M., Reed, S. and Petillot, Y. (2004), 'Applications of sonar simulation in object classification', In , Institute of Acoustics, Leicestershire, UK, September.

Bello, P.A. (1963), 'Characterization of randomly time-variant linear channels', *IEEE Trans. Commun.*, Vol. 11, No. 4, December, pp. 360–393.

Bourne, D.E. and Kendall, P.C. (1977), *Vector Analysis and Cartesian Tensors*, Thomas Nelson and Sons, 2 ed.

Bracewell, R.N. (1986), *The Fourier Transform and its Applications*, McGraw-Hill, 2 ed.

Bray, T., Paoli, J., Sperberg-McQueen, C.M., Maler, E. and Yergeau, F. (2004), 'Extensible Markup Language (XML) 1.0', W3C recommendation, February.

Brookner, E. (Ed.) (1978), *Radar Technology*, Artech House Inc.

Brown, R.G. and Hwang, P.Y.C. (1997), *Introduction to Random Signals and Applied Kalman Filtering*, John Wiley and Sons, 3 ed.

Burnett, D.S. (1988), *Finite Element Analysis*, Addison-Wesley Publishing Co.

Burns, G., Daoud, R. and Vaigl, J. (1994), 'LAM: An open cluster environment for MPI', In *Proc. Supercomputing Symposium*, pp. 379–386.

Cafforio, C., Pratti, C. and Rocca, F. (1991a), 'SAR data focusing using seismic migration techniques', *IEEE Trans. Aerosp. Electron. Syst.*, Vol. 27, No. 2, March, pp. 194–207.

Cafforio, C., Prati, C. and Rocca, F. (1991b), 'Full resolution focusing of Seasat SAR images in the frequency-wave number domain', *J. Robotic Systems*, Vol. 12, No. 3, pp. 491–510.

Callow, H.J. (2003), *Signal Processing for Synthetic Aperture Sonar Image Enhancement*, PhD thesis, Department of Electrical and Computer Engineering, University of Canterbury, New Zealand, April.

Callow, H.J. (2005), Personal communications, December.

Callow, H.J., Hayes, M.P. and Gough, P.T. (2002), 'Wavenumber domain reconstruction of SAR/SAS imagery using single transmitter and multiple-receiver geometry', *IEEE Electronics Letters*, Vol. 38, No. 7, March, pp. 336–338.

Carey, R., Bell, G. and Marrin, C. (1997), *The Virtual Reality Modeling Language (VRML97): International Standard ISO/IEC 14772-1:1997*, Technical Report, The VRML Consortium.

Carrera, W.G., Goodman, R.S. and Majewski, R.M. (1995), *Spotlight Synthetic Aperture Radar: Signal Processing Algorithms.*, Artech House.

Cho, Z.H., Jones, J.P. and Singh, M. (1993), *Foundations of Medical Imaging*, Wiley Interscience.

Christensen, C., Aina, T. and Stainforth, D. (2005), 'The challenge of volunteer computing with lengthy climate model simulations', In *First IEEE International Conference on e-Science and Grid Technologies*, IEEE, Melbourne, December.

Chung, T.J. (2002), *Computational Fluid Dynamics*, Cambridge University Press.

Cook, C.E. and Bernfeld, M. (1967), *Radar Signals: An Introduction to Theory and Application*, Academic Press Inc.

Courmontagne, P., Chaillan, F. and Lerda, O. (2006), 'SAS image de-noising by the curvelet stochastic matched filter transform', In *Oceans 2006 Asia-Pacific*, IEEE, Singapore, May.

Cumming, I.G., Wong, F.H. and Raney, R.K. (1992), 'A SAR processing algorithm with no interpolation', In *International Geoscience and Remote Sensing Symposium*, IEEE, pp. 376–379.

Curlander, J.C. and McDonough, R.N. (1992), *Synthetic Aperture Radar: Systems and signal processing*, John Wiley & Sons, Inc.

Dainty, J.C., Goodman, J.W., Parry, G., McKechnie, T.S., Françon, M. and Ennos, A.E. (1975), *Laser Speckle and Related Phenomena*, Vol. 9 of Topics in Applied Physics, Springer-Verlag.

Davis, B.J. (2001), *Investigation of the Effects of First-order Multi-path Propagation from the Sea Surface in Synthetic Aperture Sonar*, Master's thesis, University of Arizona.

de Heering, P. (1982), *A Synthetic Aperture Sonar Study*, Technical Report, Huntech-Lapp Systems Ltd., Scarborough, Ontario, August.

Del Grosso, V.A. (1974), 'New equations for the speed of sound in natural waters (with comparisons to other equations)', *J. Acoust. Soc. Am.*, Vol. 56, pp. 1084–1091.

Desai, M.D. and Jenkins, W.K. (1992), 'Convolution backprojection image reconstruction for spotlight mode synthetic aperture radar', *IEEE Trans. Image Processing*, Vol. 1, No. 4, October, pp. 505–517.

Douglas, B.L. and Lee, H. (1992), 'Synthetic aperture active sonar imaging', In *IEEE Conference on Acoustics, Speech, and Signal Processing*, IEEE, pp. 37–40.

Douglas, B.L. and Lee, H. (1993), 'Synthetic-aperture sonar imaging with a multiple-element receiver array.', In *IEEE International conference on Acoustics, Speech, and Signal Processing*, IEEE, April, pp. 445–448.

Duffy, D.G. (2001), *Green's Functions with Applications*, Chapman and Hall.

Elzinga, J. and Hearn, D.W. (1972), 'Geometrical solutions for some minimax location problems', *Transportation Science*, pp. 379–394.

Etter, C. (1991), *Underwater Acoustic Modeling: Principles, Techniques and Applications*, Elsevier Science Publishers Ltd.

Fienup, J.R. (1989), 'Phase error correction by shear averaging', In *Signal Recovery and synthesis III*, Optical Society of America, pp. 14–16.

Fisher, F.H. and Simmons, V.P. (1977), 'Sound absorption in sea water', *J. Acoust. Soc. Am.*, No. 62, pp. 558–564.

Foley, J.D., van Dam, A., Feiner, S.K. and Hughes, J.F. (1997), *Computer Graphics: Principles and Practice*, Addison-Wesley, 2 ed.

Fortune, S.A. (2005), *Phase error estimation for synthetic aperture imagery*, PhD thesis, Department of Electrical and Computer Engineering, University of Canterbury, New Zealand, June.

Franceschetti, G., Iodice, A., Riccio, D. and Ruello, G. 'Simulation of SAR raw signal relevant to oil slicks in ocean scenes', In *IEEE Trans. Geosci. Remote Sensing*.

Franceschetti, G., Iodice, A., Riccio, D. and Schirinzi, G. (1992), 'SARAS: A synthetic aperture radar (SAR) raw signal simulator', *IEEE Trans. Geosci. Remote Sensing*, Vol. 30, No. 1, January. Missing last page(s).

Franceschetti, G., Migliaccio, M. and Riccio, D. (1998a), 'On ocean SAR raw signal simulation', *IEEE Trans. Geosci. Remote Sensing*, Vol. 36, No. 1, January, pp. 84–100.

Franceschetti, G., Iodice, A., Migliaccio, M. and Riccio, D. (1998b), 'A novel across-track SAR interferometry simulator', *IEEE Trans. Geosci. Remote Sensing*, Vol. 36, No. 3, May, pp. 950–962.

Franceschetti, G., Iodice, A., Migliaccio, M. and Riccio, D. (1999), 'Scattering from natural rough surfaces modeled by fractional Brownian motion two-dimensional processes', *IEEE Trans. Antennas Propagat.*, Vol. 47, No. 9, September, pp. 1405–1415.

Franceschetti, G., Iodice, A. and Riccio, D. (2000), 'Scattering from dielectric random fractal surfaces via method of moments', *IEEE Trans. Geosci. Remote Sensing*, Vol. 38, No. 4, July, pp. 1644–1653.

Franceschetti, G., Iodice, A., Riccio, D. and Ruello, G. (2001), 'An electromagnetic model for SAR raw signal simulation of urban areas', In *IEEE/ISPRS Workshop on Remote Sensing and Data Fusion over Urban Areas*.

Franceschetti, G., Iodice, A., Riccio, D. and Ruello, G. (2002), 'A 2-D Fourier domain approach for spotlight SAR raw signal simulation of extended scenes', In *Geoscience and Remote Sensing Symposium*, IEEE, June, pp. 853–855.

Francois, R.E. and Garrison, G.R. (1982), 'Sound absorption based on ocean measurements. Part II: boric acid contribution and equation for total absorption', *J. Acoust. Soc. Am.*, Vol. 72, pp. 1879–1890.

Frölind, P.O. (2004), 'Fast back-projection SAR processing using precision interpolation kernels', In *EUSAR 2004*, IEEE, Ulm, Germany, May.

Gilmour, G.A. (1978), 'Synthetic aperture side-looking sonar system', *J. Acoust. Soc. Am.*, Vol. 65, No. 2, May, p. 557. Review of U.S. Patent 4,088,978.

Goff, J.A. and Jordan, T.H. (1989), 'Stochastic modeling of seafloor morphology: resolution of topographic parameters by sea beam data', *IEEE J. Oceanic Eng.*, Vol. 14, No. 4, October, pp. 326–337.

Goodman, J.W. (1968), *Fourier Optics*, McGraw-Hill.

Goodman, J.W. (1985), *Statistical Optics*, Wiley.

Gough, P.T. (2003), Personal communications.

Gough, P.T. and Hawkins, D.W. (1997), 'Imaging algorithms for a strip-map synthetic aperture sonar: Minimizing the effects of aperture errors and aperture undersampling', *IEEE J. Oceanic Eng.*, Vol. 22, No. 1, January, pp. 27–39.

Gough, P.T., Nooncheste r, M.A., Hunter, A.J. and Hayes, M.P. (2006), 'Imagery from a multi-frequency SAS: a comparison of simulated and experimental results', In *International conference on synthetic aperture sonar and synthetic aperture radar*, Institute of Acoustics, Lerici, Italy, September.

Greenfield, P., Miller, T., White, R., Hsu, J.C., Barrett, P. and Küpper, J. (2004), *Numarray (Release 0.8)*, Space Telescope Science Institute, Baltimore, Maryland, January.

Groen, J. (2006), *Adaptive motion compensation in sonar array processing*, PhD thesis, Netherlands organization for applied scientific research (TNO), June.

Hamilton, E.L. (1980), 'Geoacoustic modelling of the sea floor', *J. Acoust. Soc. Am.*, Vol. 68, pp. 1313–1340.

Hamilton, E.L. and Bachman, R.T. (1982), 'Sound velocity and related properties in marine sediments', *J. Acoust. Soc. Am.*, Vol. 72, pp. 1891–1904.

Hansen, R.C. (1981), *Geometric Theory of Diffraction*, IEEE Press.

Hansen, R.E., Sæbø, T.O., Callow, H.J., Hagen, P.E. and Hammerstad, E. (2005), 'Synthetic aperture processing for the HUGIN AUV', In *Oceans Europe 2005*, Brest, France, June.

Hardin, R.H. and Tappert, F.D. (1973), 'Applications of the split-step Fourier method to the numerical solution of nonlinear variable coefficient wave equations', *SIAM*, No. 15.

Harding, C.M., Johnson, R.A. and Lane, R.G. (1999), 'Fast simulation of a Kolmogorov phase screen', *Applied Optics*, No. 38, April, pp. 2161–2170.

Harvey, J.E., Vernold, C.L., Krywonos, A. and Thompson, P.L. (1999), 'Diffracted radiance: a fundamental quantity in nonparaxial scalar diffraction theory', *Applied Optics*, Vol. 38, No. 31, November, pp. 6469–6481.

Hawkins, D.W. (1996), *Synthetic Aperture Imaging Algorithms: with application to wide bandwidth sonar.*, PhD thesis, Department of Electrical and Electronic Engineering, University of Canterbury, New Zealand, October.

Hawkins, D.W. and Gough, P.T. (1995a), 'Multi-resonance design of a Tonpilz transducer using the finite element method', *IEEE Trans. Ultrason., Ferroelect., Freq. Contr.*, Vol. 43, No. 5, September.

Hawkins, D.W. and Gough, P.T. (1995b), 'Recent sea trials of a synthetic aperture sonar', December.

Hawkins, D.W. and Gough, P.T. (2004), 'Temporal doppler effects in SAS', In *Proc. Institute of Acoustics*.

Hayes, M.P. (1989), *A CTFM Synthetic Aperture Sonar*, PhD thesis, Department of Electrical and Electronic Engineering, University of Canterbury, New Zealand, September.

Hayes, M.P. (2002), 'A real-time beam steering system for KiwiSAS-IV', In *Proceedings of Electronics New Zealand Conference, ENZCON 2002*, ENZCON, Hamilton, New Zealand, September, pp. 139–144.

Hayes, M.P. (2004), 'Multipath reduction with a three element interferometric synthetic aperture sonar', In *ECUA 2004*, Norway.

Hayes, M.P. and Gough, P.T. (1992), 'Broad-band synthetic aperture sonar', *IEEE J. Oceanic Eng.*, Vol. 17, No. 1, January, pp. 80–94.

Hayes, M.P., Barclay, P.J., Gough, P.T. and Callow, H.J. (2001), 'Test results from a multi-frequency bathymetric synthetic aperture sonar', In *Oceans 2001*, Honolulu, Hawaii, November, pp. 1682–1687.

Hayes, M.P., Barclay, P.J. and Hawkins, T.J. (2002), 'An embedded compact PCI computer system for a synthetic aperture sonar towfish', In *Proceedings of Electronics New Zealand Conference, ENZCON 2002*, ENZCON, Dunedin, New Zealand, November, pp. 139–144.

Hayes, M.P., Hunter, A.J., Barclay, P.J. and Gough, P.T. (2005), 'Estimating layover in broadband synthetic aperture sonar bathymetry', In *IEEE*, Brest, France, June.

Hayes, M.P., Barclay, P.J. and Gough, P.T. (2006), 'Test results from a multiple-baseline interferometric synthetic aperture sonar', In *ECUA 2006*, Portugal, June.

Haykin, S. (1994), *Communication Systems*, John Wiley and Sons, 3 ed.

Hoppe, H. (1997), 'View-dependent refinement of progressive meshes', In *Computer Graphics and Interactive Techniques*, pp. 189–198.

Hovanessian, S.A. (1980), *Introduction to synthetic array and imaging radars*, Artech House.

Hunt, F.V. (1978), *Origins in Acoustics: the science of sound from antiquity to the age of Newton*, Yale University Press.

Hunter, A.J. and Hayes, M.P. (2004), 'A distributed acoustic renderer for SAS image simulation', In *IVCNZ 2004*, IVCNZ, Akaroa, New Zealand, November.

Hunter, A.J. and Hayes, M.P. (2005a), 'Towards more accurate shadow modelling for simulated SAS imagery', In *Oceans 2005*, IEEE, Brest, France, June.

Hunter, A.J. and Hayes, M.P. (2005b), 'Fast interpolation of beampatterns for partially-occluded and time-variant facets using a fourier domain warping method', In *IVCNZ 2005*, IVCNZ, Dunedin, New Zealand, November.

Hunter, A.J., Hayes, M.P. and Gough, P.T. (2003a), 'A comparison of fast factorised back-projection and wavenumber algorithms for SAS image reconstruction', In *WCU 2003*.

Hunter, A.J., Hayes, M.P. and Gough, P.T. (2003b), 'Simulation of wideband interferometric SAS imagery', In *Oceans 2003*, IEEE/MTS, San Diego, USA, September.

Hunter, A.J., Hayes, M.P. and Gough, P.T. (2006a), 'Fast fourier-domain modelling for a sas simulator with application to time-variant targets, aspect-dependent occlusions, and doppler effects', In *Oceans 2006 Asia-Pacific*, IEEE, Singapore, May.

Hunter, A.J., Gough, P.T. and Hayes, M.P. (2006b), 'Interferometric SAS: a comparison of simulated and experimental results', In *International conference on synthetic aperture sonar and synthetic aperture radar*, Institute of Acoustics, Lerici, Italy, September.

Huss-Lederman, S. (1997), *MPI-2: Extensions to the Message-Passing Interface*, Technical Report, University of Tennessee, Knoxville, Tennessee, July.

Jakowatz, Jnr., C.V., Wahl, D.E., Eichel, P.H., Ghiglia, D.C. and Thompson, P.A. (1996), *Spotlight-Mode Synthetic Aperture Radar: A Signal Processing Approach*, Kluwer Academic Publishers, Boston.

Jean, F. (2006), 'Shadows, a new synthetic aperture sonar system by IXSEA SAS', In *Oceans 2006 Asia-Pacific*, IEEE, Singapore.

Jensen, F.B., Kuperman, W.A., Porter, M.B. and Schmidt, H. (1993), *Computational Ocean Acoustics*, Modern Acoustics and Signal Processing, American Institute of Physics.

Johnson, K.A., Hayes, M.P. and Gough, P.T. (1995), 'Estimating sub-wavelength sway of sonar towfish', *IEEE J. Oceanic Eng.*, Vol. 20, No. 4, October, pp. 258–267.

Kalman, R.E. (1960), 'A new approach to linear filtering and prediction problems', *Transactions of the ASME – Journal of Basic Engineering*, Vol. 82, pp. 35–45.

Kernighan, B.W. and Ritchie, D.M. (1988), *The C Programming Language*, Prentice Hall Inc., 2 ed.

Kim, J. and Lee, S. (2001), 'Truly selective refinement of progressive meshes', In *Graphics Interface*, pp. 101–110.

Kinsler, L.E., Frey, A.R., Coppens, A.B. and Sanders, J.V. (2000), *Fundamentals of Acoustics*, John Wiley and Sons, 4 ed.

Kirchhoff, G.R. (1882), 'Zur theorie der lichtstrahlen'.

Kirkup, S. (1998), *The Boundary Element Method in Acoustics*.

Lane, R.G., Glindemann, A. and Dainty, J.C. (1992), 'Simulation of a Kolmogorov phase screen', *Waves in Random Media*, No. 2, pp. 209–224.

Larson, S.M., Snow, C.D., Shirts, M. and Pande, V.S. (2002), 'Folding@Home and Genome@Home: using distributed computing to tackle previously intractible problems in computational biology', In *Computational Genomics*, Horizon Press.

Latteier, A., Pelletier, M., McDonough, C. and Sabaini, P. (2005), *The Zope Book*, Zope Corporation, Fredericksburg, Virginia, 2.6 ed.

Leroy, C.C. (1968), 'Formulas for the calculation of underwater pressure in acoustics', *J. Acoustical Society of America*, Vol. 44, No. 2, pp. 651–653.

Liang, Z. and Lauterbur, P.C. (2000), *Priciples of Magnetic Resonance Imaging*, Series in Biomedical Engineering, IEEE Press.

Lockwood, S., Brown, A. and Lee, H. (2001), 'Backward propagation image reconstruction techniques for bistatic synthetic-aperture radar imaging systems with circular-aperture configurations', In *Signals, Systems and Computers, 2001*, pp. 110–115.

M^{c}Corkle, J. and Rofheart, M. (1996), 'An order $n^2 \log(n)$ backprojector algorithm for focusing wide-angle wide-bandwidth arbitrary-motion synthetic aperture radar', *SPIE*, pp. 25–36.

Medwin, H. (1975), 'Speed of sound in water: a simple equation for realistic parameters', *J. Acoust. Soc. Am.*

Mie, G. (1908), 'Beitrge zur optik trber medien, speziell kolloidaler metallsungen', *Ann. Phys. Leipzig*, No. 25, pp. 377–445.

Migliaccio, M. (1992), 'Use of SARAS in post-processing techniques', In *IGARSS*, pp. 294–296.

Milman, A.S. (1993), 'SAR imaging using the $\omega - k$ migration', *International Journal of Remote Sensing*, Vol. 14, pp. 1965–1979.

Moore, G.E. (1965), 'Cramming more components onto integrated circuits', *Electronics Magazine*, April.

Moore, J. and Pizer, R. (1984), *Moment methods in electromagnetics: techniques and applications*, Wiley.

Morse, P.M. (1968), *Theoretical Acoustics*, McGraw-Hill Book Company.

Mourad, P.D. and Jackson, D.R. (1989), 'High frequency sonar equation models for bottom backscatter and forward loss', In *Oceans 1989*, IEEE, pp. 1168–1175.

Munson, B.R., Young, D.F. and Okiishi, T.H. (1998), *Fundamentals of Fluid Mechanics*, John Wiley and Sons, 3 ed.

Neilson, R.O. (1991), *Sonar Signal Processing*, Artech House Inc.

Newman, M.E.J. and Barkema, G.T. (1999), *Monte Carlo Methods in Statistical Physics*, Clarendon Press.

Ogilvy, J.A. (1991), *Theory of Wave Scattering from Random Rough Surfaces*, Adam Hilger.

Otto, S. (1995), *MPI: A Message-Passing Interface standard*, Technical Report, University of Tennessee, Knoxville, Tennessee, June.

Phu, P., Ishimaru, A. and Kuga, Y. (1993), 'Controlled millimeter-wave experiments and numerical simulations on the enhanced backscattering from one-dimensional very rough surfaces', *Radio Science*, Vol. 28, No. 4, July–August, pp. 533–548.

Pilbrow, E.N. (2007), *Synthetic Aperture Sonar Micronavigation Using An Active Acoustic Beacon*, PhD thesis, Department of Electrical and Computer Engineering, University of Canterbury.

Pilbrow, E.N., Gough, P.T. and Hayes, M.P. (2002), 'Inertial navigation system for a synthetic aperture sonar towfish', In *ENZCON*, Dunedin, New Zealand, November, pp. 157–162.

Pinto, M., Bellettini, A., Wang, L.S., Munk, P., Myers, V. and Pautet, L. (2004), 'A new synthetic aperture sonar design with multipath mitigation', In *Proceedings of the High-Frequency Ocean Acoustics Conference*, La Jolla, California, March.

Preparata, F.P. and Shamos, M.I. (1985), *Computational Geometry: An Introduction*, Springer-Verlag.

Quesson, B.A.J., Schippers, P., Groen, J., Sabel, J.C. and Driessen, F.P.G. (2005), 'Validation of high frequency acoustic target modeling', In *Oceans Europe 2005*, Brest, France, June.

Raney, R.K., Runge, H., Bamler, R., Cumming, I.G. and Wong, F.H. (1994), 'Precision SAR processing using chirp scaling', *IEEE Trans. Geosci. Remote Sensing*, Vol. 32, No. 4, July, pp. 786–799.

Rayleigh, L. (1945), *The theory of sound*, Vol. 2, Dover Publication, Inc.

Rice, S.O. (1951), 'Reflection of electromagnetic waves from slightly rough surfaces', *Pure Applied Mathematics*, Vol. 4, pp. 351–378.

Rihaczek, A.W. (1969), *Principles of High Resolution Radar*, McGraw Hill Inc.

Riordan, J.E., Omerdic, J.E. and Toal, D. (2005), 'Real-time implementation and application of a sidescan sonar simulator', In *Oceans 2005 Europe*, IEEE, Brest, France, June.

Robert, M.K., Groen, J. and Konijnendijk, N.J. (2005), 'SIMONA: A multi-purpose acoustic data simulator for development and testing of sonar signal processing', In *UDT Europe 2005*.

Rohan, P. (1991), *Introduction to electromagnetic wave propagation*, Artech House.

RUNGE, H. AND BAMLER, R. (1992), 'A novel high precision SAR focusing algorithm based on chirp scaling', In *International Geoscience and Remote Sensing Symposium*, pp. 372–375.

SAMMELMANN, G.S. (1998), 'Computer-readable software and computer-implemented method for performing an integrated sonar simulation', U.S. Patent 6096085, March.

SAMMELMANN, G.S. (2001), 'Propagation and scattering in very shallow water', In *Oceans 2001*, IEEE, Honolulu, Hawaii, November, pp. 337–344.

SAMMELMANN, G.S. (2003), 'High frequency images of proud and buried 3-D targets', In *Oceans 2003*, IEEE, San Diego, California, September, pp. 266–272.

SAMMELMANN, G.S. (2005), Personal communications, August.

SHIPPEY, G., BANKS, S. AND PIHL, J. (2005), 'SAS image reconstruction using fast polar back projection: comparisons with fast factored back projection and fourier-domain imaging', In *Oceans 2005 Europe*, IEEE, June.

SKOLNIK, M. (1990), *Radar Handbook*, McGraw Hill Inc., 2 ed.

SMITH, G.D. (1985), *Numerical Solution of Partial Differential Equations: Finite Difference Methods*, Oxford applied mathematics and computing science series, 3 ed.

SOLIN, P. (2006), *Partial differential equations and the finite element method*, Wiley Interscience.

SOUMEKH, M. (1994), *Fourier Array Imaging*, Prentice Hall, Englewood Cliffs, NJ.

SOUMEKH, M. (1999), *Synthetic Aperture Radar Signal Processing with MATLAB Algorithms*, John Wiley & Sons, Inc.

SPENCER, A.J.M. (1980), *Continuum Mechanics*, Longman.

SQUYRES, J.M. AND LUMSDAINE, A. (2003), 'A component architecture for LAM/MPI', In *Proc. 10th European PVM/MPI Users' Group Meeting*, Springer-Verlag, Venice, Italy, September–October.

STOLT, R.H. (1978), 'Migration by Fourier transform', *Geophysics*, Vol. 43, No. 1, February, pp. 23–48.

STRAUSS, W.A. (1992), *Partial Differential Equations: An Introduction*, John Wiley and Sons.

SUN MICROSYSTEMS (2002), *Sun ONE Grid Engine Administration and User's Guide*, Sun Microsystems.

Taflove, A. and Hagness, S.C. (2000), *Computational electrodynamics : the finite-difference time-domain method*, Artech House.

Thompson, C.J., Hahn, S. and Oskin, M. (2002), 'Using modern graphics architectures for general-purpose computing: a framework and analysis', In *International Symposium on Microarchitecture (MICRO-35)*, IEEE/ACM, Istanbul, Turkey, November, pp. 306–318.

Thorsos, E.I. (1995), 'An investigation of the small-slope approximation for scattering from rough surfaces. Part I. Theory', *J. Acoustic Society of America*, Vol. 97, No. 4, April.

Ulander, L.M.H., Hellsten, H. and Stenström, G. (2003), 'Synthetic-Aperture Radar processing using fast factorized back-projection', *IEEE Trans. Aerosp. Electron. Syst.*, Vol. 39, No. 3, July, pp. 760–776.

Urick, R.J. (1975), *Principles of Underwater Sound*, McGraw-Hill.

van Rossum, G. (2003), *Python reference manual*, Python Labs, December.

Van Trees, H.L. (1968), *Detection, Estimation, and Modulation Theory*, Vol. 3, John Wiley and Sons.

Voronovich, A.G. (1985), 'Small-slope approximation in wave scattering by rough surfaces', *Soviet Physics - Journal of Experimental and Theoretical Physics*, Vol. 62, No. 1, July, pp. 65–70.

Voronovich, A.G. (1996), 'Non-local small-slope approximation for wave scattering from rough surfaces', *Institute of Physics, Waves in random media*, No. 6, pp. 151–167.

W. W. Bonifant, J. (1999), *Interferometric Synthetic Aperture Sonar Processing*, Master's thesis, Georgia Institute of Technology, July.

Welzl, E. (1991), 'Smallest enclosing disks (balls and ellipsoids)', *New Results and New Trends in Computer Science*, Vol. 555, pp. 359–370.

Wilson, W.D. (1960), 'Speed of sound in sea water as a function of temperature, pressure, and salinity', *J. Acoust. Soc. Am.*, Vol. 32.

Wolf, E. and Marchand, E.W. (1964), 'Comparison of the Kirchhoff and the Rayleigh-Sommerfield theories of diffraction at an aperture', *J. Opt. Soc. Am.*, Vol. 54.

Zhou, B. and Greenhalgh, S.A. (1998), 'Composite boundary-valued solution of the 2.5-D Green's function for arbitrary acoustic media', *Geophysics*, No. 63, pp. 1813–1823.

Ziomek, L.J. (1995), *Fundamentals of Acoustic Field Theory and Space-Time Signal Processing*, CRC Press.

INDEX